amU
Aix Marseille Université

NNT : 2024AIXM0001

THÈSE DE DOCTORAT

Soutenue à AMU — Aix-Marseille Université
le 6 Juin 2025 par

Muhammad Luthfi FAJRI

Designer nanostructures from nanocubes as building blocks

Discipline
Physique et Sciences de la Matière

Spécialité
Matière Condensée et Nanosciences

École doctorale
ED 352 – Physique et Sciences de la Matière

Laboratoire/Partenaires de recherche
CINaM – Centre Interdisciplinaire des nanosciences de Marseille

Composition du jury

Mona TRÉGUER-DELAPIERRE Professeure ICMCB, CNRS - Université de Bordeaux	Rapporteure
Benjamin ABÉCASSIS Directeur de Recherches CNRS - ENS de Lyon	Rapporteur
Marco FAUSTINI Professeur LCMCP, CNRS - Sorbonne Université	Examinateur
Sophie CARENCO Directrice de recherche CINaM, CNRS - Aix-Marseille Université	Présidente du jury
Beniamino SCIACCA Chargé de Recherche CINaM, CNRS - Aix-Marseille Université	Directeur de thèse

cnrs

CINaM

Affidavit

Je soussigné, Muhammad Luthfi Fajri, déclare par la présente que le travail présenté dans ce manuscrit est mon propre travail, réalisé sous la direction scientifique de Beniamino Sciacca, dans le respect des principes d'honnêteté, d'intégrité et de responsabilité inhérents à la mission de recherche. Les travaux de recherche et la rédaction de ce manuscrit ont été réalisés dans le respect à la fois de la charte nationale de déontologie des métiers de la recherche et de la charte AMU relative à la lutte contre le plagiat.

Ce travail n'a pas été précédemment soumis en France ou à l'étranger dans une version identique ou similaire à un organisme examinateur.

Fait à Marseille le 8 Avril 2025



Cette œuvre est mise à disposition selon les termes de la Licence Creative Commons Attribution - Pas d'Utilisation Commerciale - Pas de Modification 4.0 International.

List of publications and conference participations

List of publications produced during thesis project:

1. A. Capitaine, **M. L. Fajri**, B. Sciacca, Pushing the limits of capillary assembly for the arbitrary positioning of sub-50nm nanocubes in printable plasmonic surfaces. Small Methods 2024, 8. 2, 2300373, url: :https://doi.org/10.1002/smtd.202300373
2. **Fajri, M. L.**, Kossowski, N., Bouanane, I., Bedu, F., Poungsripong, P., Juliano-Martins, R., Majorel, C., Margeat, O., Le Rouzo, J., Genevet, P., and Sciacca, B., Designer metasurfaces via nanocube assembly at the air-water interface. ACS Nano, 2024, 18. 38, 26088–26102, url: :https://doi.org/doi/10.1021/acsnano.4c06022
3. **Fajri, M. L.**, Capitaine, A., Santinacci, L., and Sciacca, B., Silver nanocube epitaxy via nanogap-induced electrostatics, Small Methods, 2025, url: :https://doi.org/doi/10.1002/smtd.202401304

Participation in conferences and summer schools during the thesis period:

1. Fajri., M. L., and Sciacca, B., Monocrystalline Aluminium Nanopatterns using Nanocubes Building Blocks as Photovoltaics, CNRS Thematic School PVSchool 2022 “Physics of Solar Cells: from basic principles to material science", 3-8 April 2022, Les Houches, France - *Poster presentation*

   url: https://sunlit-team.eu/pv-school-2022/
2. Fajri, M. L. Bouanane, I., Poungsripong, P., Capitaine, A., Margeat, O., Le Rouzo, J., and Sciacca, B., Langmuir-Blodgett nanocube assembly technique: towards monocrystalline continuous films and complex nanostructures, 13th Meetings on Nanosciences Advances, 26 September 2022, Porquerolles, France - *Oral and poster presentation*

   url: https://cnano-paca.fr/conf/mna2022/program.html

3. Fajri, M. L., Bouanane, I., Poungsripong, P., Capitaine, A., Margeat, O., Le Rouzo, J., and Sciacca, B., Langmuir-Blodgett nanocube assembly technique for the fabrication of complex nanostructures, Journée de la Chimie Sud-PACA 2023, 31 March 2023, Marseille, France - *Oral presentation*

   url: https://new.societechimiquedefrance.fr/wp-content/uploads/2023/03/BoA_JdlC2023.pdf

4. Fajri, M. L., Kossowski, N., Bouanane, I., Bedu, F., Poungsripong, P., Martins, R. J., Majorel, C., Margeat, O., Le Rouzo, J., Genevet, P., and Sciacca, B., Nanocubes assembly *à la carte*, E-MRS 2023 Fall Meeting, 18-21 September 2023, Warsaw, Poland - *Oral presentation*

   url: https://www.european-mrs.com/sites/default/files/pdf/emrs_program_21.09.pdf

5. Fajri, M. L., Kossowski, N., Bouanane, I., Bedu, F., Poungsripong, P., Martins, R. J., Majorel, C., Margeat, O., Le Rouzo, J., Genevet, P., and Sciacca, B., Nanocubes assembly *à la carte*, Particle-Based Materials Symposium 2023, 5-6 October 2023, Braunschweig, Germany - *Oral presentation*

   url: https://www.rsc.org/events/detail/76781/particle-based-materials-symposium-2023-pbm-2023

6. Fajri, M. L., Kossowski, N., Bouanane, I., Bedu, F., Poungsripong, P., Martins, R. J., Majorel, C., Margeat, O., Le Rouzo, J., Genevet, P., and Sciacca, B., Nanocubes assembly *à la carte*, 2023 MRS Fall Meeting, 26 November-1 December 2023, Boston, USA - *Oral presentation*

   url: https://www.mrs.org/meetings-events/annual-meetings/archive/meeting/presentations/view/2023-mrs-fall-meeting/2023-mrs-fall-meeting-3952317

Résumé et mots clés

Les réseaux de nanostructures métalliques suscitent un grand intérêt en photonique à l'échelle nanométrique. Les méthodes classiques " top-down ", telles que la lithographie par faisceau d'électrons, permettent de créer des nanostructures complexes et arbitraires, mais restent coûteuses, peu productives, limitent la cristallinité et induisent une rugosité de surface. L'auto-assemblage dirigé par gabarit (templated self-assembly), combinant motifs top-down et nanoparticules colloïdales synthétisées par voie bottom-up, constitue une alternative plus accessible, moins coûteuse et offrant un meilleur contrôle de la composition atomique et de la cristallinité. Cependant, positionner chaque nanoparticule comme une "brique Lego" avec une exactitude nanométrique pour construire des architectures complexes demeure difficile.

Cette thèse explore l'utilisation de nanocubes comme briques élémentaires pour fabriquer des nanostructures aux formes définies par le concepteur. Les nanocubes sont choisis pour leurs propriétés plasmoniques et leur géométrie cubique qui permet potentiellement de fusionner des particules adjacentes en structures monocristallines continues. La recherche s'articule en deux volets : le premier étudie l'assemblage de nanocubes en méta-atomes variés via des moules en PDMS et des techniques d'assemblage à l'interface air-eau. Le second volet concerne la modification chimique post-assemblage. Nous présentons une méthode de soudure épitaxiale de nanocubes d'argent sans agent réducteur, évitant la nucléation homogène nuisible à la qualité optique, mettant en évidence le rôle inattendu des nanointerstices via des interactions électrostatiques. Par ailleurs, nous avons étudié la croissance contrôlée d'argent sur des nanocubes d'or, entraînant une élongation anisotrope et des structures complexes, soulignant l'importance de l'espacement initial entre particules comme guide de croissance directionnelle. Enfin, nous montrons nos premières tentatives de fabrication de nanoparticules d'aluminium en forme d'octopodes par gravure chimique sélective de nanocubes supportés sur substrat.

Mots clés: plasmonique, nanostructures, épitaxie, or, argent, aluminium, nanomotifs, nanocubes, bottom-up, templated self-assembly, nanomateriaux.

Abstract and keywords

Arrays of metallic nanostructures are of great interest in nanoscale photonics. Conventional top-down methods, such as electron beam lithography, allow the creation of complex and arbitrary nanostructures but are costly, have limited throughput, offer poor crystallinity control, and introduce surface roughness. Templated self-assembly, combining top-down patterned templates with bottom-up synthesized colloidal nanoparticles, provides a more accessible, cost-effective alternative with improved control over atomic composition and crystallinity. However, positioning each nanoparticle as a "Lego block" with nanoscale accuracy to build complex architectures remains challenging.

This thesis explores using nanocubes as building blocks for fabricating custom-shaped nanostructures. Nanocubes were chosen due to their plasmonic properties and cubic geometry, which can potentially fuse adjacent particles into continuous monocrystalline structures. The research is divided into two parts: first, assembling nanocubes into varied meta-atoms using nanopatterned PDMS molds and air-water interface assembly techniques; second, chemically modifying these assembled structures post-assembly. We demonstrate a method of epitaxial welding of silver nanocubes without a reducing agent, avoiding unwanted nucleation that would deteriorate optical quality, highlighting the unexpected role of nanogaps mediated by electrostatic interactions. Additionally, we studied controlled silver overgrowth on gold nanocubes, resulting in anisotropic elongation and complex structures, emphasizing the critical role of initial particle spacing as a directional growth guide. Finally, we present our initial efforts in fabricating aluminum octopod nanoparticles through selective chemical etching of substrate-supported aluminum nanocubes.

Keywords: plasmonic, nanostructures, epitaxy, gold, silver, aluminum, nanopatterning, nanocubes, bottom-up, templated self-assembly, nanomaterials.

Résumé étendu

Introduction

Les réseaux de nanostructures métalliques suscitent un vif intérêt dans le domaine multidisciplinaire de la photonique à l'échelle nanométrique. Traditionnellement, les méthodes de nanofabrication dites " top-down ", telles que la lithographie par faisceau d'électrons, permettent de créer des nanostructures complexes, arbitraires et à haute résolution. Toutefois, ces approches présentent plusieurs limites : elles sont coûteuses, peu productives, offrent un contrôle limité sur la cristallinité des matériaux et induisent une rugosité de surface indésirable.

L'auto-assemblage dirigé par gabarit (templated self-assembly) s'impose comme une alternative prometteuse, combinant des moules fabriqués par des techniques top-down avec des nanoparticules colloïdales synthétisées par voie bottom-up. Cette approche hybride se révèle généralement plus accessible, plus économique, et permet un meilleur contrôle de la composition atomique et de la qualité cristalline. Malgré ces avantages, la réalisation de motifs nanométriques complexes à partir de nanoparticules agissant comme des " briques Lego " reste un défi majeur. Une telle précision exige un positionnement déterministe des nanoparticules avec une exactitude nanométrique, un objectif encore difficile à atteindre de manière fiable.

Cette thèse explore l'utilisation de nanocubes comme briques élémentaires pour la fabrication de nanostructures aux formes définies par le concepteur. Les nanocubes sont choisis non seulement pour leurs propriétés plasmoniques intéressantes, mais aussi pour leur géométrie cubique, qui offre la possibilité de fusionner des particules adjacentes en structures monocristallines continues.

Ce travail s'articule en deux volets principaux. Le premier volet porte sur l'assemblage de nanocubes en méta-atomes de formes variées, organisés en réseaux à l'aide de moules en PDMS nanostructurés et de techniques d'assemblage à l'interface air-eau. Le second volet est consacré à la modification chimique post-assemblage de ces nanostructures supportées sur substrat.

Nous présentons notamment une méthode de soudure épitaxiale de nanocubes d'argent en solution, réalisée sans agent réducteur, permettant ainsi de supprimer la nucléation homogène qui compromettrait la qualité optique des structures finales. Ce procédé met en évidence le rôle inattendu des nanointerstices dans la promotion de la soudure épitaxiale, induite par des interactions électrostatiques.

Par ailleurs, une autre approche consiste à faire croître de l'argent sur des nanocubes d'or de manière contrôlée, menant à une élongation anisotrope et à la formation de

structures complexes. Nos résultats suggèrent que la taille initiale du nanointerstice joue un rôle déterminant dans le mode de croissance, en facilitant soit la soudure interparticulaire, soit une extension directionnelle anisotrope. Bien que le mécanisme précis reste à élucider, ces travaux introduisent un principe de conception selon lequel les interstices entre particules peuvent servir de gabarits physiques à la croissance dirigée.

Enfin, nous présentons nos premières tentatives de fabrication de nanoparticules d'aluminium en forme d'octopodes, par gravure chimique sélective de nanocubes d'aluminium supportés sur substrat. Ces structures, aux pointes acérées, présentent un fort potentiel pour des applications en spectroscopie Raman exaltée de surface (SERS) à l'échelle d'une seule nanoparticule.

Métasurfaces sur mesure par assemblage de nanocubes à l'interface air-eau

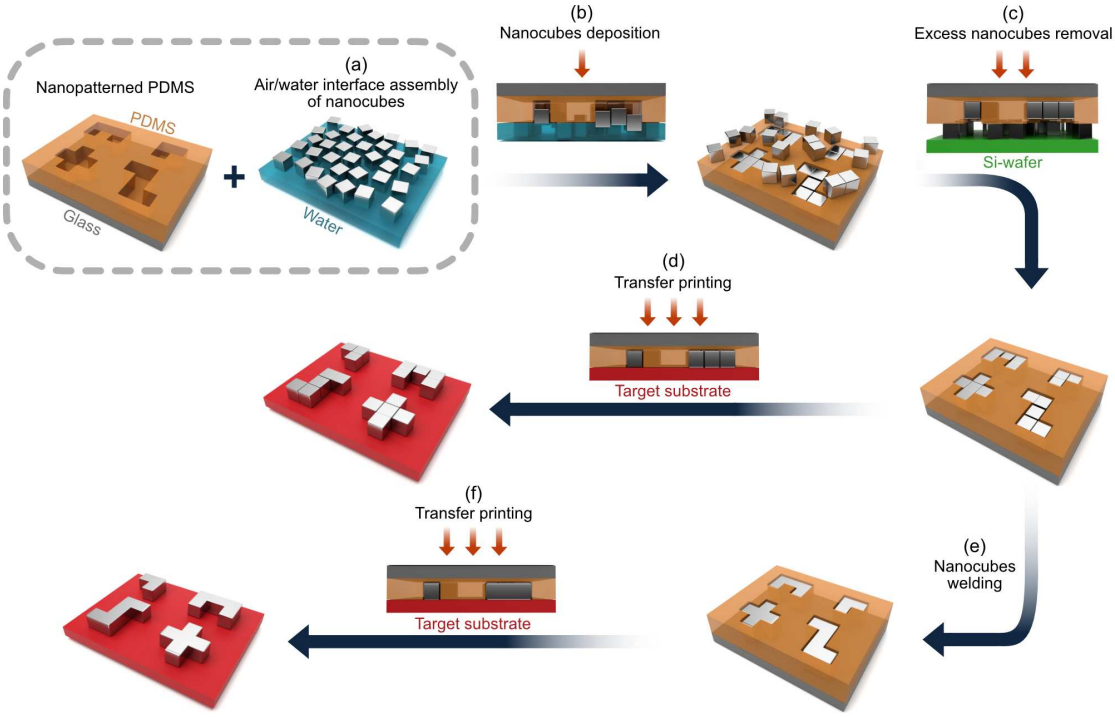

Figure 1.: Schéma de fabrication de nanostructures à partir de nanocubes. Le procédé comprend: (a) la dispersion des nanocubes à l'interface air-eau, (b) l'assemblage dirigé des nanocubes, (c) l'élimination des nanocubes en excès. Deux voies sont ensuite possibles: (d) l'impression par transfert des nanocubes assemblés sur le substrat cible, ou (e) la soudure des nanocubes pour former des nanostructures continues, suivie de (f) l'impression par transfert sur le substrat cible.

Le Chapitre 2 explore l'utilisation de l'assemblage à l'interface air-eau pour former dans un premier temps une monocouche dense de nanocubes, utilisés comme briques de construction, qui est ensuite transférée sur des substrats en polydiméthylsiloxane (PDMS) nanostructurés, indépendamment de la densité, de la forme ou de la taille des motifs. Nous avons réalisé des optimisations paramétriques clés, notamment la densité de nanoparticules à l'interface, l'angle de dépôt et la méthode d'assemblage. Cette approche permet de fabriquer des réseaux de nanostructures constitués de méta-atomes complexes, avec une densité élevée et une résolution latérale à l'échelle d'une seule nanoparticule sur des surfaces de l'ordre du sous-millimètre. Le processus d'assemblage est illustré dans la Figure 1.

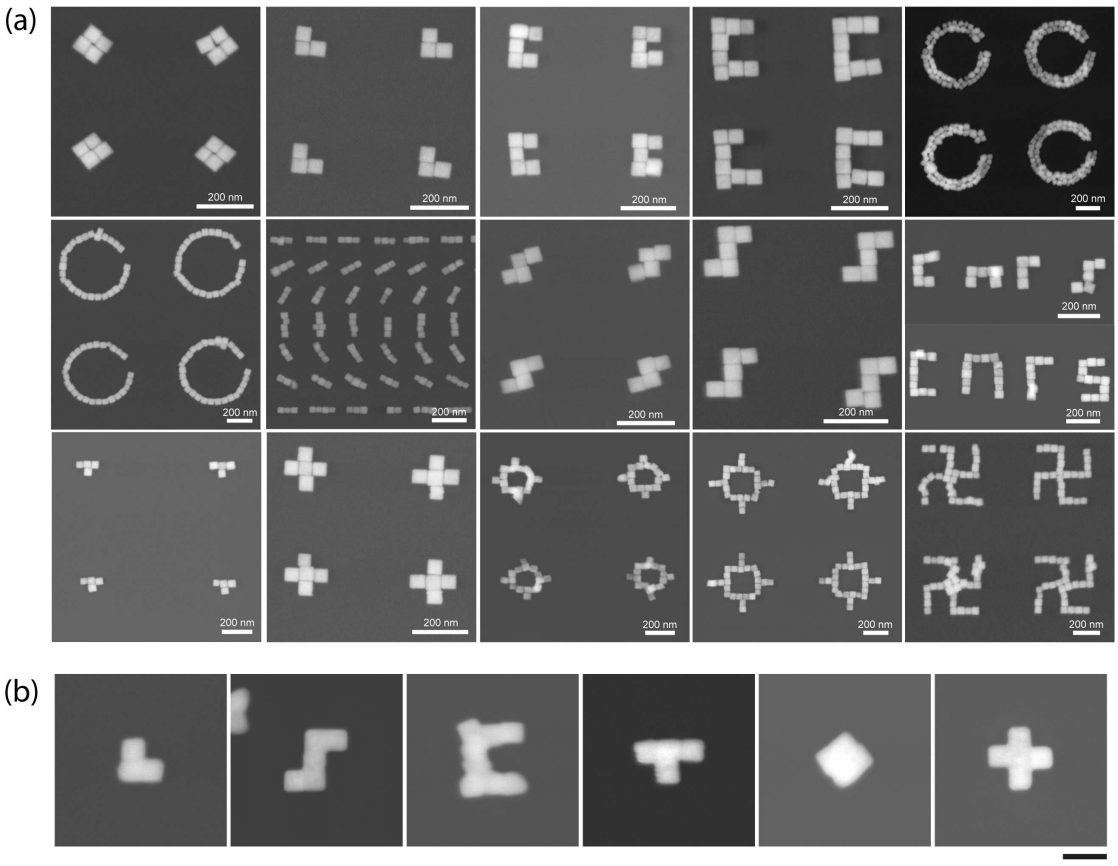

Figure 2.: (a) Images MEB montrant l'assemblage de nanocubes d'argent en différentes configurations géométriques de méta-atomes. (b) Formation de nanostructures monocristallines continues par soudure chimique de nanocubes d'or. Barre d'échelle : 100 nm.

Nous démontrons l'assemblage de nanocubes en géométries complexes de méta-atomes, rarement réalisables avec les techniques conventionnelles. Celles-ci incluent des formes en U, L, croix, S et T, ainsi que des gammadions, des résonateurs en anneau fendu et des structures de type Pancharatnam–Berry (PB), comme illustré en Figure 2a. En outre, comme montré en Figure 2b, ces nanocubes assemblés peu-

vent être transformés en nanostructures continues par épitaxie de nanocubes. Cela est réalisé en utilisant une méthode précédemment rapportée pour les nanocubes d'or[1]. Nous montrons également qu'il est possible de réaliser l'épitaxie avec des nanocubes d'argent, en suivant une stratégie décrite en détail au Chapitre 3. Ce processus de soudure permet de relier les nanocubes adjacents, formant ainsi des méta-atomes monocristallins pouvant être transférés du PDMS vers divers substrats par impression par contact. À titre de démonstration, nous présentons une métasurface à dichroïsme circulaire composée de méta-atomes en forme de gammadions capables d'absorber sélectivement la lumière en fonction de sa polarisation circulaire. De plus, nous présentons une métasurface Pancharatnam–Berry capable de dévier la lumière transmise selon la longueur d'onde et la chiralité du faisceau incident polarisé circulairement.

Épitaxie de nanocubes d'argent par interaction électrostatique induite par nanointerstice

Dans le Chapitre 3, nous nous concentrons sur la soudure épitaxiale de nanocubes d'argent, permettant la fabrication de nanostructures monocristallines d'argent aux géométries arbitraires. Ce travail complète celui initié par la Dre Anna Capitaine dans sa thèse de doctorat[2]. Notre étude propose une méthode en solution pour souder des nanocubes d'argent sans recourir à un agent réducteur. Cette approche empêche la nucléation homogène en solution, qui dégraderait autrement la qualité optique des nanostructures.

Nous avons observé que les nanointerstices jouent un rôle clé dans la promotion d'une croissance anisotrope, largement induite par les interactions électrostatiques entre des nanocubes étroitement espacés. Pour maintenir un équilibre entre dissolution des nanocubes, croissance contrôlée et préservation de leur forme, il a été essentiel d'optimiser certains paramètres tels que la température, la concentration en acide nitrique, et l'ajout d'agents stabilisants de forme comme les ions bromure et le trifluoroacétate d'argent. La soudure ne s'est révélée efficace que lorsque les nanocubes étaient positionnés à proximité immédiate les uns des autres. En revanche, ceux présentant des espacements plus importants ne se soudaient pas, probablement en raison d'un manque d'espèces d'argent disponibles en l'absence d'un agent réducteur. Cette observation renforce l'hypothèse selon laquelle l'accumulation d'ions dans le nanointerstice, sous l'effet d'interactions électrostatiques, est à l'origine du processus de soudure.

En combinant cette stratégie de soudure avec différentes méthodes d'assemblage de nanoparticules, notamment l'assemblage capillaire et l'assemblage à l'interface air-eau, nous démontrons la construction ascendante de nanostructures monocristallines complexes, comme illustré dans la Figure 3. Ces résultats sont confirmés par des images TEM montrant l'alignement des plans cristallins au niveau des jonctions soudées.

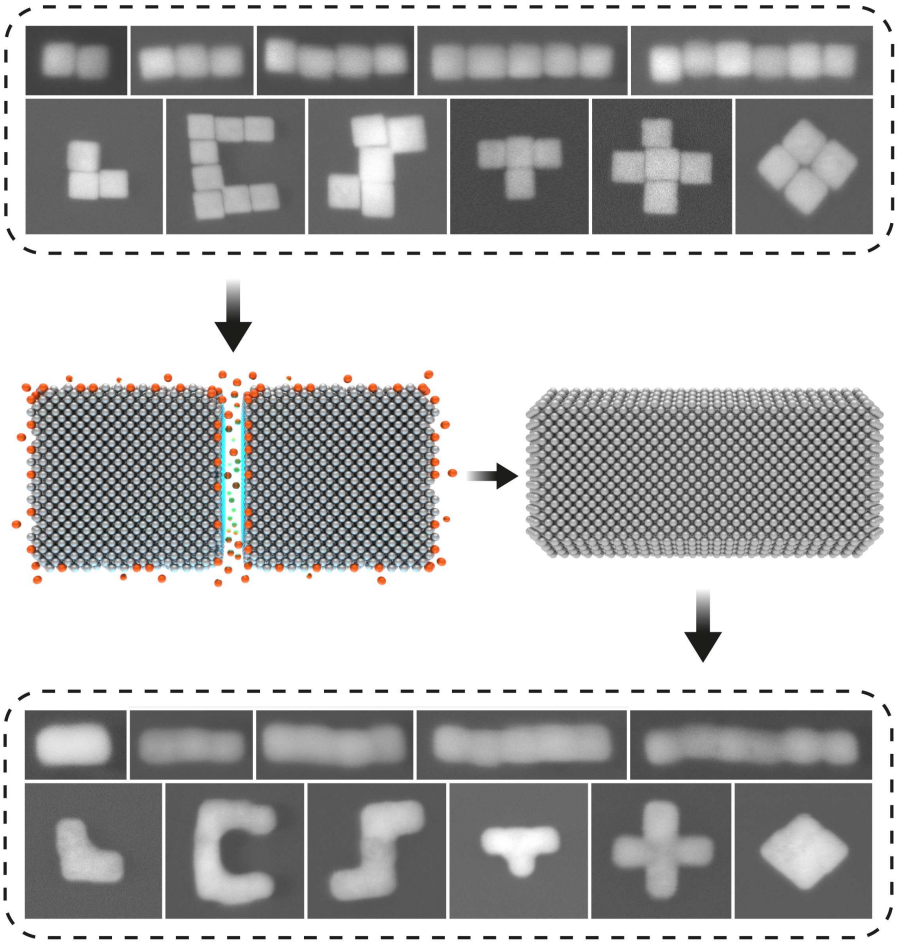

Figure 3.: Images MEB et schémas illustrant la soudure épitaxiale de nanocubes d'argent assemblés en méta-atomes de formes variées.

Croissance contrôlée de nanocubes supportés sur substrat : épitaxie de nanocubes et croissance anisotrope

Le chapitre 4 traite de la surcroissance chimique de nanocubes déposés sur un substrat. L'objectif était d'adapter une méthode bien connue de synthèse colloïdale de type cœur-coquille afin d'obtenir une soudure épitaxiale. Bien que des conditions de soudure constantes n'aient pas été entièrement atteintes, le processus de surcroissance de l'argent a conduit à deux résultats distincts, comme illustré dans la Figure 4 : la soudure entre nanocubes et l'élongation anisotrope.

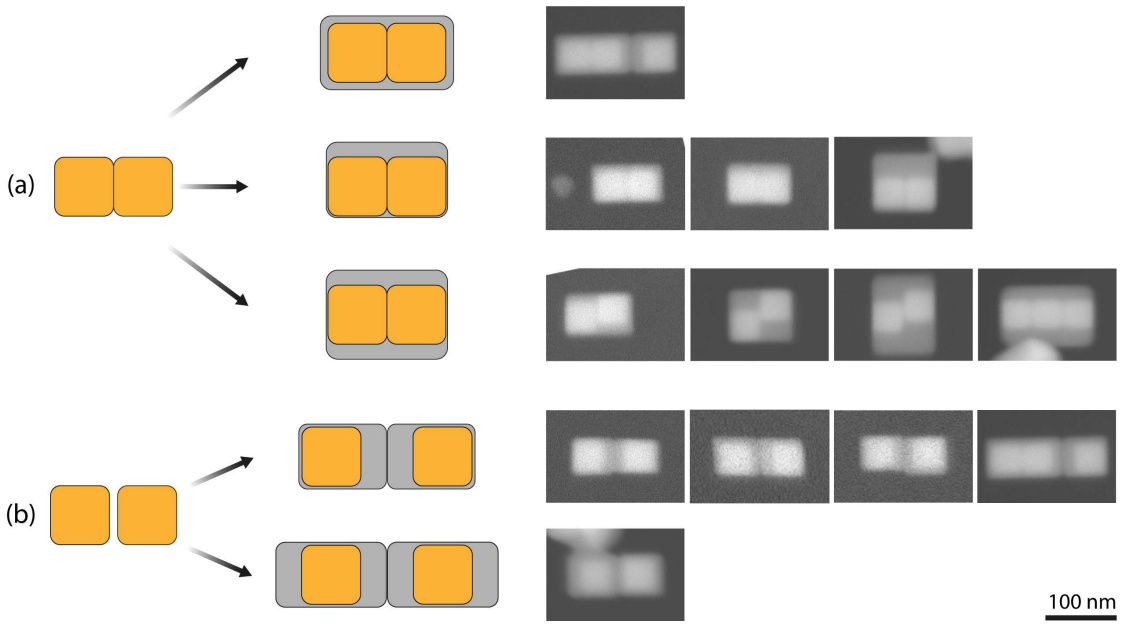

Figure 4.: Images MEB illustrant deux types distincts de surcroissance d'argent sur des dimères de nanocubes d'or : (a) soudure nanométrique : nanocubes d'or placés à très faible distance, et (b) surcroissance anisotrope : nanocubes d'or séparés par des interstices plus larges.

Comme confirmé dans la Figure 5, nous avons constaté que la contamination par le PVP (polyvinylpyrrolidone) était probablement un facteur clé contribuant à l'augmentation de la croissance anisotrope observée. La Figure 5a montre que l'augmentation de la concentration de PVP dans la solution de surcroissance est corrélée à un rapport d'aspect plus élevé dans les structures en dimère obtenues. Cela suggère que le PVP joue un rôle important dans l'orientation de la dynamique de croissance. Une analyse quantitative plus poussée dans les Figures 5c et 5d vient appuyer cette conclusion. En effet, lorsque la concentration de PVP augmente, la croissance de l'argent dans les directions extérieures du dimère, désignées par a, b et c, est progressivement inhibée. En parallèle, la croissance dans l'interstice entre les nanocubes (direction x) est renforcée. Ces observations indiquent que le PVP pourrait empêcher la déposition de matière sur les facettes exposées des nanocubes tout en favorisant une croissance localisée dans la région confinée entre les particules, ce qui amplifie l'anisotropie.

Nos observations suggèrent que le nanointerstice initial joue un rôle déterminant dans le mode de surcroissance, qu'il s'agisse de soudure ou de croissance anisotrope. Il peut soit favoriser la connexion entre particules, soit agir comme un guide physique dirigeant la croissance de manière directionnelle. Pour approfondir cette hypothèse, nous avons utilisé des dimères de nanocubes comme système modèle et mené des études paramétriques systématiques en faisant varier le temps de réaction, la concentration en PVP, la température, la taille des graines et la forme des particules. Ces expériences ont montré que ce principe de conception pourrait potentiellement

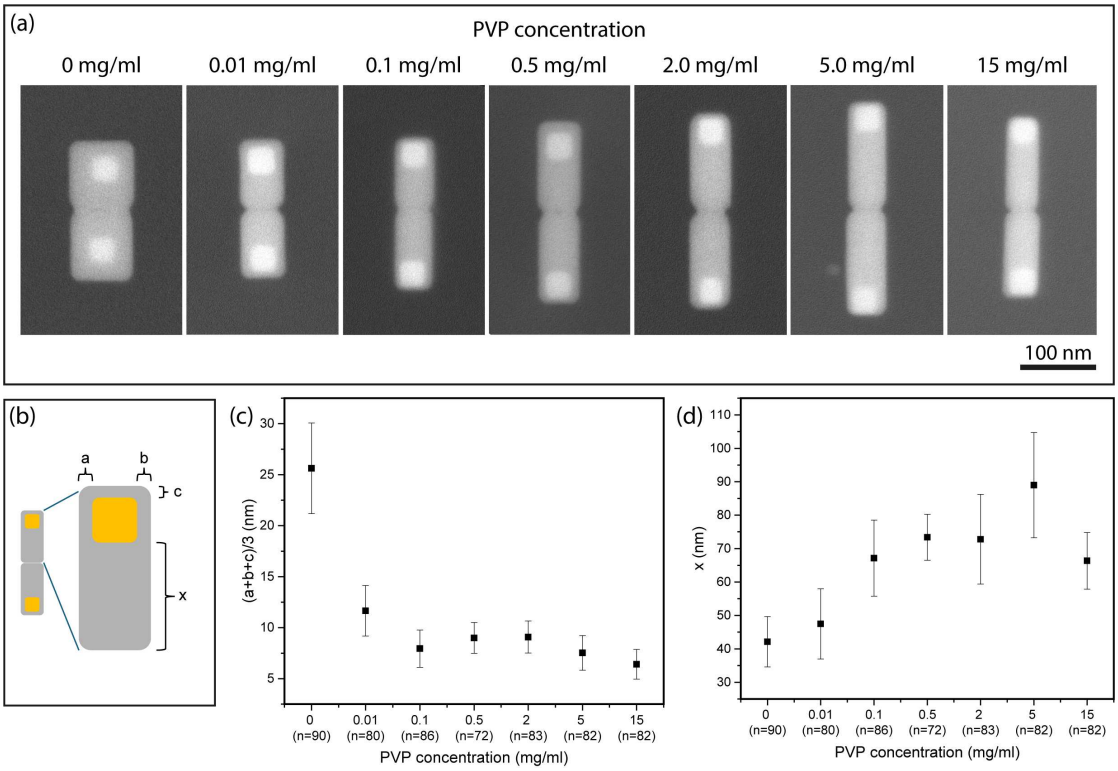

Figure 5.: (a) Images MEB représentatives montrant la surcroissance d'argent sur des dimères de nanocubes d'or déposés sur des substrats en verre, après réaction à 70°C pendant 3 heures sous différentes concentrations de PVP. (b) Schéma illustrant les directions de surcroissance de l'argent sur les dimères de nanocubes d'or, définies comme a, b, c et x. (c) Mesure quantitative de la surcroissance moyenne le long des directions a, b et c. (d) Mesure quantitative de la surcroissance d'argent au sein de l'interstice entre les particules (direction x). n = nombre d'échantillons.

être étendu à la construction de nanostructures plus complexes au-delà des simples dimères. Bien que le mécanisme exact à l'origine de cette croissance anisotrope reste à élucider, le cadre présenté dans ce chapitre introduit une approche prometteuse pour la fabrication de nanostructures complexes, où l'intervalle interparticulaire sert d'indice structurel pour guider la croissance directionnelle. Dans l'ensemble, ces résultats apportent des pistes précieuses pour l'ingénierie des interfaces nanocristallines et le développement de nanostructures monocristallines adaptées aux métasurfaces optoélectroniques.

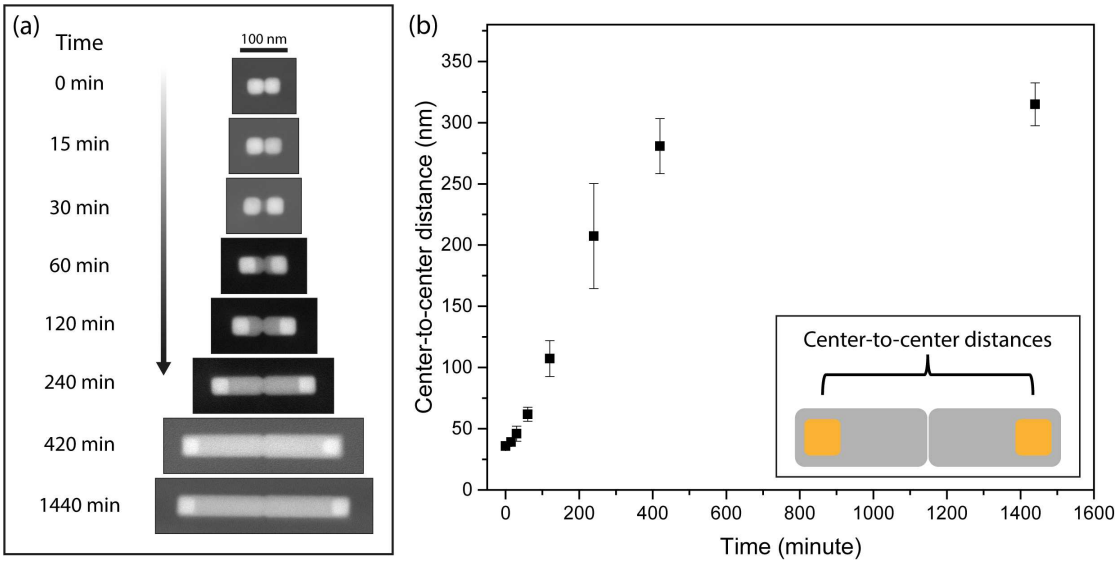

Figure 6.: (a) Images MEB représentatives montrant la surcroissance d'argent sur des dimères de nanocubes d'or déposés sur des substrats en verre, réalisée à 70°C en présence de 5.0 mg/mL de PVP, à différents temps de réaction. (b) Mesure quantitative de la surcroissance d'argent dans l'intervalle interparticulaire, représentée par la distance entre les centres des nanocubes. Encadré : illustration schématique définissant la mesure de centre à centre.

Perspectives - Octopodes en aluminium à angles vifs obtenus par gravure anisotrope de nanocubes

Enfin, le chapitre 5 a été initialement consacré à l'exploration de la soudure épitaxiale de nanocubes d'aluminium par gravure chimique, en utilisant un mélange d'acide chromique et phosphorique comme agent de gravure. Bien que la soudure reproductible n'ait pas été atteinte, nous présentons des résultats préliminaires démontrant une stratégie alternative permettant de fabriquer des nano-octopodes d'aluminium directement sur un substrat. En exploitant une gravure anisotrope, nous avons pu contrôler la transformation morphologique des nanocubes en octopodes ramifiés aux pointes acérées. Comme illustré à la Figure 7, le degré d'affûtage des pointes et l'étendue de la ramification peuvent être finement ajustés en modulant la durée de gravure. La microscopie électronique en transmission (MET) a confirmé que les pointes des octopodes conservent leur caractère cristallin après gravure, indiquant la préservation de la structure métallique sous-jacente. Par ailleurs, une caractérisation optique par spectroscopie de diffusion en champ sombre a mis en évidence une évolution spectrale en accord avec les changements morphologiques observés. Notamment, un décalage vers le bleu de la résonance plasmonique a été observé à mesure que les structures développaient des pointes plus nettes. Cette approche de gravure contrôlée constitue ainsi une voie prometteuse pour l'ingénierie de nanos-

tructures en aluminium aux géométries personnalisées, ouvrant la voie à de nouvelles applications en tant que plateformes pour la spectroscopie Raman exaltée de surface (SERS).

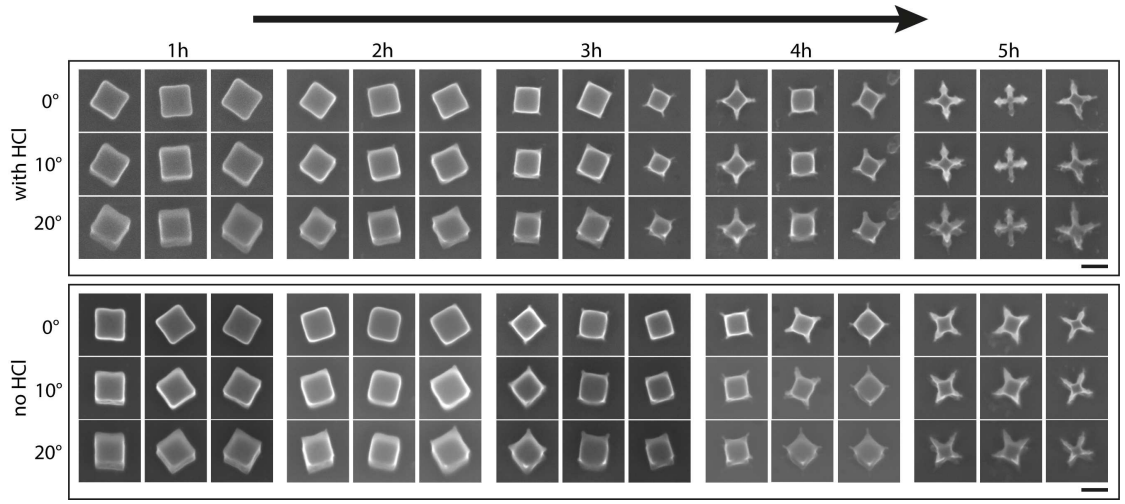

Figure 7.: Images MEB inclinées montrant la morphologie des nanocubes d'aluminium gravés pendant différentes durées, avec et sans addition de HCl.

De manière générale, cette thèse contribue au développement de stratégies de fabrication de nanostructures métalliques en utilisant des nanoparticules métalliques comme éléments de base, combinées à des techniques d'assemblage dirigé par gabarit, afin de créer des structures de complexité accrue. Elle explore également la modification structurale de ces nanoparticules assemblées par des approches chimiques en solution. Tout au long de ce travail, une attention particulière a été portée à la qualité des matériaux obtenus ainsi qu'à la résolution latérale à l'échelle de la nanoparticule individuelle. Si plusieurs des questions de recherche initiales posées au début de ma thèse ont trouvé des réponses, certaines restent encore ouvertes, tandis que de nouvelles interrogations ont émergé. Les points suivants mettent en lumière certaines de ces questions en suspens, qui pourraient constituer des pistes pour de futures recherches.

Extrait du Chapitre 2 :

- L'une des principales limites de la technique d'assemblage réside dans la reproductibilité de l'étape de retrait des nanocubes en excès. Quelles méthodes alternatives pourraient offrir une meilleure régularité et précision pour cette étape ?
- Un facteur important contribuant au manque de reproductibilité est la nature manuelle de cette opération de retrait, qui introduit une variabilité rendant difficile l'interprétation d'études systématiques sur l'influence de la profondeur des tranchées. D'après notre expérience, la méthode fonctionne de manière satisfaisante pour des tranchées d'environ 80–90 nm de profondeur, mais devient peu fiable pour des motifs plus superficiels, comme ceux de 55 nm. Si un

système automatisé était développé pour standardiser cette étape, une question importante serait alors : quelle est la profondeur de tranchée optimale pour garantir un assemblage efficace et reproductible des nanoparticules ?

- Par ailleurs, serait-il possible d'appliquer une stratégie d'assemblage séquentiel sur des gabarits présentant des tranchées plus profondes afin de construire des nanostructures ayant une épaisseur verticale supérieure à celle d'un seul nanocube ?

Extrait du Chapitre 3 :

- Quelle est la distance maximale entre deux nanocubes (nanogap) permettant encore une soudure épitaxiale réussie de nanocubes d'argent ?
- Si les nanocubes ne sont pas parfaitement alignés face à face, quel est l'angle maximal de désalignement initial pouvant tout de même aboutir à une structure monocristalline après soudure ?

Extrait du Chapitre 4 :

- Quelle est la distance minimale de nanogap nécessaire pour permettre une interconnexion épitaxiale entre deux nanocubes ?
- Quelle est la distance maximale de nanogap permettant encore une surcroissance anisotrope dans les dimères de nanocubes d'or ?
- Quel est le mécanisme sous-jacent à la surcroissance anisotrope dans les dimères de nanocubes d'or ? Pourquoi la soudure ne se produit-elle pas dans l'interstice alors que la surcroissance y est observée ?
- Quel est le mécanisme de surcroissance anisotrope dans les dimères composés de nanoparticules non cubiques ?
- Le nanogap subnanométrique apparemment présent entre les dimères surcroissants pourrait-il être exploité pour des applications fonctionnelles ?
- Cette stratégie de surcroissance anisotrope peut-elle être étendue à d'autres matériaux que l'or et l'argent ?

Extrait du Chapitre 5 :

- Quelle est la morphologie tridimensionnelle complète des octopodes en aluminium, et comment la fine couche d'oxyde est-elle répartie sur ces structures ?
- Quel est le mécanisme sous-jacent responsable de la gravure anisotrope observée sur les nanocubes d'aluminium ?
- Ce processus de gravure pourrait-il être réalisé en milieu colloïdal (en solution) et, dans ce cas, quelles en seraient les conditions optimales ?
- Si la reformation de la couche d'oxyde pouvait être efficacement empêchée après la gravure, serait-il envisageable de réaliser une surcroissance sur les nanocubes d'aluminium ? Cela pourrait s'avérer utile non seulement pour la soudure épitaxiale, mais aussi comme plateforme pour la synthèse colloïdale à base de germes.

Acknowledgements

This PhD journey has been many things: long, intense, humbling, and at times, surprisingly exciting, and also both intellectually and personally rewarding. I owe a great deal of thanks to the people who've been part of it, whether directly in the lab or indirectly through their prayers, support, and encouragement.

First and foremost, I want to thank my supervisor, Beniamino Sciacca, for your care, enthusiasm, availability, and giving me the freedom to explore, mess up, learn, and grow. Thank you for your trust, your support and guidance. All of which I truly appreciate.

I would also like to sincerely thank the jury members for their time, thoughtful evaluation, and valuable feedback. In addition, I warmly thank the members of my Comité de Suivi Individuel, Professor Marco Faustini and Professor Jean-Manuel Raimundo, for their support, guidance, and constructive advice throughout the course of this doctoral journey.

I am also grateful to the past and current members of the CNAM team (formerly SUNE) for creating a stimulating, supportive, and collaborative environment. Special thanks go to Lionel Santinacci for his valuable discussions, collaboration, and assistance in navigating technical and administrative challenges, as well as for his efforts in organizing the team events. I am especially thankful to Anna for her immense help in helping me adapt to PhD work, and for her support, discussions, and collaboration on a major part of this thesis. I would also like to thank Piw and Vyshnav for the many laughs and memories we shared, both in the lab and beyond, during dinners, travels, and conferences. These moments were a welcome break and helped me refresh the mind away from lab work. My thanks also go to Luigi, Sugi, and Ali for their humour, support, engaging discussions, help with experiments, and the overall positive atmosphere they brought to the lab, which made the workdays lighter and more enjoyable. Thank you also to Gaëlle, Sueyeong, Karim, Nayef, and Blanche for being such wonderful officemates and for creating a cheerful and supportive workspace. Finally, I am grateful to Charles, Clémence, Georgia, Kik, Saai, Yudha, Surya, Diego, Kostis, Julien, Pierre, Mohit, Ashwin, Lea, and many others for the moments we shared together.

I would also like to thank Ibtissem Bouanane for introducing me to the nanocube assembly technique, as well as the group of Professor Patrice Genevet. In particular, I thank Renato Juliano-Martins and Clément Majorel for their assistance with the experimental setup and measurement of the metasurfaces during our visit in Nice, and Nicolas Kossowski for his contributions on the optical simulations. Their expertise and support have enriched this project in countless ways.

Many thanks to Alexandre Altié and Damien Chaudanson for their support with electron microscopy, which constitutes a major part of this work, and for their trust in allowing me to work independently on the machine outside of regular hours. I am also grateful to Frédéric Bedu and Igor Ozerov for their help with cleanroom procedures and electron beam lithography. I would like to thank Cyril Coudreau and Gilles Arthaud for their technical support, and Frédéric Brunel for his assistance with the Milli-Q water system, chemical supplies, and bunker logistics.

On a personal note, I would like to express my heartfelt appreciation to my family back home, my mother, my father, my older brother, my little sister and little brother, for their constant prayers, encouragement, patience, and belief in me. I would also like to thank Mas Dede and Mbak Sarah for their care and support, making Marseille feels more like a home away from home.

Finally, I am grateful for the opportunities and challenges encountered along the way, each of which has helped me grow both personally and professionally.



"jer basuki mawa beya"

Contents

Affidavit 2

List of publications and conference participations 3

Résumé et mots clés 5

Abstract and keywords 6

Résumé étendu 7

Acknowledgements 17

Contents 20

List of Figures 24

List of Tables 29

General Introduction 30

1. State-of-the-art 33

1.1. Why shape and crystallinity is important in metallic nanostructures? . 35

1.1.1. Localized surface plasmon resonance 35

1.1.2. Metallic nanostructures in optoelectronic devices 37

1.1.3. Grain boundaries on metallic nanostructures 43

1.1.4. Conclusion 45

1.2. Fabrication of monocrystalline nanostructures with arbitrary shapes . 46

1.2.1. Conventional approach 46

1.2.2. Bottom-up nanoparticles self-assembly 49

1.2.3. Templated self-assembly approach 53

1.2.4. The air-water interface assembly 57

1.2.5. Conclusion 61

1.3. Towards monocrystalline nanostructures from assembled nanocubes . 61

1.3.1. Wet-chemical structural modification of assembled nanoparticles 61

1.3.2. Towards monocrystalline nanostructures 62

1.3.3. Conclusion 65

1.4. Thesis motivation 65

2. Designer metasurfaces *via* nanocube assembly at the air-water interface **67**
2.1. Introduction . . . 69
2.2. Results and discussion . . . 70
2.2.1. Nanopatterning from nanocubes at the air-water interface assembly . . . 70
2.2.2. Assembly with nanoparticles of various shapes . . . 76
2.2.3. Continuous monocrystalline meta-atoms . . . 83
2.2.4. Transfer printing onto a substrate . . . 84
2.2.5. Nanocubes assembly mechanism . . . 85
2.2.6. Optical characterization . . . 91
2.2.7. Nanocubes assembly into Pancharatnam-Berry (PB) phase metasurface . . . 92
2.3. Conclusion . . . 99

3. Silver nanocube epitaxy *via* nanogap-induced electrostatics **100**
3.1. Introduction . . . 102
3.2. Results and discussion . . . 103
3.2.1. What drives silver nanocube welding? . . . 105
3.2.2. Optimizing conditions for silver nanocubes welding . . . 106
3.2.3. Electrochemical analysis of spotaneous silver dissolution . . . 108
3.2.4. Epitaxial welding towards complex nanostructures . . . 111
3.2.5. TEM characterization of welded nanostructures . . . 112
3.2.6. Optical characterization . . . 114
3.3. Conclusion . . . 115

4. Controlled overgrowth of substrate-supported nanocubes: nanocube epitaxy and anisotropic growth **116**
4.1. Introduction . . . 118
4.2. Results and discussion . . . 119
4.2.1. Overgrowth on substrate-supported silver nanocubes . . . 119
4.2.2. Anisotropic overgrowth on substrate-supported nanocubes: dimer model . . . 121
4.3. Conclusion . . . 146

5. Perspectives - Sharp-cornered aluminum octopods via anisotropic nanocube etching **147**
5.1. Introduction . . . 149
5.2. Results and discussion . . . 150
5.2.1. Effort toward nanocube epitaxial welding and observation of anisotropic etching . . . 150
5.2.2. Formation of aluminum octopods with adjustable degree of branching . . . 152
5.2.3. Characterization of aluminum octopods . . . 155
5.2.4. Preliminary assessment of aluminum octopods for SERS . . . 158

5.3. Conclusion . . . 159

General conclusion **160**

Bibliography **164**

APPENDIX **190**

A. Nanoparticles synthesis **191**
A.1. Materials and methods . . . 191
A.1.1. Chemicals and Materials . . . 191
A.1.2. Synthesis of ~40 nm silver nanocubes by polyol synthesis . . . 191
A.1.3. Synthesis of PVP-capped ~30, ~36, ~40, ~48, and ~53 nm gold nanocubes . . . 193
A.1.4. Synthesis of PVP-capped ~63, ~80, and ~100 nm gold nanocubes 197
A.1.5. Synthesis of ~43 nm gold icosahedra . . . 199
A.1.6. Synthesis of gold octahedra . . . 200
A.1.7. Synthesis of aluminum nanocubes . . . 201

B. Nanocube assembly at the air-water interface: Materials and methods **203**
B.1. Materials and methods . . . 203
B.1.1. Chemicals and Materials . . . 203
B.1.2. Fabrication of silicon master by electron beam lithography . . . 203
B.1.3. Fabrication of patterned PDMS . . . 205
B.1.4. Assembly of silver nanocubes using Langmuir trough . . . 206
B.1.5. Assembly on a small homemade PTFE well . . . 206
B.1.6. Excess nanocubes removal . . . 207
B.1.7. Transfer Printing . . . 207
B.1.8. Nanocubes chemical welding . . . 208
B.1.9. Low-density nanocubes on UVO-treated vs untreated nanopatterned PDMS substrates . . . 208
B.2. Supporting information . . . 209

C. Silver nanocube epitaxy *via* nanogap-induced electrostatics: Materials and methods **210**
C.1. Materials and methods . . . 210
C.1.1. Chemicals and materials . . . 210
C.1.2. Nanocubes synthesis and assembly . . . 210
C.1.3. Chemical welding . . . 211
C.1.4. Electrochemical characterizations . . . 211
C.2. Supporting information . . . 212
C.2.1. Standard potential calculations . . . 212
C.2.2. Work functions of the metals . . . 214
C.2.3. Nitric acid oxidation of silver nanocubes . . . 214

C.2.4. Multiphysics simulations 215

D. Controlled overgrowth of substrate-supported nanocubes: Materials and methods 225
D.1. Materials and methods 225
D.1.1. Chemicals and materials 225
D.1.2. Overgrowth of silver-shell on silver nanocubes 225
D.1.3. Overgrowth of silver-shell on gold nanocubes 226
D.1.4. Anisotropic overgrowth of silver-shell on gold nanocubes 226
D.2. Supporting information 228

E. Sharp-cornered aluminum octopods via anisotropic nanocube etching: Materials and methods 234
E.1. Materials and methods 234
E.1.1. Chemicals and materials 234
E.1.2. Preparation of chromic-phosphoric acid (1.8% CrO3 and 7.1% H3PO4) 234
E.1.3. Anisotropic etching of aluminum nanocubes on silicon substrate 234
E.2. Supporting information 235

F. Nanocubes thermal welding 241
F.0.1. Thermal welding of silver nanocubes 241

List of Figures

1. Assemblage de nanocubes à l'interface air-eau . . . 8
2. Assemblage de nanocubes d'argent en différentes configurations géométriques de méta-atomes . . . 9
3. Images MEB et schémas illustrant la soudure épitaxiale de nanocubes d'argent assemblés en méta-atomes de formes variées. . . . 11
4. Deux types distincts de surcroissance d'argent sur des dimères de nanocubes d'or. . . . 12
5. Surcroissance d'argent sur des dimères de nanocubes d'or sous différentes concentrations de PVP . . . 13
6. Évolution de la surcroissance d'argent sur des dimères de nanocubes d'or à différents temps de réaction. . . . 14
7. Images MEB inclinées montrant la morphologie des nanocubes d'aluminium gravés pendant différentes durées, avec et sans addition de HCl . . . 15

1.1. LSPR . . . 36
1.2. LSPR sensor . . . 37
1.3. LSPR sensor . . . 38
1.4. Split-ring resonator . . . 40
1.5. Examples of various meta-atom geometries . . . 41
1.6. Pancharatnam-Berry phase metasurface . . . 42
1.7. Monocrystallinity in plasmonic nanostructures . . . 43
1.8. Silver transparent electrodes . . . 45
1.9. Czochralski method . . . 46
1.10. Molecular beam epitaxy . . . 47
1.11. Lithography processes . . . 48
1.12. Free energy landscape of self-assembly . . . 50
1.13. Self-assembly of nanocubes . . . 52
1.14. Free energy landscape in templated self-assembly . . . 54
1.15. Nanoparticles imprint lithography . . . 55
1.16. Template-assisted DNA-mediated assembly . . . 56
1.17. Capillary assembly of nanoparticles . . . 57
1.18. Air-liquid interface assembly . . . 58
1.19. Nanoparticles assembly using Langmuir trough . . . 59
1.20. Templated self-assembly using air-liquid interface assembly . . . 60
1.21. Templated self-assembly using air-liquid interface assembly . . . 63

1.22. Templated self-assembly using air-liquid interface assembly 64

2.1. Nanocubes assembly at air-water interface 71
2.2. Various meta-atoms from nanocubes assembly 72
2.3. Assembly on the best sample 73
2.4. Various meta-atoms from nanocubes assembly 74
2.5. Assembly of individual nanocube. 75
2.6. Assembly of 32 nm Au rounded nanocubes on various meta-atoms . . 76
2.7. Assembly of 40 nm Ag nanocubes on large split-ring pattern 76
2.8. Assembly of 55 nm Ag nanocubes on various meta-atoms 77
2.9. Assembly of 43 nm Au icosahedra on various meta-atoms 78
2.10. Assembly of 43 nm Au icosahedra on various meta-atoms 79
2.11. Assembly of 43 nm Au icosahedra on various meta-atoms 80
2.12. Assembly of ~40 nm Ag nanocubes on grid 80
2.13. Assembly of ~48 nm Au nanocubes on various meta-atoms 81
2.14. Assembly of ~48 nm Au nanocubes on various meta-atoms 82
2.15. Welded gold nanocubes 83
2.16. Silver nanocubes assembly transferred on Si-wafer. 84
2.17. Silver nanocubes assembly transferred on glass post-welding. 85
2.18. Silicon master mold 85
2.19. Filling fraction calculation 86
2.20. Nanocube assembly mechanism 87
2.21. Assembly influenced by surface tension 88
2.22. Assembly influenced by PDMS surface 89
2.23. Assembly influenced by dipping angle 90
2.24. Dark-field images and transmission spectra of various meta-atoms . . 91
2.25. Circular dichroism of gammadion meta-atoms 92
2.26. Pancharatnam-Berry metasurface from nanocubes 94
2.27. Assembly of ~40 nm Ag nanocubes on PB metasurface 95
2.28. FDTD simulation for incident LCP 96
2.29. FDTD simulation for incident RCP 97
2.30. Comparison before and after welding of PB metasurface 98
2.31. Comparison before and after welding of PB metasurface 98

3.1. Diagram of nanocubes assembly and epitaxial welding 103
3.2. Nanogap before and after $NaBH_4$ treatment 104
3.3. Multiphysics simulation of silver nanocubes welding 106
3.4. Welding parameter adjustment on PDMS substrate 107
3.5. CV of Ag nanocubes on glassy carbon 109
3.6. Ag nanocubes on glassy carbon 110
3.7. CV of Ag nanocubes on glassy carbon in solution 110
3.8. Collage image of welded Ag nanostructures 112
3.9. TEM images of welded nanostructures 113
3.10. Dark-field scattering spectra of unwelded and welded L-shape and Cross-shape nanostructures. 114

4.1. Overgrowth of silver on silver nanocubes at diferent time 120
4.2. SEM images showing silver overgrowth on gold nanocubes drop-cast onto silicon and glass substrates. 122
4.3. Behavior of silver overgrowth on gold nanocubes dimer 122
4.4. SEM images illustrating anisotropic silver overgrowth on gold nanocubes drop-cast onto a silicon substrate resulting from PVP contamination. . 123
4.5. Silver overgrowth on gold nanocubes dimer under different PVP concentrations 124
4.6. Selected SEM images showing more pronounced silver overgrowth within the gaps of nanocube dimers compared to individual nanocubes 125
4.7. Evolution of silver overgrowth on gold nanocube dimers at various reaction times 125
4.8. Multiple cycles of silver overgrowth on gold nanocube dimers 126
4.9. Effect of temperature on silver overgrowth of gold nanocube dimers . . 127
4.10. Arrhenius plot of silver overgrowth on gold nanocubes dimer 128
4.11. Control experiments investigating the effect CTAC: CTAC was replaced with CTAB 129
4.12. Schematic illustration of the possible mechanisms involved in the anisotropic overgrowth process 130
4.13. Comparison of nanogap sizes in PVP-capped and CTAC-capped gold nanocube dimers before and after $NaBH_4$ treatment 131
4.14. EM images of silver overgrowth on PVP-capped gold nanocubes deposited on glass substrates subjected to different pretreatments 133
4.15. SEM images of silver overgrowth on CTAC-capped gold nanocubes deposited on glass substrates subjected to different pretreatments 133
4.16. First operando spectroscopy experiment of anisotropic overgrowth . . 136
4.17. Second operando spectroscopy experiment on anisotropic overgrowth 137
4.18. Design rules for anisotropic silver overgrowth on gold nanocubes . . . 141
4.19. Silver surface diffusion on the central nanocube during the overgrowth process. 142
4.20. SEM images of overgrown nanostructures captured at a 25° tilt 143
4.21. SEM images of silver overgrowth on gold nanocube dimers with varying cube sizes 143
4.22. Silver overgrowth on gold icosahedra and octahedral nanoparticles . . 144
4.23. Silver overgrowth at 80°C on 55 nm silver nanocubes arranged in a grid pattern on a glass substrate via nanoparticle imprint lithography, followed by reaction 145

5.1. Etching of drop-cast ~113nm aluminum nanocubes on a silicon substrate using a mixture of chromic-phosphoric acid and HCl 151
5.2. SEM images showing the effect of etching time on ~113 nm aluminum nanocubes drop-cast onto a silicon substrate 153
5.3. Tilted SEM images showing the morphology of aluminum nanocubes etched at different durations, with and without the addition of HCl . . 154

5.4. 40° tilted SEM images showing the morphology of aluminum nanocubes after 5 hours of etching in chromic-phosphoric acid without the addition of HCl . . . 154
5.5. TEM image of a selected aluminum octopod, with high-magnification views highlighting four corner tips and the central region. . . . 156
5.6. Scattering spectra of individual nanoparticles after etching for 0, 1, 2, 3, 4, and 5 hours. . . . 157
5.7. SERS spectra of PABA . . . 158

A.1. 40 nm Ag nanocubes synthesis . . . 192
A.2. 30 nm Au nanocubes synthesis . . . 194
A.3. 36 nm Au nanocubes synthesis . . . 194
A.4. 40 nm Au nanocubes synthesis . . . 195
A.5. 48 nm Au nanocubes synthesis . . . 195
A.6. 53 nm Au nanocubes synthesis . . . 196
A.7. 63 nm Au nanocubes synthesis . . . 197
A.8. 80 nm Au nanocubes synthesis . . . 198
A.9. 100 nm Au nanocubes synthesis . . . 198
A.10. 43 nm Au icosahedra synthesis . . . 199
A.11. SEM images of gold octahedra . . . 200
A.12. SEM images of aluminum nanocubes synthesized with reaction times of 20, 30, and 40 minutes. . . . 202

B.1. Silicon master mold . . . 204
B.2. Setup for excess nanocubes removal and tranfer printing . . . 209

C.1. Ag nanocubes after ligand removal on Si . . . 216
C.2. Pourbaix diagram for Ag^{+} . . . 217
C.3. Ag nanocubes welding on Si . . . 218
C.4. Ag wleding parameter adjustment on different substrates . . . 218
C.5. Control experiments on dark condition . . . 219
C.6. Control experiments regarding CF_3COO^{-} precursor . . . 219
C.7. Control experiments on Argon purged welding solution . . . 220
C.8. Large area SEM images of welded Ag dimer . . . 221
C.9. Complementary TEM images of welded Ag nanostructures obtained from LB films . . . 222
C.10. Complementary TEM images of 2x2 nanocubes meta-atoms . . . 223
C.11. Bright-field and dark-field TEM images of 2x2 nanocubes square meta-atoms. . . . 224

D.1. Setup for the silver overgrowth reaction . . . 226
D.2. Multiple silver overgrowth on silver nanocubes . . . 228
D.3. Variation in reagent addition rate for the overgrowth of silver on silver nanocubes . . . 229

D.4. Variation in silver reagents for the overgrowth of silver on silver nanocubes on silicon substrate . . . 230
D.5. Variation in silver reagents for the overgrowth of silver on silver nanocubes on glass substrate . . . 231
D.6. SEM images showing silver overgrowth on gold nanocubes assembled into grid patterns on a glass substrate via nanoparticle imprint lithography. 232
D.7. SEM images illustrating silver overgrowth on gold nanocubes assembled within split-ring-patterned PDMS trenches. . . . 233
D.8. Homemade setup for operando spectroscopy during silver overgrowth on gold nanocube dimers . . . 233

E.1. TEM images of aluminum nanocubes synthesized after 40 minutes of reaction time. . . . 235
E.2. Successive etching of drop-cast ~113 nm aluminum nanocubes on a silicon substrate using chromic-phosphoric acid at 85°C. . . . 236
E.3. Formation of tip-to-tip conical dimer nanoparticles resulting from anisotropic etching of aluminum nanorod byproducts . . . 237
E.4. SEM EDX elemental analysis of the silicon substrate and the aluminum octopod . . . 237
E.5. TEM image of a selected aluminum octopod, with high-magnification views highlighting four corner tips . . . 238
E.6. TEM image of a selected aluminum octopod, with high-magnification views highlighting four corner tips . . . 239
E.7. SEM images of aluminum octopods captured at different tilt angles, illustrating shape transformation under prolonged electron beam exposure 240

F.1. SEM images of assembled silver nanocubes thermally welded on nanopatterned PDMS at 250°C. . . . 242

List of Tables

1.1. Types of interactions driving nanoparticle assembly 51

4.1. Rate constants calculated at 120 min 129
4.2. Silver overgrowth data for Arrhenius plot 129

C.1. Standard thermodynamic properties of chemical substances[221]. . . . 215

General Introduction

The ability to transform and assemble materials has been pivotal in shaping the evolution of society and technology since ancient times. Its significance is evident in the way prehistoric periods are commonly classified based on the primary materials used to make tools, such as the Stone Age, Bronze Age, and Iron Age. As humanity progresses, the introduction of new materials and technology, tools used in manufacturing processes and daily life have become increasingly complex. They now consist of components with increasingly intricate shapes and materials, assembled to serve a variety of purposes. In current modern life, it is difficult to imagine a world without functional machines made from assembled, multi-shaped, and multi-material components, like personal computers, mobile phones, cars, and airplanes. This underscores the profound importance of technologies that enable the shaping and assembly of materials in advancing human civilization.

In the contemporary era of nanotechnology, this progress is particularly evident, driven by the meticulous manipulation of materials at the nanometer scale to fabricate nanostructures. Nanostructures are generally agreed, although loosely defined, as structures having at least one dimension within the 100-nanometer range. The interest in creating such structures stems from several reasons. First, whether driven by curiosity or artistic pursuits, humans are inherently drawn to the ability to shape and manipulate materials at a scale once perceived impossible.

The second lies in the more fundamental characteristic of nanostructures: they can exhibit behaviors distinct from those of bulk materials. As the size decreases, the number of atoms is reduced, leading to fewer available electron energy levels. This results in discrete electronic energy states, giving rise to notable phenomena associated with interband and intraband electron transitions, as observed in quantum dots, for example. When the size becomes sufficiently small, conduction electrons in the metals also become spatially confined, leading to the phenomenon of localized surface plasmon. Additionally, as the size reduces, the proportion of surface atoms becomes significantly much larger than that of the interior. This, in turn, creates a much higher density of reactive sites involved in surface processes such as adsorption and chemical transformations (catalysis), resulting in several-fold increase in reactivity. What about shape? The shape of nanostructures is also a crucial characteristic, as it influences charge transport and confinement. Moreover, it dictates the arrangement of surface atoms, which directly affects the distribution of active sites and, consequently, their functional properties[3, 4].

The third reason relates to the statistical properties of ensembles formed by numerous individual interaction events. When a single nanostructure interacts with

energy or materials (analytes), it produces a response signal. By arranging many such nanostructures, either in an array of orderly or disorderly manner, over a given area, the cumulative interactions generate a collective signal. This collective of many individual responses can lead to statistically meaningful events, which is particularly useful in applications such as sensors, enhancing their sensitivity and reliability[5].

Fourth, when nanostructures are arranged in close proximity, they can interact with one another, leading to collective properties that do not present at the individual level. These interactions can result in unique optical or electronic behaviors, making them valuable for applications in plasmonics and photonics[5, 6].

The quality of a nanostructure plays a crucial role in determining the performance of functional devices. One key aspect of quality is the presence of grain boundaries in the crystalline structure. While grain boundaries can be deliberately engineered for certain applications, such as catalysis, where they have beneficial effects[7], they are generally undesirable in photonic and electronic devices due to their tendency to cause energy loss. In metals, grain boundaries reduce electrical conductivity and increase optical losses[8, 9], while in semiconductors, they serve as recombination centers for generated excitons, negatively impacting efficiency. Thus, achieving high-quality, monocrystalline nanostructures through appropriate nanofabrication techniques is essential for optimizing device functionality.

Nanofabrication approaches are generally categorized into three main groups: top-down methods, bottom-up methods, and their combination, known as templated assembly. The top-down approach involves reducing the size of a bulk materials through lithographic processes. This method can offer high resolution (sub-10 nm)[10] and allows precise control over the geometry and arrangement of nanostructures according to design specifications. However, it relies on expensive specialized equipment, such as electron beam lithography (EBL), and is often time-consuming and complex, posing challenges for large-scale production. In contrast, bottom-up methods involve assembling nanostructures from smaller building blocks, such as molecules, polymers, or colloidal particles composed of polymers, semiconductors, or metals. These approaches are more cost-effective and provide better control over atomic composition and crystallinity. However, they offer limited flexibility in determining the geometry and arrangement of nanostructures on surfaces.

To overcome the limitations of both methods, templated assembly combines the strengths of both approaches by using top-down-fabricated templates to guide the organization of nanoparticles. While this strategy helps bridge the gap between precision and scalability, achieving deterministic positioning and arrangements of nanoparticles remains a significant challenge.

The research presented in this thesis is aimed to explore the possibility to fabricate nanostructures using nanoparticles as building blocks, with shape corresponding to the designer's wish *via* templated assembly. Here, we mostly focus on the use of silver and gold nanocubes as a building block to create structures with a higher degree of complexity. Beyond their intriguing plasmonic properties, their cubic geometry is chosen because the possibility to transform adjacent nanocubes into continuous

nanostructure with monocrystalline quality[1, 11]. In overall, this thesis can be summarized into two main parts. The first part investigates the assembly of nanocubes into variously shaped meta-atoms arranged in arrays using air-water interface assembly techniques. The second part focuses on the structural modification of the assembled nanostructures on substrates through wet-chemical approaches, including epitaxial welding, overgrowth processes, and chemical etching.

This thesis starts, in Chapter 1, with an overview to fundamental phenomena intended to assist non-specialist readers. It further outlines current progress in nanostructuring processes, nanoparticle assembly techniques, and chemical methods for structural modifications. Key state-of-the-art studies relevant to this thesis will be highlighted to set the stage for subsequent chapters.

Chapter 2 will focus on the assembly of nanoparticles, with particular emphasis on nanocubes, using the air-water interface assembly technique to create designer meta-atoms with diverse geometries.

Chapter 3 is devoted on the silver nanocubes epitaxial welding, enabling the creation of monocrystalline silver nanostructures with arbitrary shapes. This chapter complements the work initiated by Dr. Anna Capitaine in her doctoral thesis[2].

Chapter 4 discusses chemical overgrowth techniques applied to substrate-supported nanocubes, aiming to achieve effective welding. Additionally, the chapter describes observed phenomena related to anisotropic overgrowth.

Finally, Chapter 5 reports on efforts to develop aluminum-based nanostructures from nanocubes as a potential platforms for single-nanoparticle Surface-Enhanced Raman Scattering (SERS).

1. State-of-the-art[1]

In this chapter, I will discuss the importance of shape and monocrystallinity in metallic nanostructures, particularly in relation to their optical properties. I then will present an overview of current templated nanoparticle assembly methods that enable the fabrication of metallic nanostructures with designer-defined geometries. In addition, I will explore wet-chemical strategies capable of transforming assembled metal nanocubes into continuous monocrystalline structures. The chapter concludes by outlining several fundamental questions that form the central motivation for this PhD thesis.

[1]Part of this chapter has been published in: M. L. Fajri , N. Kossowski, I. Bouanane, F. Bedu, P. Poungsripong, R. Juliano-Martins, C. Majorel, O. Margeat, J. L. Rouzo, P. Genevet, B. Sciacca, "Designer metasurfaces *via* nanocube assembly at the air-water interface" *ACS Nano* **2024**, 18, 38, 26088-26102

Summary

1.1. Why shape and crystallinity is important in metallic nanostructures? . 35
1.1.1. Localized surface plasmon resonance 35
1.1.2. Metallic nanostructures in optoelectronic devices 37
1.1.2.1. Sensors 37
1.1.2.2. Metasurface 39
1.1.3. Grain boundaries on metallic nanostructures 43
1.1.4. Conclusion 45
1.2. Fabrication of monocrystalline nanostructures with arbitrary shapes . 46
1.2.1. Conventional approach 46
1.2.1.1. Monocrystalline bulk materials 46
1.2.1.2. Nanostructuring of bulk materials 48
1.2.1.3. Conclusion 49
1.2.2. Bottom-up nanoparticles self-assembly 49
1.2.3. Templated self-assembly approach 53
1.2.4. The air-water interface assembly 57
1.2.5. Conclusion 61
1.3. Towards monocrystalline nanostructures from assembled nanocubes . 61
1.3.1. Wet-chemical structural modification of assembled nanoparticles 61
1.3.2. Towards monocrystalline nanostructures 62
1.3.3. Conclusion 65
1.4. Thesis motivation 65

1.1. Why shape and crystallinity is important in metallic nanostructures?

1.1.1. Localized surface plasmon resonance

As briefly mentioned earlier in the introduction, nanostructures are intriguing for several reasons. Among them, metallic nanostructures stand out due to their remarkable optical properties, which arise from the behavior of their free electrons. These electrons can collectively oscillate in-phase in response to an external electromagnetic field, giving rise to plasmonic excitation. A plasmon can be understood as a quasi-particle associated with these collective electron oscillations. When these oscillations occur at the interface between two materials with opposing dielectric constants (such as a metal and a dielectric medium), they give rise to surface plasmons[12]. When incident photons have a frequency that matches the natural oscillation frequency of these surface plasmons, a resonance condition is met. This leads to a significant amplification of the oscillation amplitude and results in strong absorption and scattering of light. This phenomenon is known as surface plasmon resonance (SPR)[13]. However, in the case of metallic nanostructures or nanoparticles, where the volume is sufficiently small, these surface plasmons become spatially confined, preventing them from propagating along the material's surface. Instead, they remain localized to the nanostructure, giving rise to localized surface plasmon resonance (LSPR)[14, 15].

The mechanism can be classically explained, as illustrated in 1.1a. When an isotropic spherical metal nanoparticle interacts with an external electric field, the free electrons within the metal become polarized, causing the electron cloud to shift away relative to the positively charged ion core. Since the nanoparticle's dimensions are much smaller than the wavelength of the incident light, it experiences a homogeneous but time varying electric field [16]. This displacement creates a dipole, with opposing charges promoting depolarizing field acting as a restoring force[17]. As the electric field oscillates over time, the electron cloud moves back and forth in opposition to the field, leading to a collective oscillation of free electrons localized around the nanoparticle core [15, 16].

Mathematically, this phenomenon can be simplified using Mie theory to describe the extinction cross section (the sum of absorption and scattering) of a spherical metal nanoparticle[15]:

$$C_{ext} = \frac{24\pi^2 R^3 \epsilon_m^{3/2}}{\lambda} \left[\frac{\epsilon_i}{(\epsilon_r + 2\epsilon_m)^2 + \epsilon_i^2} \right] \tag{1.1}$$

Here, C_{ext} is the extinction cross section, R is the radius, ϵ_m is the dielectric constant of the surrounding environment, and ϵ_r and ϵ_i are the real and imaginary components of metal's dielectric constant. This expression highlights how both the size of the

nanoparticle (Figure 1.1b) and the properties of the surrounding medium influence the extinction behavior. It is worth noting that the constant factor of 2 in front of ϵ_m reflects the spherical geometry of the particle[12]. However, this analytical solution is only valid for simple shapes such as spheres and spheroids. For more complex geometries, researchers often use numerical methods like the finite-difference time-domain (FDTD) method. In this approach, each particle is discretized into N polarizable elements, each capable of interacting with the applied electromagnetic field, which is computed step-by-step in the time domain. This method enables the approximation of the optical response of nanoparticles with arbitrary shapes and sizes[12].

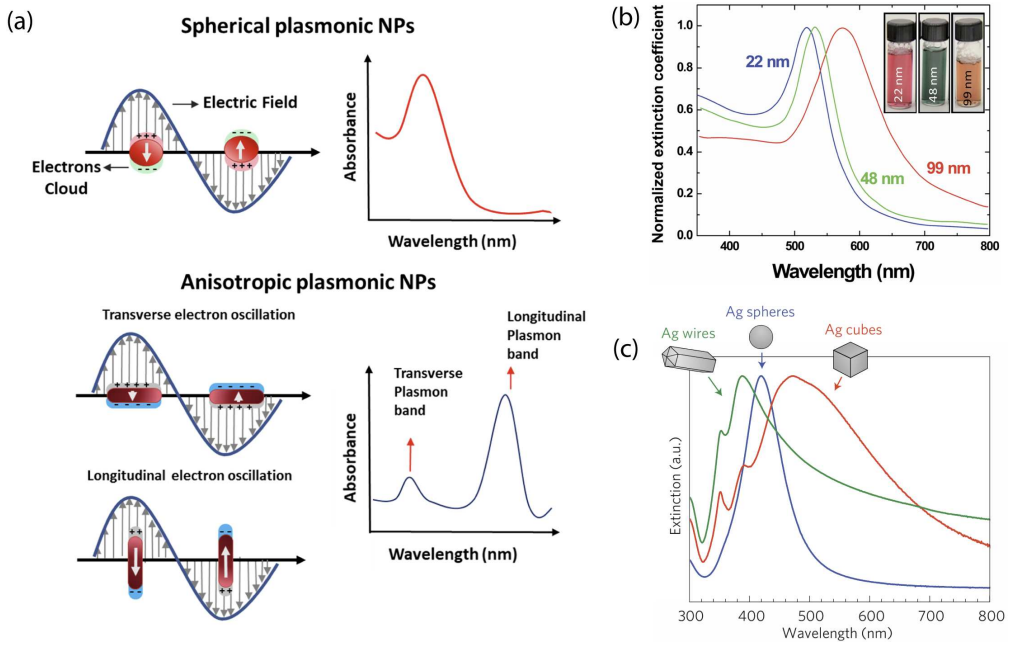

Figure 1.1.: (a) LSPR excitation and extinction spectra for plasmonic nanospheres and nanorods (reproduced from ref. [18]), (b) Normalized extinction spectra of gold nanospheres of different sizes (reproduced from ref. ([19]), (c) Normalized extinction spectra for Ag wire, cube and sphere nanoparticles (reproduced from ref. [13])

The shape of nanoparticles has a significant impact on their extinction spectra, as shown in 1.1a. Unlike isotropic shapes such as spheres, anisotropic nanostructures such as metallic nanorods, exhibit a split plasmonic band. The orientation of the nanorods relative to the electric field plays a crucial role in determining their plasmonic response. When the electric field is aligned with the major (long) axis of the nanorod, it induces a longitudinal plasmon oscillation, resulting in a plasmon band at lower energies. Conversely, when the field is aligned with the minor (short) axis, it produces a transverse plasmon oscillation corresponding to a band at higher energies [16]. More complex geometries, such as nanocubes, enable the excitation of multiple plasmon modes, as illustrated in 1.1c. The presence of features such as

sharp corners, edges, and flat facets in nanostructures with more complex geometries supports a richer set of localized plasmon resonances. This increased tunability allows for the design of functional materials with tailored optical properties, expanding their potential applications.

1.1.2. Metallic nanostructures in optoelectronic devices

1.1.2.1. Sensors

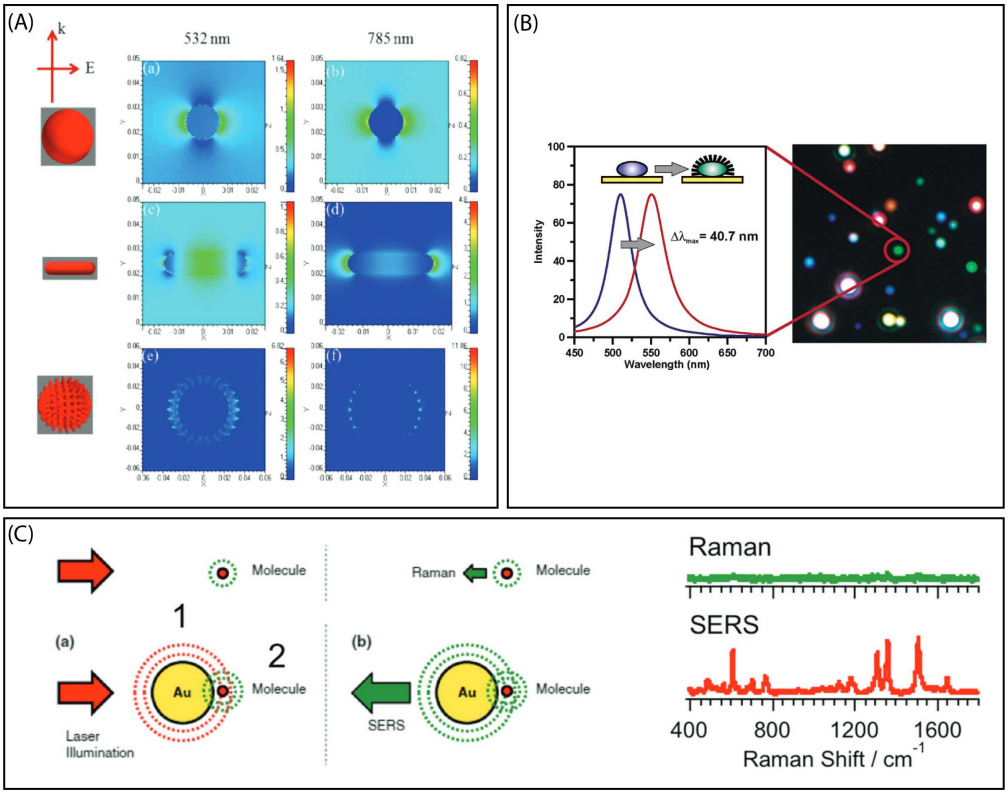

Figure 1.2.: (A) EM field distributions and intensities for nanorods and nanostars, compared to spherical NPs, upon excitation at two different wavelengths indicating that the highest near-field is generated at the LSPR wavelength and focused at the sharp tips of anisotropic NPs (here at 785 nm). Note that the LSPR wavelength for an Au sphere is around 520 nm (reproduced from ref. [20]), (B) A dark-field optical image of a field of Ag nanoparticles and an individual Ag nanoparticle sensor before and after functionalization with hexadecanethiol. (reproduced from ref. [21]), (C) Basic SERS electromagnetic mechanism. (reproduced from ref. [20])

Upon excitation of localized surface plasmons, a significantly amplified local electromagnetic field (near-field) is generated at the nanoparticle surface relative to the incident excitation field. At the single-nanoparticle level, this near-field enhancement can be further increased and precisely focused by modifying the particle geometry.

Shapes with sharp corners and edges exhibit intensified electric fields, especially at their vertices, as shown in Figure 1.2A[20]. The regions exhibiting high near-field enhancements are termed "hotspots." Additionally, hotspots can also form within narrow gaps (1–10 nm) between adjacent nanoparticles or between a nanoparticle and a metallic mirror[20, 22].

When analyte molecules are positioned within hotspots, two common sensing mechanisms are typically employed. As described by equation 1.1, the position of the extinction maximum is sensitive to changes in the dielectric constant of the surrounding environment. Thus, the presence of analyte molecules in this region alters the local dielectric constant, causing a measurable shift in the extinction peak (Fig. 1.2B). This approach is particularly effective for detecting analyte concentrations and monitoring kinetic binding events[14]. However, changes in dielectric constant alone is not informative to identify which molecules are being bound.

The second approach is associated with Raman spectroscopy, enabling chemical fingerprinting of Raman-active molecules. As illustrated in Figure 1.2C (top), the Raman scattering from free molecules is typically very weak. However, when a molecule (2) is positioned near a metallic nanoparticle (1), the Raman signal can be greatly enhanced [20, 23]. This enhancement occurs because molecules located at hotspots experience a significantly stronger local electromagnetic field than the incident laser field, resulting in amplified Raman scattering (a). Additionally, the Raman-scattered radiation emitted by the molecule can further excite the nanoparticle's LSPR, leading to re-emission of an enhanced near-field (b). Together, these two effects result in a strong amplification of the molecule's Raman signal, a phenomenon referred to as Surface-Enhanced Raman Spectroscopy (SERS)[20, 23].

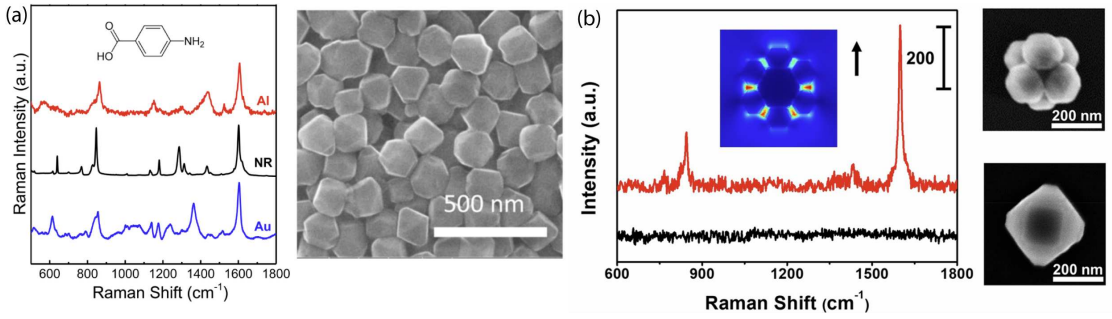

Figure 1.3.: (a) SERS spectra of p-aminobenzoic acid (PABA) on aluminum (red) and gold (blue) substrates, with the normal Raman spectrum as a reference (black)(reproduced from ref. [24]), (b) SERS spectra of PABA on aluminum nanohexapods (red) compared to aluminum nanoparticles without internal nanogaps (black). The inset highlights the electromagnetic hotspots located within the internal nanogap region(reproduced from ref. [25]).

Gold and silver nanoparticles of various shapes and sizes are widely used as platforms for Surface-Enhanced Raman Scattering (SERS) applications, owing to their well-established synthesis methods and excellent plasmonic properties. In contrast,

aluminum nanoparticles has been relatively less explored for SERS, primarily due to the less mature state of its synthesis associated to precise control over particle size and shape. However, aluminum presents several attractive advantages: it is significantly lower in cost and offers broad tunability of its plasmonic resonance, spanning from the ultraviolet (UV) to the near-infrared (NIR) region of the spectrum.

Tian et al. demonstrated that aggregates of aluminum nanoparticles can serve as SERS substrates for molecular identification, such as detecting p-aminobenzoic acid (PABA). The native oxide layer on aluminum acts as a beneficial linker between molecules and the substrate, preventing nonspecific adsorption on the metallic surface. As shown in Figure 1.3a, a distinct peak at 1439 cm^{-1}, corresponding to the symmetric stretching of the carboxylate (-COO^-) group, appears for PABA on the aluminum nanocrystal substrate, indicating specific binding to the oxide surface. In contrast, this peak is absent on gold nanoparticle substrates, where a peak at 1362 cm^{-1} appears instead, attributed to C-N stretching due to interaction of the amine group with the gold surface. These spectral differences suggest that aluminum nanoparticle aggregates enable SERS detection of functional groups beyond the commonly used thiol or amine moieties, potentially broadening the scope of detectable molecular species. Furthermore, Peng and coworkers demonstrated single-particle SERS using aluminum nanohexapods containing internal nanogaps. These structures exhibited significantly enhanced Raman signals compared to aluminum nanoparticles lacking such internal gaps (Figure 1.3).

1.1.2.2. Metasurface

Previously, we discussed that an individual subwavelength metallic nanostructure can be polarized by an external electric field, resulting in enhanced and confined electromagnetic fields (near-fields) within regions smaller than the incident wavelength. For small nanostructures with simple geometries, such as spheres or rods, polarization results in dipole-like behavior.

Arranging multiple subwavelength metallic nanostructures into ordered arrays can produce novel and unique optical properties that are not present in isolated nanoparticles. In such arrays, each nanostructure serves as a fundamental building block, known as a "meta-atom." When these meta-atoms are periodically arranged in three dimensions, the resulting structures are termed "metamaterials." Alternatively, arranging meta-atoms into two-dimensional periodic patterns yields structures called "metasurfaces"[17].

By modifying the geometry of the nanostructures, more complex plasmonic modes, including multipolar resonances, can be induced. The simplest examples involve bending nanorods geometry into V-shaped or split-ring meta-atoms. As illustrated in Figure 1.4, varying the orientation of the resonant electric field can modulate the charge-density distribution, leading to asymmetric (1.4a) and symmetric (1.4b) resonance modes. Interestingly, in the asymmetric mode, the oscillation of charges within the nanostructure resembles a circulating ring current, producing an out-of-

plane magnetic dipole moment. This unique property is particularly attractive for fabricating materials with a negative refractive index[17].

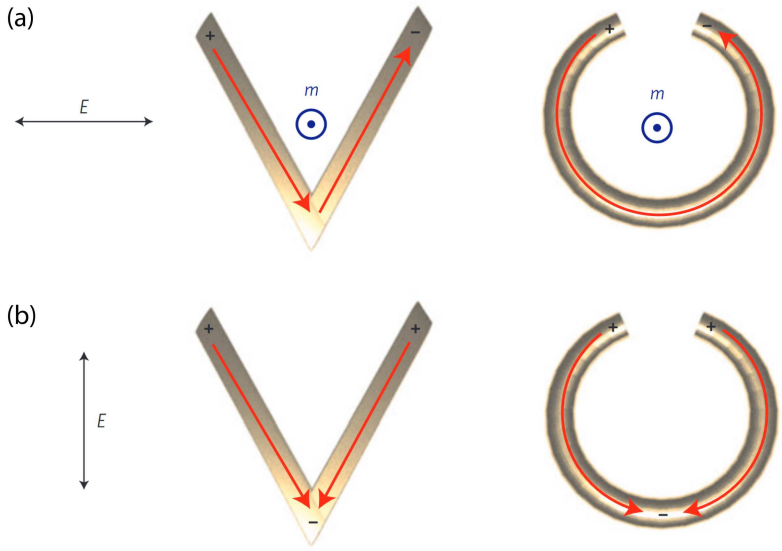

Figure 1.4.: Magnetic dipole moment (*m*,blue) induced by charge-density redistribution (red arrows) upon plasmon excitation (*E*) in V-shaped and split-ring-shaped meta-atoms: (a) asymmetric resonance, (b) symmetric resonance (reproduced from ref. [17]).

Moreover, designing meta-atoms with specific geometric features allows the creation of near-fields with chiral characteristics. These chiral near-fields produce strong chiroptical effects in the far-field, particularly circular dichroism, which refers to the difference in absorption between right- and left-circularly polarized light. As a result, combining plasmonic nanostructures with chiral molecules significantly enhances their typically weak interactions with light. This enhancement opens promising avenues for highly sensitive detection of molecular chirality and enantiomer identification[17, 26]. Figures 1.5f-i shows examples of chiral meta-atoms.

In periodic arrays of meta-atoms, the plasmonic modes can be altered in three distinct ways due to interactions between adjacent meta-atoms[17]. First, when meta-atoms are positioned in close proximity, their electromagnetic near-fields interact with each other. This interaction modifies the local electromagnetic field around each meta-atom, altering how they get polarized and leading to new hybridized modes[17]. For structures with simple geometries, such as spherical dimer, Nordlander and co-workers described these hybridized plasmon modes using an analogy to the combination of atomic orbitals into molecular orbitals, as explained in molecular orbital theory[27–29]. Examples of this phenomenon are shown in Figures 1.5g and 1.5h, where chiroptical properties arise from specific arrangements of achiral nanostructures, which individually do not exhibit chiroptical activity.

Second, when meta-atoms are arranged with separations smaller than the resonance

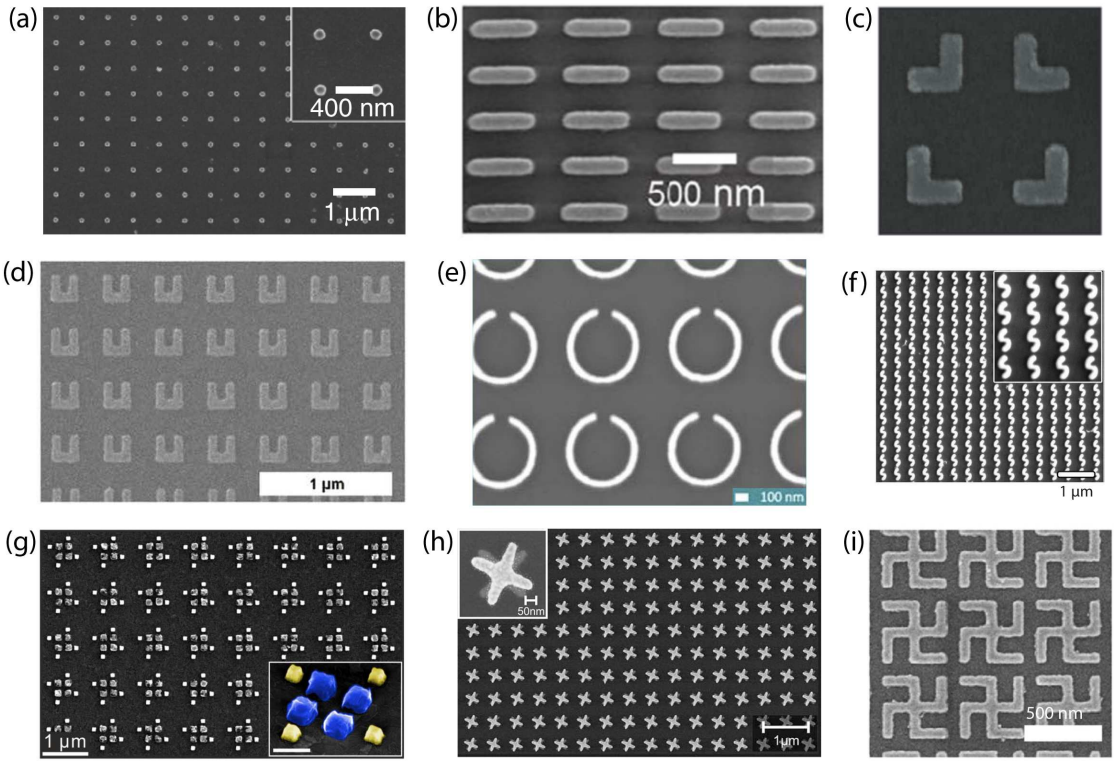

Figure 1.5.: Examples of various meta-atom geometries: (a) circular (reproduced from ref. [30]), (b) rod-shaped(reproduced from ref. [31]), (c) L-shaped (reproduced from ref. [32]), (d) U-shaped (reproduced from ref. [33]), (e) split-ring (reproduced from ref. [34]), (f) S-shaped (reproduced from ref. [35]), (g) squares arranged in a ratchet-wheel pattern (reproduced from ref. [36]), (h) twisted stacked crosses (reproduced from ref. [37]), and (i) gammadion (reproduced from ref. [38]).

wavelength, but still far enough apart that the near-field interactions is minimal. In this arrangement, gradually varying the geometry or orientation of each meta-atom across the surface allows precise control of the phase of transmitted or reflected light waves. This can result in effects such as anomalous reflection and refraction [17]. A prominent example is the Pancharatnam-Berry metasurface, which typically consists of identical anisotropic meta-atoms, such as nanorods, arranged with gradually varying orientations.

Wen and coworkers demonstrated an example of Pancharatnam-Berry metasurface to characterize the state of polarization of light[39]. As illustrated in Figure 1.6a-b, all nanorods have identical geometric dimensions and are spaced by a fixed center-to-center distance s in both the x- and y-directions. The angular orientation (φ) of each nanorod changes incrementally along the x-direction, rotating clockwise by an increment of $\pi/8$, while remaining constant in the y-direction. Consequently, each repeating unit along the x-direction comprises eight nanorods whose orientations span from 0 to π.

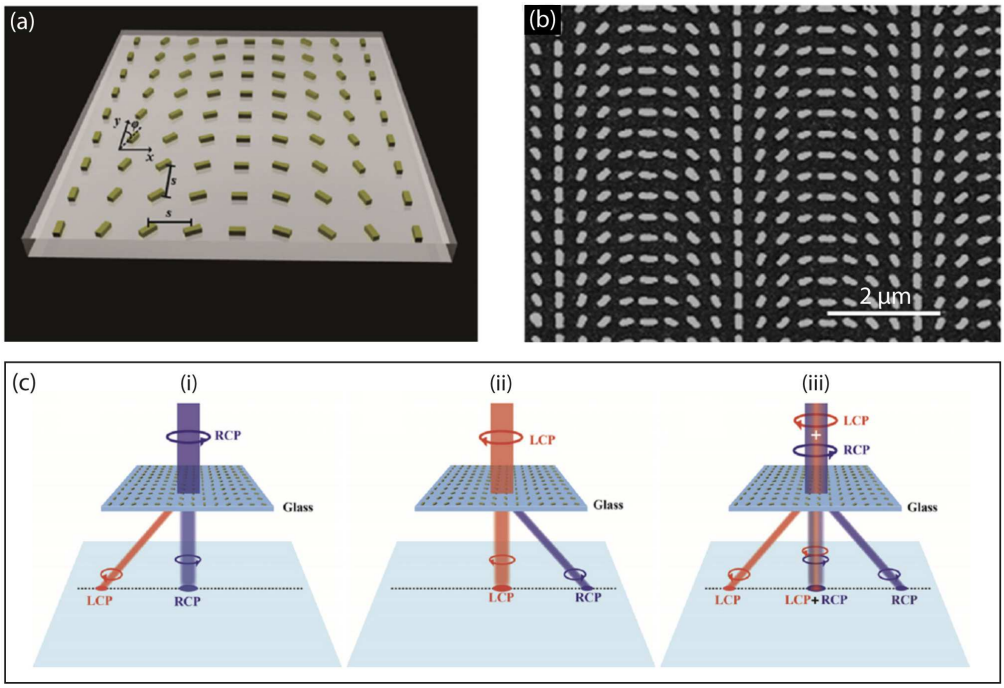

Figure 1.6.: (a) Schematic illustration of a Pancharatnam-Berry phase metasurface. (b) Scanning electron microscopy (SEM) image of the fabricated metasurface. (c) Schematic showing the polarization states of refracted light after interaction with the metasurface. Three cases of incident polarized light are presented: (i) right-circularly polarized (RCP), (ii) left-circularly polarized (LCP), and (iii) a combination of RCP and LCP polarization. The regularly refracted beam maintains both the polarization state and propagation direction of the incident beam. In contrast, the anomalously refracted beam emerges with opposite polarization handedness and is directed at an angle relative to the incident beam (reproduced from ref. [39]).

Figure 1.6c schematically illustrates the method used to analyze the polarization state of transmitted light through the metasurface. When right-circularly polarized (RCP) light is incident normally onto the metasurface [Figure 1.6c (i)], the regularly refracted beam retains both the polarization state (RCP) and propagation direction of the incoming beam. Additionally, the anomalously refracted beam experiences a polarization conversion to left-circular polarization (LCP) and is deflected toward the left side (as viewed from the detector).Conversely, when the incident beam is LCP [Figure 1.6c (ii)], the anomalously refracted beam becomes RCP and is deflected in the opposite direction. If the incident beam contains both RCP and LCP components [Figure 1.6(c) (iii)], the metasurface partially converts these into anomalously refracted beams of opposite handedness, causing them to diverge to opposite sides relative to the regularly refracted beam. Such Pancharatnam-Berry metasurfaces enable precise manipulation of the transmitted wavefront and polarization, facilitating diverse applications such as beam steering[39], light focusing[40], and generating optical

vortices[41], all achievable using a thin and flat optical device.

Third, when the distance between meta-atoms is comparable to their resonance wavelength, interactions between particles occur primarily through far-field diffraction rather than near-field coupling[17]. Under these conditions, scattered light waves from individual meta-atoms can overlap and interfere constructively reinforcing each other across the entire array, forming collective modes called surface lattice resonances. Surface lattice resonances typically have much narrower spectral widths compared to the plasmon resonances of individual particles, resulting in sharper and stronger optical responses[17, 42]. Such enhanced spectral features are particularly advantageous in applications like sensing, as the narrower resonance allows greater sensitivity to subtle changes in surface refractive index, thereby lowering detection limits and improving sensor performance[42].

1.1.3. Grain boundaries on metallic nanostructures

Upon excitation by an external electric field, conduction electrons in metallic nanostructures collectively oscillate. However, this coherent electron motion quickly dissipates energy through radiative (photon emission) and non-radiative (heat generation) pathways, causing the oscillation to lose coherence. This process, termed damping, primarily results from various electron collision/scattering events, such as electron-electron, electron-phonon, electron-surface, and electron-defect scatterings[16].

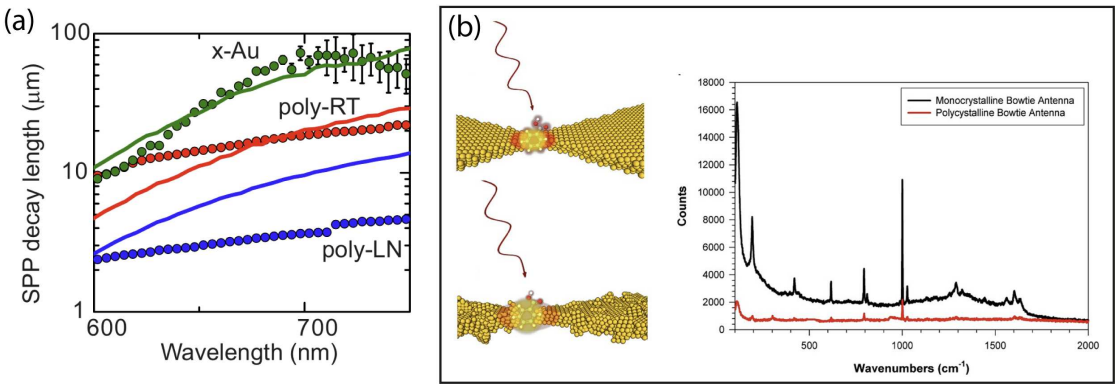

Figure 1.7.: (a) Surface plasmon polariton (SPP) propagation length as a function of excitation wavelength for three different gold samples: monocrystalline gold (x-Au, green dots), polycrystalline gold deposited at room temperature (poly-RT, red dots), and polycrystalline gold deposited at liquid-nitrogen temperature (poly-LN, blue dots). Solid lines represent calculated propagation lengths derived from experimentally measured dielectric constants for each respective sample(reproduced from ref. [43]). b) Surface-enhanced Raman scattering (SERS) spectra of benzoic acid measured using monocrystalline and polycrystalline gold bowtie nanoantennas, clearly demonstrating enhanced SERS performance for the monocrystalline structures(reproduced from ref. [44]).

Structural imperfections, such as grain boundaries and surface roughness, significantly impact the optical properties of plasmonic nanostructures by increasing electron-defect scattering[45]. Grain boundaries, which are interfaces separating distinct crystalline regions within polycrystalline materials, disrupt electron flow by acting as scattering centers. This disruption reduces the coherence and efficiency of collective electron oscillations. Using cathodoluminescence imaging spectroscopy, Kuttge and coworkers [43] demonstrated that surface plasmon polariton propagation length decreases as the crystal grain size becomes smaller. Figure 1.7a compares the propagation lengths for excitation wavelengths ranging from 600 to 750 nm in gold thin films with different crystallinities: monocrystalline gold (x-Au, green dots), polycrystalline gold with an average grain diameter of 80 nm (poly-RT, red dots), and polycrystalline gold with an average grain diameter of 50 nm (poly-LN, blue dots).

The use of high-quality monocrystalline plasmonic materials has demonstrated significant advantages across various plasmonic applications. For example, Mkhitaryan and coworkers summarized comparison of their experimental result with previous studies indicating that monocrystalline plasmonic metasurfaces exhibit higher quality factors compared to their polycrystalline counterparts[9]. Furthermore, as illustrated in Figure 1.7b, Grayli *et al.* reported that single-crystal plasmonic bowtie nanoantennas provide enhanced local electromagnetic field intensity, resulting in improved performance in Surface-Enhanced Raman Spectroscopy (SERS) relative to polycrystalline nanoantennas [44]. Additionally, Boroviks and Martin showed that nonlinear optical processes, such as second-harmonic generation, which rely on highly concentrated electromagnetic fields, also significantly benefit from using single-crystal plasmonic nanostructures [46].

Aside from plasmonic applications, metallic nanostructures are also widely employed as transparent conductive electrodes. Such electrodes are integral components in technologies like touchscreens, flexible electronics, and photovoltaic devices, where optical transparency combined with high electrical conductivity is crucial[47]. Typically, these transparent electrodes are designed as interconnected metallic grid-like networks with carefully chosen pitches (spacing) that allow transmission of visible light. However, the presence of grain boundaries in these metallic networks significantly impacts performance as they disrupt electron movement, leading to increased electrical resistivity and thus reduced electrical conductivity. This reduction in conductivity translates into energy losses, diminished device efficiency, and higher power consumption. Sciacca and coworkers [48] reported fabricating transparent silver-grid electrodes by combining soft-conformal imprint lithography with a solution-based silver growth process using Tollens' reaction (as illustrated in Figure 1.8a). Their results, presented in Figure 1.8b, demonstrate that silver grids grown via the solution-based approach exhibit lower sheet resistance compared to evaporated silver grids of identical thickness (30 nm). The authors attribute this improved conductivity to the larger grain size (~60 nm vs ~15 nm) achieved in solution-grown silver. Specifically, the fabricated silver-grid electrodes exhibited a sheet resistance as low as 7.9 Ω/sq with an optical transmission of 82.9%, weighted by the AM1.5 photon density standard. The authors further calculated that monocrystalline silver grids of identical dimensions

would theoretically achieve even lower resistances, as the absence of grain boundaries would significantly reduce electron scattering. In a more recent study, Bleiji *et al.* [49] demonstrated electrochemically grown silver-grid networks with high aspect ratios, achieving performance with a sheet resistance as low as 3.7 Ω/sq at a high optical transmission of 95.9% (AM1.5-weighted), despite having smaller average grain sizes (~32 nm). We attribute this improved performance to differences in grid geometry and the smoother surfaces achieved through electrochemical deposition, resulting in substantially reduced electron-surface scattering.

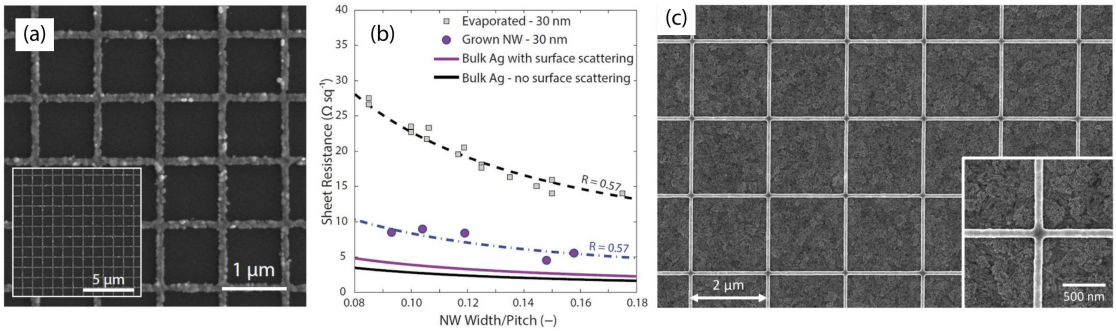

Figure 1.8.: (a) SEM image of a solution-grown silver-grid network(reproduced from ref. [48]). (b) Sheet resistance as a function of the nanowire width-to-pitch ratio. Square and circular data points represent experimental measurements, while dotted lines correspond to theoretical calculations that consider grain size and reflection coefficients. The solid line represents theoretical calculations for monocrystalline silver grids, with and without accounting for surface scattering (reproduced from ref. [48]). (c) SEM image of an electrochemically deposited, template-assisted silver nanowire grid with a pitch of 2 μm(reproduced from ref. [49]).

1.1.4. Conclusion

In summary, the optical and functional performance of plasmonic nanostructures is closely depend to both their geometric design and material quality. The specific shape of these nanostructures strongly influences the possible plasmonic modes and electromagnetic field enhancements. Such geometric sensitivity enables numerous applications, from chemical and biological sensing to advanced light-manipulating metasurfaces. For example, Pancharatnam-Berry metasurfaces rely on precisely varying the spatial orientation of meta-atoms to control wavefronts and polarization at subwavelength scales. However, achieving optimal plasmonic performance also critically depends on material crystallinity. Grain boundaries, common in polycrystalline materials, disrupt electron flow, decreasing resonance coherence, field enhancement, and electrical conductivity. Therefore, developing accessible and cost-effective fabrication methods capable of producing arbitrary monocrystalline nanostructures

without grain boundaries is essential. This approach offers the potential to significantly enhance device performance, minimize losses, and fully exploit the unique properties of nanoscale metallic systems.

1.2. Fabrication of monocrystalline nanostructures with arbitrary shapes

1.2.1. Conventional approach

The conventional approach to creating monocrystalline nanostructures with arbitrary shapes typically begins with bulk monocrystalline materials, which are subsequently reduced in size and shaped through lithography processes.

1.2.1.1. Monocrystalline bulk materials

There are two primary methods for fabricating bulk monocrystalline materials: the Czochralski method and the epitaxial vapor-transfer process.

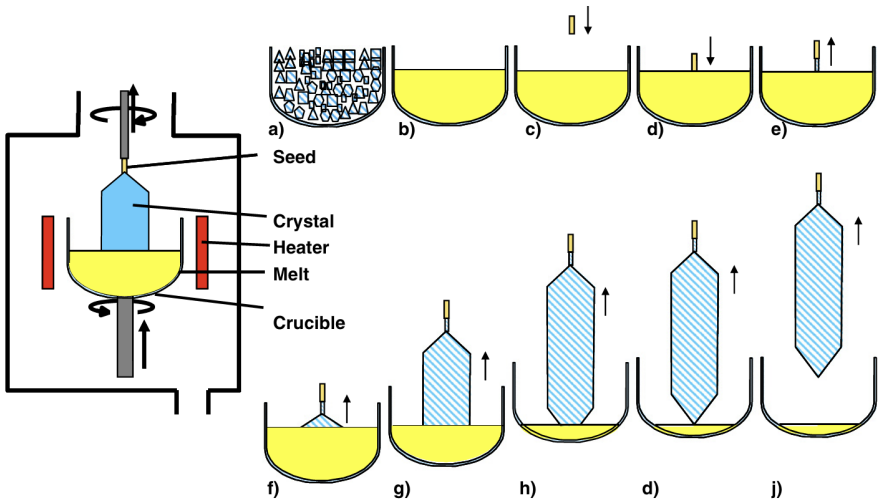

Figure 1.9.: Schematic of the Czochralski method (left) and an illustration of the sequential steps (a–j). (a) The polycrystalline feedstock is melted (b) in a crucible. (c, d) The seeding procedure begins as the seed crystal is dipped into the melt, followed by (e) Dash necking, (f) shouldering, (g) cylindrical growth, (h) formation of the end cone, (i) crystal lift-off, and (j) cooling and removal of the grown crystal. (reproduced from ref. [50])

The Czochralski method is a well-established technique for growing large, high-quality monocrystalline materials, most commonly used for fabricating semiconductor crystals like silicon, but also adaptable for certain metal and oxide crystals[51–53]. As shown in Figure 1.9, the process begins with a small seed crystal, a single crystal of

the desired material, which is dipped into a crucible containing the molten form of the material. The seed is then slowly withdrawn while rotating, allowing the molten material to solidify onto the seed in a controlled manner, forming an extended single crystalline ingot. A slow pulling rate ensures the atoms arrange themselves in the same lattice structure as the seed, maintaining monocrystallinity. Once the process is complete, the bulk ingot is cut into thinner wafers for subsequent lithographic processing.

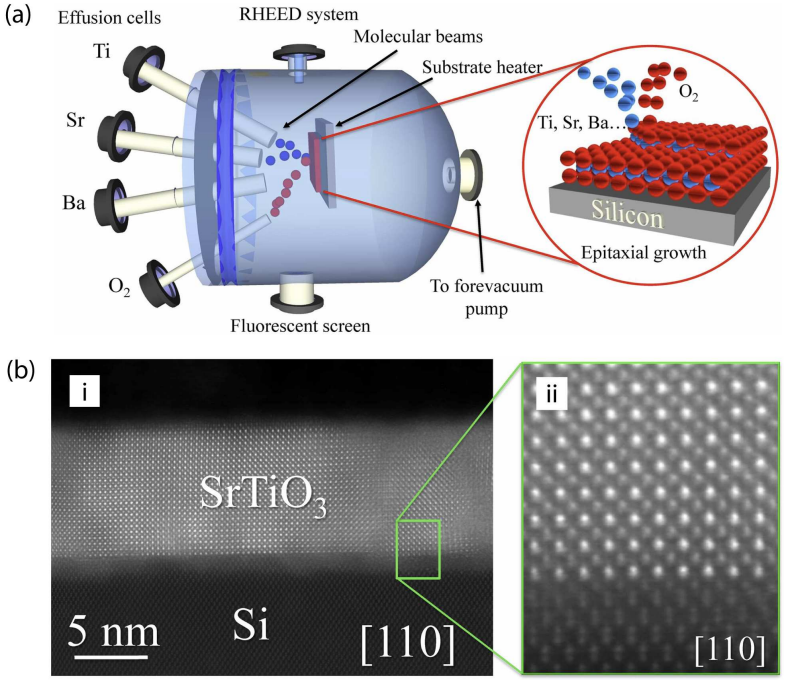

Figure 1.10.: (a) Schematic representation of a MBE dedicated to epitaxial oxide growth and (b) Cross-sectional HAADF-STEM image of a $SrTiO_3$ thin film epitaxially grown on silicon substrate by MBE (i) and enlarged view of the interface showing the epitaxial relationship (ii)(reproduced from ref. [54])

While the Czochralski method produces bulk monocrystalline ingots, another approach involves fabricating monocrystalline thin films through epitaxial vapor-transfer processes. The process is atomistic in nature, meaning that the deposition species are atoms or molecules or a combination of both. Among the most common methods are chemical vapor deposition (CVD) and molecular beam epitaxy (MBE)[55, 56]. As shown in Figure 1.10a, the process involves introducing precursor gases into a reaction chamber, where they undergo reactions on a heated substrate surface, leading to the deposition of a solid material. When the substrate is a monocrystalline surface, the deposited atoms adopt the same crystallographic orientation, a process known as epitaxy. However, for epitaxy to occur effectively, the lattice constants of the substrate and the deposited material must be closely matched. This poses a significant limitation for epitaxy, as it is necessary to select substrate materials with compatible

lattice parameters to minimize lattice mismatch. Epitaxy can be categorized into two types: Homoepitaxy, where the deposited material is the same as the substrate, enabling the growth of high-purity, defect-free crystals. Heteroepitaxy, where the substrate and deposited material are different, allows for the creation of complex layered structures while maintaining a crystalline order[55, 57]. Figure 1.10b shows the heteroepitaxy of $SrTiO_3$ thin film epitaxially grown on silicon substrate by MBE.

1.2.1.2. Nanostructuring of bulk materials

To fabricate arbitrary nanostructures from bulk materials, lithography process is commonly used. The two most prevalent methods are photolithography and electron beam lithography (EBL). Photolithography involves exposing photosensitive resist, coated with a patterned mask, to light, thereby transferring the mask design onto the resist. Conventional UV photolithography, however, is limited by the diffraction of light, typically achieving a resolution of around 1 μm[58]. More advanced techniques, such as extreme ultraviolet lithography (EUVL), utilize shorter wavelengths (13.5 nm) to push the resolution below 10 nm. Despite its high precision, the adoption of EUVL is restricted due to its exorbitant cost, reaching up to US$150 million[59]. As a result, this limits its use primarily to major technology companies.

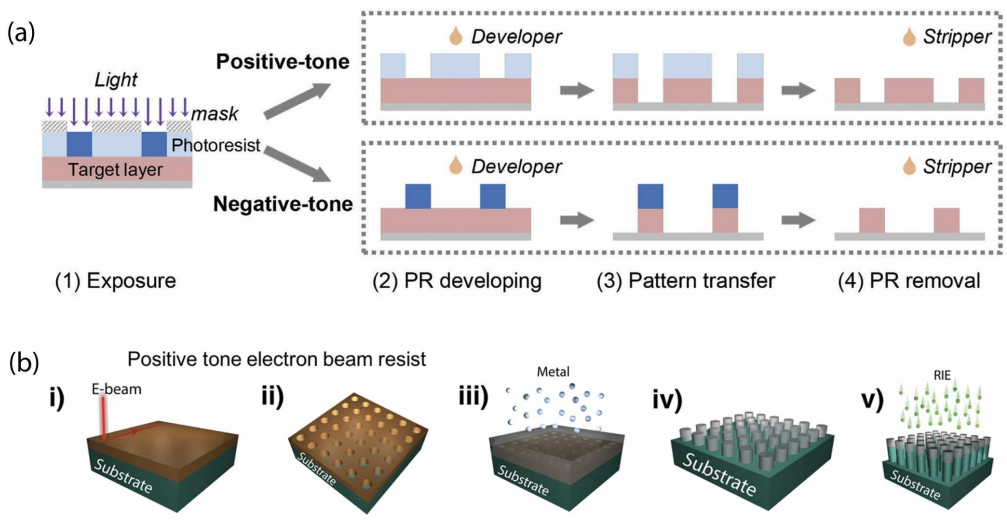

Figure 1.11.: (a) Schematic description of the UV photolithography process using positive-tone and negative-tone photoresists (PR)[60]. (b) (i) Beam exposure on positive tone resist. (ii) Nanoholes are left behind after resist development. (iii) and (iv) Metallic nanodots are fabricated after metal evaporation or sputtering followed by lift off. (v) We can also use the metal as etch mask for reactive ion etching (RIE) to fabricate high aspect ratio nanopillar arrays(reproduced from ref. [61]).

In parallel, direct-write techniques such as laser lithography and STED lithogra-

phy (Stimulated Emission Depletion) offer high-resolution patterning without the need for physical masks. Laser lithography uses tightly focused laser beams to define microscale to nanoscale features[62], while STED lithography leverages a depletion laser to confine exposure below the diffraction limit[63], enabling sub-100 nm resolution. However, both approaches suffer from inherently low throughput due to their serial, point-by-point writing processes, making them less practical for large-area nanomanufacturing.

A more accessible method for fabricating high-resolution, arbitrary nanostructures is EBL. This technique employs a focused electron beam to directly write patterns onto the resist-coated substrate, enabling the creation of complex nanostructures with resolutions smaller than 10 nm[10]. Although EBL offers greater flexibility and precision, the high operational costs and lengthy processing times associated with EBL render large-scale production unfavorable.

Following the lithography process, where patterns are defined on the resist, the next step typically involves depositing a metal hard mask via physical vapor deposition, followed by etching to transfer the pattern onto the underlying material. However, these etching steps often introduce surface roughness and defects[64, 65], which can significantly affect both the bulk and surface quality of the nanostructure. Such imperfections are critical to minimize, as they contribute to optical losses and degrade the spectral response[66].

1.2.1.3. Conclusion

In summary, conventional methods for fabricating monocrystalline materials, such as the Czochralski process and electron beam epitaxy, combined with nanopatterning techniques like electron beam lithography, provide high-quality monocrystalline structures and precise control over pattern design, including geometry and spatial positioning. However, these approaches are often introduces surface defects, costly, time-consuming, and impractical for large-scale applications. Developing more efficient and cost-effective fabrication methods is crucial, as it could accelerate technological advancements by enabling broader access to high-performance nanostructured devices.

1.2.2. Bottom-up nanoparticles self-assembly

Using nanoparticles as building blocks for fabricating complex nanostructures offers several advantages over conventional top-down approaches. This method is cost-effective, allows precise control over nanoparticle size, shape, and atomic composition, and provides superior material quality due to the inherent monocrystallinity of colloidal nanoparticles[67, 68]. However, achieving uniformity and homogeneity in nanoparticle size and shape remains a significant challenge in colloidal synthesis. Encouragingly, recent advancements in synthetic methodologies, such as seed-mediated growth and the extensive use of various chemical ligands, have significantly improved control over particle uniformity. Among various nanoparticle assembly

techniques, self-assembly is effective for constructing ordered architectures. In this process, nanoparticles spontaneously organize into well-defined structures under carefully managed conditions, driven by thermodynamically favorable interactions.

The term self-assembly is broad and used across many disciplines. According to Whitesides and Grzybowski in 2002[6], it can be considered as the autonomous arrangement of components without human interventions. Examples range from the self-organization of base pairs in DNA and the formation of cellular structures in living organisms to the alignment of planets and stars in planetary systems[6]. However, in the context of nanoparticles, self-assembly is not entirely "without human interventions". The organization of individual nanoparticles can be guided and controlled by embedding assembly information into the building blocks, achieved through the careful design of their properties and interactions[5].

Nanoparticles in solution are so small that they constantly undergo Brownian motion, driven by thermal fluctuations in their surrounding environment. Due to this random motion, a nanoparticle will deviate from its initial position (r_0) in the absence of any external driving force, following the equation[5]:

$$\frac{1}{3}\langle (r-r_0)^2 \rangle = \frac{k_B T}{6\pi a \eta} t = 2Dt \tag{1.2}$$

where T is the temperature, a is the particle diameter, η is the viscosity of the surrounding fluid, (k_B) is the Boltzmann constant, and D is the diffusion coefficient.

The small size of nanoparticles, combined with their random thermally induced motion, makes it extremely challenging to assemble them individually using a "pick-and-place" technique. To direct nanoparticles to specific spatial positions and maintain their arrangement relative to one another, one must overcome the random, diffusive forces of Brownian motion, which operates at an energy scale of $k_B T$[5].

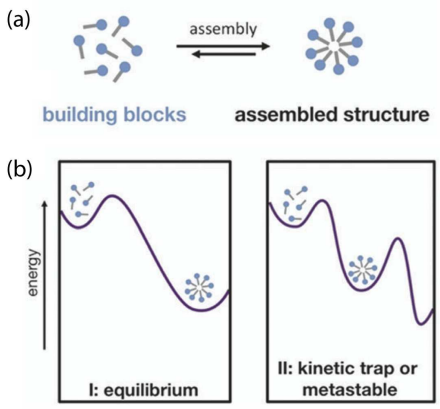

Figure 1.12.: Free energy landscape occupied by different classes of self-assemblies(reproduced from ref. [69])

Thermodynamically, this overcome of energy barrier in nanoparticle self-assembly

is driven by the reduction in free energy as the system transitions from dispersed nanoparticles (monomers) to an assembled state. This process can be visualized using an energy landscape, as shown in Figure 1.12, where different possible assembled states correspond to energy minima. The deepest minimum represents the thermodynamic equilibrium state, characterized by high stability and resistance to structural changes. However, even at equilibrium, assemblies remain dynamic, monomers can continuously exchange between the assembled structure and the surrounding solution. This dynamic exchange and reversibility are critical, as they enable the system to reach and maintain its lowest-energy, most stable configuration [69]. In contrast, kinetically trapped or metastable states correspond to local minima on the energy landscape. These states are less stable and can potentially transition to lower-energy configurations if sufficient energy is provided to overcome the associated energy barriers. Additionally, there is another type of assembly called a dissipative non-equilibrium state, in which energy must be continuously supplied to maintain the assembled structure. Once the energy input ceases, the assembly disintegrates, returning the system to a dispersed state [69, 70].

Interaction	Typical range (order of magnitude)
Covalent	0.1-0.2 nm
Van der Waals	1 nm
Electrostatic	1 nm (polar)-100 nm (apolar)
Hydrophobic	1 nm
Capillary	1 mm

Table 1.1.: Types of interactions driving nanoparticle assembly[5, 71].

Multiple interparticle interactions (Table 1.1) take part in nanoparticle self-assembly. Practically, achieving specific assembled structures requires control over these interactions, which can be managed by adjusting solvent conditions, ligand chemistry, or nanoparticle shape. Additionally, external fields, such as magnetic, electric, or optical fields, can further guide the self-assembly process by driving dispersed nanoparticles into ordered configurations. Through manipulation of these parameters, nanoparticles can be directed toward specific energy minima, enabling control over the resulting structural arrangements and their associated properties[72].

Gao and coworkers demonstrated control over the self-assembly of silver nanocubes by modifying their surface ligands. Specifically, replacing poly(vinyl pyrrolidone) (PVP) ligands with polyethylene glycol (PEG) allowed selective assembly of nanocubes into one-dimensional chains arranged either in face-to-face or edge-to-edge configurations (Figure 1.13a)[73]. Expanding upon this strategy, Wang and coworkers from the same research group achieved more complex two-dimensional checkerboard patterns by carefully balancing interactions between long-chain hydrophilic ligands and short-chain hydrophobic ligands on silver nanocubes (Figure 1.13b)[74]. Highlighting the importance of nanoparticle geometry, Luo et al. investigated the formation mechanisms of three-dimensional supercrystals assembled from silver nanoparticles with

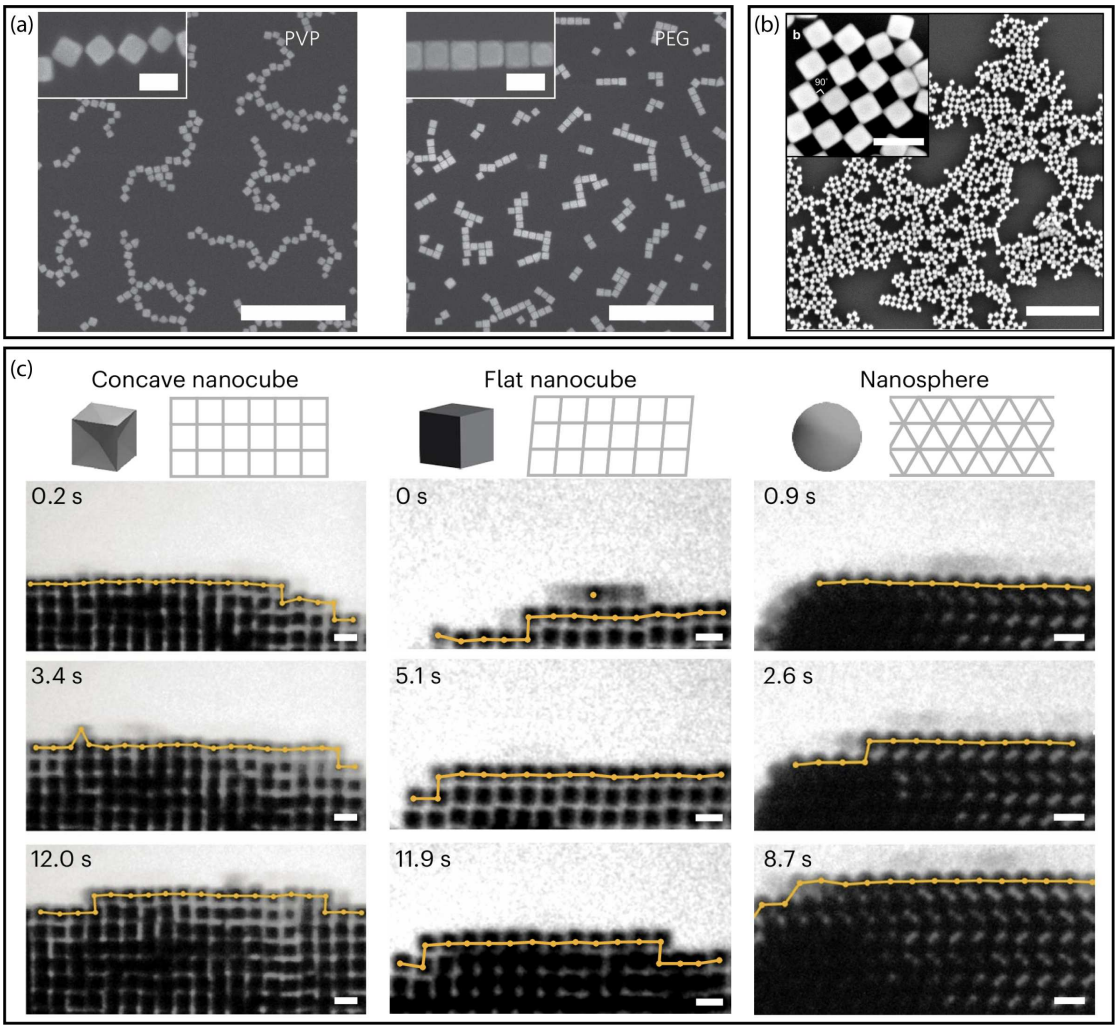

Figure 1.13.: Examples of nanocube self-assembly: (a) SEM images illustrating ligand-dependent assembly: PVP-thiol modified nanocubes assemble into an edge-to-edge configuration after solvent annealing, whereas PEG-alkanethiol modified nanocubes assemble into a face-to-face configuration following combined solvent and thermal annealing(reproduced from ref. [73]). (b) Checkerboard-pattern self-assembly of silver nanocubes achieved by carefully balancing hydrophilic and hydrophobic interactions through ligand manipulation (reproduced from ref. [74]). (c) Time-lapse liquid-phase TEM images showing layer-by-layer crystal growth: a simple cubic crystal formed from concave nanocubes, a rhombic crystal from flat nanocubes, and a hexagonal close-packed crystal from nanospheres. The yellow lines indicate the projections of newly forming crystal layers[75]. Scale bars: (a) 1 μm, inset: 100 nm; (b) 500 nm, inset: 100 nm; (c) 100 nm.

different shapes. Using liquid-phase transmission electron microscopy, they observed distinct layer-by-layer growth pathways: concave nanocubes formed simple cubic crystals, flat nanocubes assembled into rhombic crystals, and nanospheres arranged into hexagonal close-packed structures (Figure 1.13c)[75]. These studies together illustrate the essential role of ligand chemistry and nanoparticle geometry in directing and controlling nanoparticle self-assembly.

In summary, bottom-up self-assembly leverages chemically synthesized nanoparticles as building blocks to construct highly ordered architectures through controlled interparticle interactions. Compared to conventional top-down fabrication methods, this approach provides clear advantages, including lower cost, precise control over nanoparticle size, shape, and atomic composition, as well as superior material quality inherent to monocrystalline colloidal particles. However, achieving the same degree of flexibility regarding arbitrary shapes and precise spatial arrangements of meta-atoms, as obtained through electron beam lithography, remains challenging. Consequently, developing alternative nanoparticle assembly techniques is necessary to bridge this capability gap.

1.2.3. Templated self-assembly approach

In conventional self-assembly, most of the assembly information are encoded in the nanoparticles themselves through their size, shape, and surface chemistry. While external parameters such as temperature, solvent conditions, and applied fields can influence the process, the assembly pathway is largely dictated by the intrinsic properties of the building blocks. To expand the degree of control, additional assembly information can be "imprinted" onto the substrate, guiding where and how nanoparticles are trapped and organized. This approach is known as templated self-assembly[5].

It is important to note that the template used in templated self-assembly is typically fabricated using top-down techniques, such as lithography, to precisely define the geometry and spatial arrangement of the meta-atoms[5]. To construct metasurfaces at the single-nanoparticle level, the template must achieve a resolution that matches the projected size of the nanoparticles, which can be demanding in terms of fabrication complexity and cost. A more practical and cost-effective alternative involves creating a single high-resolution master template that can be replicated multiple times using soft lithography with polymeric molds such as PDMS or PMMA. In essence, this approach combines the precision of top-down patterning with the versatility and scalability of bottom-up nanoparticle synthesis, offering a hybrid strategy for constructing ordered metasurfaces.

As shown in Table 1.1, various types of interactions contribute to nanoparticle assembly. In templated self-assembly, these interactions can be encoded into the substrate to create particle-surface interactions that generate potential wells (regions of local free energy minima where nanoparticles can become trapped and assembled). Each type of interaction differs in strength and range, influencing the depth and shape of the energy landscape[5].

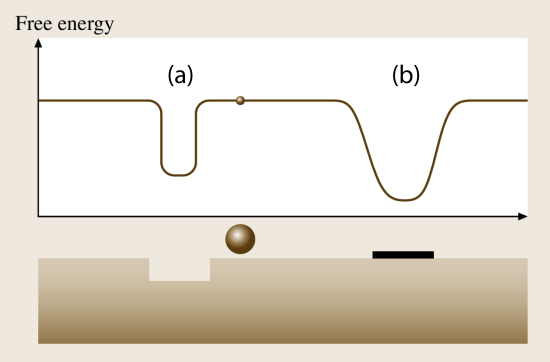

Figure 1.14.: Free-energy landscape in templated self-assembly, illustrating how moving particles become trapped at binding sites. Different types of traps correspond to distinct potential-well shapes, influencing particle behavior during assembly(reproduced from ref. [5])

Figure 1.14 illustrates different types of trapping sites and how they affect the assembly process. When nanoparticles undergo random motion due to Brownian diffusion and encounter binding sites, they may become immobilized. If the binding site involves a strong but short-range interaction, the potential well exhibits a steep wall, making it difficult for a particle to escape once trapped. Examples of such traps include topographical wells (Figure 1.14a) or covalent interactions, both of which create deep, sharply defined minima. Conversely, if the interaction is longer-ranged, it produces a more gradual or sloped potential well. In this case, a nanoparticle approaching the vicinity of the trap experiences a guiding force that pulls it toward the energy minimum (Figure 1.14b). Electrostatic and capillary interactions are typical examples of long-range interactions that facilitate this type of directed assembly. These variations in potential well profiles directly influence placement accuracy and the overall yield of the templated assembly process[5].

One example of templated self-assembly is surface-templated electrophoretic deposition that leverages electrostatic interactions between nanoparticles and a nanopatterned substrate under the influence of an applied electric field[67]. This method offers speed and scalability, yet its use is confined to conductive substrates, thereby limiting its applicability for transfer onto different substrates. It is worth noting that this limitation is not absolute, as modifications to thin insulating substrates can expand its applicability[76]. While it excels in creating arrays of individual nanoparticles, its potential to obtain arbitrarily complex meta-atoms remains largely unexplored.

Nanoparticle imprint lithography (NIL) is yet another method which leverages mechanical force and topographical trap to direct nanoparticles into assembled state. This technique offers the advantage of one-step printing and the capability to fabricate complex nanostructures over large areas[65, 77–79]. However, precise colloidal concentration is crucial; insufficient quantities result in suboptimal filling, whereas an excess leaves nanoparticle residue on the substrate, deteriorating the resulting

nanopattern[65]. This is problematic because concentration optimization is necessary for distinct pattern types and densities, making assembly on templates with non-uniform pattern distributions challenging. As illustrated in Figure 1.15a, silver nanocubes tend to accumulate around ring-shaped meta-atoms, leaving unwanted residue. Figures 1.15b–d further show the variations in colloidal concentration lead to different assembly outcomes. In addition, nanoimprinting directly prints the assembly into the target substrate rather than onto the PDMS mold. This could impede subsequent chemical or thermal post-treatments if the target substrate is delicate. Finally, nanoparticle imprint lithography typically relies on specialized nanoimprint equipment that is costly and might not be accessible to many.

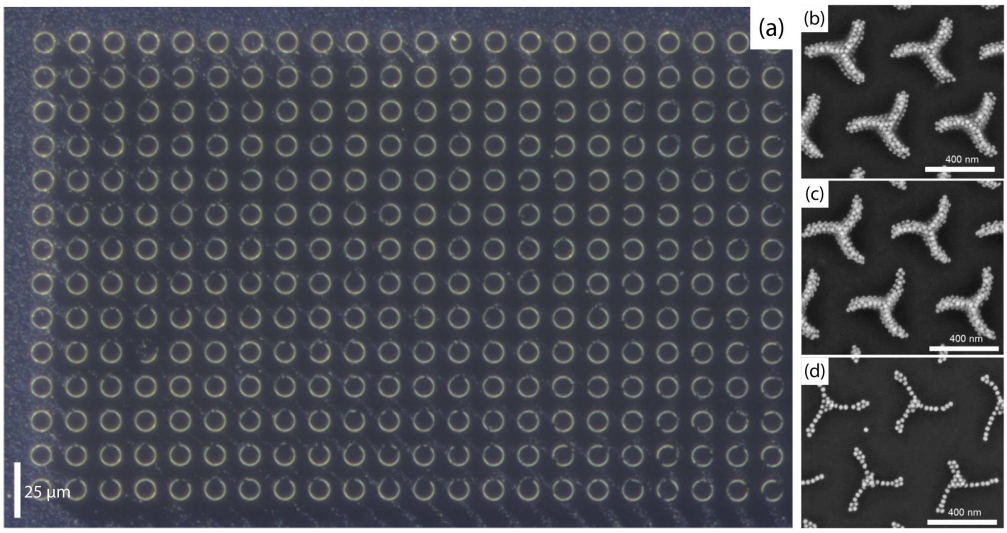

Figure 1.15.: (a) Optical image of silver nanocubes arranged in a ring pattern (reproduced from ref. [65]). (b–d) SEM images of triskelion patterns formed by 27 nm gold nanospheres at different concentrations: (b) 50 mM, (c) 30 mM, and (d) 15 mM(reproduced from ref. [79]).

Another elegant method worth mentioning is the template-assisted DNA-mediated assembly, which offers precise control over the positioning of nanoparticles across large areas. As shown in Figure 1.16a, DNA-functionalized nanocubes are arranged onto a patterned template consisting of a PMMA layer coated on a gold-coated silicon substrate. Pores are patterned into the PMMA using electron beam lithography (EBL), and the base of each pore (exposed gold) is functionalized with thiolated DNA strands (red). Nanocubes modified with complementary DNA (blue) selectively bind to these sites. After the assembly process, the sacrificial PMMA layer is dissolved, leaving the nanoparticles precisely positioned. This approach enables the fabrication of various configurations, including individual nanocubes for metasurfaces (Figure 1.16b), S-shaped meta-atoms (Figure 1.16c), and selective placement of nanocubes of different sizes using pore templates of corresponding dimensions (Figures 1.16d-e). However, the necessity of using electron beam lithography to create a sacrificial template renders repeated fabrication expensive[80, 81].

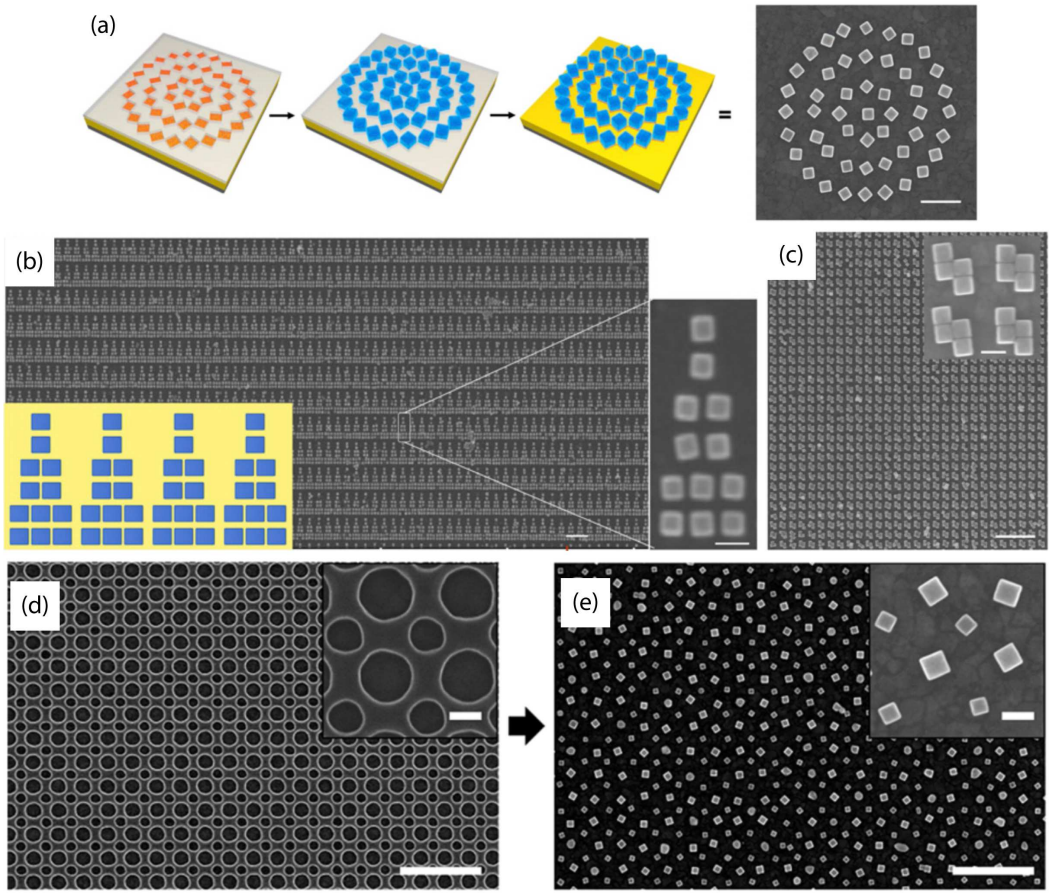

Figure 1.16.: (a) Template-assisted DNA-mediated assembly(reproduced from ref. [81]). (b) Assembly of silver nanocubes into a metasurface for anomalous reflection(reproduced from ref. [81]). (c) 90 nm silver nanocubes forming S-shaped meta-atoms(reproduced from ref. [81]. (d–e) Size-selective assembly using templates with two pore sizes (d) and two nanocube sizes (e)(reproduced from ref. [80]). Scale bars: (a) 300 nm; (b) 1 μm, inset: 100 nm; (c) 100 nm; (d–e) 1 μm, insets: 100 nm.

Another method, capillary assembly utilizes capillary forces at the receding meniscus to position individual nanoparticles onto a topographically patterned substrate[1, 82–86]. This technique achieves assembly configurations that elude traditional self-assembly, particularly excelling in arranging low-density individual nanoparticles or 1D arrays. As illustrated in Figures 1.17a-b, this method successfully assembles nanoparticles into discrete meta-atoms and linear structures with varying nanoparticle lateral dimensions. However, achieving densely packed and complex continuous nanoscale geometries in a single step remains a challenge[87], often requiring multiple sequential assembly cycles[86]. Figures 1.17d-g highlight the difficulty of assembling nanoparticles onto high-density patterns and demonstrate how the orientation of the template and the direction of meniscus movement during drying significantly influence nanoparticle deposition.

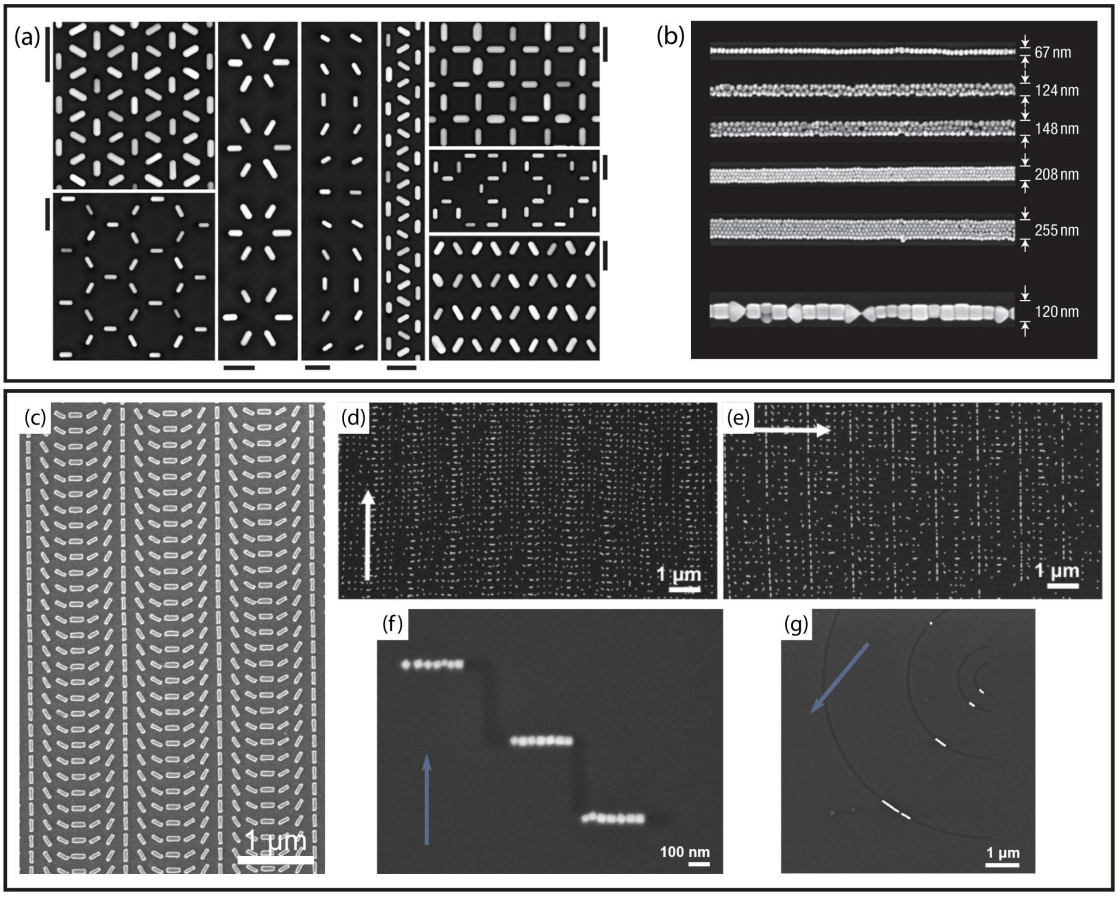

Figure 1.17.: SEM images of capillary-assembled nanoparticles: (a) Individual gold nanorods arranged in various configurations (scale bars: 250 nm)(reproduced from ref. [84]). (b) Linear assemblies of 60 nm gold nanoparticles; bottom row: 100 nm silver nanoparticles(reproduced from ref. [82]). (c) PB metasurface master template fabricated via EBL. (d–e) Dense PB metasurfaces from 40 nm gold nanocubes with different assembly directions. (f) Stair-like patterns from 40 nm silver nanocubes. (g) Semi-circular patterns of 50 nm gold nanocubes. Arrows indicate the direction of assembly. (c–g) reproduced from ref. [2].

1.2.4. The air-water interface assembly

The phenomenon of nanoparticles monolayer becoming trapped at the air-water interface was first reported in the 1980 by Pieranski[88], who observed that 245 nm polystyrene nanospheres could remain confined at the interface despite undergoing vigorous Brownian motion. He attributed this behavior to the presence of a potential energy well at the interface that is deeper than the thermal energy(k_BT)[88]. This trapping capability is largely attributed to water's high surface tension, which supports a dense layer of otherwise non-buoyant nanoparticles at the interface[89]. It is widely known that not only water but also other high-surface-tension solvents, such as diethylene glycol (DEG) and glyceryl triacetate, are effective media for interfacial

nanoparticle assembly[90–92]. The effectiveness of interfacial trapping is strongly influenced by size and surface wettability of the nanoparticle. The latter is largely governed by the interaction between the surface ligands of the nanoparticles and the liquid subphase[93]. Today, the air-water interface is widely recognized as a versatile platform for the self-assembly of a broad range of nanoparticles, accommodating diverse compositions, morphologies, and sizes over large areas with high ordering potential. Figure 1.18 illustrates how nanoparticles monolayer of various materials, geometries, and sizes can be assembled into ordered structures using air-liquid interface techniques.

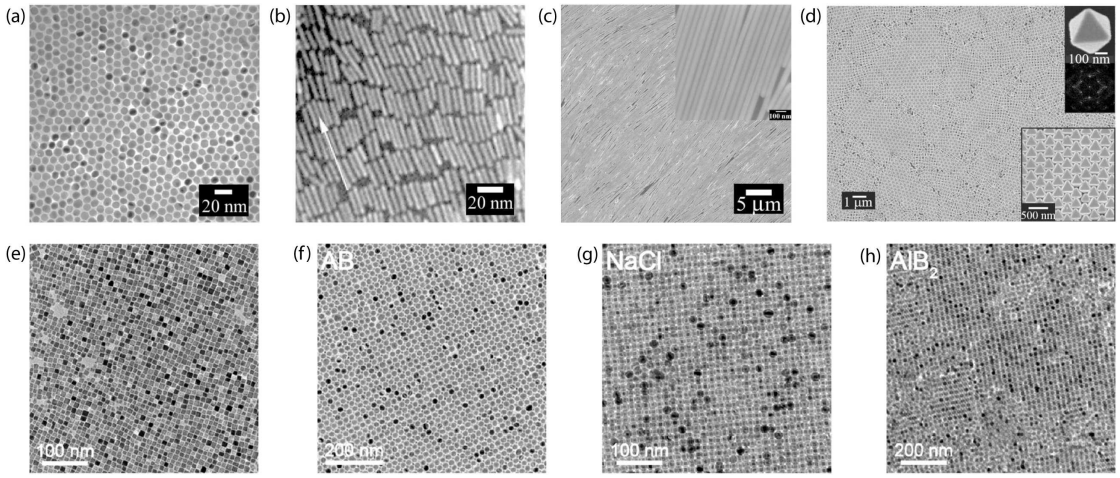

Figure 1.18.: Examples of close-packed nanoparticle monolayers assembled via the air–liquid interface method: (a) platinum nanospheres[89], (b) $BaCrO_4$ nanorods[89], (c) silver nanowires[89], (d) silver octahedra[89], (e) $CsPbBr_3$ nanocrystal[92]. Binary nanocrystal superlattice monolayers composed of $CsPbBr_3$ and Fe_3O_4 with different structural motifs: (f) AB-type, (g) NaCl-type, and (h) AlB_2-type[92].

To achieve more reproducible nanoparticle assemblies with controllable surface density, the Langmuir trough is commonly employed (Figure 1.19a). Originally developed for assembling monolayers of amphiphilic molecules at the air-water interface, this method enables precise control over molecular or nanoparticle packing density using movable compression barriers. The degree of compression is quantified by the surface pressure (Π), which is measured using a Wilhelmy plate and plotted as a pressure-area isotherm (Figure 1.19b). When amphiphilic molecules are first spread onto the water surface, they orient with their hydrophilic heads facing the water and hydrophobic tails pointing away. In this initial "gas-like" phase, molecules are sparsely distributed with large voids between them, reflected by the flat region of the isotherm. As the barriers compress the layer, intermolecular distances decrease, increasing the likelihood of interaction and leading to a "liquid-condensed" phase, indicated by a gradual rise in Π. Further compression brings the molecules into a closely packed arrangement, restricting their mobility and resulting in a "solid-like" phase. This

transition is marked by a steep, nearly vertical increase in the isotherm curve (Figure 1.19b)[94]. Further compression of the barriers will lead to the collapse of the monolayer forming a disordered multilayer assembly.

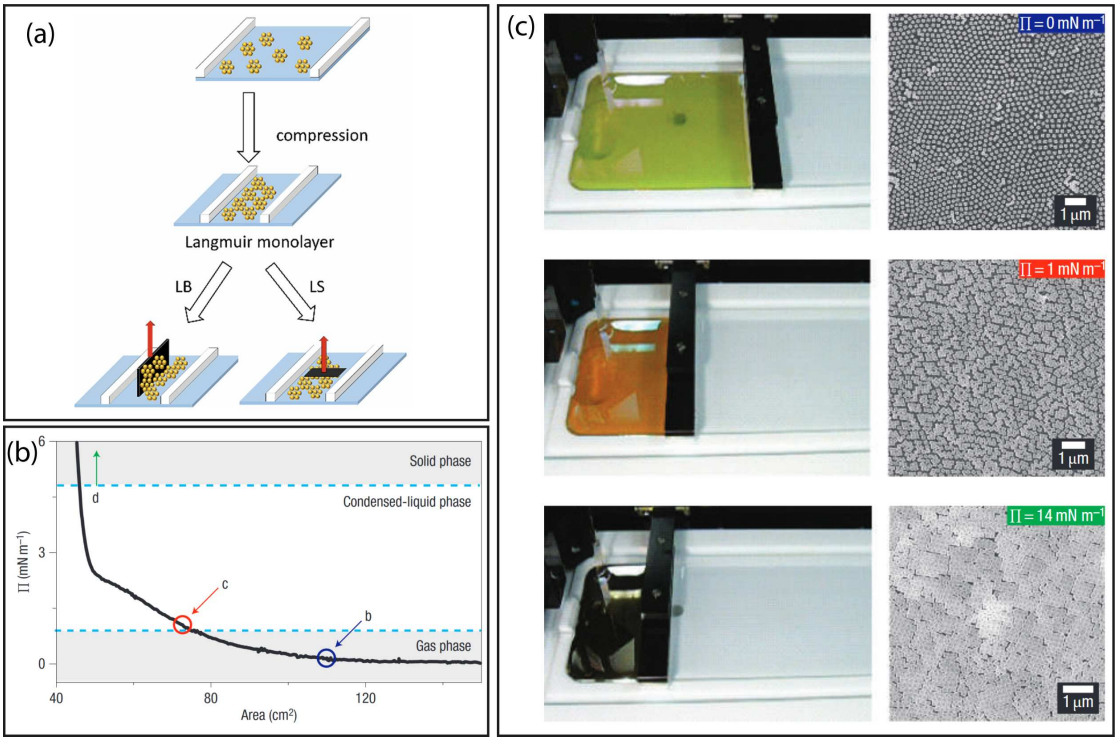

Figure 1.19.: (a) Schematic illustration of Langmuir compression, showing the merging of nanoparticle domains followed by sequential transfer onto a solid substrate using Langmuir-Blodgett (LB) and Langmuir–Schaefer (LS) techniques(reproduced from ref. [94]). (b) Pressure-area isotherm recorded during Langmuir compression(reproduced from ref. [95]). (c) Optical photographs of a nanoparticle film on a liquid surface and corresponding SEM images after transfer to a silicon substrate at surface pressures of Π = 0, 1.0, and 14 mN m^{-1}(reproduced from ref. [95]).

A similar behavior is observed in nanoparticle monolayers, such as the assembly of silver cuboctahedra. As shown in Figures 1.19b and 1.19c, increasing compression of the barriers leads to a higher packing density of the nanoparticles. In such systems, the assembly process is governed by a combination of interparticle forces, including van der Waals attractions, steric repulsion, and capillary interactions at the interface[94, 96]. Interestingly, Huang and coworkers proposed a different assembly mechanism for nanoparticles at low surface pressures[97, 98]. Unlike the freely mobile molecules in 2D plane in a gas-like phase, nanoparticles spread from a volatile carrier solvent tend to form small domains as the solvent evaporates. Compression of the barriers then causes these domains to merge, forming larger islands on the interface [97, 98].

To utilize the assembled monolayers as functional materials, it is often necessary to transfer them onto a solid substrate. This can be achieved using the Langmuir-Blodgett

(LB) technique, where a vertically oriented substrate is immersed and withdrawn through the nanoparticle-covered air-water interface. Alternatively, the Langmuir-Schaefer (LS) technique involves gently lowering a horizontally positioned substrate onto the interface to make contact with the assembled layer, facilitating monolayer transfer. Both methods are illustrated in Figure 1.19a[94]. Figure 1.19c shows the resulting nanoparticle assemblies transferred onto a silicon substrate using the LB method.

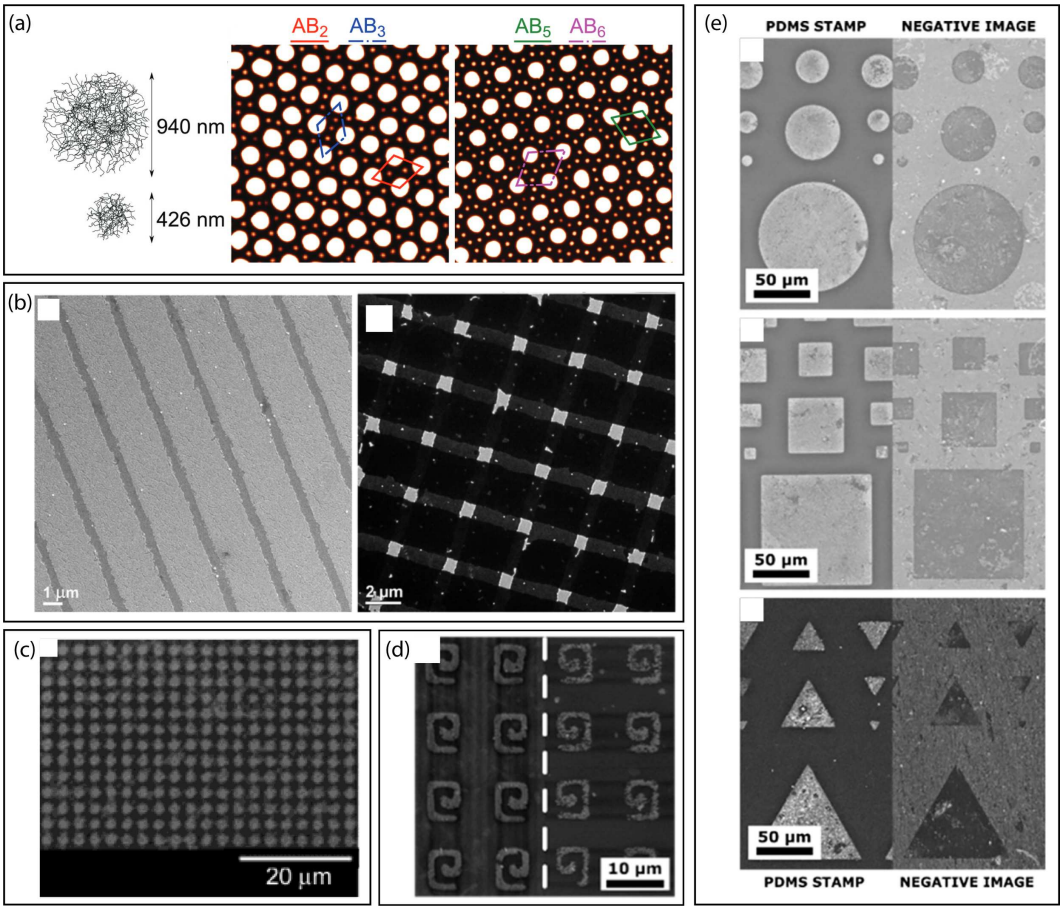

Figure 1.20.: (a) AFM images ($10 \times 10\ \mu m^2$) showing various configurations in deposited binary arrays, from large and small PNIPAM microgels (reproduced from ref. [99]). (b) SEM images of line grating patterns formed from AlB_2-type binary nanocrystal superlattices (BNSLs) composed of semiconducting CdSe@CdS core/shell quantum dots and dielectric β-$NaGdF_4$ nanocrystals. Also shown is a grid pattern formed from AlB_2-type BNSLs of FeO_x and Au nanocrystals, fabricated via sequential transfer printing of self-assembled BNSLs(reproduced from ref. [91]). (c) SEM images of patterned μ-dot arrays from a γ-Fe_2O_3 nanoparticle Langmuir film transferred onto a silicon wafer(reproduced from ref. [100]). (d-e) SEM images of a PDMS stamp after lift-off (left), and the corresponding negative pattern imprinted onto an AuNP monolayer donor substrate (right).(reproduced from ref. [101])

Several studies have demonstrated the use of these techniques to fabricate arrays of individual nanoparticles[99]. When combined with pre-patterned templates, they allow for the creation of arbitrary geometric structures. For instance, integrating interfacial assembly with microcontact printing can produce micropatterned lines, while the sequential transfer printing of it can be used to generate grid patterns[91, 102]. By employing differently shaped templates, it is also possible to form a wide variety of patterns, including dots[100], spirals, circles, triangles, and squares[101], each capable of organizing clusters of nanoparticles into well-defined configurations.

1.2.5. Conclusion

Overall, the current techniques for template-directed nanoparticle assembly in metasurfaces with sub-100 nm features are predominantly categorized into three types, based on the arrangement of nanoparticles in the constituent building-blocks (meta-atoms): (1) isolated nanoparticles (0D meta-atoms)[80, 82–84, 99, 103, 104]; (2) nanoparticles arranged adjacent to one another in a linear fashion, forming lines with lateral resolution of one or more nanoparticles (1D meta-atoms)[1, 77]; and (3) meta-atoms formed by aggregates or clusters of small nanoparticles (typically much smaller than the meta-atom feature dictated by the template) [78, 79, 105–107]. However, a more precise assembly in which individual nanoparticles are arranged adjacent to one another to construct complex geometric meta-atoms at the resolution of single nanoparticles remains challenging. Two of the most recent work reported the fabrication of 2D meta-atoms with a single nanoparticle lateral resolution (<100 nm) are S-shaped and ring-shaped obtained with DNA-mediated assembly and nanoparticle imprint lithography, respectively[65, 81].

1.3. Towards monocrystalline nanostructures from assembled nanocubes

1.3.1. Wet-chemical structural modification of assembled nanoparticles

The concept of post-assembly epitaxial structural modification of substrate-supported nanoparticles using wet-chemical approaches is an intriguing area of research. It offers opportunities beyond the limits of conventional colloidal synthesis, including: (i) the ability to access nanostructure geometries that are otherwise difficult or impossible to achieve through standard colloidal routes, and (ii) control over the spatial arrangement and orientation of nanoparticles relative to each other or to the substrate[108]. Importantly, these advantages are gained while still retaining the core benefits of wet-chemical synthesis namely, precise control over shape, tunable atomic composition, and the ability to produce high-quality crystalline materials. Many studies have demonstrated the substrate-supported, seed-mediated overgrowth of nanoparticles

into various intricate shapes, including branched nanostars[109], nanocrescents[110], nanowires[111], nanorods[112–114], nanocubes[115–117], nanotriangles[118–120], tetrahexahedrons[118], Wulff-shaped nanoparticles[118], and decahedral nanostructures[121, 122]. Combining this approach with galvanic replacement reactions further enables the formation of even more complex cage-like nanostructures [117].

In conventional seed-mediated colloidal synthesis, two growth processes can occur: heterogeneous overgrowth on seed nanoparticles and undesired homogeneous nucleation. While the former is typically favored, the latter is detrimental, as it leads to unwanted particles and reduces overall synthesis efficiency. To overcome this, strategies are implemented to maintain the atomic concentration below the critical level at which homogeneous nucleation occurs[123]. However, for substrate-supported seed growth, the complexity increases since nucleation can happen both in the solution and directly on the substrate surface, further complicating process control[108]. The Mirkin group demonstrated that careful control of growth conditions, including temperature and concentrations of metal precursors, surfactants, and reducing agents, can effectively suppress homogeneous nucleation in solution[116]. Furthermore, the Neretina group reported the use of acetonitrile as a solvent during silver overgrowth to prevent unwanted homogeneous nucleation. Acetonitrile complexes with silver ions, significantly reducing their reduction potential and thereby suppressing undesired particle formation[120]. The same group also introduced a plasmon-mediated growth approach, wherein hot electrons generated by plasmonic seed nanoparticles act as reducing agents[121, 124]. Additionally, their group also utilized sonication to remove unwanted byproducts, successfully increasing yields[117, 122]. Although it seems effective, this method primarily benefits only to nanostructures strongly bound to the substrate.

In most of the studies discussed so far, the final nanostructures are typically grown from individual seeds. However, greater opportunities arise if multiple seeds can first be arranged close together on a substrate in a specific configuration, followed by controlled overgrowth to create a single, more complex nanostructure. For instance, Côté and coworkers utilized the Langmuir-Blodgett assembly of gold nanoparticles together with polymer micelles at the air-water interface. This approach resulted in gold nanoparticles forming a circular arrangement around each micelle. After transferring these assemblies onto substrates and performing subsequent overgrowth, distinctive nanocrescent structures were obtained[110]. This example highlights how arranging multiple seeds in defined configurations can guide the formation of sophisticated nanostructures. One could further envision the rich variety of structures achievable if these seeds could be positioned arbitrarily.

1.3.2. Towards monocrystalline nanostructures

An interesting approach proposed by Sciacca and coworkers in 2017 involved first assembling silver nanocubes into specific configurations as seeds, followed by a wet-chemical overgrowth step to form unified structures whose geometry differed from

the original shape of the seed. As shown schematically in Figure 1.21a, they employed capillary assembly to organize silver nanocubes into linear arrays on patterned PDMS molds. Thanks to the low surface energy of PDMS, the assembled nanocube arrays could be easily transferred onto another substrate via contact printing. Subsequently, a chemical overgrowth reaction using Tollens' reagent was carried out, resulting in continuous one-dimensional nanostructures derived from the original discrete nanocubes.

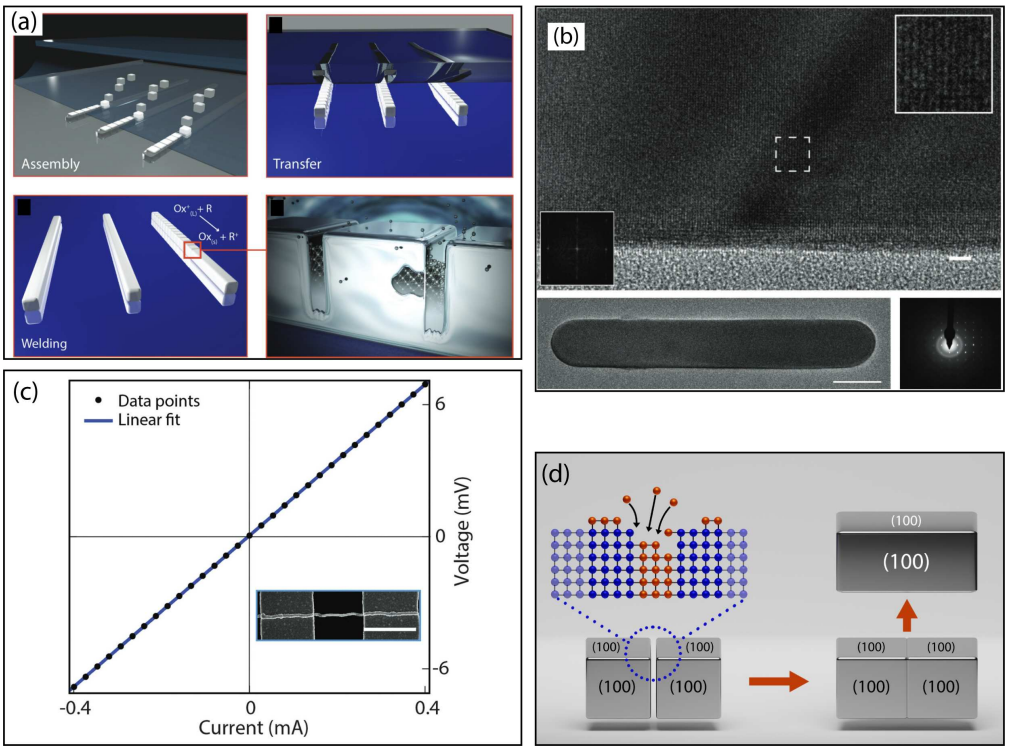

Figure 1.21.: (a) Schematic of the capillary assembly of nanocubes on a patterned PDMS template, their subsequent transfer onto a substrate, and epitaxial overgrowth forming interconnected nanocube structures(reproduced from ref. [11]). (b) TEM characterization: the upper image shows atomic columns at the junction between two silver nanocubes, revealing perfect crystallographic alignment; the lower image shows seven interconnected nanocubes, with the corresponding SAED pattern confirming monocrystallinity throughout the entire structure(reproduced from ref. [11]). (c) Electrical characterization of a welded nanocube line measuring 6 μm in length(reproduced from ref. [11]). (d) Schematic depiction of epitaxial welding, demonstrating how closely positioned FCC nanocubes can fuse into a single monocrystalline nanostructure.

Notably, the crystallographic orientation of silver nanocubes, characterized by their well-defined (100) facets, facilitates epitaxial interconnections during overgrowth, yielding monocrystalline structures (Figure 1.21d). The bottom image in Figure 1.21b shows a TEM micrograph of seven interconnected nanocubes, along with the cor-

responding selected-area electron diffraction (SAED) pattern confirming monocrystallinity throughout the entire assembly. Additionally, the top image clearly demonstrates continuous atomic columns at the junction between two nanocubes, underscoring the precise crystallographic alignment and the excellent structural quality achieved by this method.

Electrical characterization further supported this quality, showing an ohmic response and an intrinsic resistivity of 2.0×10^{-8} Ωm, which closely matches theoretical values for defect-free silver. However, a notable challenge with this epitaxial welding technique is unwanted secondary nucleation on the substrate. This issue is clearly illustrated in the inset of Figure 1.21c which shows numerous small nuclei formed on the substrate surface. Such secondary nucleation could negatively impacts the optical properties of the final nanostructure, indicating the need for further optimization of the overgrowth conditions.

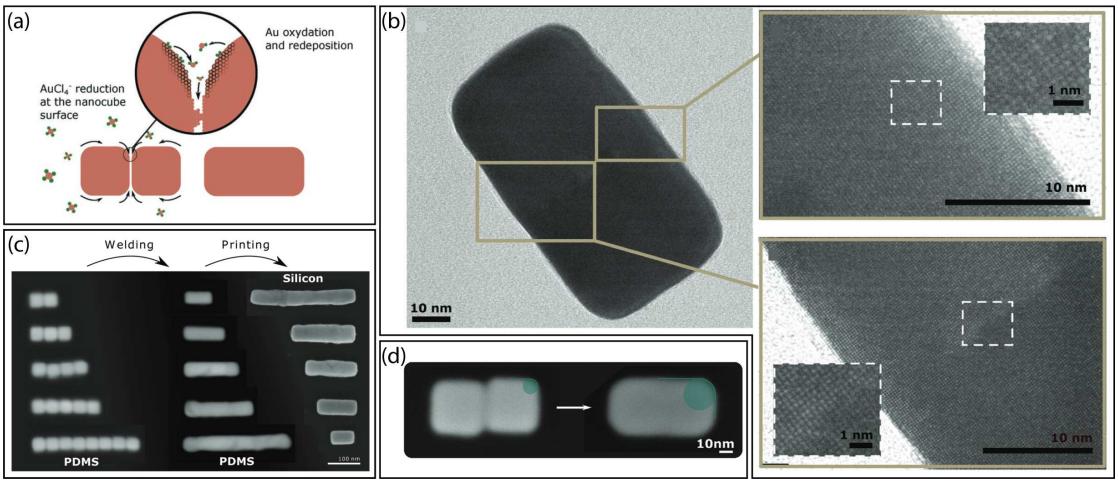

Figure 1.22.: (a) Schematic illustrating the welding mechanism of gold nanocubes involving simultaneous oxidative etching and epitaxial growth(reproduced from ref. [1]). (b) TEM characterization displaying atomic columns at the junction between two nanocubes, indicating crystallographic alignment (reproduced from ref. [1]). (c) SEM image series showing gold nanorods of varying aspect ratios assembled from two, three, four, five, and eight 38 nm gold nanocubes. Images show the assemblies before epitaxial welding in PDMS (left), after epitaxial welding in PDMS (middle), and after transferring onto silicon substrates (right)(reproduced from ref. [1]). (d) Illustration showing an increase in radius of curvature following welding, attributed to oxidative etching at the corners of the original nanocubes(reproduced from ref. [1]).

An alternative strategy developed within our group was reported by Capitaine and Sciacca, who demonstrated the epitaxial welding of closely positioned gold nanocubes in an acidic HNO_3 solution without any additional reducing agents, effectively suppressing homogeneous nucleation[1]. In this approach, competitive oxidative etching at the corners of the nanocubes and simultaneous heterogeneous nucleation at their

surfaces ensure that sub-nanometer gaps between adjacent cubes are filled (Figure 1.22a). High-resolution TEM imaging (Figure 1.22b) confirmed the monocrystalline quality and crystallographic alignment at the junction between two welded nanocubes. Furthermore, by combining this method with templated capillary assembly, they successfully fabricated monocrystalline gold nanorods arranged into one-dimensional lines with tunable aspect ratios (Figure 1.22c). However, as depicted in Figure 1.22d, this technique has the disadvantage of oxidative etching, which causes corner rounding, thus altering the final shape of the nanostructures.

1.3.3. Conclusion

In summary, although the epitaxial welding process still has room for improvement, assembling nanocubes in close proximity followed by epitaxial welding remains a promising approach for fabricating complex, monocrystalline nanostructures. This approach is not limited solely to simple one-dimensional line nanostructures but could enable far more intricate designs, including two-dimensional arrangements resembling polyominoes or even more sophisticated three-dimensional configurations. Such capabilities highlight the significant potential of epitaxial welding as a versatile tool in nanoscale materials engineering.

1.4. Thesis motivation

In this chapter, I discussed the importance of shape and monocrystallinity in metallic nanostructures, along with a look at current methods for templated nanoparticle assembly that allow us to build metal nanostructures as designer's wish. I also discussed wet-chemical approaches that can transform assembled metal nanocubes into continuous, monocrystalline nanostructures.

At the beginning of my PhD, one of the techniques extensively explored by our group was capillary assembly. Although capillary assembly is versatile, this method is inherently challenging due to its sensitivity to multiple parameters, such as colloidal concentration, temperature, drag speed, and humidity. Its complexity is further increased by its dynamic nature: nanoparticles continuously move from the bulk suspension toward the contact line as it recedes along the patterned template. At this contact line, nanoparticles fill the trenches sequentially, making the assembly process particularly sensitive not only to defects within the patterns but also to density and geometry of the patterns, and their orientation relative to the direction of the contact line.

This complexity raises several open questions. For example, what would happen if, instead of dynamically filling trenches as the contact line moves during capillary assembly, we filled them simultaneously by using a densely packed nanoparticle monolayer? If this static approach is successful, how could then we selectively remove excess nanoparticles that remain outside the trenches? Additionally, what are the geometric constraints or limitations of trenches for effective filling? Could such an

assembly method be utilized in practical, functional applications? Finally, can these assembled nanoparticles be interconnected into monocrystalline nanostructures using previously reported epitaxial welding methods?

Furthermore, the epitaxial welding process itself raises additional intriguing questions. Can the epitaxial welding approach, previously demonstrated for gold nanocubes using oxidative etching and overgrowth, be adapted to silver nanocubes? or even aluminum nanocubes? If the existing oxidative etching approach proves ineffective, could a more controlled chemical overgrowth process facilitate better epitaxial welding without inducing unwanted secondary nucleation on the substrate?

Addressing these fundamental questions has been the central motivation of this PhD thesis, and the detailed findings from this investigation are presented in the subsequent chapters.

2. Designer metasurfaces *via* nanocube assembly at the air-water interface[1]

The advent of metasurfaces has revolutionized the design of optical instruments, and recent advancements in fabrication techniques are further accelerating their practical applications. However, conventional top-down fabrication of intricate nanostructures proves to be expensive and time-consuming, posing challenges for large-scale production. Here, we propose a cost-effective bottom-up approach to create nanostructure arrays with arbitrarily complex meta-atoms displaying single nanoparticle lateral resolution over submillimeter areas, minimizing the need for advanced and high-cost nanofabrication equipment. By utilizing air-water interface assembly, we transfer nanoparticles onto templated polydimethylsiloxane (PDMS) irrespective of nanopattern density, shape, or size. We demonstrate the robust assembly of nanocubes into meta-atoms with diverse configurations generally unachievable by conventional methods, including U, L, cross, S, T, gammadion, split-ring resonators, and Pancharatnam-Berry metasurfaces with designer optical functionalities. We also show nanocube epitaxy at near ambient temperature to transform the meta-atoms into complex continuous nanostructures that can be swiftly transferred from PDMS to various substrates via contact printing. Our approach potentially offers a large-scale manufacturing alternative to top-down fabrication for metal nanostructuring, unlocking possibilities in the realm of nanophotonics.

[1]Major part of this chapter has been published in: M. L. Fajri , N. Kossowski, I. Bouanane, F. Bedu, P. Poungsripong, R. Juliano-Martins, C. Majorel, O. Margeat, J. L. Rouzo, P. Genevet, B. Sciacca, "Designer metasurfaces *via* nanocube assembly at the air-water interface" *ACS Nano* **2024**, 18, 38, 26088-26102

Summary

2.1. Introduction . . . 69
2.2. Results and discussion . . . 70
2.2.1. Nanopatterning from nanocubes at the air-water interface assembly . . . 70
2.2.2. Assembly with nanoparticles of various shapes . . . 76
2.2.3. Continuous monocrystalline meta-atoms . . . 83
2.2.4. Transfer printing onto a substrate . . . 84
2.2.5. Nanocubes assembly mechanism . . . 85
2.2.5.1. Estimating the nanocube filling fraction . . . 86
2.2.5.2. Effect of nanocube density and dipping angle on split-ring filling fraction . . . 87
2.2.6. Optical characterization . . . 91
2.2.7. Nanocubes assembly into Pancharatnam-Berry (PB) phase metasurface . . . 92
2.2.7.1. PB working principle . . . 92
2.2.7.2. Experimental results and simulations . . . 93
2.3. Conclusion . . . 99

2.1. Introduction

The development of metasurfaces has sparked considerable interest across multiple fields, such as chemo- and photo-sensing[125–127], metalens[128, 129], holography[128, 130], catalysis[131], and light emitters[132]. Despite these exciting prospects, a critical challenge persists: the development of a low-cost, facile, yet versatile technique for nanostructuring materials with intricate arbitrary geometries and nanometer resolution. Conventionally, top-down electron beam lithography (EBL) has been employed for creating complex nanostructures with resolutions smaller than 10 nm[10]. However, the high costs and lengthy processing times associated with EBL render large-scale production unfavorable. Additionally, the subsequent utilization of physical vapor deposition lacks control over crystallinity[133], and etching processes introduce surface roughness and defects[65]. These factors significantly impact the bulk and surface quality of the material, which are critical for minimizing losses and improving the spectral response of such nanopatterns[66].

An alternative approach is nanoimprint lithography (NIL), in which an elastomeric stamp such as PDMS is molded from a high-resolution master template fabricated *via* EBL. The mold is then used to mechanically imprint the nanopattern into a thermo- or UV-curable resin, which can be polymeric or a sol-gel-based compound[134, 135]. A key advantage of this approach is its non-destructive nature towards the master pattern, enabling the creation of virtually unlimited replica at an affordable cost. While NIL offers scalability and high throughput, it suffers from nanostructures shrinkage, residual layers and limitations in material selection, especially metals, which are of high interest for plasmonic applications[136]. To circumvent this, strategies like the use of metal-organic inks as resists have been proposed, followed by heat treatment[137]. However, these approaches often yield nanostructures with undesirable defects, such as rough surfaces, cracks and grain boundaries[138].

Bottom-up self-assembly, utilizes chemically synthesized nanoparticles as building blocks to create ordered architectures driven by chemical interactions[67]. This method offers distinct advantages, such as low cost, fine control over size, shape, atomic-level compositions, and the unmatched material quality of monocrystalline colloidal building blocks. However, thermodynamics restricts the viable geometries of the resulting architectures and their organization on a surface[67, 68].

To address these challenges, templated self-assembly, emerged as an encouraging solution[133, 139, 140]. Herein, we introduce an approach for the fabrication of nanostructure arrays with arbitrary 2D meta-atoms with single nanoparticle lateral resolution. This is achieved with a homemade setup, in which a monolayer of nanoparticles densely assembled on an air-water interface is subsequently transferred to a nanopatterned PDMS substrate.

Leveraging this method, each nanoparticle serves as a foundational building block unit, facilitating the assembly into intricate nanopatterns, including but not limited

to arrays of U-shaped, L-shaped, cross-shaped, S-shaped, and T-shaped, polygonal-shaped, gammadion, split-ring resonators, and spatially varying Pancharatnam-Berry metasurfaces. Such intricate designs have proven elusive with traditional assembly techniques. Given their optimal properties as building blocks for monocrystalline nanostructures[1, 11], we primarily focus on nanocubes. Nonetheless, our technique's versatility is further underscored by the assembly of other nanoparticles, such as gold icosahedra and gold nanocubes of different sizes.

Next, exploring the potential for optoelectronic applications, we investigated the optical properties of nanocube assemblies into Pancharatnam-Berry metasurface, and compared them to finite-difference time-domain (FDTD) simulations. Finally, we show the possibility to make continuous nanostructures *via* nanocube chemical welding at near ambient temperature. We first use nanocubes as a nanoscale building block to first access complex shapes and then welding them together to get continuous planar structures. This two-step process provides a bottom-up pathway for crafting intricate nanostructures, which are challenging, if not impossible to produce through conventional chemical synthesis alone. This approach enables the synthesis of nanostructures with truly arbitrary geometries beyond that of conventional Platonic solids. Such capability holds significant value for the design of plasmonic metasurfaces in the visible range, as their performance is intricately linked to the geometric attributes of their constituent meta-atoms.

2.2. Results and discussion

2.2.1. Nanopatterning from nanocubes at the air-water interface assembly

As depicted in Figure 2.1, the fabrication process begins by assembling nanocubes into a high-density monolayer at the air-water interface (Fig. 2.1a). This monolayer is then transferred onto a pre-patterned PDMS substrate *via* nanocubes deposition (Fig. 2.1b), achieved by simply bringing the two into contact. Any excess nanocubes lying outside the intended nanopatterned trenches are subsequently removed *via* selective contact printing (excess nanocubes removal, Fig. 2.1c). This step ensures that only nanocubes conforming to the desired nanopattern are retained within the trenches. Following this, two alternative pathways are available: the remaining nanocubes can either be directly transferred onto a target substrate through transfer printing (Fig. 2.1d) or subjected to a welding process on the PDMS mold to create a continuous nanostructure (Fig. 2.1e). The latter can then also be transferred to the target substrate using the same transfer printing technique (Fig. 2.1f).

Here, we used 55 nm silver nanocubes (AgNCs). As mentioned previously, following the nanocubes deposition process (Fig. 2.1b), it is evident that, although some nanocubes were confined within the trenches, the majority remained as residuals deposited outside these features (see Figs. 2.20a bottom inset images, 2.21, and 2.23). To address this, we conducted the critical step of removing excess nanocubes (Fig. 2.1c).

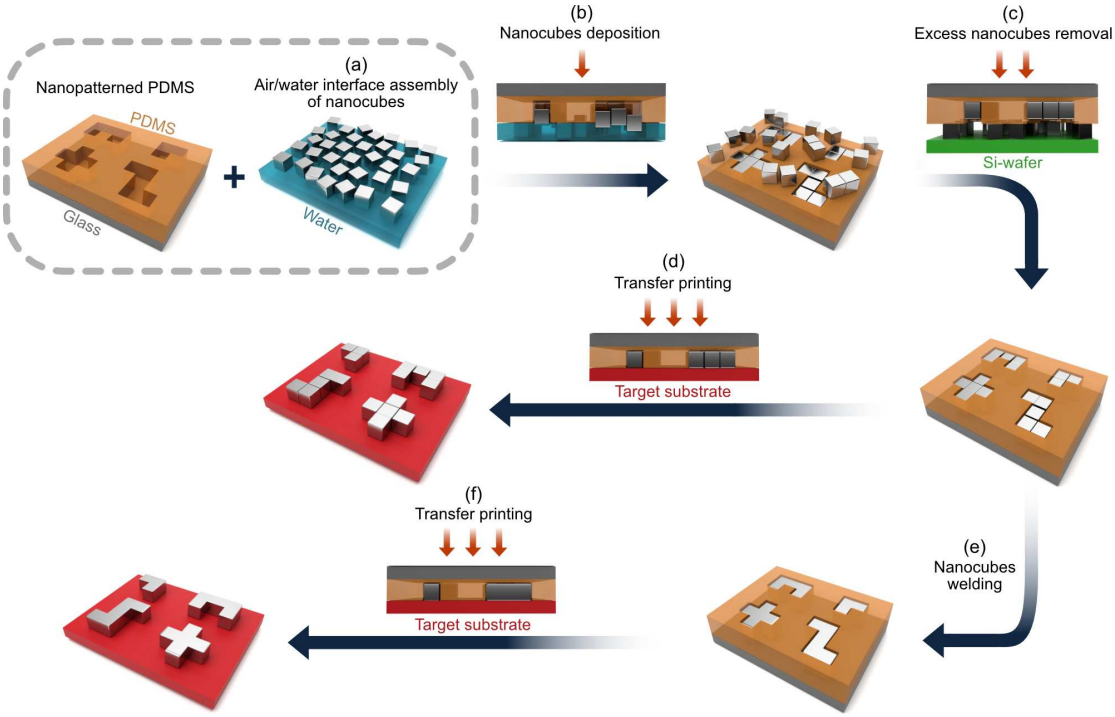

Figure 2.1.: Diagram of nanopattern fabrication from nanocubes. The process involves: (a) nanocubes dispersion at the air-water interface, (b) nanocubes directed assembly, (c) excess nanocubes removal. Subsequent pathways include: (d) transfer printing of assembled nanocubes onto target substrate, or (e) welding of nanocubes to form continuous nanostructures, followed by (f) transfer printing onto target substrate.

This was carried out by putting the silver nanocubes deposited on PDMS in contact with a clean silicon wafer using the homemade setup shown in Appendix B.2. Silicon's higher surface energy and atomically flat surface facilitate the transfer of nanocubes that come into contact with it. Nanocubes outside the trenches are more likely to contact the silicon wafer due to their positioning, resulting in their transfer while leaving behind the nanocubes within the trenches. Before making contact, we added a small droplet of PVP/Ethanol solution onto the silicon wafer (see Appendix B.1.6 for details). As reported previously, PVP reduces Van der Waals interactions between the nanocubes and the substrate, promoting the mobility of the nanocubes[78]. After achieving conformal contact, we heated the setup to approximately 40° C to evaporate the solvent before retraction.

As depicted in Figure 2.2, our technique effectively eliminates most extraneous nanocubes while preserving those situated in the trenches. In our best samples, the removal process was highly effective across thousands of square micrometers, as evidenced by Figure 2.3. It is worth emphasizing that the removal of nanocubes is a delicate and nuanced process due to the nature of selective transfer, requiring careful

control of the critical parameters (detailed experimental procedures are provided in the Appendix B). In our experience, a trench depth larger than the nanocube size yields better results for nanocube removal. For all masters used, the depth is greater than the nanocube dimension (80-93 nm). When the depth is equivalent to the nanocube dimension, although deposition into the trench appears to work, the removal step is less reproducible.

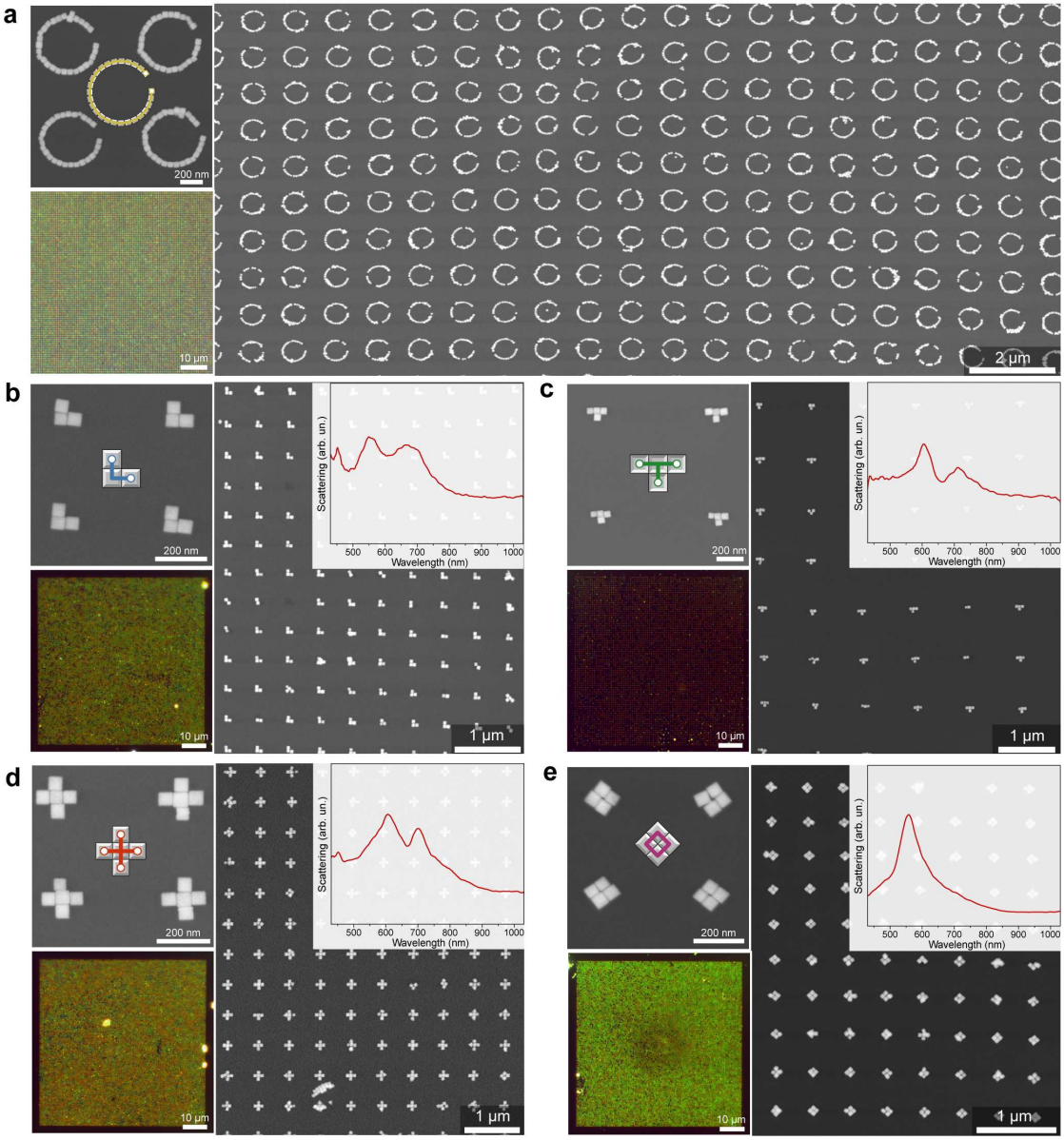

Figure 2.2.: Assembly of 55 nm AgNCs on different basic meta-atoms with their corresponding measured dark-field scattering and dark-field images. a, Split-ring resonator. b, L-shape. c, T-shape. d, Cross-shape. e, Diamond-shape.

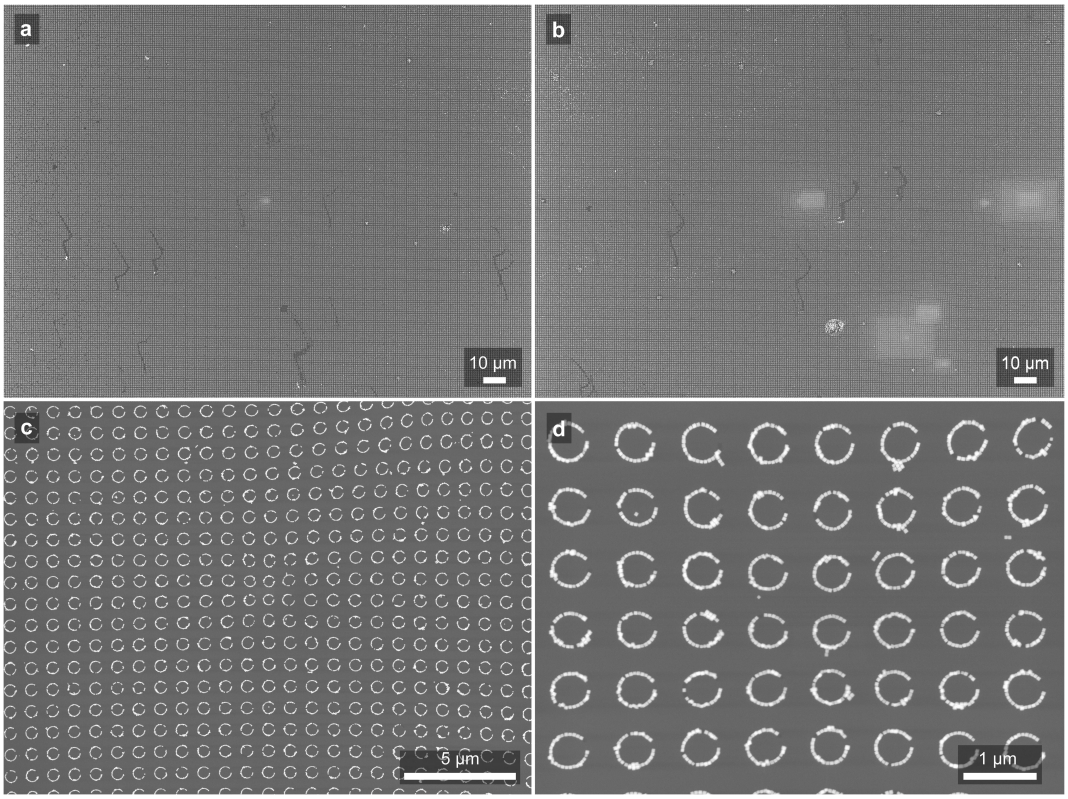

Figure 2.3.: Assembly of ~55 nm silver nanocubes on small split-ring patterned-PDMS after nanocubes removal on the best sample.

To investigate the capability of our technique in assembling nanocubes into a diverse array of geometric configurations, first we performed experiments featuring a range of fundamental meta-atoms with single nanocube lateral resolution. In fact, we argue that the realization of a truly arbitrary pattern requires the capability to accomplish five elemental meta-atoms. This includes arcs in addition to the four possible combinations where, for a given nanocube, any of the four neighboring positions is occupied by another nanocube. This yields straight lines, 90º angles, T-intersections and cross-intersections. Figure 2.2 showcases the results, including structures with curved elements highlighted in yellow, like split-rings (Fig. 2.2a), as well as those featuring multiple junctions including L-shaped geometries with two junctions in blue (Fig. 2.2b), T-shaped forms with three junctions in green (Fig.2.2c), and cross-shaped configurations with four indicated by red color (Fig. 2.2d). Figure 2.2e further demonstrates that our method enables the assembly of diamond-like configurations, consisting of 2x2 nanocubes in a face-to-face orientation, represented in purple. In addition, our technique allows for the assembly of nanocubes in a linear arrangement, as displayed in Figure 2.26b. Given the successful assembly of these foundational shapes, which include straight lines, curves, and intersections, we believe the technique holds promise in facilitating the fabrication of an extensive range of complex nanostructures that incorporate these elements.

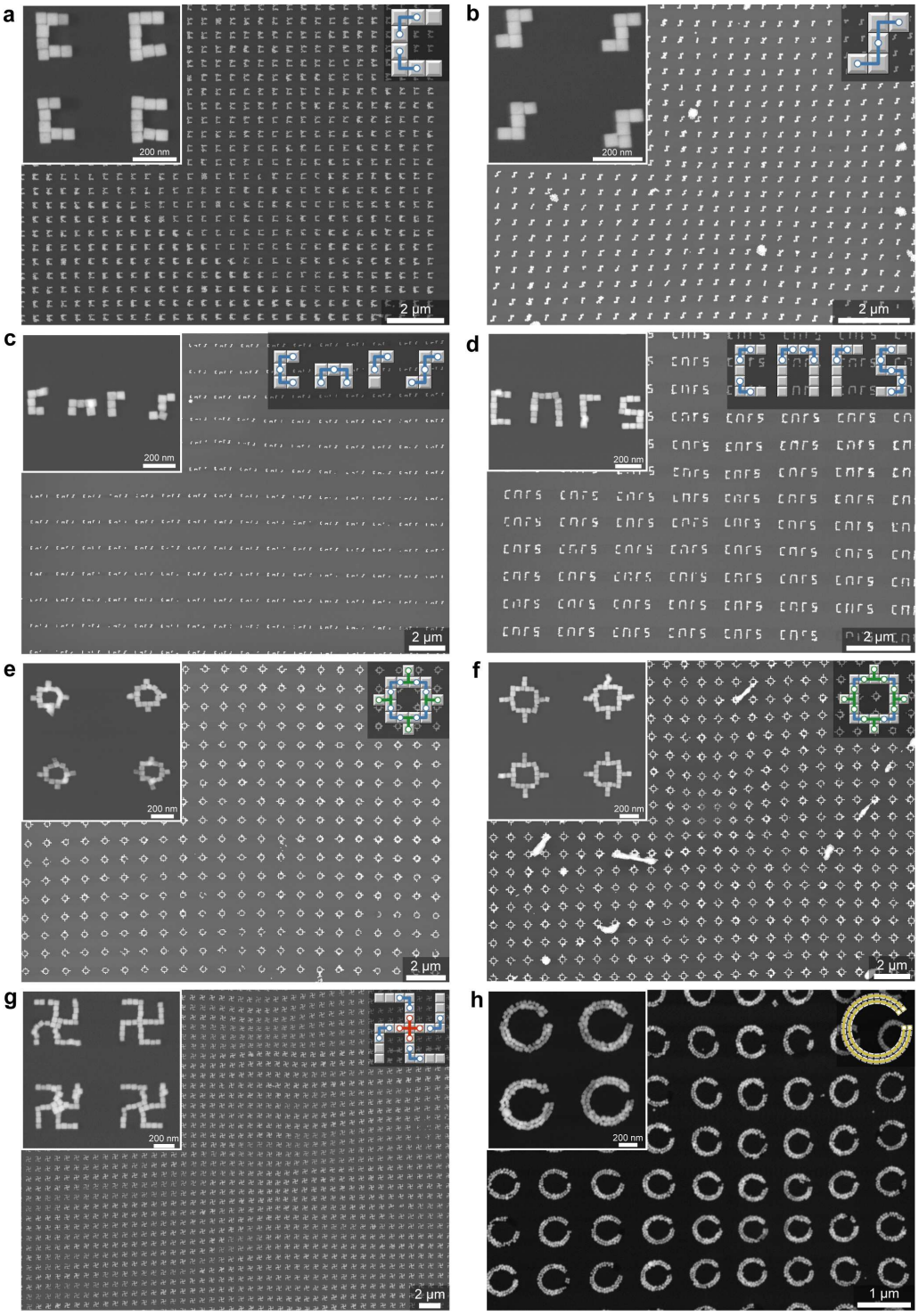

Figure 2.4.: Assembly of 55 nm AgNCs on nanopatterns of a, C-shape, b, S-shape, c-d composed meta-atoms representing the CNRS letters (small and large respectively), e, small polygonal shape, f, larger polygonal shape, and g, chiral gammadion. h, Assembly of 40 nm AgNCs on ~80 nm width split-ring pattern.

Expanding on these findings, Figure 2.4 showcases how we extended the technique's capabilities to assemble more complex designs, encompassing a variety of foundational geometries. The varied configurations include C-shaped patterns that pair two L-shaped geometries with their junctions oriented in the same direction (Fig. 2.4a), as well as S-shaped designs featuring opposite-facing L-shaped configurations (Fig. 2.4b). More intricate structures also can be obtained, such as the CNRS letters at varying scales, built from multiple L-shaped elements (Figs. 2.4c and 2.4d), polygonal patterns featuring both T- and L-junctions (Figs. 2.4e and 2.4f), gammadion shapes that integrate cross and L geometries (Fig. 2.4g) displaying circular dichroism (Fig. 2.25), and split-ring patterns with a lateral thickness equivalent to two nanocubes (Fig. 2.4h). The insets color-code the fundamental geometric shapes that comprise each complex design, enhancing visual clarity. It is worth noticing that arrays encompassing multiple meta-atoms in their basic repeating unit can be obtained, as shown in Figs 2.4c and 2.4d), where four different meta-atoms next to each other are realized. While some of these designs hold relevance for plasmonics, certain configurations depicted in Figures 2.2d, 2.4e, and 2.4f are also promising for transparent electrodes through pattern interconnection. Additionally, as shown in Figure 2.5, although this is not our primary focus, we also demonstrate the possibility of obtaining single-particle assemblies.

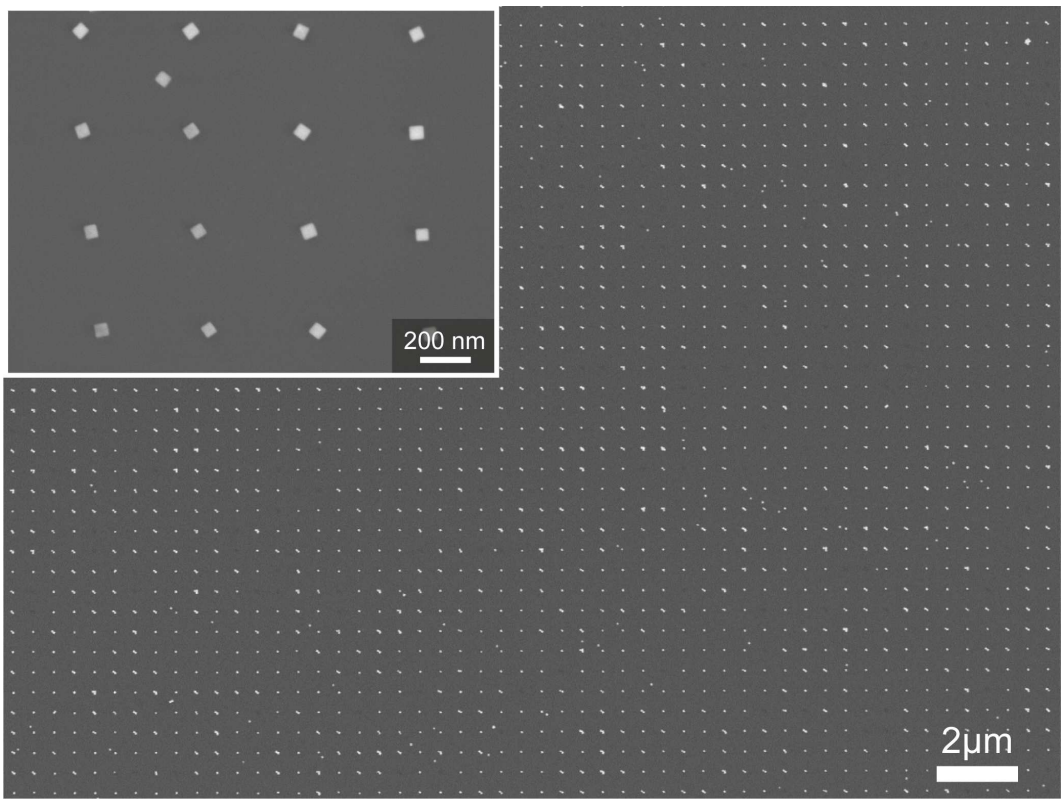

Figure 2.5.: Assembly of individual nanocube.

2.2.2. Assembly with nanoparticles of various shapes

To demonstrate the versatility of this technique, we successfully extended our exploration to the assembly of various other materials, including 40 nm silver nanocubes, 32 nm rounded gold nanocubes, 43 nm gold icosahedra, and 48 nm gold nanocubes (See Figs. 2.6, 2.7, 2.8, 2.9, 2.10, 2.11, 2.13, 2.14, and 2.27).

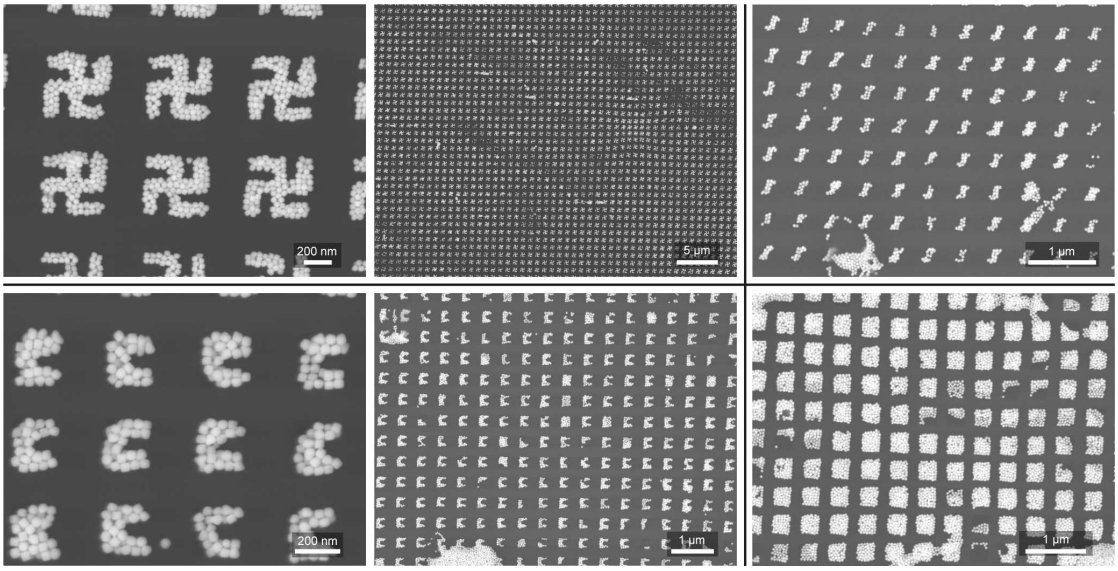

Figure 2.6.: Assembly of ~32 nm rounded gold nanocubes on variously patterned PDMS surfaces.

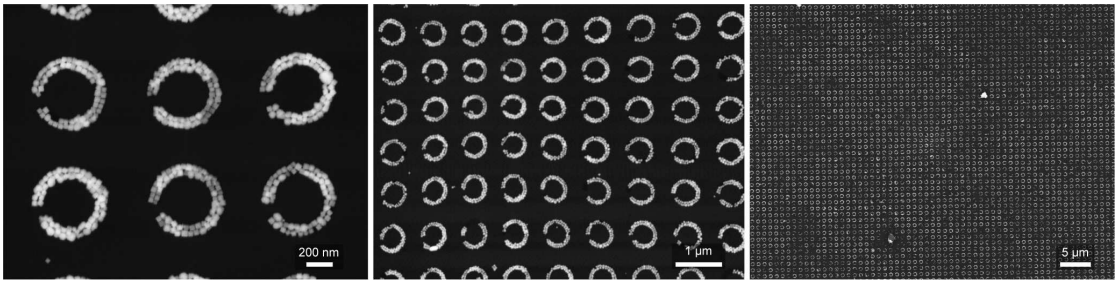

Figure 2.7.: Assembly of ~40 nm silver nanocubes on large split-ring patterned PDMS surface.

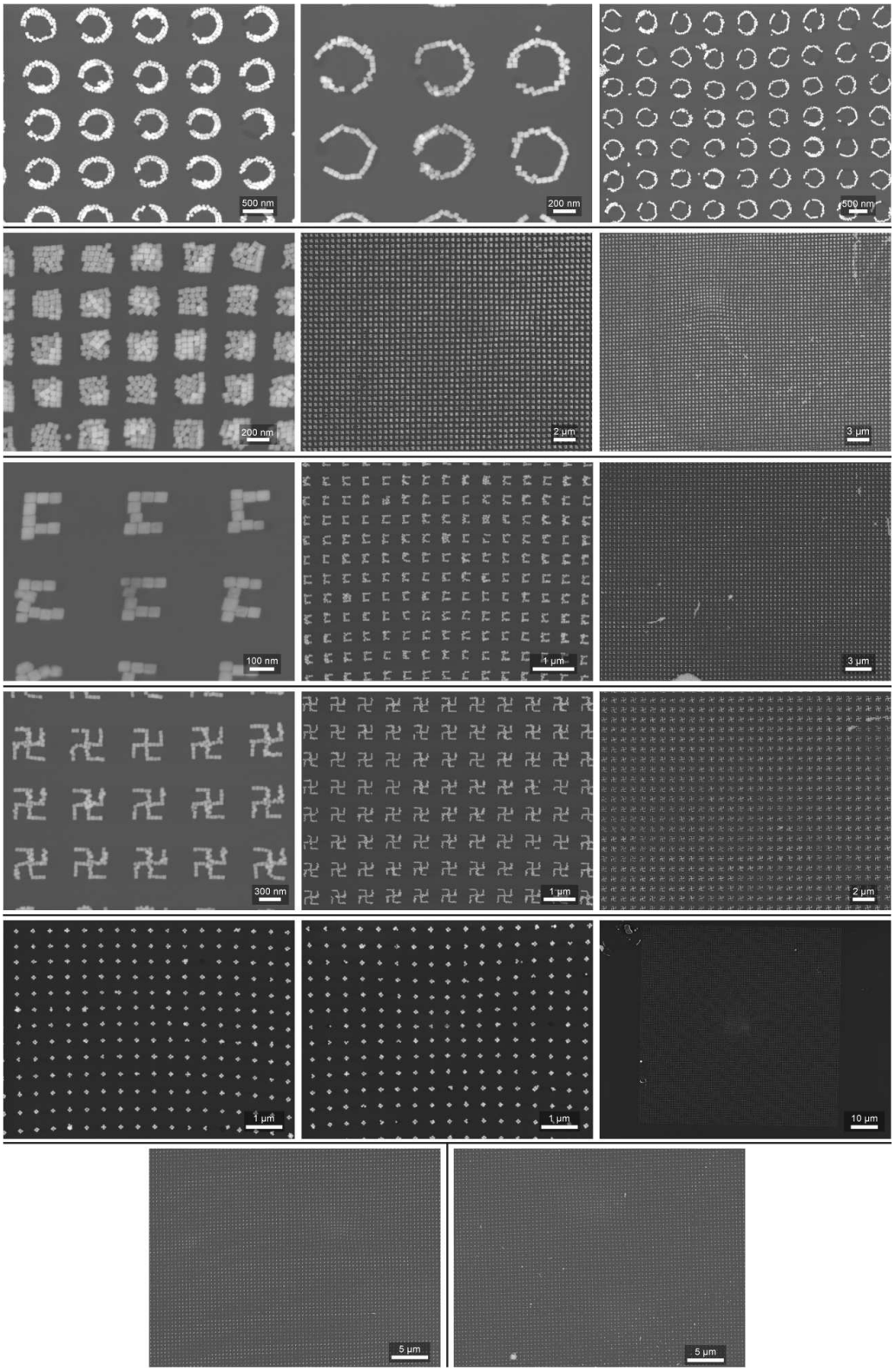

Figure 2.8.: Assembly of ~55 nm silver nanocubes on variously patterned PDMS surfaces.

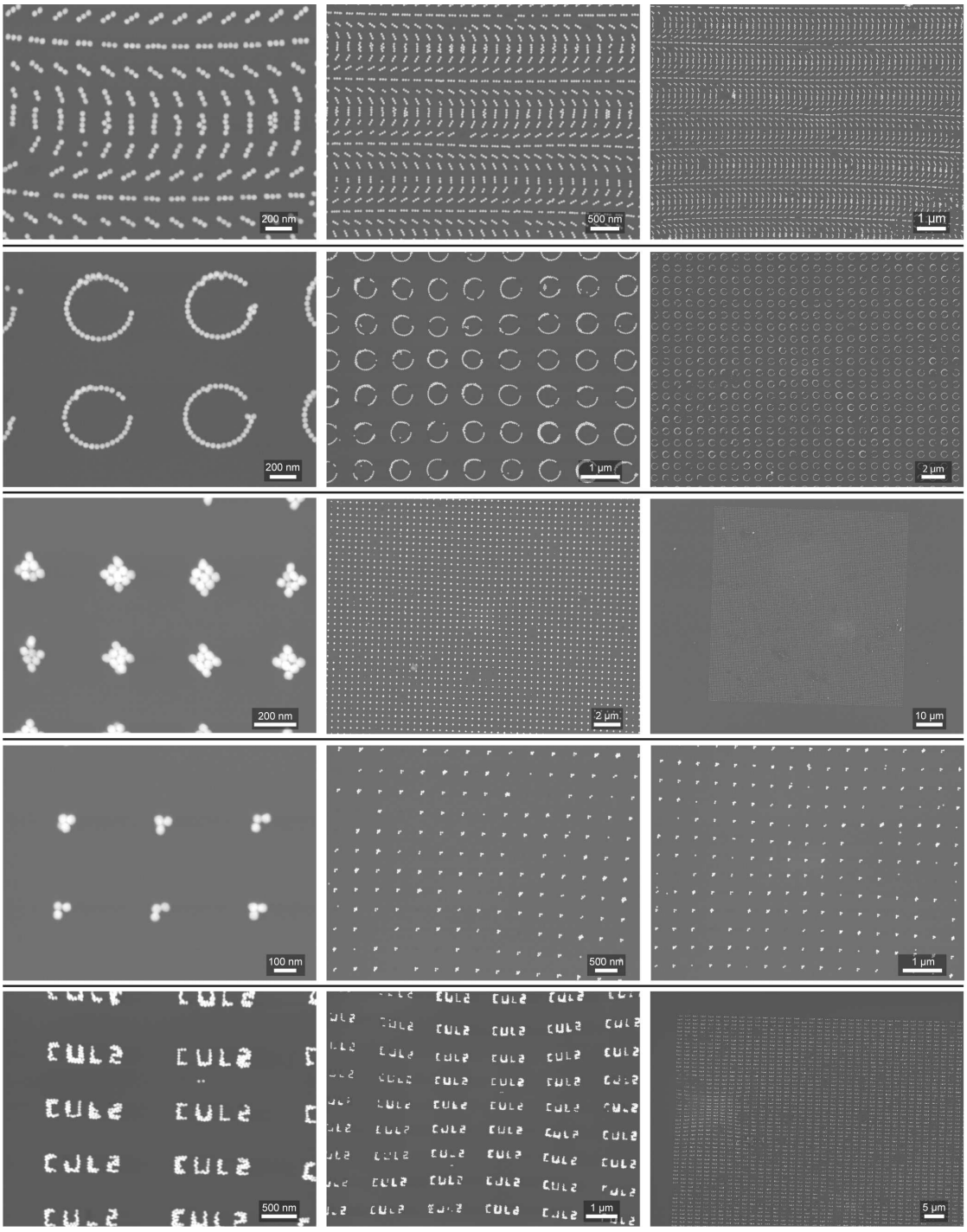

Figure 2.9.: Assembly of ~43 nm gold icosahedra on variously patterned PDMS surfaces.

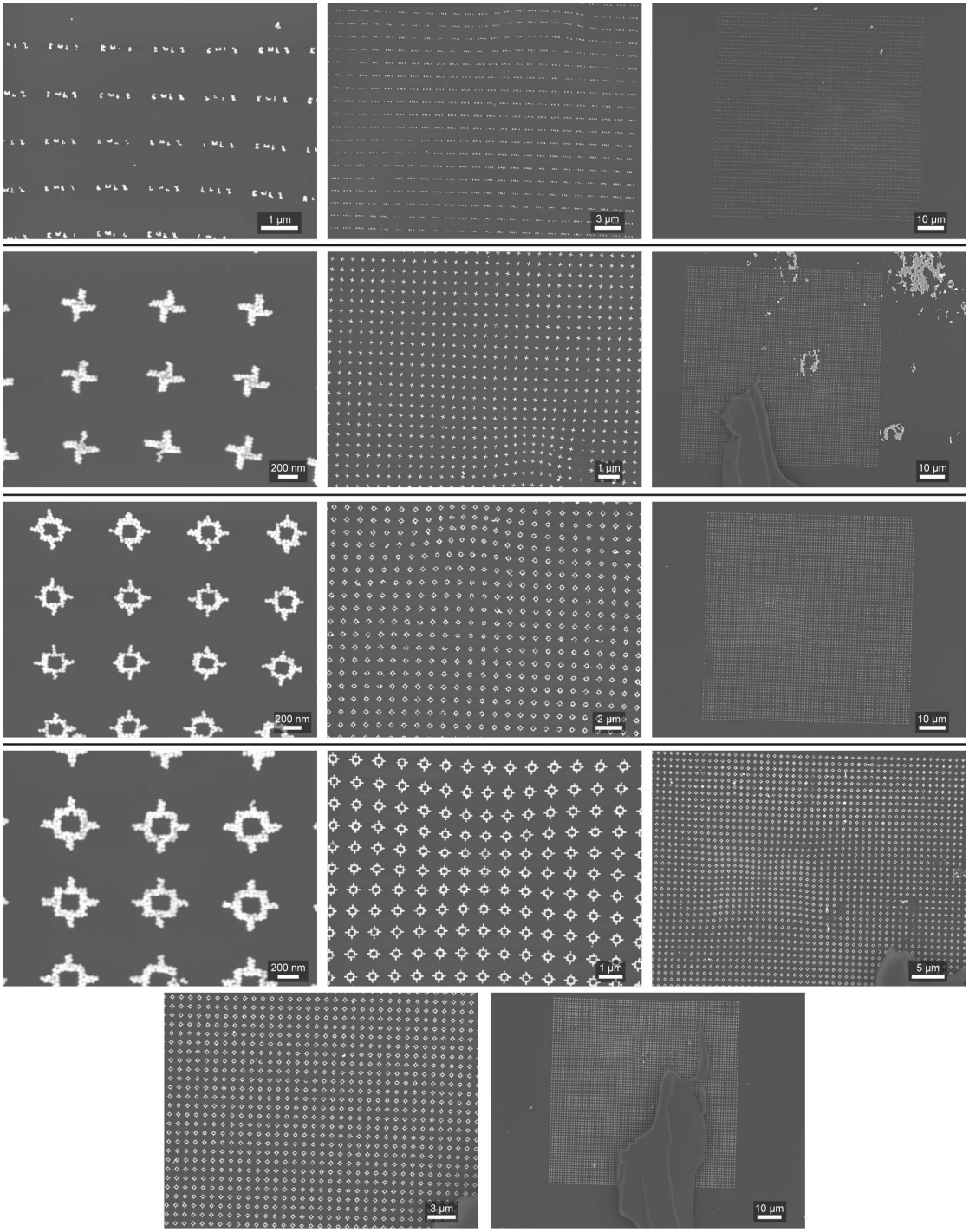

Figure 2.10.: Assembly of ~43 nm gold icosahedra on variously patterned PDMS surfaces.

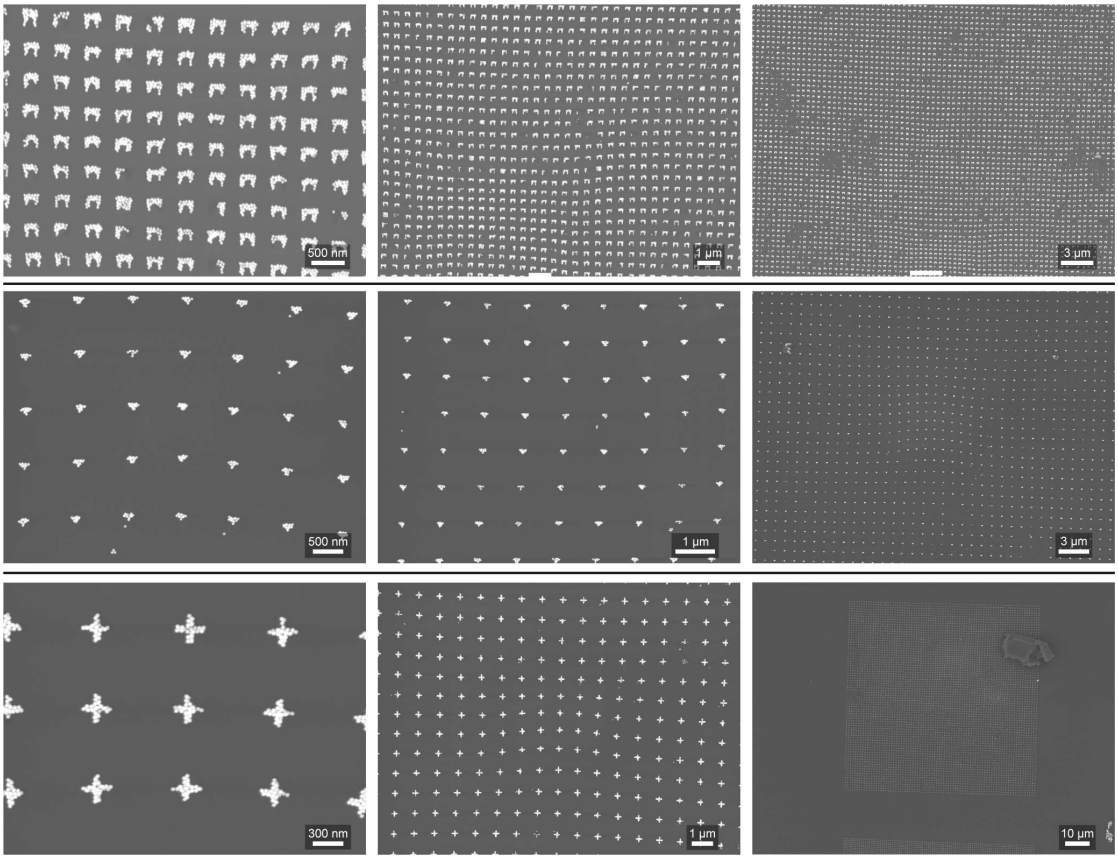

Figure 2.11.: Assembly of ~43 nm Au icosahedra on variously patterned PDMS surfaces.

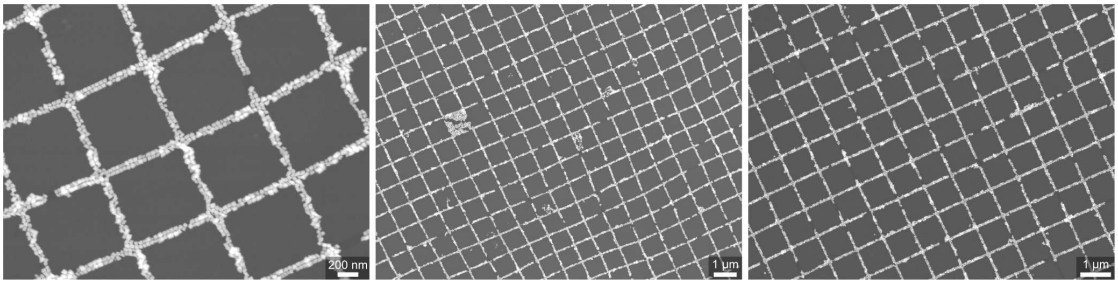

Figure 2.12.: ~40 nm silver nanocubes assembled on a grid patterned PDMS substrate.

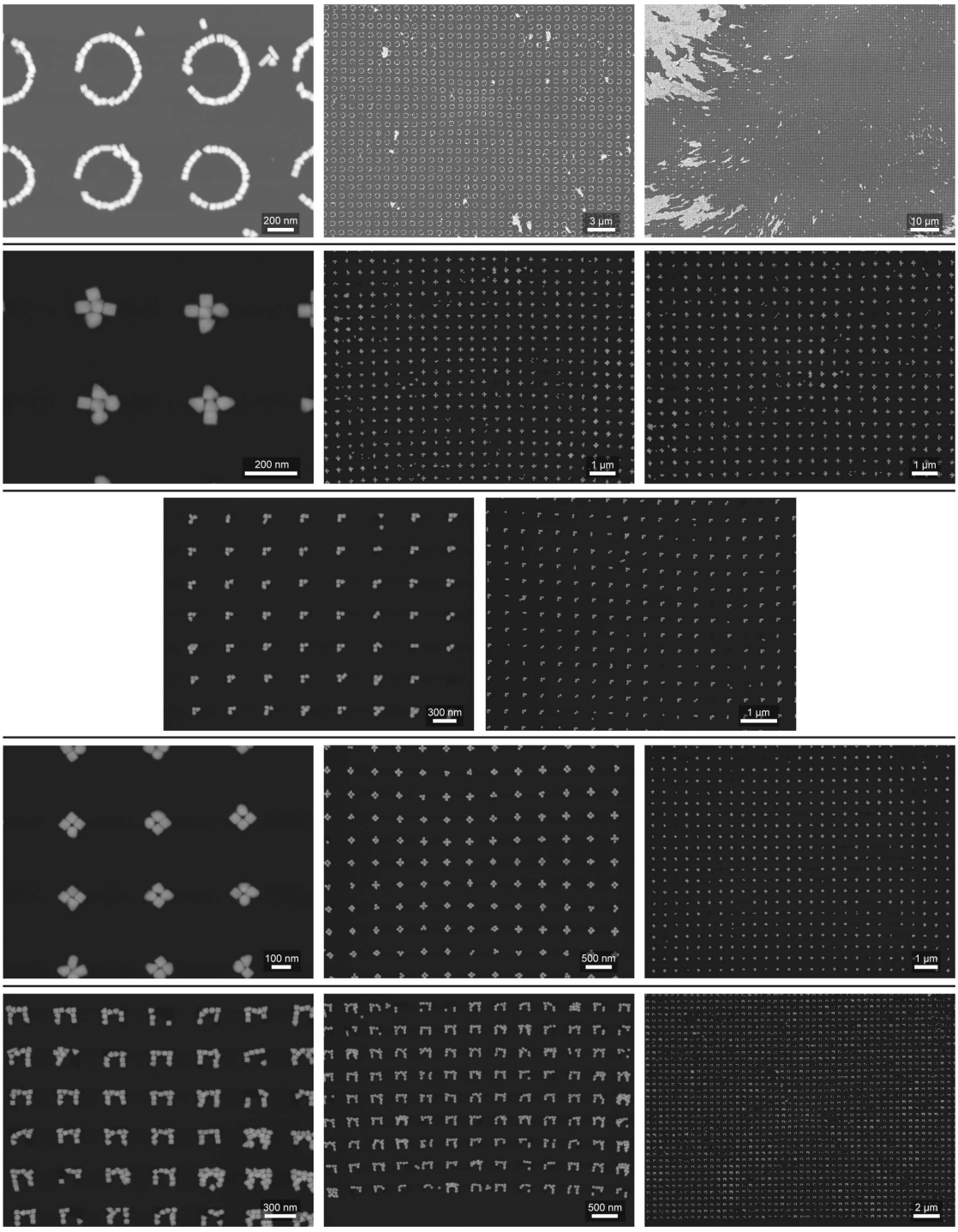

Figure 2.13.: Assembly of ~48 nm gold nanocubes on variously patterned PDMS surfaces.

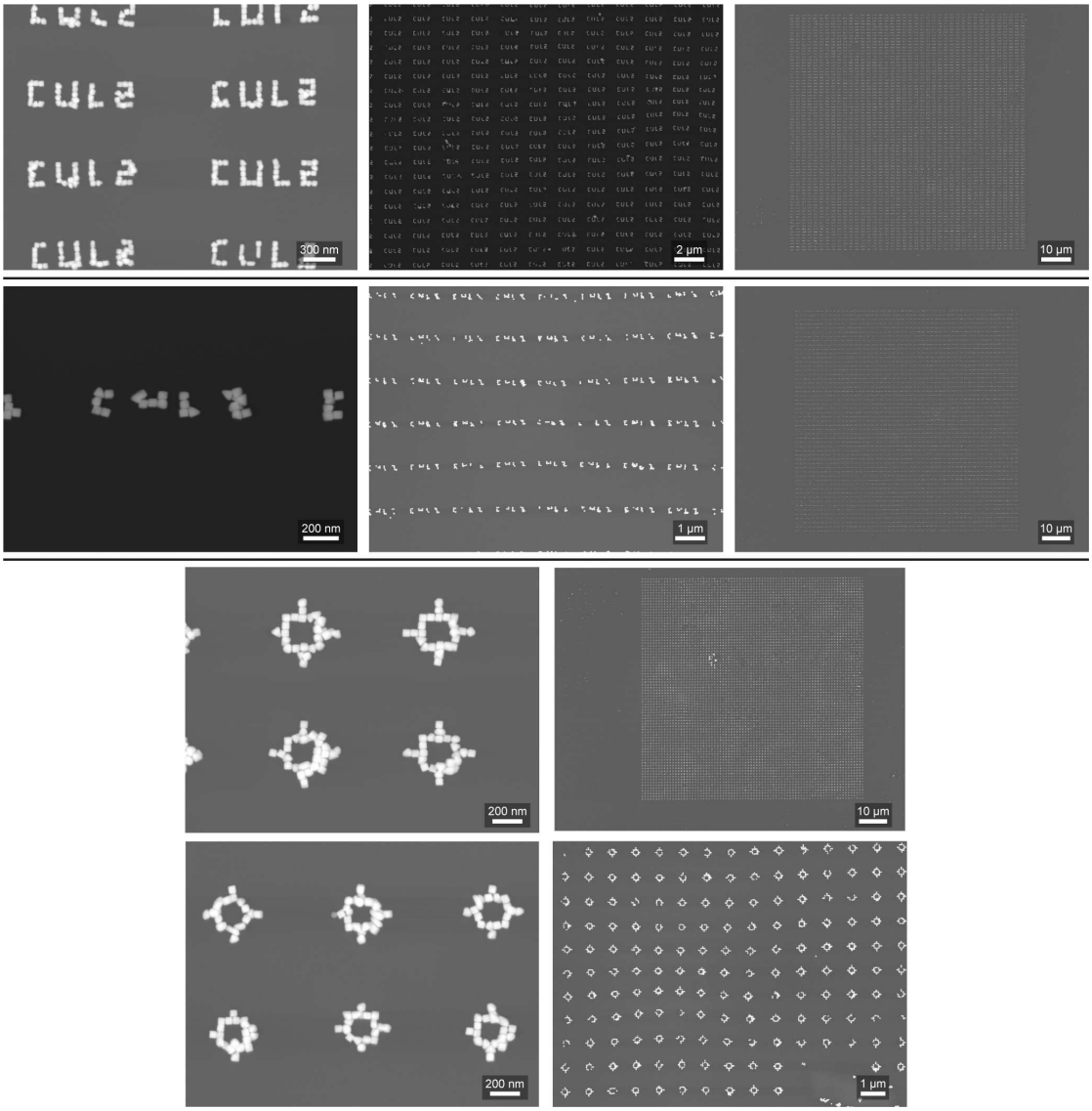

Figure 2.14.: Assembly of ~48 nm gold nanocubes on variously patterned PDMS surfaces.

2.2.3. Continuous monocrystalline meta-atoms

We further explored the possibility of creating continuous nanopatterns via nanocube epitaxy. By integrating capillary assembly with epitaxial welding, we aim to establish an entirely bottom-up fabrication strategy capable of producing complex structures at sub-100 nm scales with single-nanoparticle lateral resolution. To date, reports have only demonstrated chemical welding of nanocubes assembled linearly through capillary forces, resulting in rod-like monocrystalline structures either by direct overgrowth[11] or by oxidative etching and regrowth[1]. Here, we extend the oxidative etching and growth strategy previously introduced by our group for gold[1] to fabricate more intricate monocrystalline gold nanostructures (Fig. 2.15a). Additionally, we successfully adapted this approach to silver nanocubes, demonstrating their effective epitaxial welding into continuous silver nanostructures (Fig. 2.15b). The detailed mechanism underlying the epitaxial welding of silver nanocubes is discussed further in Chapter 3.

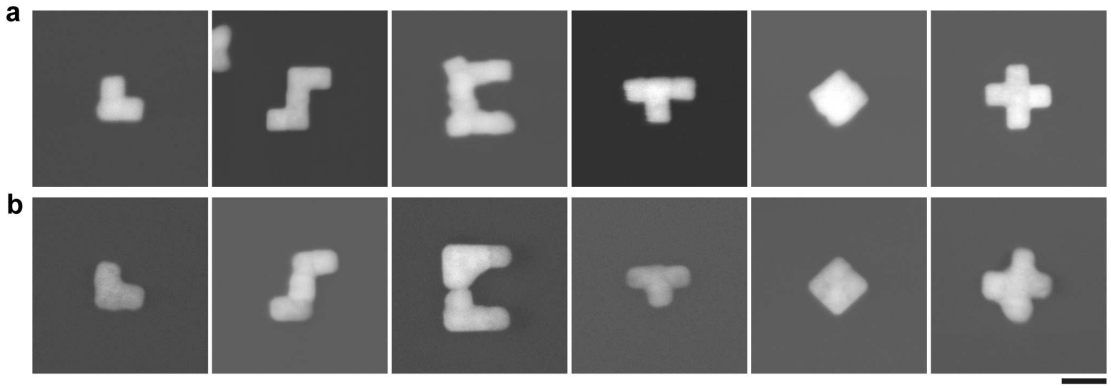

Figure 2.15.: Continuous monocrystalline nanostructures *via* chemical welding for a) gold and b) silver. Scale bar is 100 nm in length.

Commonly, nanoparticles like nanocubes are capped with protective ligands to maintain their shape and inhibit coalescence and Ostwald ripening[141]. The first stage of the process, therefore, entails the removal of these capping ligands. In this work, sodium borohydride serves this function, as it effectively eliminates ligands such as organothiols and adsorbed substances like poly(N-vinylpyrrolidone) (PVP) in this case[142].

The welding process taking place in the 45°C-80°C temperature range and acidic pH, induces nanocube etching and atomic diffusion, particularly from high-energy facets such as corners and edges towards the flat surfaces of the nanocubes. When the nanocubes are closely packed in a face-to-face orientation, this facilitates their interconnection into a smooth structure, that is monocrystalline given the identical crystal orientation of adjacent nanocubes. As a bottom-up solution-based methodology, chemical welding enables the formation of continuous nanostructures at near-ambient temperature, as demonstrated in Figure 2.15a and 2.15b for gold and silver nanocubes, respectively.

2.2.4. Transfer printing onto a substrate

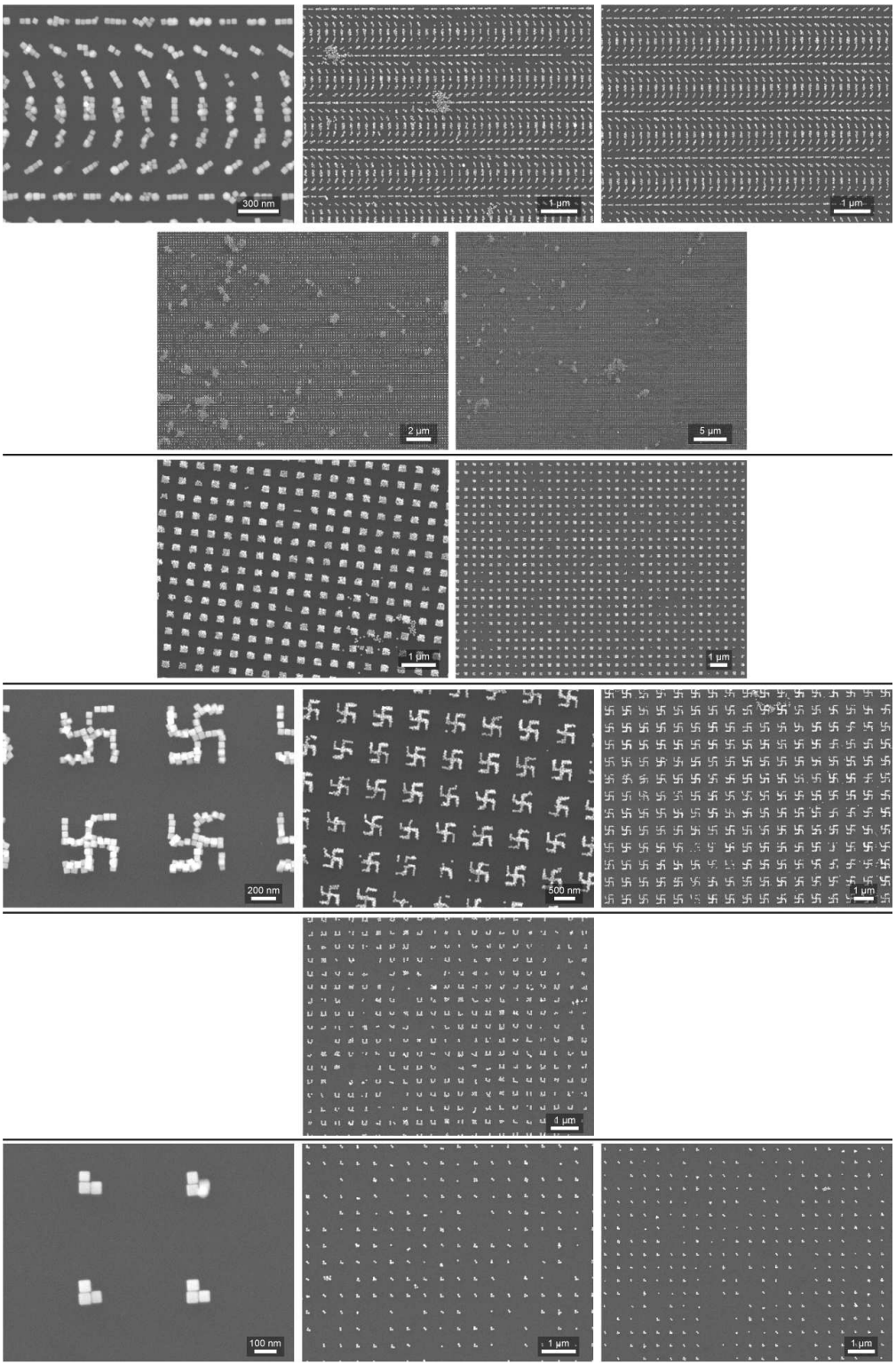

Figure 2.16.: Silver nanocubes assembly transferred on Si-wafer.

Having successfully demonstrated the assembly of diverse nanocube configurations, our next objective is to validate their transfer onto functional substrates through transfer printing. This step represents a vital proof-of-concept for practical applications. In this context, we leveraged the low surface energy of PDMS substrates to facilitate the transfer across a wide variety of substrates. During the transfer, we applied a force ranging from 65-75 N at 75°C, which assured a conformal contact between the nanocubes and the target substrate. Prior studies underscored the benefit of elevated temperature in reducing adhesion between nanocubes and PDMS, thereby enhancing their contact with the substrate and increasing the overall transfer yield[143, 144]. We validated the versatility of our approach by successfully transferring of unwelded and welded nanocubes to silicon wafers and glass, as detailed in Figures 2.16 and 2.17.

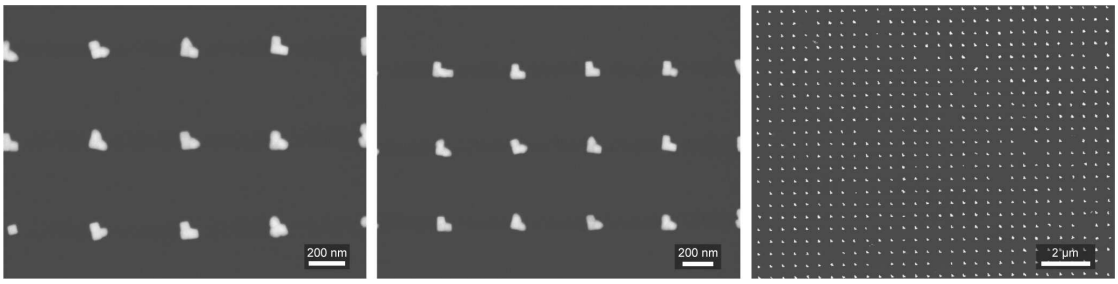

Figure 2.17.: Chemically welded gold nanocubes assembly transferred on a glass substrate.

2.2.5. Nanocubes assembly mechanism

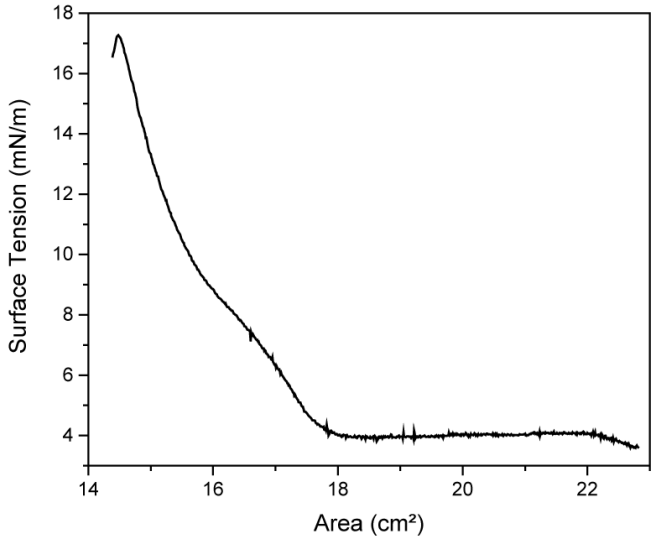

Figure 2.18.: The isotherm for assembly of 0.58 mL 55 nm commercial silver nanocubes.

To understand the mechanism of nanocubes assembly into the trenches, we chose 55 nm monodisperse silver nanocubes and a PDMS mold with a split-ring array as our model system. The split-ring trenches are approximately 80 nm deep and have widths ranging around 55-60 nm (Appendix B.1b). We employed a Langmuir trough (KSV NIMA) to assemble nanocubes on the air-water interface, which allows adjustments to the surface tension and facilitates monitoring through isotherms (See Fig. 2.18 and Fig. 2.20c), thereby providing insights into the density of nanocubes on the water surface[95].

2.2.5.1. Estimating the nanocube filling fraction

Here we introduce the term "split-ring filling fraction", representing the assembly yield, as a quantitative metric to assess the number of nanocubes deposited within each split-ring. A filling fraction of one indicates complete filling of a split-ring with 27 nanocubes, while a filling fraction of zero denotes an empty split-ring (See Fig. 2.19).

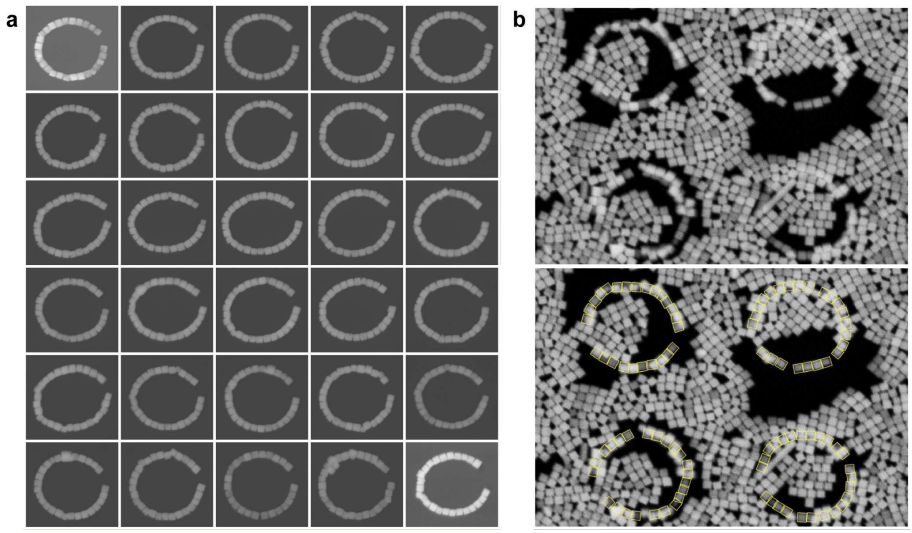

Figure 2.19.: a, Snapshots of selected fully filled small split-ring using 55 nm Ag-NCs. Average nanoparticles filling = 27 nanoparticles/split-ring. b, Calculation of nanocubes inside a small split-ring.

Nanocube filling fraction on a small split-ring nanopattern was manually calculated as follows:

$$\text{Filling fraction} = \frac{\text{Number of nanocubes in a small split} - \text{ring}}{\text{Average nanocube filling}} \tag{2.1}$$

The number of nanocubes in a split-ring is calculated from the nanocubes that are directly observable inside the trench. In cases where nanocubes are not visible due to the second layer blocking their view, it is assumed that the nanocubes underneath are closely compact (refer to Fig. 2.19b).

2.2.5.2. Effect of nanocube density and dipping angle on split-ring filling fraction

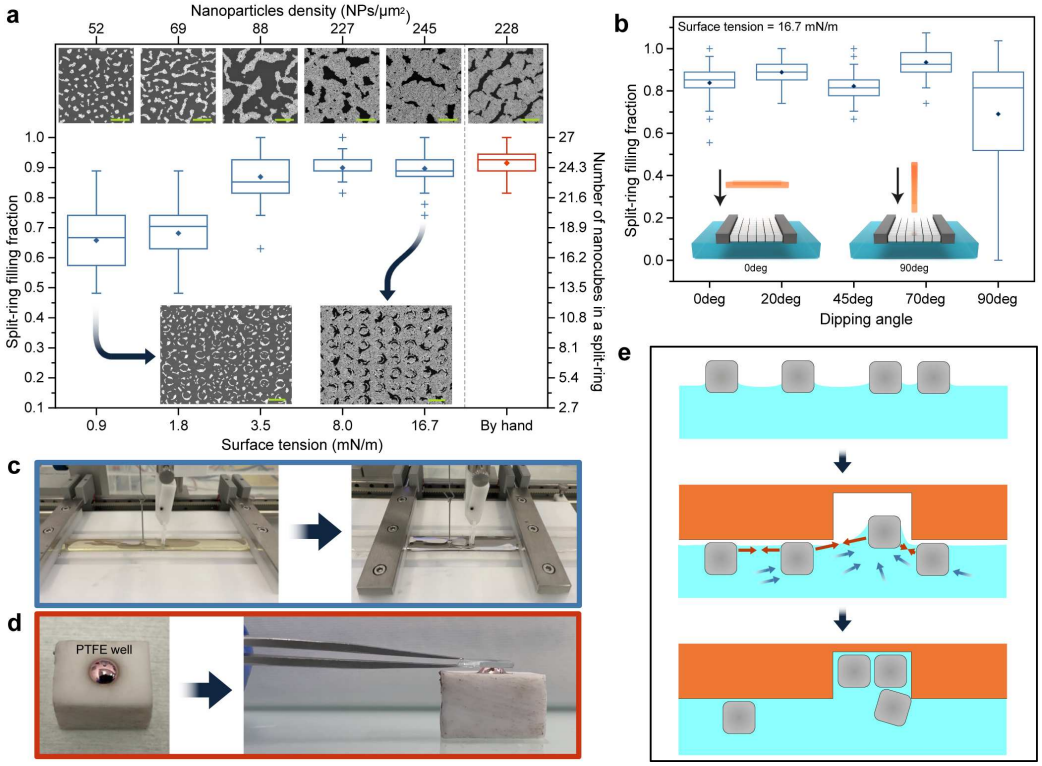

Figure 2.20.: Nanocubes assembly using air-water interface assembly technique. a, Filling fractions of nanocubes inside split-ring nanopattern at different surface tension deposited using a Langmuir trough at 0° dipping angle (blue) vs. using PTFE well by hand (red). The color code of the box plot is the same as that used for c and d. Top insets depict nanocubes density in relation to surface tension on a flat PDMS surface, while bottom insets show density with respect to nanopatterned PDMS surfaces. Scale bars are 1 μm in length. b, Nanocubes assembly at different dipping angles at ~16.7 mN/m. Insets depict the orientations of nanopatterned PDMS substrate (orange) during nanocubes deposition: horizontal alignment at 0 degree and vertical alignment at 90 degree. Center line: Median. Diamond: Average. Box: Interquartile range. Whiskers: Maximum and minimum. Crosses: Outliers. N = 42-63 samples. c, Nanocubes assembly using Langmuir trough with automated deposition. d, Nanocubes assembly using PTFE well with manual deposition by hand. e, Proposed mechanism of nanocubes filling. Light blue color indicates water subphase, orange color indicates nanopatterned PDMS substrate, dark blue arrows indicate water flux, and red arrows indicate attractive capillary forces.

As evident in Figure 2.20a, a direct relationship emerges between surface tension (and consequently nanocube density) and the likelihood of nanocubes filling the trenches. Specifically, a higher surface tension, leading to increased nanocube density,

improves the filling fraction. To offer context, for this specific pattern, ~28 nanoparticles (NPs)/μm^2 would be needed to perfectly fill the split-ring if deposition would take place inside the trenches only. This is a direct consequence of the split-ring area and periodicity. The optimal filling fraction is achieved at a density of approximately 227 NPs/μm^2, resulting in an average filling fraction of about 0.90. Interestingly, even at a reduced density of 52 NPs/μm^2 (less than a quarter of the optimum density), the average filling fraction remains notably high at around 0.66.

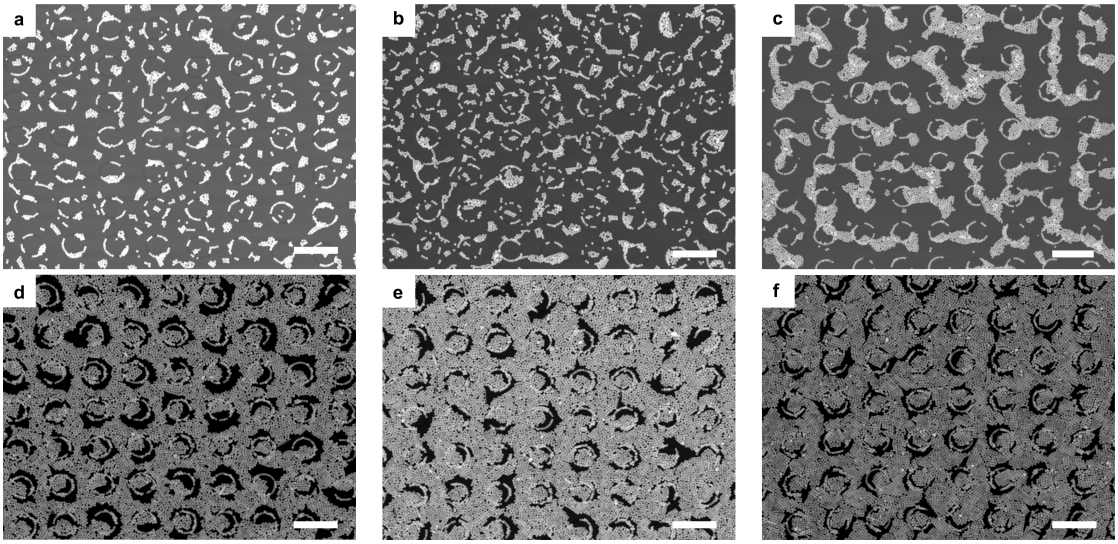

Figure 2.21.: Nanocube assembly at different surface tension (55 nm AgNCs). a, 0.9 mN/m. b, 1.8 mN/m. c, 3.5 mN/m. d, 8.0 mN/m. e, 16.7 mN/m. f, by hand. Scale bar is 1 µm in length.

This finding raises questions about the mechanism behind the concentration of nanoparticles in the trenches. Are the positions of nanoparticles floating on the air-water interface fixed upon contact with the PDMS substrate (Fig. 2.1b), or do they move to occupy the trenches? Our hypothesis posits that if the nanocubes were homogenously distributed at the air-water interface and were spatially immobilized upon deposition onto the patterned PDMS substrate, a density of 52 NPs/μm^2 would theoretically result in a significantly lower filling fraction of about 0.14 (substantially lower than our experimental findings by five-fold). Additional evidence from Figures 2.21 and 2.23 suggests that although a monolayer forms on the air-water interface, the trench regions are partially covered with a second layer of nanocubes after deposition. This observation refutes the idea that they are fixed upon contact, thus suggesting that nanocubes remain mobile during or after contact with the PDMS substrate.

To investigate it, we assembled low-density nanocubes on water and then deposited them onto two PDMS substrates, one UV/Ozone-treated to enhance interaction with nanocubes and the other left untreated. The detailed procedure is shown in Appendix B.1.9. Figure 2.22 shows that nanocubes tend to assemble individually on the treated (hydrophilic) substrate, whereas they form compact face-to-face alignment, particularly within trenches, on the untreated substrate. This further confirms the presence

of mobility upon transfer to the substrate, and lateral capillary forces, influenced by surface perturbations at the air-water interface, could be a contributing factor[145].

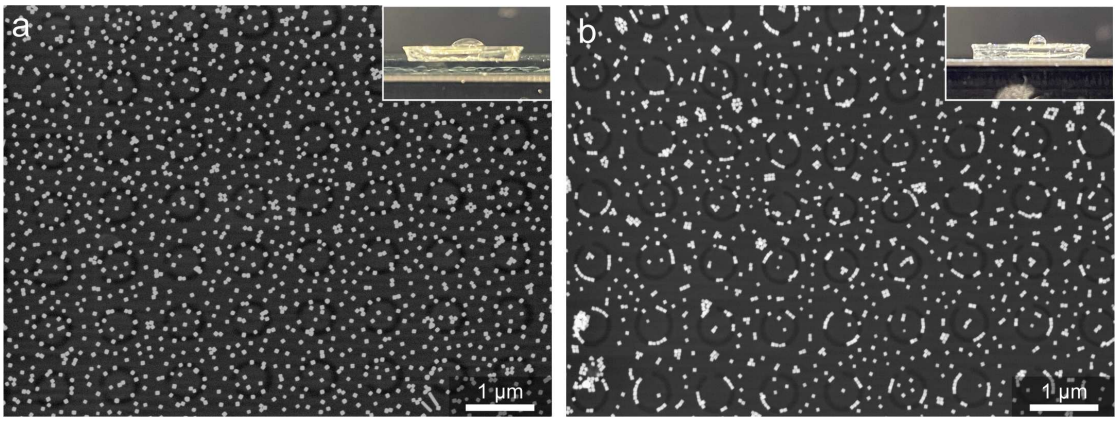

Figure 2.22.: Assembly of low-density nanocubes on a, UV/Ozone-treated PDMS substrates and b, untreated PDMS substrates. Insets are water contact angle test on the substrates.

Two hypotheses were considered. Our first hypothesis is that, before complete drying, the remaining water layer forms a meniscus around the nanoparticles and leads to attractive long-range immersion capillary forces. These forces might concentrate nearby nanoparticles into the trenches due to local pinning at the edges of topographic features during evaporation. Further bolstering this effect are Van der Waals interactions among nanocubes and between the inner surfaces of the trenches[146]. However, this mechanism is expected to take place on substrates with a macroscopic contact angle between 10 and 30°[146]. By contrast, our PDMS substrate exhibits a much larger contact angle of approximately 105°.

The second hypothesis involves long-range attractive capillary forces due to the formation of capillary multipoles. The capping molecule of nanoparticles used in this study is PVP, an amphiphilic compound. This degree of hydrophilicity causes nanoparticles to be partially immersed in the water phase[147]. Anisotropic nanoparticles with characteristics like angular or irregular shapes, surface roughness, or chemical inhomogeneity can cause undulations at the nanoparticle surface's contact line. These undulations, in turn, lead to perturbation in the surrounding liquid interface, and the overlap of these distortions creates an attractive force between nanoparticles[96, 145, 148]. When the nanopatterned PDMS substrate contacts the assembly, an instantaneous water flux fills the trenches with some nanoparticles acting as initial seeds that attract more nanoparticles *via* the long-range forces mentioned above. This mechanism of nanoparticle concentration in the trenches is illustrated in Figure 2.20e.

Utilizing the Langmuir trough, we also investigated the impact of the dipping angle on the filling fraction at a fixed NP density. Specifically, we found that tilting the substrate at angles of 0°, 20°, 45°, and 70° maintained an average filling fraction above 0.82, as shown in Figure 2.20b. These angles correspond to the ratios of projected

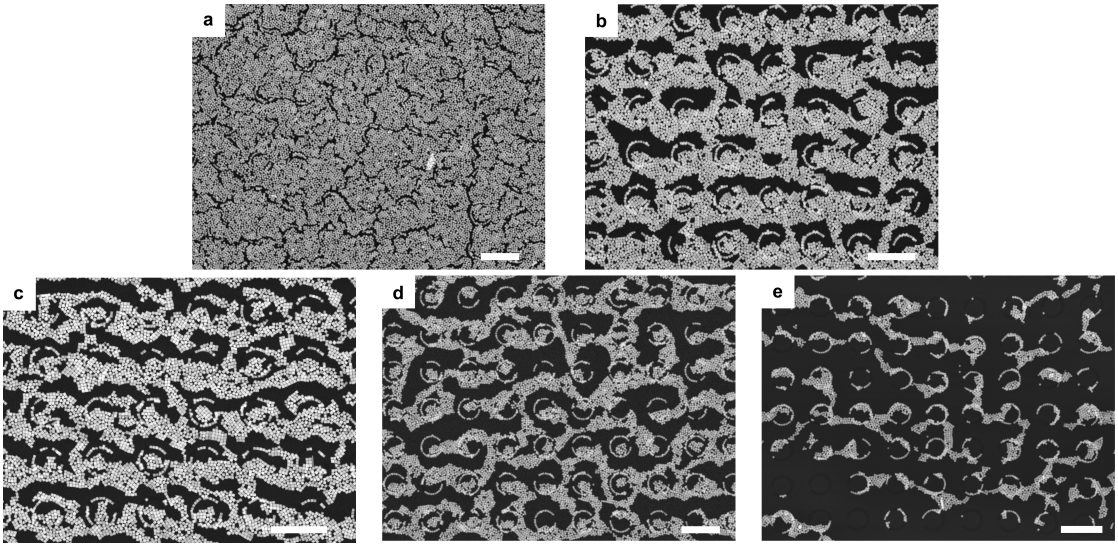

Figure 2.23.: Nanocube assembly at different dipping angles at 16.7 mN/m (55 nm AgNCs). a, 0°. b, 20°. c, 45°. d, 70°. e, 90°. Scale bar is 1 μm in length.

assembly areas of 1:0.94:0.71:0.34, respectively. By assuming a nanoparticle density of 245 NPs/μm^2 at 0°, we determined that the densities at 20°, 45°, and 70° correspond to roughly 230, 173, and 84 NPs/μm^2, respectively. This observation aligns well with the data presented in Figure 2.20a. However, the deposition at 90° appears to be less effective, likely because the projection of the PDMS substrate towards the assembly of the nanocube monolayer is theoretically zero at this angle. Additionally, the low surface energy of PDMS contributes to a decreased interaction with the assembly. There may still be some transfer into the trenches, possibly because of a degree of wetting. From these experiments, we found that having nanocube density above a certain threshold is a crucial requirement for successful nanocube filling into a nanopattern. Conversely, the slight tilting of the PDMS substrate during deposition seems to be of lesser importance.

Following the insights gained from our previous experiments, we achieved significant assembly efficiency with a simple homemade PTFE well, taking advantage of the fact that the assembly yield is almost independent on the dipping angle. As shown in Figure 2.20a, this method yielded filling fractions comparable to those obtained using the Langmuir trough, as long as sufficient nanocube density was maintained. This procedure took under than 20 minutes to complete, significantly faster than the Langmuir method, whose extended duration resulted from factors like dust removal in non-cleanroom conditions and equilibration time, especially when compared to samples prepared at 70º. Additionally, we found that with the same amount of nanocube solution we could prepare 3x to 4x more samples, as a result of the Langmuir trough design that impeded to efficiently transfer the entire monolayer. Overall, this was more efficient in terms of both time and material usage. These efficiencies, however, may vary based on the customized nanopattern area, surface area of the well, and Langmuir trough size.

2.2.6. Optical characterization

To assess their optical behavior, we performed transmission measurements on the nanocube meta-atom arrays shown in Figure 2.2. The corresponding spectra are presented in Figures 2.24 and 2.25c. It is important to note that the small peaks observed around 540 nm and 570 nm in the spectrum of the T-shaped meta-atoms are not physical features of the structures themselves, but rather artefacts arising from imperfect baseline correction during the spectral measurement.

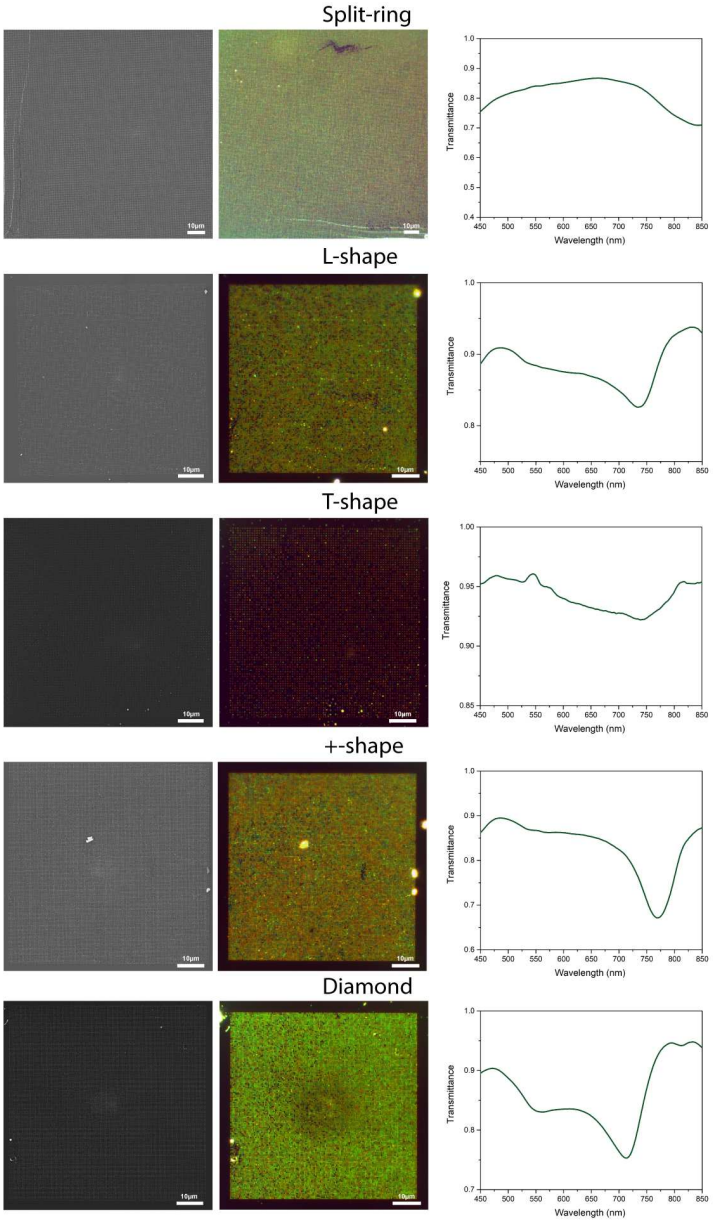

Figure 2.24.: SEM images, dark-field images, and transmission spectra of different meta-atoms arrays. The collection spot is ~26 μm and each spectrum correspond to an average of three different positions.

Among the different geometries, the gammadion-shaped meta-atoms exhibit a pronounced circular dichroism, as demonstrated in Figure 2.25d. This optical activity confirms the chiral response of the metasurface and highlights its potential for polarization-dependent applications.

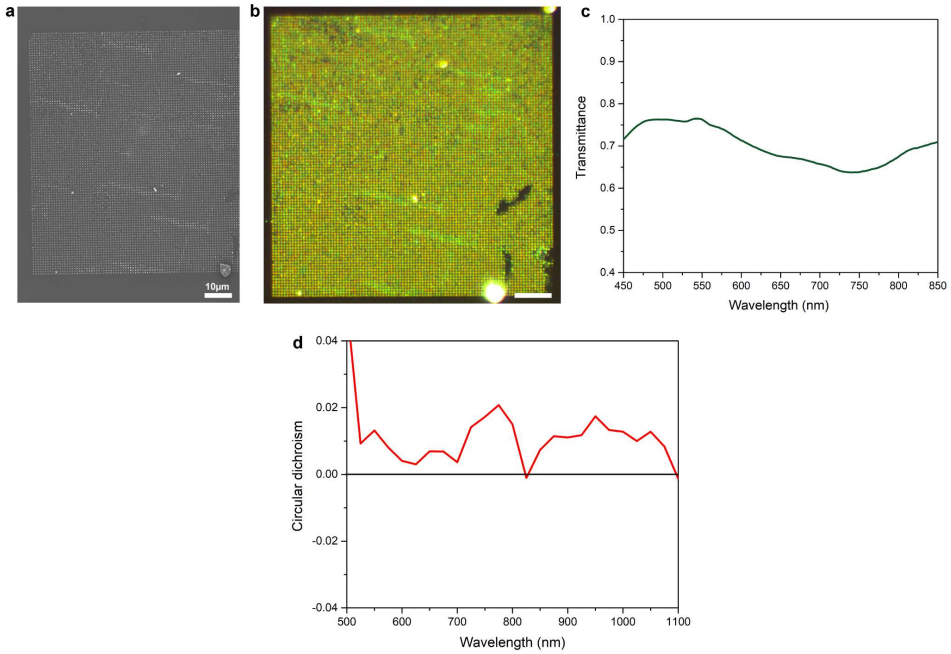

Figure 2.25.: Circular dichroism of the gammadion nanopattern shown in Figure 3g: a, SEM image. b, dark-field image. c, transmission spectrum. The size of the light beam exposed to the sample for the transmission measurement is ~26 μm in diameter. d, Circular dichroism of the array for reflected light.

2.2.7. Nanocubes assembly into Pancharatnam-Berry (PB) phase metasurface

This work, concerning the optical measurement setup, design, and simulation of the Pancharatnam-Berry metasurface, was carried out in collaboration with the group of Prof. Patrice Genevet, who led the modeling and simulation efforts.

2.2.7.1. PB working principle

Traditional optical components like lenses and waveplates modulate wavefront in the process of light propagation. However, they are bulky, hindering miniaturization and integration[149]. In contrast, metasurfaces consist of subwavelength arrangement of nanostructures, on a single flat surface, whose carefully designed properties allow controlling the light and achieving similar functionalities[150]. A specific example of

metasurfaces is the Pancharatnam-Berry (PB) metasurface, designed to manipulate the wavefront of circularly polarized (CP) light[151]. PB metasurfaces rely on the introduction of geometrical phase shifts induced by the interaction of CP light with an array of identical, but spatially rotated, meta-atoms. To achieve such behavior, the meta-atoms should exhibit anisotropic behavior, i.e., a difference of response between the two eigen-polarization axes.

Supposing light incident on an array of identically oriented birefringent meta-atoms, each designed to operate as nano-waveplates by introducing a phase shift of exactly π between both of its eigen-polarization axis, the transmitted light emerges with a spin-flip from left circular (LCP) to right circular polarization (RCP), and reciprocally from RCP to LCP. Upon spin-flip operation, the phase of the converted light beam experiences a geometric phase retardation equal to twice the rotation of the nanostructure[39, 41, 149]. If we consider instead an array of identically oriented but arbitrary birefringent meta-atom, i.e. for a nanostructure geometry leading arbitrary amplitude and phase modulation between both eigen-polarization axes, the situation is slightly more complex. The transmitted light emerges with converted polarization, resulting from the superposition of two waves with distinct circular polarization modulation: an ordinary wave transmitted with the phase and polarization of the incoming light; (ii) an extraordinary crossed CP wave generated with a given amplitude and a transmission phase equal to twice the rotation of the nanostructure.

If we now consider interfaces decorated with a distribution of building blocks with linearly varying rotation, the transmitted wavefront on the crossed polarization is linearly modulated in phase. Note that because of the super-periodicity induced by the repetition of the rotation (for every π full rotation of the nanorod), both transmitted and converted beams are diffracted. In other words, the metasurface acts as a normal grating for the transmitted beam and acts as a blazed grating for the converted beam, resulting in an asymmetric deflection pattern. Such PB metasurfaces could be realized using array of metallic nanorod supporting anisotropic plasmonic resonances[152, 153].

2.2.7.2. Experimental results and simulations

Herein, we introduce a PB metasurface deflector constructed *via* a bottom-up approach, utilizing an array of silver nanocubes, each approximately 40 nm in size, assembled on a pattern of six nanorods trenches in a PDMS substrate. These nanorod trenches house 3-4 nanocubes each, organized with a linearly varying orientation along the x-axis and rotated at incremental angles of $\pi/6$, as depicted in Figure 2.26g, effectively yielding to a 2π phase control. The nanocubes are separated by an estimated 1-2 nm gap due to their PVP capping. We set the center-to-center distance between the nanorods at roughly 210 nm in both x and y directions. Figure 2.26b shows an electron microscope image of the metasurface, illustrating the fidelity of nanocube assembly. The photograph of the PB metasurface corresponding to the green rectangular area in the inset of Figure 2.26b, shows its macroscopic scale, limited only by the size of the nanopatterned area of the Si master employed. Figure

2.27 presents low-magnification SEM images of nanocubes assembled on the PB metasurface, taken from a different sample.

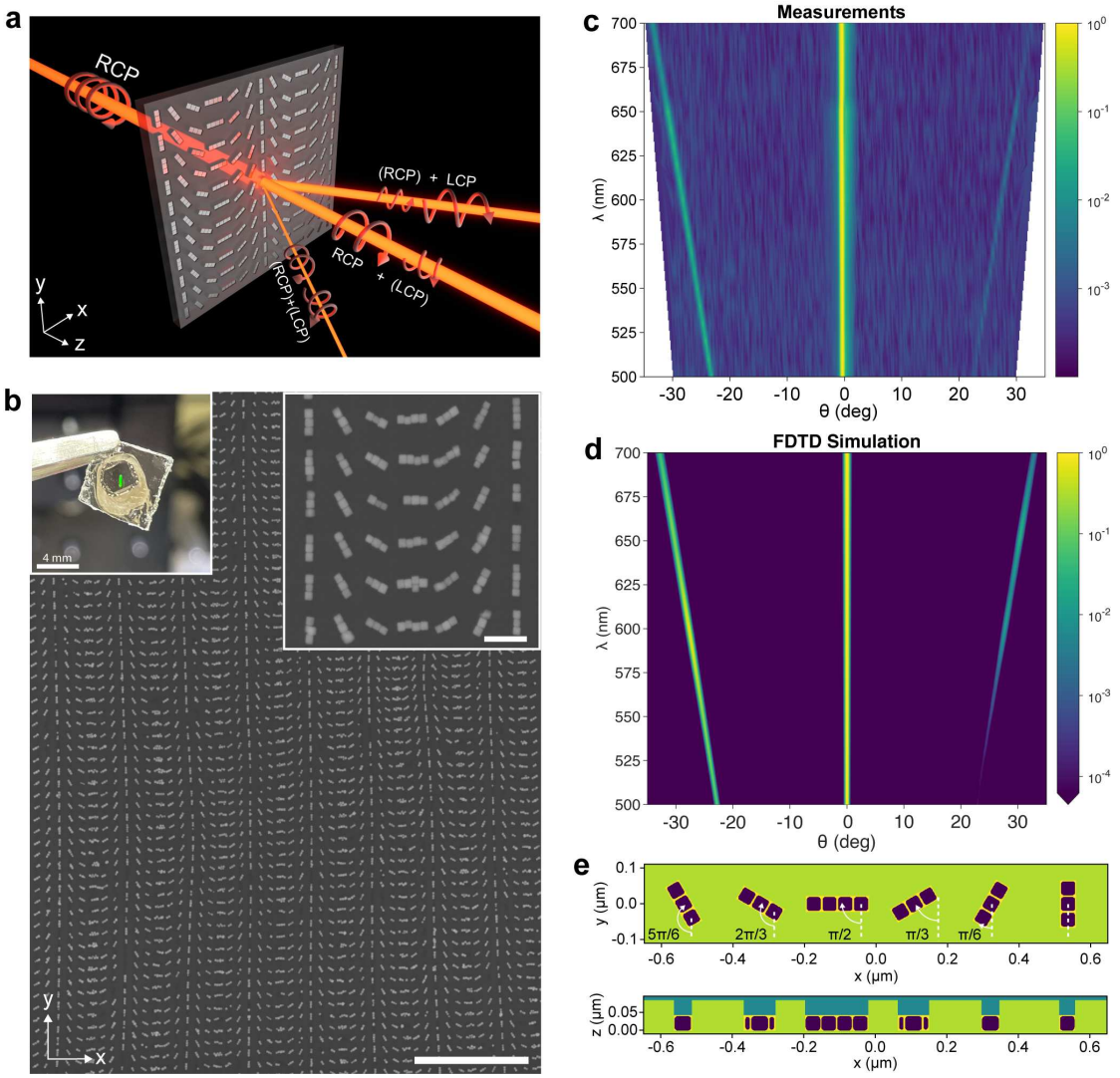

Figure 2.26.: Bottom-up Pancharatnam-Berry metasurface from nanocubes. a, Illustration of wavelength-dependent light steering after RCP light passes through the metasurface. b, Photographic and SEM images of nanocubes assembly on nanopatterned PDMS after the excess nanocubes removal. Scale bars are 200 nm in the inset and 2 μm in the main image. c, Experimental results of steering angle on the wavelength of incident RCP light. d, FDTD simulation results of steering angle on the wavelength of incident RCP light. The intensities for c and d are normalized relative to the peak intensity at each wavelength and are presented on a logarithmic scale (base 10). e, Geometry of simulated meta-atoms in a unit cell.

Next, we performed optical characterization to assess the metasurface performance in terms of beam steering. Our tests ranged the incident light's wavelength from 500 to 700 nm and examined its deflection in transmission on both right circularly polarized

(RCP) and left circularly polarized (LCP) light. We emphasize that this particular design is optimized to efficiently convert polarization at the PB half waveplate design, and this is numerically expected to occur around 600 nm (Fig. 2.26d and 2.29), in agreement with experimentally observed conversion efficiency data in Figure 2.26c. Note that we are characterizing the metasurface over a relatively broadband spectral region, and the nanostructure spectral response have to be considered to correctly interpret the experimental results.

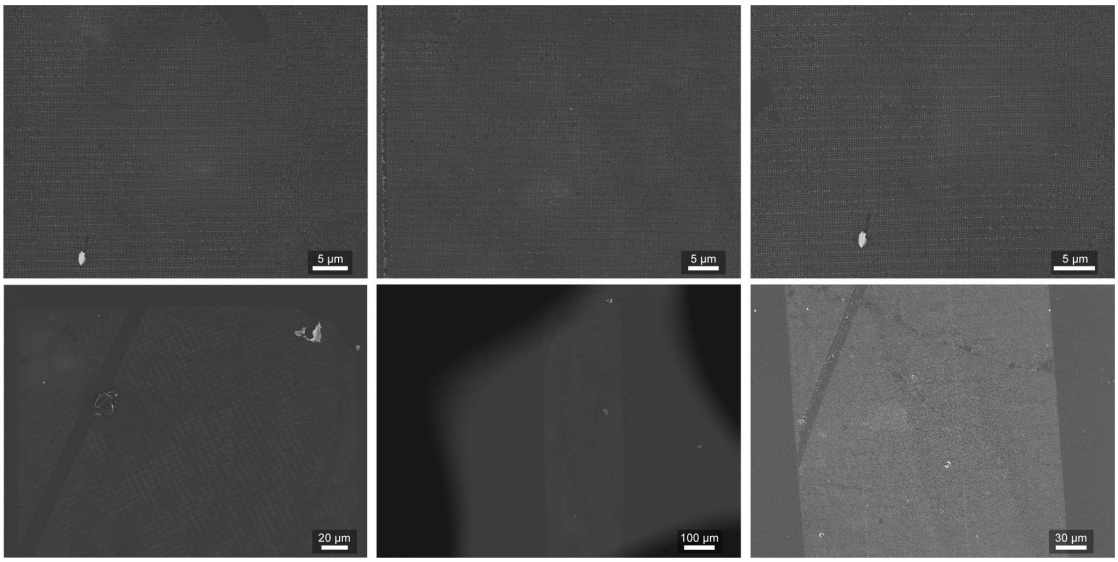

Figure 2.27.: Assembly of ~40 nm silver nanocubes on a PB metasurface patterned PDMS surface.

As Figure 2.26c illustrates, the far-field intensity presents an asymmetrical behavior between the left and right deflected beams demonstrating the functionality of the PB metasurface. A more important portion of the incident RCP light was deflected to the left at angles between -23° at 500 nm and -34° at 700 nm. This angle shift as a function of the wavelength is well-known[154] and corresponds to the blazed angle. On the other side, the right fainted deflected beam corresponds to the superposition of the $+1^{st}$ order of the RCP light and the $+2^{nd}$ order LCP light whose amplitudes depend on the quality of the blazed grating, i.e. linear phase gradient, and the polarization conversion efficiency. Near-field effects between the PB antennas affect the polarization conversion efficiency and may alter the phase gradient, reducing the blazed grating efficiency. Conversely, LCP light behaved in the opposite manner, as shown in Figure 2.28.

Besides, we observed that larger wavelengths of the incident polarized light resulted in greater steering angles as it is expected. Measurements for higher deflection angles at smaller wavelengths were not undertaken experimentally, resulting in their absence from the dataset in Figure 2.26c. These experimental results aligned well with FDTD simulations, shown in Figure 2.26d, where the period between each nanostructure forming the PB metasurface is given by the master template at 210 nm (Figure 2.26e).

We noticed slight difference between simulation and experimental result particularly near 700 nm of incident light which probably due to fabrication defect[155]. It is worth noticing that measurements were performed with a collimated beam with a spot size in the order of 100 microns, therefore probing over 121000 meta-atoms; despite the unavoidable presence of defects over such a large scale, the experimental data are still close to simulations. This indicates that the assembly is reasonably homogeneous at a relatively large scale. Finally, it is worth emphasizing that after nanocube epitaxy the optical response does not change dramatically, as previously observed for Au nanocubes[1]. This can be appreciated in Figure 2.31 that shows the deflection properties of a PB metasurface after welding.

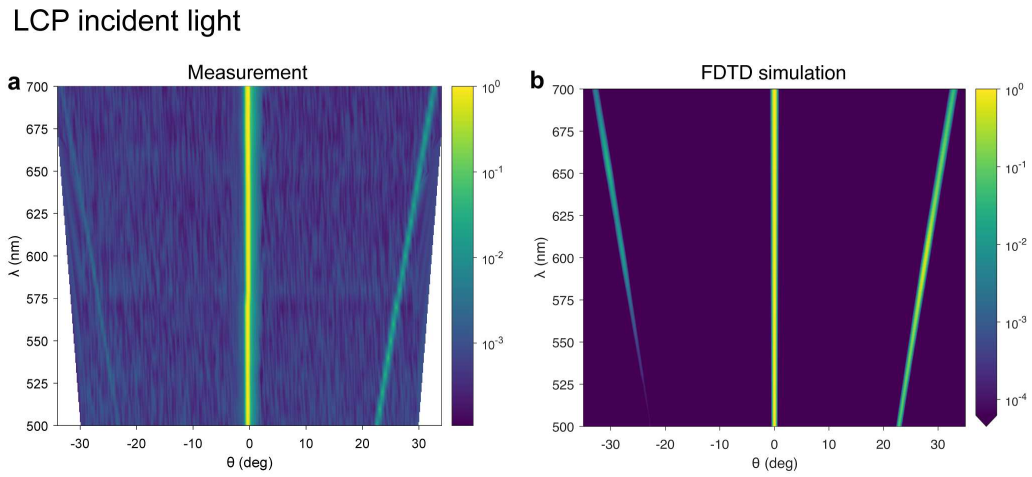

Figure 2.28.: FDTD simulation for incident LCP: a, Experimental results of steering angle on the wavelength of incident LCP light. b, FDTD simulation results of steering angle on the wavelength of incident RCP light. Intensities of a and b have been normalized with respect to the highest intensity for each wavelength and plotted in log10 scale.

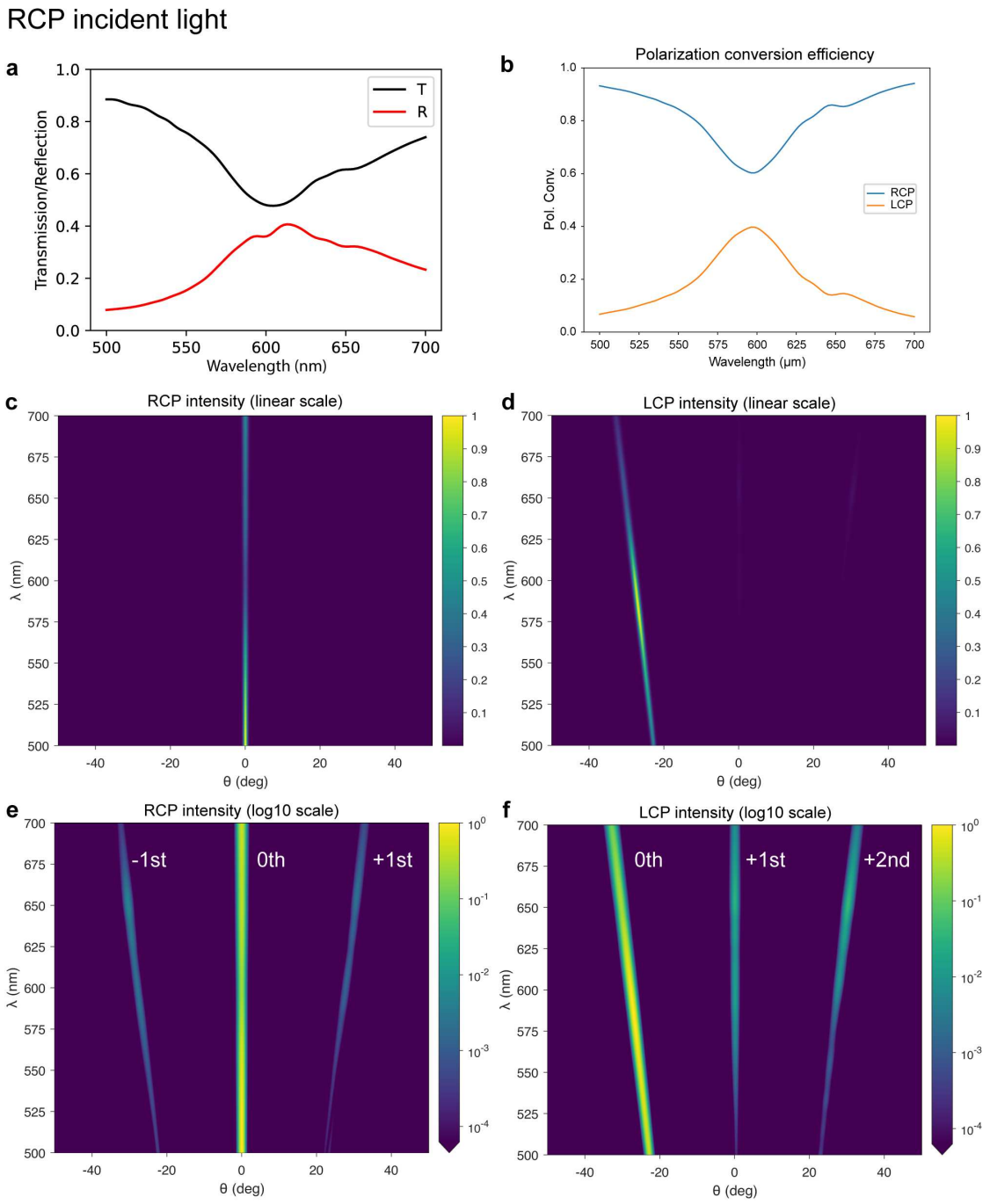

Figure 2.29.: FDTD simulation for incident RCP: a, Total (RCP + LCP) transmission and reflection efficiencies. b, Polarization conversion efficiency. c, Intensity in the farfield of RCP of transmitted field in linear scale. d, Intensity in the farfield of LCP of transmitted field in linear scale. e, Intensity in the farfield of RCP of transmitted field in log10 scale. f, Intensity in the farfield of LCP of transmitted field in log10 scale.

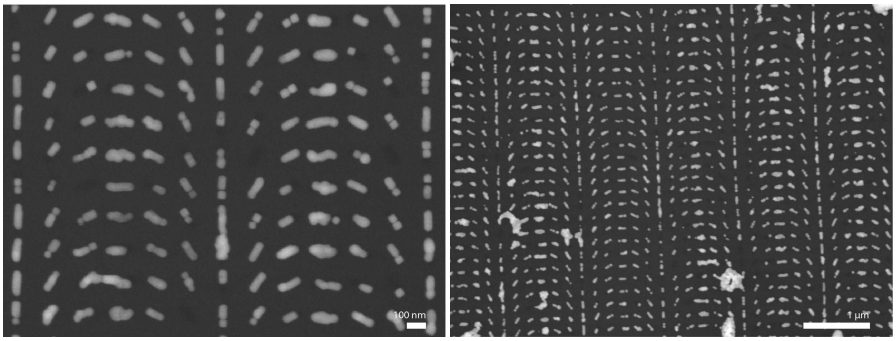

Figure 2.30.: Example of assembly of nanocubes as PB metasurface post-welding.

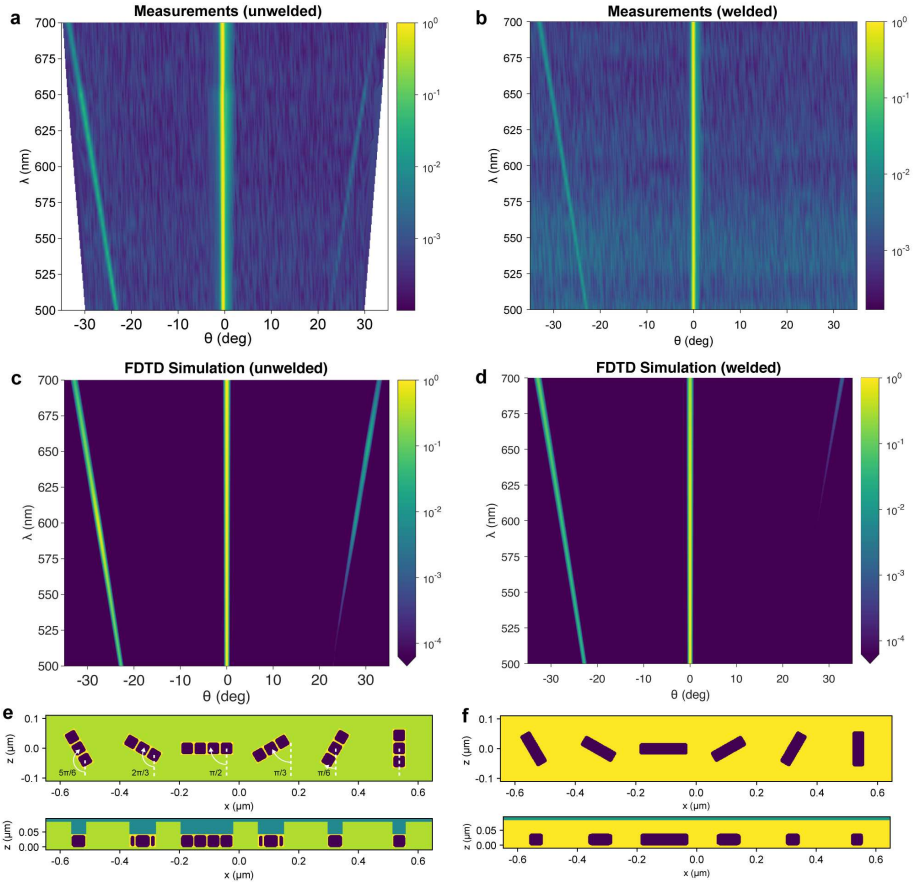

Figure 2.31.: Comparation before and after welding. Experimental results of steering angle on the wavelength of incident RCP light on: a, unwelded and b, welded PB-metasurface. FDTD simulation results of steering angle on the wavelength of incident RCP light on: c, unwelded and d, welded PB-metasurface. The intensities for a-d are normalized relative to the peak intensity at each wavelength and are presented on a logarithmic scale (base 10). e-f, Geometry of simulated meta-atoms in a unit cell.

2.3. Conclusion

In this study, we introduce a strategy for nanoparticle assembly using an air-water interface to engineer intricate and densely-packed nanopatterns. Unlike conventional capillary assembly, which relies on dynamic trapping of nanoparticles in trenches, our method leverages a static process, in which the transfer of nanocubes into the whole patterned area happens all at once occurring in much shorter time range. This circumvents the complications often associated with dynamic systems, such as fluctuations in temperature, humidity, meniscus pinning, trap defects, and density, factors that can otherwise obstruct effective assembly. We have shown an understanding of substrate tilting and mainly nanocube density during deposition is key to achieving optimal assembly conditions. Notably, our approach transfers nanocubes into the trap as a dense monolayer, which remains largely uninfluenced by variables that commonly affect capillary assembly leading to contact line instability. It is noteworthy to emphasize that the assembly and removal procedures are entirely independent of the nanopattern density and meta-atoms geometry.

It is important to acknowledge that while our method offers a high degree of flexibility, regardless of pattern geometry and density, further optimization is needed to achieve flawless assembly at a larger scale. Improving the monodispersity of the nanocubes and refining the fidelity of geometric patterns on the Si-master, could lead to improvements. Furthermore, the nanocube removal yield varies from sample to sample and can be improved with more sophisticated equipment enabling to finely control the contact conformality and the approach-retraction speed, that is known to greatly influence the transfer of nanocubes, specifically due to changes in adhesion at the PDMS/nanocubes interface[156, 157]. Or by advanced selective functionalization approaches to introduce an adhesion asymmetry between nanocube outside and inside the trenches. However, this goes beyond the purview of this study. In summary, this study establishes a foundational framework for employing a bottom-up approach to fabricate metasurfaces, nanostructured metal transparent electrodes, and complex-shaped nanoparticles; challenges that conventional chemical synthesis still struggle to achieve. We contend that the methodologies and understandings shared here significantly enhance and broaden the existing methodologies for nanoparticle assembly, widening the opportunities for the integration of inexpensive bottom-up nanostructures in optoelectronic and nanoelectronic devices.

3. Silver nanocube epitaxy *via* nanogap-induced electrostatics[1]

Silver nanostructures are highly valued in nanophotonic devices due to their appealing plasmonic properties and affordability relative to gold. Yet, fabricating high-quality, monocrystalline silver nanostructures, with full control over the shape, is challenging. We introduce a mild, liquid-phase method for the epitaxial welding of adjacent monocrystalline silver nanocubes in reductant-free conditions to prevent the formation of detrimental nuclei on the surface that could degrade the nanostructures' optical qualities. We thoroughly investigate the mechanism and find that the nanocubes themselves can act as reducing agents, promoting growth preferentially into the gap as a result of electrostatic interactions. By controlling experimental parameters such as temperature, pH, and the introduction of capping agents, we achieve a balance between nanocube epitaxy and shape retention. Finally, by applying this procedure to nanoparticle assembled in predefined meta-atoms, we demonstrate the feasibility of creating intricate silver nanostructures, that are monocrystalline as verified by transmission electron microscopy. This advancement paves the way for bottom-up fabrication of optical metasurfaces that can be swiftly integrated in devices.

[1]Major part of this chapter has been published in: M. L. Fajri , A. Capitaine, L. Santinacci, B. Sciacca, "Silver Nanocube Epitaxy via Nanogap-induced Electrostatics" *Small Methods* **2025**, 2401304

Summary

3.1. Introduction 102
3.2. Results and discussion 103
3.2.1. What drives silver nanocube welding? 105
3.2.2. Optimizing conditions for silver nanocubes welding 106
3.2.3. Electrochemical analysis of spotaneous silver dissolution 108
3.2.4. Epitaxial welding towards complex nanostructures 111
3.2.5. TEM characterization of welded nanostructures 112
3.2.6. Optical characterization 114
3.3. Conclusion 115

3.1. Introduction

The interest of silver nanostructures for nanophotonic devices stems from their appealing plasmonic properties and cost-effectiveness compared to gold. However, achieving low-cost fabrication of the highest-quality monocrystalline silver nanostructures with arbitrary shapes remains a significant challenge. Meanwhile, the importance of single-crystalline grade nanostructures in such devices has been reported by many[8, 9, 45, 158–160]. One approach for fabricating monocrystalline structures of arbitrary shapes involves substrate-based epitaxial growth, which produces single crystalline thin films that are then nanostructured using lithography processes such as electron beam lithography (EBL). Yet, this method's demands for high temperatures and/or high vacuum, and lattice-matched substrates[160], combined with the high costs and time requirements of EBL, that also introduces defects due to etching, further complicates fabrication. This challenge, therefore, spurred research into directed assembly of nanoparticles that allows their placement in desired locations on a substrate with high fidelity[65, 67, 133]. However, this method still results in the assembly of discrete nanoparticles separated by capping agents and gaps that prevent direct electrical contact and extended monocrystalline complex structures, thereby restricting the full exploitation of the shape-dependent plasmonic properties[65, 81, 86, 161].

While the monocrystalline quality of interconnections formed through nanowelding has been previously investigated in systems such as quantum dots[162], metallic nanorods[163], and 2D semiconducting nanoplatelets[164], the interplay between nanowelding quality and the flexibility to design arbitrary geometrical arrangements in nanoparticle assemblies was not largely addressed. Several studies have presented various strategies for connecting assembled metal nanoparticles, including nanorods assembled in meshes sintered through plasma treatment[165–168], nanospheres assembled in grids through photochemical welding[85], clusters of nanospheres assembled in dot arrays sintered through thermal annealing[169, 170] and in rings through chemical welding[110, 171]. These approaches focus primarily on the interconnection process itself, with limited attention to other critical aspects such as the crystalline quality of the connections or the retention of precise shapes in nanostructures with sub-100 nm features.

One approach to address this challenge involved transforming substrate-supported silver nanocubes into monocrystalline nanorods using a solution-based chemical synthesis[11]. Employing a Tollens' reagent based on glucose as reducing agent for a diamminesilver(I) complex, this process promoted nanocubes overgrowth and their epitaxial connection. However, this also led to unwanted homonucleation in solution and heteronucleation on the substrate, which can impact the final nanostructures' overall quality. The development of chemical procedures that avoid the use of exogenous reducing agents appears to be the most effective strategy for suppressing entirely unwanted nucleation, but encounters challenges in solution-based processes, where

metal sources are typically in ionic forms. Capitaine and Sciacca recently reported an effective approach to weld gold nanocubes, relying on the migration of gold atoms from corners into gaps through dissolution and redeposition via a disproportionation reaction, which entirely suppresses unwanted nucleation[1]. Unfortunately, this reaction is unique to gold and it is not readily transferable to other metals such as silver.

Inspired by this concept of welding via the rearrangement of surface atoms, we investigate a new synthetic framework to achieve epitaxy between silver nanocubes without using an exogenous reducing agent, thereby overcoming the nucleation issues associated with previously reported overgrowth strategy. We show that this approach is compatible with various supports including nanopatterned polydimethylsiloxane (PDMS), hence enabling the integration of intricate monocrystalline silver nanostructures onto new substrates via contact printing. This methodology was first explored by Dr. Anna Capitaine, and all results originating from her work are cited accordingly and further detailed in her doctoral thesis[2].

3.2. Results and discussion

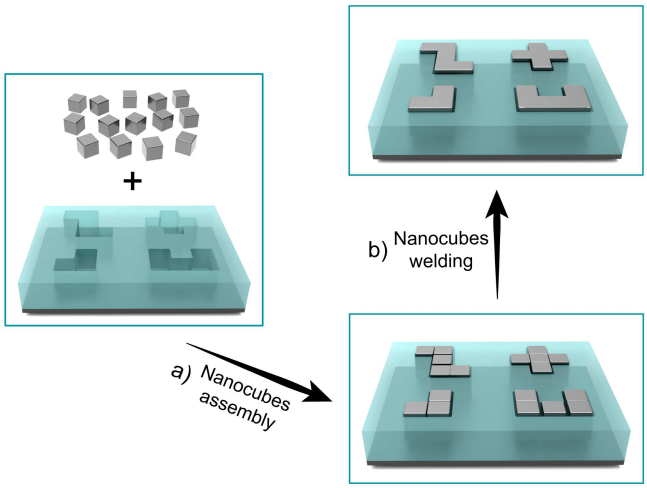

Figure 3.1.: Diagram of the process: a) nanocubes assembly on to nanopatterned PDMS substrate and b) solution-based nanocubes epitaxial welding.

Figure 3.1 provides a general overview of the strategy to obtain monocrystalline meta-atoms with a truly arbitrary geometries. First, silver nanocubes are assembled into nanopatterned trenches of various shapes realized in a PDMS substrate using reported techniques, either capillary-assisted assembly[1] or air-water interface assembly[172]. The former technique involves dragging a colloidal solution over a nanostructured PDMS mold, trapping nanocubes within the trenches at the meniscus front line, driven by convective flow from solvent evaporation[1]. Alternatively as explained in Chapter 2, the latter technique transfers a dense monolayer of nanocubes

from the air-water interface onto the nanostructured PDMS template, where a fraction of nanocubes is trapped in the trenches while the excess is deposited outside. Removing the excess leaves behind only the nanocubes assembled within the patterned trenches[172]. These techniques position the cubes face-to-face within the trenches, matching the trench geometry (Figure 3.1a) and imposing identical crystallographic orientation of the nanocube building blocks thanks to their 4-fold rotational invariance. Subsequently, epitaxial welding in solution results in extended continuous monocrystalline polyomino-like nanostructures (Figure 3.1b), which can then be transfer-printed onto other substrates, if required.

To design and investigate suitable conditions for the reductant-free epitaxial welding of silver nanocubes, we initially conducted experiments using randomly assembled nanoparticle aggregates, as also described in the doctoral thesis of Dr. Anna Capitaine[2]. These aggregates were prepared by drop-casting monodisperse silver nanocubes (ranging from 30 to 70 nm in size) onto silicon substrates. Initially, the face-to-face distance between adjacent nanocubes, determined primarily by ligand thickness, was typically on the order of a few nanometers[173]. Subsequently, we removed the polyvinylpyrrolidone (PVP) ligands from the nanocube surfaces following a previously established protocol[142] (detailed in the Appendix C.1.3). Ligand removal led to nanocubes moving closer due to enhanced van der Waals attractions and capillary forces during drying, reducing the average gap size from approximately 1.8 nm to about 0.7 nm (see Figure 3.2). The gap measurements were performed using the InteredgeDistance macro plugin in ImageJ.

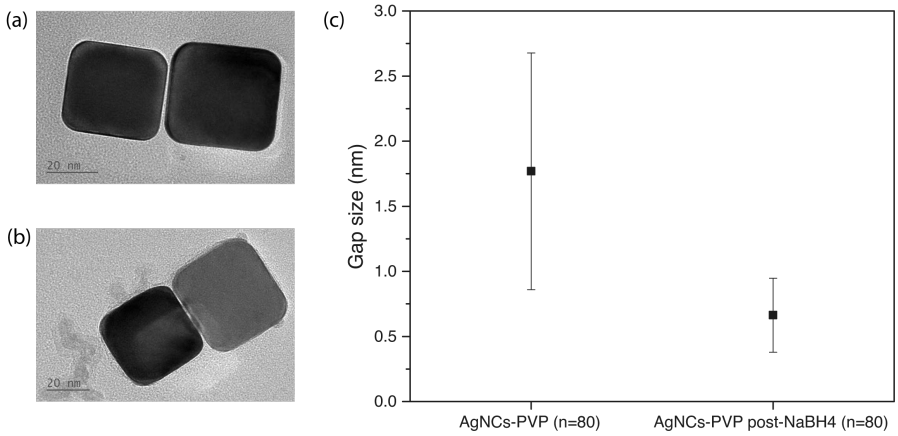

Figure 3.2.: TEM images of silver nanocube dimers: (a) Before and (b) after $NaBH_4$ treatment. Post-treatment, uncapped silver nanocubes exhibit significant instability under the TEM electron beam, leading to structural deformation, including gap welding, within seconds of exposure, as shown in (b). (c) Comparison of gap size before and after $NaBH_4$ treatment.

Although ligand removal alone did not trigger immediate welding, silver nanocubes, now ligand-free and significantly less chemically and thermally stable compared to

their gold counterparts, gradually merged into interconnected structures upon immersion in deionized water at room temperature over three days (see Figure C.1). This spontaneous merging indicates the presence of a driving force towards the formation of continuous structures. While the free energy of the system is reduced in this process (the disappearance of the two surfaces corresponds to a 17% reduction of the initial surface area considering a two-particle system), the activation barrier is sufficiently high to prevent welding in a time scale of a few hours. Regardless of the kinetics, for this to happen, it is necessary that Ag atoms are displaced into the gap. Despite surface diffusion of metal atoms can be fast, it is not sufficient to trigger the welding process as it would require anisotropic diffusion of electrically-neutral species.

3.2.1. What drives silver nanocube welding?

Previous studies have shown that silver atoms in low-coordinated sites[1, 174–176], such as cube corners, oxidize at a higher rate to Ag^+ ions in solution under oxidative dissolution conditions due to higher surface energy. This can leave behind excess electrons in the nanocubes inducing the formation of a dynamic ionic layer at their surface and in the gap as a result of Coulomb interactions. We hypothesize that in the gap, the overlap of diffuse layers and the modified electrostatic interactions (compared to an isolated nanocube) result in the accumulation of Ag^+ ions. This higher concentration in the gap makes it a privileged location for the reduction of Ag^+ ions to Ag adatoms, with electrons sourced directly from the excess present in the nanocubes themselves. This process is thermodynamically favoured as it leads to a reduction in the free energy of the system due to the decrease in surface-to-volume ratio after welding is achieved (loss of two surfaces). This heuristic analysis is corroborated qualitatively by multiphysics numerical simulations coupling electrostatics with the transport of charged species on a simplified nanocube-dimer model. These simulations were performed by Dr. Beniamino Sciacca.

Figure 3.3 shows the spatial distribution of the cation concentration, normalized by its maximum value, C/C_{max}, for various gap sizes. The net charge corresponds to the excess electrons in each nanocube, and correspondingly to the excess cations in solution in addition to the self-dissociation of water. Two different scenarios of net charge present on the nanocubes are considered, corresponding to 1q (left panel) or 3q (right panel), where q is the elementary charge. These scenarios are established to unveil the impact of the gap in limiting experimental conditions corresponding to one or a few excess electrons only, which can be a realistic condition especially in the early stages of the oxidation process. The resulting electrostatic field attracts opposite mobile charges such as cations in solution. Figure 3.3 shows the steady-state configuration, at which point the excess charge in the nanocubes is balanced by ions present in the simulation domain.

These results confirm, qualitatively, the accumulation of positive ions in the gap as a result of the concerted electrostatic action of the charged nanocubes, supporting our hypothesis. Finally, it is worth noticing that this concentration effect in the gap is

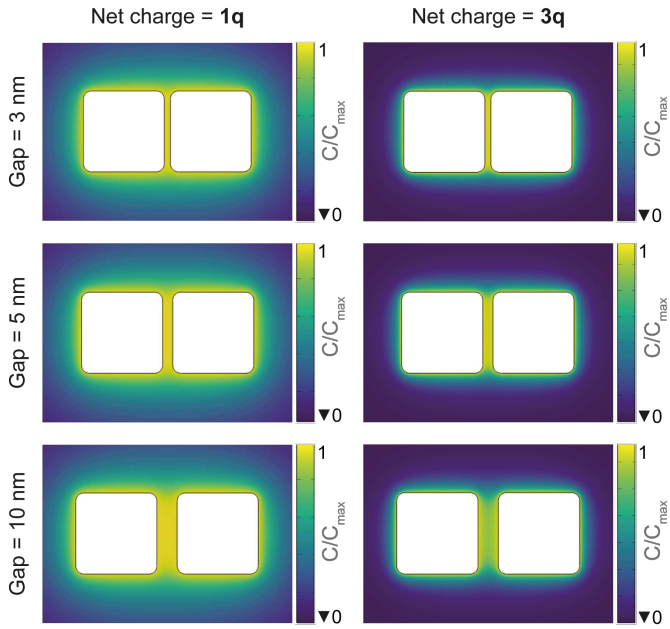

Figure 3.3.: Multiphysics simulations of a 40 nm silver nanocube dimer model system for various gap distances and net charges (q corresponds to the elementary charge). The cation concentration is given by the respective net charge, in addition to the background ion concentration of 10^{-7}M corresponding to the self-dissociation of water at pH = 7, 25°C. Ions travel throughout the simulation domain as a result of the electrostatic field until equilibrium. Note that the simulations are solved for continuous variables and as such do not account for the discreetness of electrons and ions.

enhanced with smaller gaps and larger excess charge. The dependence on the charge amount is related to the Boltzmann distribution of the ion concentration profile near an electrically charged surface, in which there is an exponential dependence with the surface potential (Poisson-Boltzmann equation). Although the purpose of this comparison is merely qualitative, we believe it sheds light on the mechanism.

3.2.2. Optimizing conditions for silver nanocubes welding

Using this spontaneous transformation as a starting point, we aimed to improve the welding kinetics and the shape retention on PDMS-supported nanocubes. We hypothesized that, in addition to temperature, the concentration of Ag^+ ions is key for a faster kinetics. We used diluted HNO_3, a known silver etchant[177, 178], to oxidize Ag atoms in low-coordinated sites, thereby increasing the availability of Ag^+ ions in solution. This significantly accelerated the transformation compared to water, as illustrated in Figure 3.4a and 3.4b. Additionally, conducting the reaction in water at elevated temperatures facilitated the merging of some face-to-face nanocubes into continuous structures more rapidly (shown in Figure 3.4c), although the impact of

temperature alone was rather limited.

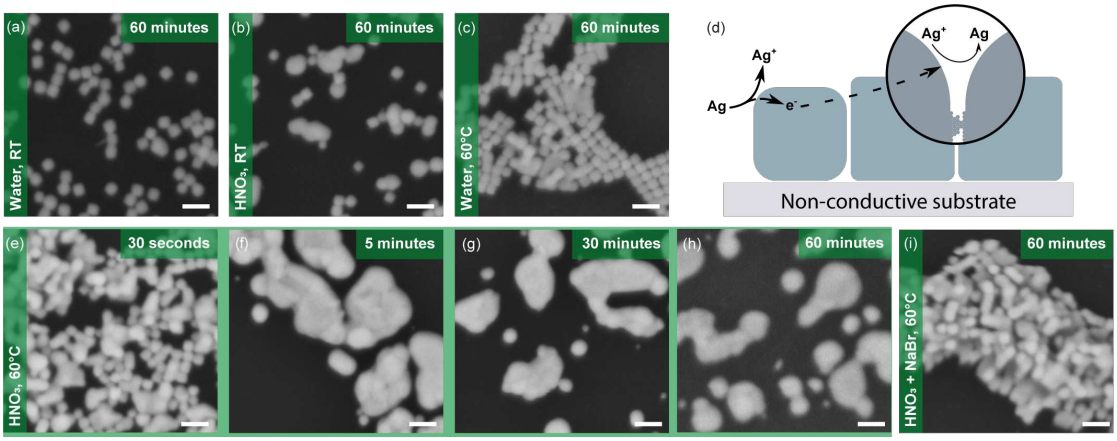

Figure 3.4.: Upon ligand removal, 40 nm silver nanocubes on PDMS were immersed for one hour in a) room temperature (RT) water, b) RT diluted nitric acid (pH = 2), and c) water at 60°C. d) A diagram of the electrochemical Ostwald ripening on insulating substrates, depicting the oxidation of Ag atoms in low coordinated sites to Ag^+ and reduction in a different site or in a different adjacent nanocube after electron tunneling. For 40 nm silver nanocubes, immersion at 60°C in diluted nitric acid (pH = 2) varied across e) 30 seconds, f) 5 minutes, g) 30 minutes, and h) 60 minutes, with i) showing the effect after 60 minutes with 50 μM NaBr added. The images selected are representative of whole surface. Scale bars measure 100 nm(all images are reproduced from ref. [2]).

Combining higher temperature with HNO_3 further increased reactivity, resulting in excessive nanocube etching and the emergence of three-dimensional structures within an hour (Figure 3.4e-h). Notable differences in samples immersed in the welding solution for 30 seconds, 5 minutes, and 30 minutes demonstrate that the reaction is not self-limiting and tends towards nanocube rounding (Figure 3.4f) and dissolution (Figure 3.4g-h), as it is evidenced by the presence of nanoparticles definitely smaller than the original nanocubes. Gap size certainly plays an important role in the welding reaction, but quantitative investigations are challenging due to the approaching of nanocubes to one another after ligand removal as a result of van der Waals interactions and drying capillary forces (Figure 3.2). It is important to emphasize that the reaction takes place in the absence of a silver salt, implying that all silver atoms filling sub-nanometer gaps must come from the nanocubes themselves, as mentioned earlier. This contrasts with the welding of gold nanocubes, which requires the presence of a gold precursor[1], and highlights a striking difference in reactivity. This is supported by the comparison of the work functions and the redox potentials of the two metals (indicated in the Appendix C.2.1 and C.2.2[2]). Such metrics clearly indicate that electron extraction and therefore metal dissolution is significantly easier on Ag than Au. As shown in the Pourbaix diagram (Appendix C.2), water, and even more so HNO_3,

can induce Ag oxidation to Ag^+. The diagram also shows the vast stability domain of the cation in aqueous solutions.

To improve shape retention, we added micromolar concentrations of NaBr to the welding solution, as bromide ions can selectively adsorb on (100) facets, reducing their surface energy and growth rate [1, 179, 180]. After systematic parameter variation, we found (on flat PDMS) an optimal balance between rapid kinetics and shape preservation by conducting the reaction at 60°C, pH = 2 with 50 μM NaBr, as shown in Figure 3.4i.

Welding experiments on various substrates, including silicon, revealed that while the impact of different parameters was similar, the optimal conditions varied slightly (see Appendix C.3). This is further evidenced in Appendix C.4, which demonstrates that silver nanocubes, when exposed to the same welding solution on diverse substrates like untreated silicon, UV/ozone-treated silicon, glass, and Si_3N_4, showed varying degrees of welding[2]. Notably, nanocubes on untreated silicon and Si_3N_4 underwent more extensive welding compared to those on glass, where oxidative etching was less pronounced, and on ozone-treated silicon, where silver deposition in the gaps appeared to be inhibited. This variability likely stemmed from the substrates' unique surface chemistries, which can affect ion diffusion through electrostatic interactions or participate in the reaction through surface oxidation[2]. This is particularly relevant for conductive substrates like silicon, in addition to the role of electron conduction.

3.2.3. Electrochemical analysis of spotaneous silver dissolution

To investigate the silver dissolution at the nanocube surface, we performed electrochemical experiments on bare or silver-coated glassy carbon (GC or GC-Ag, respectively) immersed in Ag-free or Ag-containing solutions (see Appendix C.1.4 for more details). Figure 3.5a shows cyclic voltammograms (CVs) performed on GC and GC-Ag in diluted HNO_3. As expected, when GC is exposed to HNO_3, it exhibits no reactivity. As a result, only a weak current density is measured. Conversely, electrochemical activity is observed on GC-Ag, displaying anodic and cathodic peaks centered at -0.7 and -0.56 V corresponding to the dissolution and deposition of silver, respectively.

In the case of GC-Ag in HNO_3 (Figure 3.5a), the curve shows that Ag^+ ions are present in the solution as soon as the electrode is immersed. The cathodic peak observed at -0.7 V indicates the reduction of Ag^+ to Ag. However, during the cyclic voltammetry, the potential is firstly scanned negatively from open circuit potential ($ocp \approx -0.45$ V), then towards positive voltages and, finally, back to the starting value. The observation of the cathodic peak at -0.7 V demonstrates that Ag^+ is present although no anodic polarization has been applied to strip the silver film covering the GC. It is the spontaneous silver dissolution that induces the presence of cations in the solution. A similar process occurs on nanocubes. The dissolved Ag^+ can then be redeposited at their surface preferentially in the gaps where Ag^+ concentration is higher.

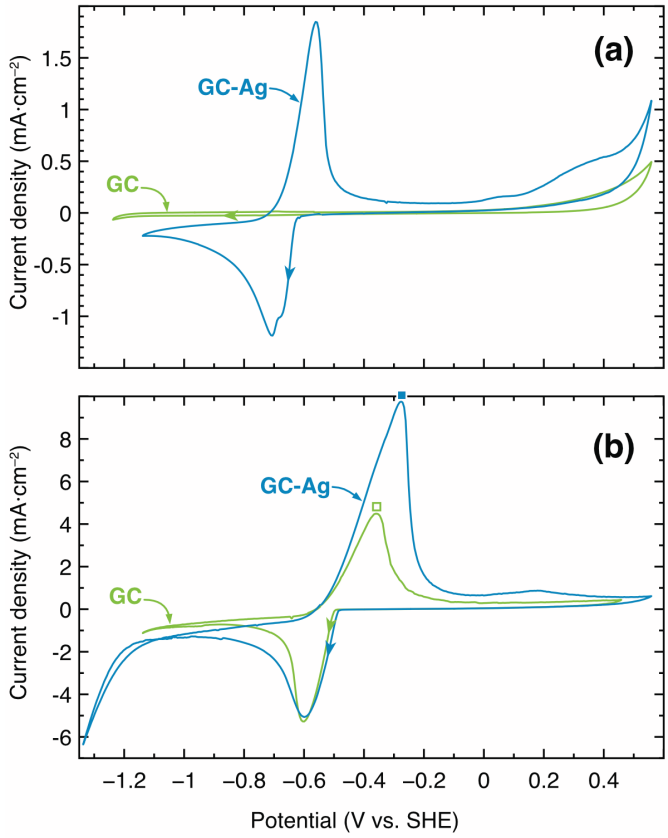

Figure 3.5.: Comparison of cyclic voltammetry performed at 20 mV·s^{-1} on GC and GC-Ag immersed (a) in 0.01 M HNO_3 and (b) in 0.01 M HNO_3 + 0.01 M CF_3COOAg (pH = 2, T = 60°C). The arrows on the curves indicate the scanning direction.

The CVs presented in Figure 3.5 also indicate that the overvoltage (η that corresponds to the difference between ocp and the onset potential for Ag^+ reduction) is relatively small (η = 33 to 165 mV depending on the experimental conditions). It demonstrates that the energy requested for the Ag deposition is low. The reduction peak is even further positively shifted when closely packed Ag nanocubes are assembled on the glassy carbon (GC-cubes, see Appendix C.1.4 for more details). Figure 3.6 shows SEM images of both GC-Ag and GC-cubes samples. A comparison of their CVs, shown in Figure 3.7 and measured in 0.01 M HNO_3, highlights distinct behavior. The cathodic peak attributed to Ag^+ reduction (* on the CV) is centered at −0.58 V (while it is −0.7 V for GC-Ag) and the onset potential for Ag^+ reduction is difficult to assign because negative current starts already from ocp. This is in line with the under potential deposition (UPD) reported for silver on single crystalline metals such as Pt[181]. Since Pt lattice is very close to Ag, UPD should proceed even more easily on Ag (100) facets of the nanocubes. Note also that the anodic peak (# on the CV) corresponding to silver stripping is positively shifted to −0.1 V. This suggests that dissolution of redeposited silver is more difficult, as it occurs mainly on the (100) facets facing each other in the gaps between the cubes.

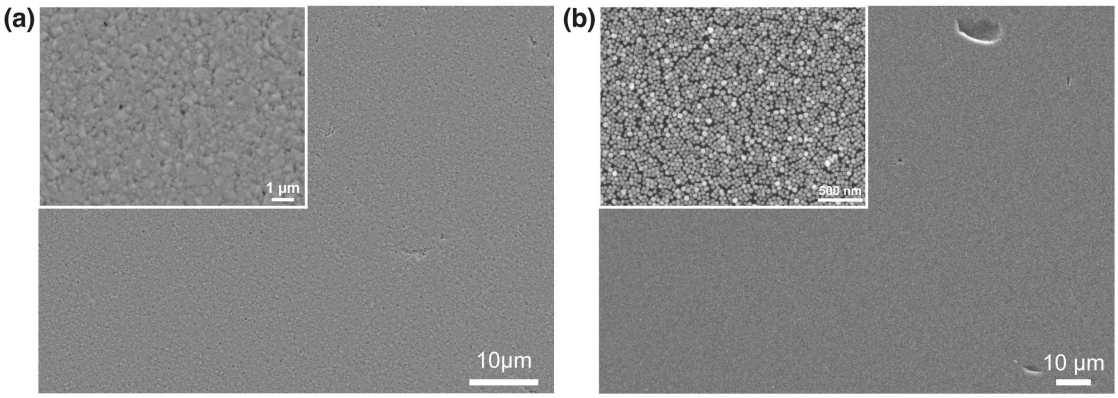

Figure 3.6.: SEM images of (a) GC-Ag: ~100 nm thick silver film on a glassy carbon *via* physical vapor deposition and (b) GC-cubes: compact assembly of ~40 nm silver nanocubes *via* Langmuir-Blodgett assembly.

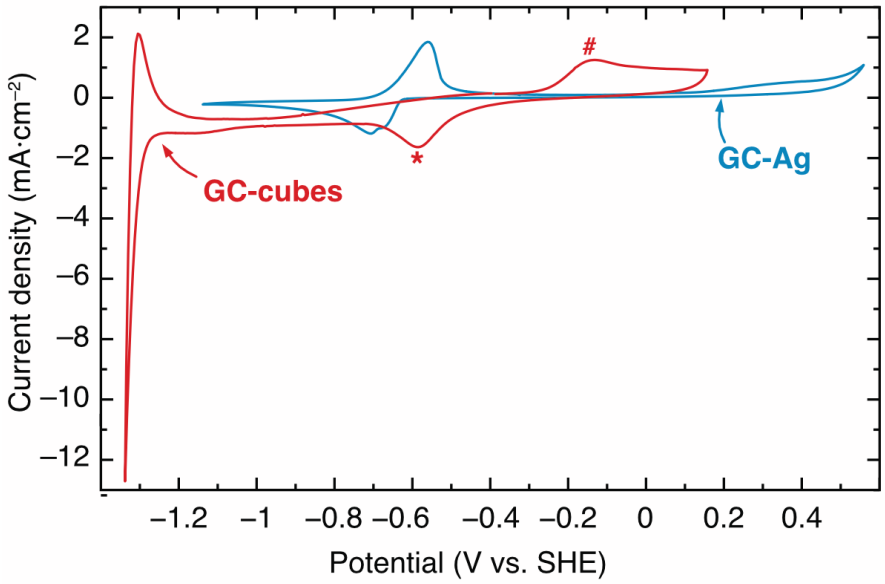

Figure 3.7.: Comparison of cyclic voltammetry performed at 20 $mV{\cdot}s^{-1}$ on GC-Ag and GC-cubes immersed in 0.01 M HNO_3 (pH = 2, T = 60°C).

The high reactivity of atoms at nanocube corners, due to higher surface energy sites[174, 175], results in their faster dissolution and the transformation of nanocubes into nanospheres at long reaction times, as observed in Figure 3.4h. Silver atoms on different sites on a single nanoparticle or on nanoparticles of different sizes, might present slightly different reduction potentials arising from differences in surface energy. Consequently, when nanoparticles on a substrate are immersed in a solution, they tend to reorganize by oxidizing at high-energy sites and redepositing (reduction) at more stable locations according to the electrochemical processes described above. This can be facilitated by electron transport through the substrate (if conductive) or by

tunneling between neighboring nanoparticles (for sub-nanometer gaps), moving from high-energy to lower-energy sites to initiate Ag^+ reduction, as depicted in Figure 3.4d and C.3d. This mechanism, previously reported as electrochemical Ostwald ripening, [182] has been used to grow silver on conductive substrates using water only, as a result from smaller nanoparticles dissolving to the benefit of larger nanoparticles. In addition, it was reported that this transformation is exacerbated by acidic conditions and in the presence of silver ions[182, 183].

3.2.4. Epitaxial welding towards complex nanostructures

Next, this approach was implemented to silver nanocubes arranged in nanopatterned PDMS trenches, and demonstrated its potential to obtain intricate monocrystalline meta-atoms. We found that the welding process was affected by the confined environment of the PDMS trenches, having lateral dimension comparable to that of the nanocubes. In these trenches, the diffusion of reactants introduced is notably altered and the availability of Ag^+ ions is limited due to the significantly lower nanocube density compared to when they are drop-casted. Identifying the ideal conditions to achieve seamless continuous nanostructures without compromising the nanocubes' morphology proved challenging, as excessive dissolution or insufficient welding were encountered when adjusting the Br^- concentration.

To mitigate this issue, an alternative strategy was explored by adding millimolars concentration of a silver salt (CF_3COOAg)[2]. This addition proved effective to significantly enhance shape retention and enabled the formation of continuous 1D nanostructures with varied aspect ratios, as demonstrated in Figures 3.8a and 3.8b displaying nanorod arrays welded together. Figure C.8 further illustrates large-area welding of nanocube dimers. In efforts to understand the underlying mechanism, control experiments conducted in dark conditions, which showed outcomes consistent with those obtained under normal lighting conditions, eliminated the possibility of light-induced silver reduction (Figure C.5). In contrast, using $AgNO_3$ as a silver source intensified the etching process due to the generation of HNO_3[184]. It is noteworthy that tests with 10 mM CF_3COONa (Figure C.6) showed that CF_3COO^- ions did not contribute to shape preservation. Despite calculations suggesting no attainable equilibrium between oxidation and growth at high silver ion concentrations, we speculate that a higher concentration of Ag^+ ions increases the likelihood of interaction, leading to their reduction via the excess electrons in the nanocubes, in accordance with the observations presented earlier.

Using air-water interface assembly technique presented in previous chapter[172], we successfully arranged nanocubes into more intricate geometries. This allows us to further test the potential of this welding approach to 2D meta-atoms. Figure 3.8c showcases the formation of continuous nanostructures from 55 nm silver nanocubes, including L, C, S, T, +, and a 2×2 nanocube square shapes. This highlights the method's adaptability in welding tightly packed nanocubes into various arrangements, with the trench geometry playing a crucial role in defining the meta-atoms' final shape.

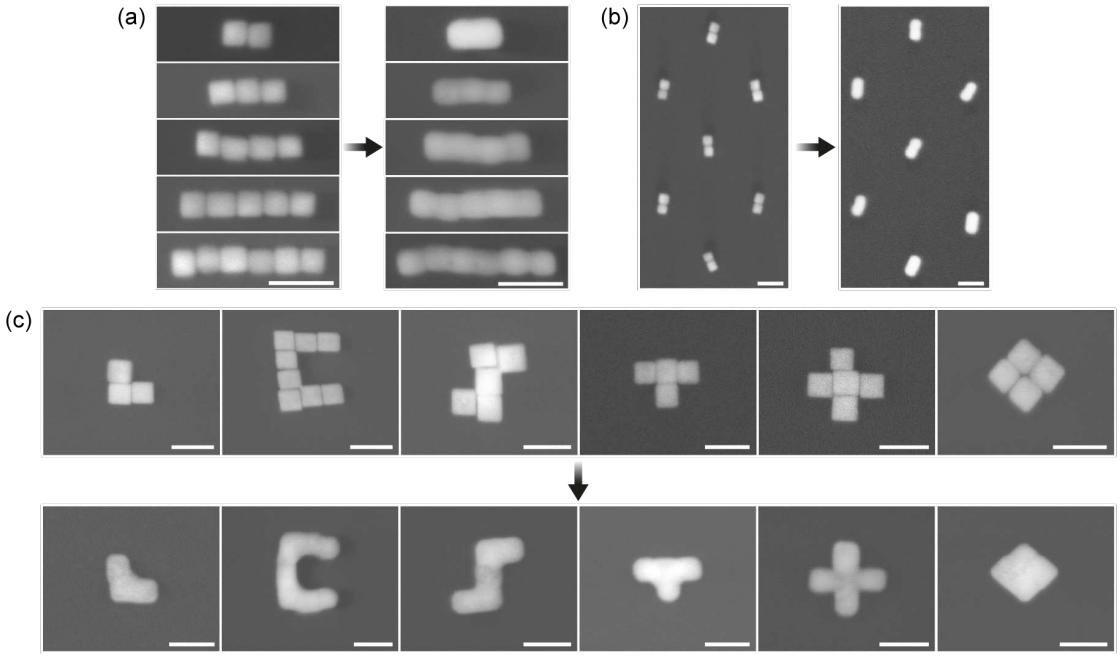

Figure 3.8.: Collage image depicting a) the formation of monocrystalline nanorods of varying lengths from 40 nm silver nanocubes after welding at 60°C for 1 hour using 10 mM CF_3COOAg at a pH = 2[2], and b) dimer arrays created under identical conditions[2]. (c) The image also demonstrates the ability to chemically weld intricate nanostructures from 55 nm AgNCs within 80-90 nm deep PDMS trenches, conducted at 80°C for 1 hour with 5-20 mM CF_3COOAg, 50 μM NaBr, and at a pH = 2. All scale bars are 100 nm in length.

Additionally, Figures 3.8 and C.8 confirm the absence of nanoparticle nuclei on the surface resulting from homonucleation, showcasing the superiority of this new chemical strategy over traditional overgrowth techniques.

3.2.5. TEM characterization of welded nanostructures

Finally, the crystallinity of the welded nanostructures was verified by transmission electron microscopy (TEM), shown in Figures 3.9a, 3.9d, and 3.9e. These images reveal that structures, ranging from 1D rods to a more complex 2D L-shape or diamonds, are monocrystalline, as confirmed by the presence of continuous atomic columns or planes across the nanocube junctions, despite some contrast can be observed in some locations. Dislocations, as well as stress and possibly thickness variations are most likely responsible for the contrast observed in some junctions. As reported previously[11], these can be relieved through a rapid thermal annealing (RTA) process. Note that, as evident from Figure 3.9, the welding takes places throughout the gap until the bottom side of the nanocubes. This finding suggests that our method can produce monocrystalline nanoparticles with intricate shapes *à la carte*, which are beyond the reach of current traditional bottom-up colloidal synthesis techniques.

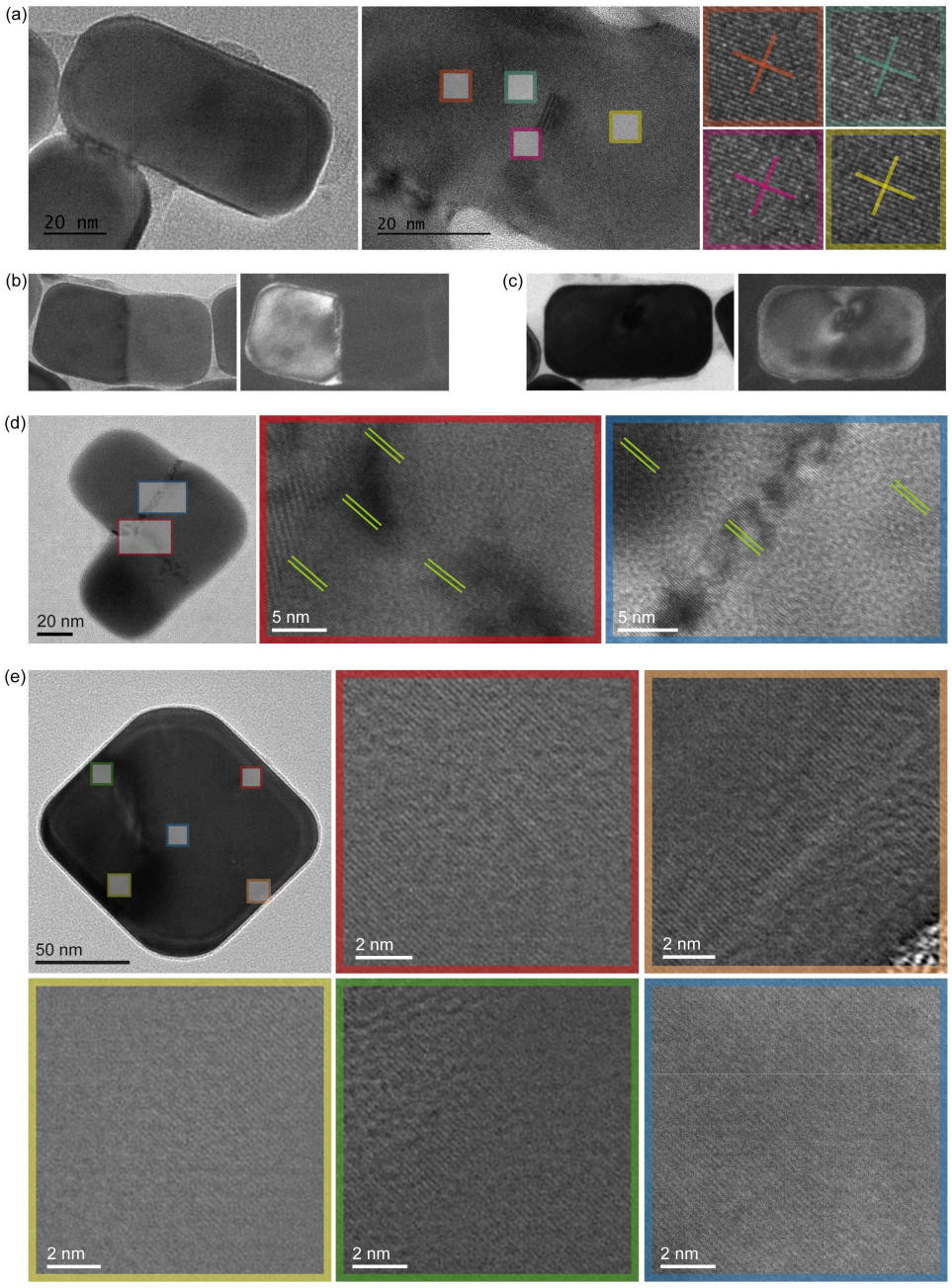

Figure 3.9.: TEM characterization of: a) dimeric ~30 nm silver nanocubes directly welded on a Si_3N_4 TEM grid, revealing a monocrystalline nanorod structure with an atomic column running through the junction[2]; b) bright and dark field images of a 1D nanostructure composed of two grains resulting from slight misalignment of nanocubes[2]; c) bright and dark field images of a monocrystalline 1D nanostructure[2]; d) L-shaped and e) 2×2 square-shaped arrangements made of 55 nm silver nanocubes, welded on nanopatterned PDMS and transferred to a TEM grid, also showing monocrystalline structure.

We hypothesize, however as illustrated in Figure 3.9b, that slight misorientations of nanocubes during assembly can also lead to the development of grain boundaries between adjacent crystals. This misalignment is evident in dark field images, where contrasts arise from electrons scattered by specific diffracting planes meeting the Bragg condition. When two welded nanocubes align crystallographically, the entire structure exhibits bright contrast, as seen in Figure 3.9c. Conversely, misaligned nanocubes result in only part of the structure showing bright contrast due to the failure of one part to meet the Bragg condition, with Figure 3.9b displaying an example where the orientation differs by less than 10°. A sharp contrast at the junction suggests the formation of grain boundaries, indicating the need for precise alignment of nanocubes before welding to form larger grains, but suggests some possibility to fabricate well defined grain boundaries for reactivity studies. Even so, we found that isolated 1D and 2D nanostructures present on the sample on the other hand are mostly monocrystalline. This can be seen in Appendices C.9, C.10, C.11, showing continuous atomic columns throughout the nanostructures and at the junction for many nanostructures. We hypothesize that capillary forces and van der Waals interactions are responsible for their perfect face-to-face arrangement.

3.2.6. Optical characterization

Figure 3.10 shows the comparison of dark-field scattering spectra of L-shaped and cross-shaped metasurfaces before and after nanowelding.

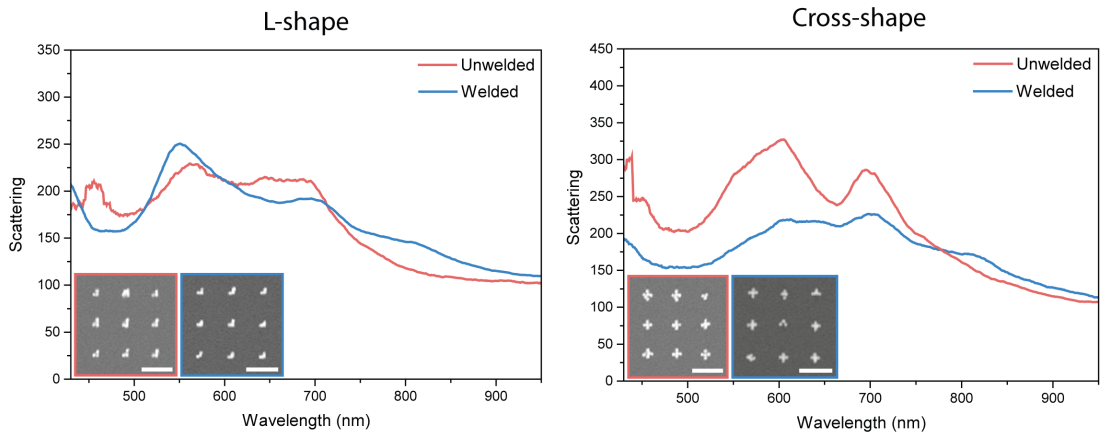

Figure 3.10.: Dark-field scattering spectra of unwelded and welded L-shape and Cross-shape nanostructures. Each spectrum correspond to an average of three different positions. Scale bars are 500 nm in length.

3.3. Conclusion

In conclusion, our study introduces a method for epitaxial welding of silver nanocubes in solution without a reducing agent, effectively preventing homonucleation that could impair the optical properties of the nanostructures. Our findings reveal the role of nanogaps in driving anisotropic growth via electrostatic interactions. We also highlight the importance of fine-tuning the welding on both flat substrates and within PDMS trenches to keep the balance between nanocube dissolution, growth, and shape retention. This is achieved by carefully adjusting the temperature, the concentration of HNO_3, and the addition of shape-stabilizing agents like Br^- and CF_3COOAg. However, we observed that effective welding occurs predominantly between closely positioned nanocubes; those spaced further apart tend not to weld epitaxially due to the insufficient presence of silver species in the absence of a reducing agent, consistently with the hypothesis of ion accumulation in the gap as a result of the concerted electrostatic action of nanocubes in close proximity. By integrating this welding approach with various directed nanoparticle assembly techniques, we pave the way for creating intricate monocrystalline nanostructures through a chemical synthesis approach, a task that remains challenging with existing colloidal synthesis techniques. This advancement opens new avenues for bottom-up fabrication methods in creating optoelectronic devices, such as metasurfaces.

4. Controlled overgrowth of substrate-supported nanocubes: nanocube epitaxy and anisotropic growth

Research into modifying nanoparticle structures after their assembly on substrates via wet-chemical methods opens promising new avenues that extend beyond the capabilities of conventional colloidal synthesis. Several studies have shown that seed-mediated overgrowth directly on solid supports can yield a wide variety of complex nanostructures. In this chapter, we explored a strategy to grow a silver shell on substrate-supported nanocubes, initially aiming to achieve epitaxial welding by adapting a well-established colloidal core-shell synthesis method. Although the optimal conditions for consistent welding were not fully achieved, we found that silver overgrowth could result in two distinct outcomes: nanowelding and anisotropic elongation. Interestingly, in the presence of polyvinylpyrrolidone (PVP), silver preferentially grew within the interparticle gap without bridging the cores, forming high-aspect-ratio nanostructures. This behavior differs from the observations in Chapter 3, where nanogaps promoted welding through electrostatic interactions. These results suggest that the initial nanogap plays a decisive role in directing the growth mode (either promoting particle interconnection or acting as a physical template that guides anisotropic elongation). To explore this mechanism further, we used nanocube dimers as a model system and performed systematic parametric studies, varying reaction time, PVP concentration, temperature, nanoparticle size, and shape. These experiments indicate that the underlying design principle could be extended to build more complex architectures beyond simple dimers. Although the exact mechanism is not yet fully confirmed, the framework established in this work introduces a new design approach in which the interparticle gap acts as a structural cue for directional growth. These findings not only deepen our understanding of nanocrystal interface engineering but also offer a pathway for developing monocrystalline nanostructures with tailored geometries, potentially enabling their integration into functional optoelectronic metasurfaces.

Summary

4.1. Introduction 118
4.2. Results and discussion 119
4.2.1. Overgrowth on substrate-supported silver nanocubes 119
4.2.2. Anisotropic overgrowth on substrate-supported nanocubes: dimer model 121
4.2.2.1. Nanowelding vs anisotropic overgrowth 121
4.2.2.2. Parametric study of anisotropic overgrowth 123
4.2.2.3. Mechanism of anisotropic overgrowth 130
4.2.2.4. Attempts on operando spectroscopy experiment 136
4.2.2.5. Designer complex nanostructures from anisotropic overgrowth 138
4.2.2.6. Control experiments 143
4.3. Conclusion 146

4.1. Introduction

As discussed in Chapter 1 of this thesis, research into modifying the structure of nanoparticles after their assembly on substrates through wet-chemical methods opens new possibilities that go beyond conventional colloidal synthesis. This strategy enables the fabrication of nanostructures with geometries that are often inaccessible through traditional solution-phase routes. It also provides precise control over how nanoparticles are arranged and oriented relative to one another and the substrate[108]. Several studies have successfully demonstrated that seed-mediated overgrowth of nanoparticles directly on substrates can produce a wide range of complex morphologies. Examples include nanostars[109], nanocrescents[110], nanowires[111], nanorods[112–114], and nanocubes[115–117], as well as more faceted shapes such as nanotriangles[118–120], Wulff-type crystals[118], tetrahexahedrons[118], and decahedral structures[121, 122]. In some cases, coupling this method with galvanic replacement has led to even more intricate cage-like nanostructures[117].

Unlike in traditional seed-mediated colloidal synthesis, chemical overgrowth of substrate-supported seeds pose additional challenges. Nucleation does not only occur in the bulk solution but can also happen directly on the substrate, making it more difficult to control[108]. To avoid these undesired effects, one must carefully manage the concentration of metal atoms to stay below the threshold that would trigger spontaneous nucleation[185]. Overall, while the strategy is promising, it demands careful tuning of chemical and physical parameters to ensure selective, high-quality growth.

In 2017, Sciacca and co-workers reported the chemical overgrowth of silver nanocubes assembled on a substrate, transforming them into monocrystalline nanorods[11]. In this study, Tollens' reagent, a diamminesilver(I) complex, was used as the silver precursor, while glucose served as the reducing agent. This combination enabled the overgrowth of the nanocubes and facilitated their epitaxial connection resulting in nanorods with sharp features owing to cubic structure. However, the reaction also led to undesirable outcomes, including homogeneous nucleation in the solution and heterogeneous nucleation on the substrate, both of which negatively affected the structural quality of the final nanorods. The study did not report any systematic tuning of the reaction conditions, which may explain the occurrence of secondary nucleation on the substrate.

In contrast, the approach presented in Chapter 3 successfully avoided secondary nucleation while achieving epitaxial welding of assembled silver nanocubes. This process relies on the selective etching of atoms from the edges and corners of the nanocubes, which are then redeposited into the nanoscale gaps between neighboring particles. As a result, effective welding requires that the nanocubes are in close proximity; otherwise, no welding is formed. Another consequence of this mechanism is the rounding of initially sharp nanocube features. Such morphological changes have

been shown to alter the optical properties of the resulting nanostructures[186].

Building on these observations, a simple yet intriguing idea arose: what if a conventional colloidal core-shell overgrowth method, typically used in solution-based syntheses, could be adapted for systems where the nanoparticle seeds are immobilized on a substrate rather than dispersed in suspension?

In 2010, Ma and co-workers reported a method for synthesizing Au@Ag core–shell nanocubes with precise control over the silver shell thickness[187]. In their approach, silver nitrate ($AgNO_3$) served as the silver precursor, ascorbic acid was used as a mild reducing agent, and cetyltrimethylammonium chloride (CTAC) acted as both the capping agent and structure-directing surfactant to promote the formation of cubic morphologies. To prevent unwanted homogeneous nucleation, they utilized a syringe pump to deliver the reagents at a controlled rate, thereby maintaining the atomic concentration below the critical threshold for spontaneous nucleation.

In this chapter, I will focus on adapting Ma's method[187] for silver overgrowth on nanocubes that have been assembled on a substrate. I begin by describing the initial efforts to achieve epitaxial welding of silver nanocubes directly on the substrate. Although the ideal conditions for welding were not fully realized, the experiments revealed a pronounced anisotropic overgrowth effect, which is discussed in detail. To further investigate this behavior, I replaced silver nanocubes with gold nanocubes. This allowed for observation of the silver shell growth behavior. In addition, I present findings on the enhanced anisotropy observed under certain conditions and report results from a set of parametric studies designed to better understand this phenomenon. These observations may offer a useful pathway for developing new methods of metal nanopatterning.

4.2. Results and discussion

4.2.1. Overgrowth on substrate-supported silver nanocubes

To demonstrate the in-situ silver overgrowth process, ~42 nm PVP-capped silver nanocubes were drop-cast onto a silicon substrate, and their structural evolution was monitored as the overgrowth reaction progressed (Figure 4.1). Following the procedure outlined in section D.1.2, the PVP ligands were first removed, and the substrate was preheated in a CTAC solution for 20 minutes, according with the reference procedure[187]. However, as shown in Figure 4.1a, comparing the initial stock nanocubes with those after being preheated in CTAC solution for 20 minutes (time = 0 min) revealed noticeable rounding of the nanocube edges. Additionally, larger nanostructures appeared, likely due to particle coalescence and/or Ostwald ripening during preheating. To minimize these undesired effects in subsequent experiments, we modified our protocol by preheating only the CTAC solution for approximately 20 minutes, rather than preheating the substrate with nanocubes.

After allowing the reaction to proceed for two hours under these conditions, the nanocubes increased in size from approximately 42 nm to 53 nm and exhibited sharper

edges, as shown in Figure 4.1b. Although secondary nucleation of silver occurred in the solution, indicated by a color shift from initially colorless to slightly whitish to slight yellow, minimal nucleation on the substrate surface was observed. However, completely ruling out substrate nucleation remains difficult, as it becomes challenging to distinguish between structures that originated from the seeded nanocubes and those formed by secondary nucleation at the end of the reaction. Conducting multiple cycles of the overgrowth process further increased the size of the nanocubes, as demonstrated in Figure D.2a and D.2b on silicon and glass substrates, respectively.

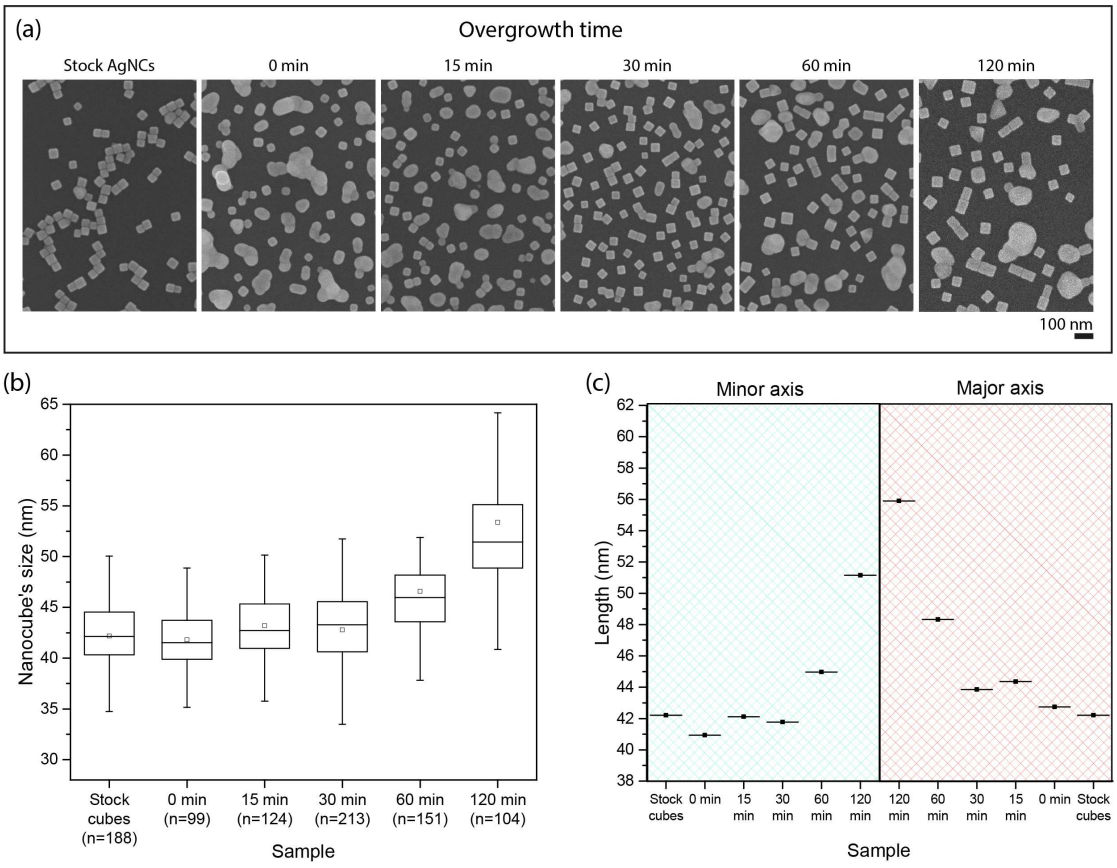

Figure 4.1.: (a) SEM images of ~42 nm silver nanocubes drop-cast onto a silicon substrate and subjected to overgrowth for different reaction times. (b) Box plot showing the size distribution of silver nanocubes as a function of overgrowth duration. Center line: median; small square: mean; box: interquartile range. (c) Plot of the average dimensions along the minor and major axes of the nanocubes at different overgrowth times. n=number of sample.

Although not exhaustive, we have explored varying several reaction parameters, including multiple overgrowth cycles (Figure D.2), reagent addition rates (Figure D.3), the choice of silver precursor (Figures D.4 & D.5), and the introduction of HNO_3 (Figures D.4 & D.5). However, achieving uniform and reproducible welding-induced overgrowth of nanocubes across the same sample remained challenging. As an example,

Figure D.3 illustrates this inconsistency clearly. While some regions showed initial welding of nanocubes with preservation of their cubic shape (Figure D.3b, top and middle images), the majority remained unwelded. In contrast, other areas within the same sample exhibited excessive overgrowth (Figure D.3b bottom image), resulting in large nanostructures with undefined morphologies and rounded edges, thereby losing the distinct cubic characteristics.

A consistent observation from the experiments involving silver overgrowth on silver nanocubes is the occurrence of anisotropic growth, particularly noticeable for nanocubes arranged face-to-face as dimers on substrates. This anisotropy can be clearly seen in Figures 4.1a, D.2, and D.3. To confirm and quantify this effect, we measured the dimensions of nanocubes (both individual and dimer structures) along their major and minor axes. The measurements, shown in Figure4.1c, reveal that the growth rates indeed differ between the two axes, confirming anisotropic overgrowth.

4.2.2. Anisotropic overgrowth on substrate-supported nanocubes: dimer model

4.2.2.1. Nanowelding vs anisotropic overgrowth

To gain further insight into the silver overgrowth process, we replaced the PVP-capped silver nanocubes with similarly sized PVP-capped gold nanocubes and performed a silver overgrowth reaction under similar condition. Due to the difference in atomic numbers between silver (Z = 47) and gold (Z = 79), imaging with a backscattered electron (BSE) detector in SEM provided clear elemental contrast between the silver and gold structures. Elements with higher atomic numbers, such as gold, have larger nuclei that more strongly deflect incident electrons. As a result, gold appears brighter in BSE images compared to silver, allowing differentiation between the two metals for the analysis of the overgrowth process.

Figure 4.2 provides representative low-magnification SEM images showing silver overgrowth on gold nanocubes deposited onto silicon and glass substrates. The images demonstrate similar overgrowth behavior on both substrates. To investigate the silver overgrowth on gold nanocube dimers more closely, representative examples were selected and are presented in Figure 4.3 (right-hand side). From these observations, we propose two types of behavior of silver overgrowth on gold nanocube dimers: The first type shows that silver preferentially grows on the outer regions, bridging the two nanocubes and forming a single continuous, rectangular-shaped nanostructure (Figure 4.3a). We presume that this occurs when gold nanocubes are placed in very close proximity. This behaviour represents the ideal outcome for applications involving epitaxial welding of nanocubes. In contrast, in the second type, silver preferentially grows within the gap between the cubes, causing anisotropic growth on the individual nanocubes (Figure 4.3b). We postulate that this happens when gold nanocubes are separated by larger distances on a substrate. In this case, interestingly, a continuous nanostructure bridging the two nanocubes does not form, and notably, the gap between the cubes remains preserved. This behavior aligns with previous observations

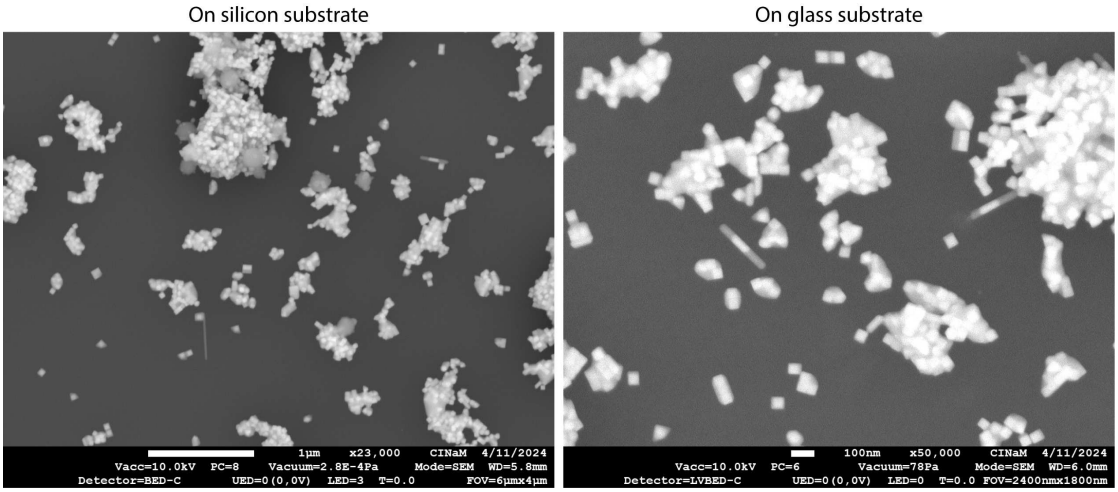

Figure 4.2.: Low-magnification SEM images showing silver overgrowth on gold nanocubes drop-cast onto silicon and glass substrates.

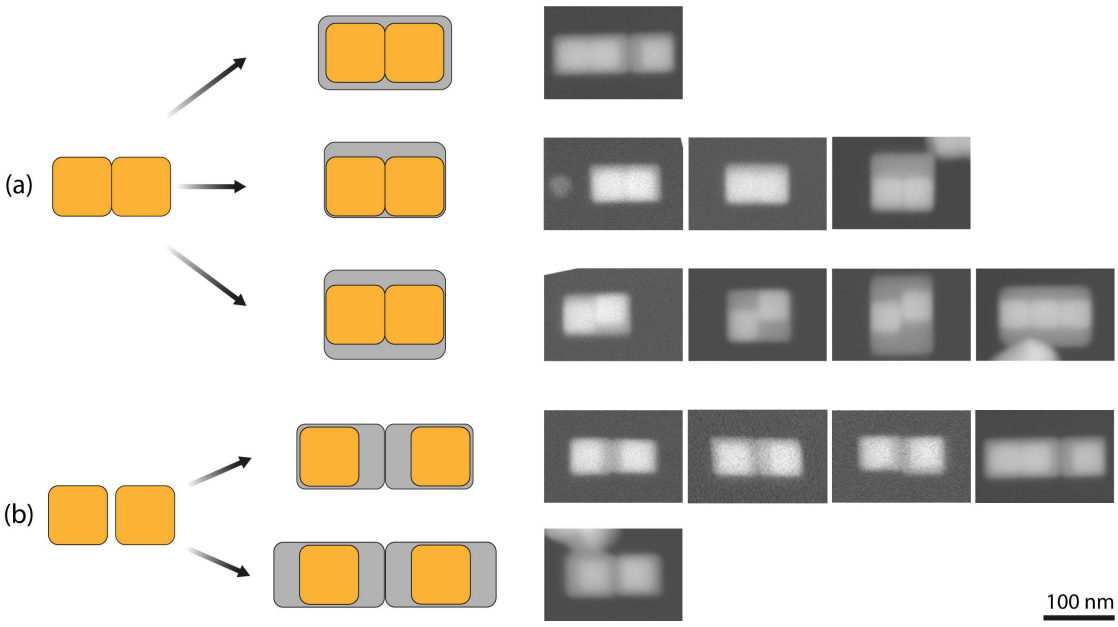

Figure 4.3.: SEM images illustrating two distinct types of silver overgrowth on gold nanocube dimers: (a) gold nanocubes positioned in close proximity, and (b) gold nanocubes separated by larger gaps.

of silver overgrowth on silver nanocube dimers (Figures 4.1a, D.2, and D.3). These observations raised an important question: is there a critical interparticle gap distance that determines which growth mode will occur? We attempted to address this question in the latter part of the chapter. However, identifying a definitive threshold has proven to be challenging.

At this stage, we hypothesized that the assembly process could bring the nanocubes into close proximity, potentially enabling epitaxial welding through subsequent silver overgrowth [the first overgrowth type (Figure 4.3a)]. However, as demonstrated in Figures D.6 and D.7, this assumption was not fully confirmed. Figure D.6 shows that silver overgrowth on gold nanocubes assembled into grids via nanoparticle imprint lithography on glass substrates indeed facilitated interconnection, even when nanocubes were aggregated or edge-to-edge rather than strictly face-to-face. Nevertheless, interconnection did not occur if the gaps between nanocubes were too large. In contrast, silver overgrowth on gold nanocubes assembled within PDMS split-ring trenches (Figure D.7) resulted in minimal interconnection, despite observable overgrowth on individual nanocubes. This reduced interconnection likely stems from the confinement effect within the PDMS trenches, altering the local distribution of reactants compared to the open arrangement on glass substrates. In positive note, secondary nucleation on the substrates was minimal in both cases.

4.2.2.2. Parametric study of anisotropic overgrowth

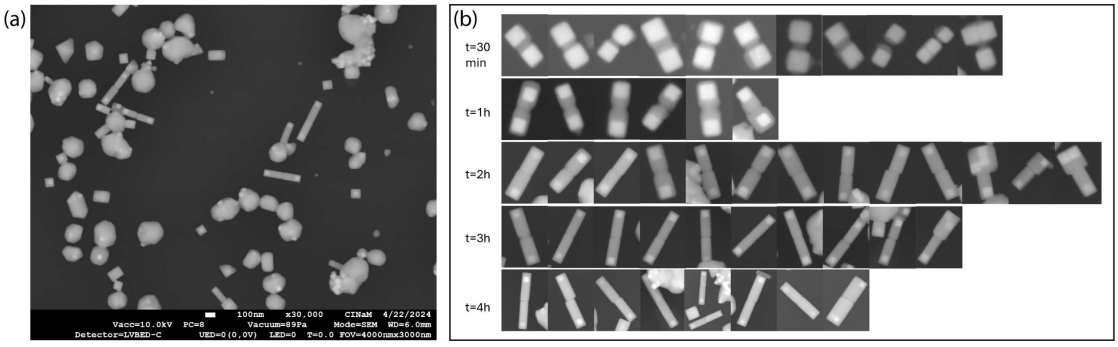

Figure 4.4.: SEM images illustrating anisotropic silver overgrowth on gold nanocubes drop-cast onto a silicon substrate resulting from PVP contamination: (a) after 3 hours of reaction; (b) sequential snapshots showing the progression of anisotropic growth at selected reaction times. Scale: gold nanocubes are ~40 nm in size.

We noted unexpected anisotropic growth in some samples (Figure 4.4) and we decided to investigate it further. This led to the discovery of the crucial role of PVP in controlling anisotropy. As shown in Figure 4.5a, increasing the concentration of PVP in the overgrowth solution correlates with a higher aspect ratio in the resulting dimer structures. This suggests that PVP plays a significant role in directing the growth dynamics. Further quantitative analysis in Figures 4.5c and 4.5d supports this conclusion. With increasing PVP concentration, silver growth along the outer directions of the dimer, labeled as a, b, and c, is progressively suppressed. At the same time, growth within the interparticle gap (x-direction) is enhanced. These findings indicate that PVP may inhibit surface deposition on the exposed cube facets while promoting localized growth in the confined region between nanocubes, thereby amplifying anisotropy. Supporting this idea, we consistently observed that growth

rates within the nanogaps were substantially higher than those on isolated nanocubes under identical conditions (see Figure 4.4a and 4.6). This clearly indicates either suppressed growth on exposed facets or preferential enhancement of growth within the gaps.

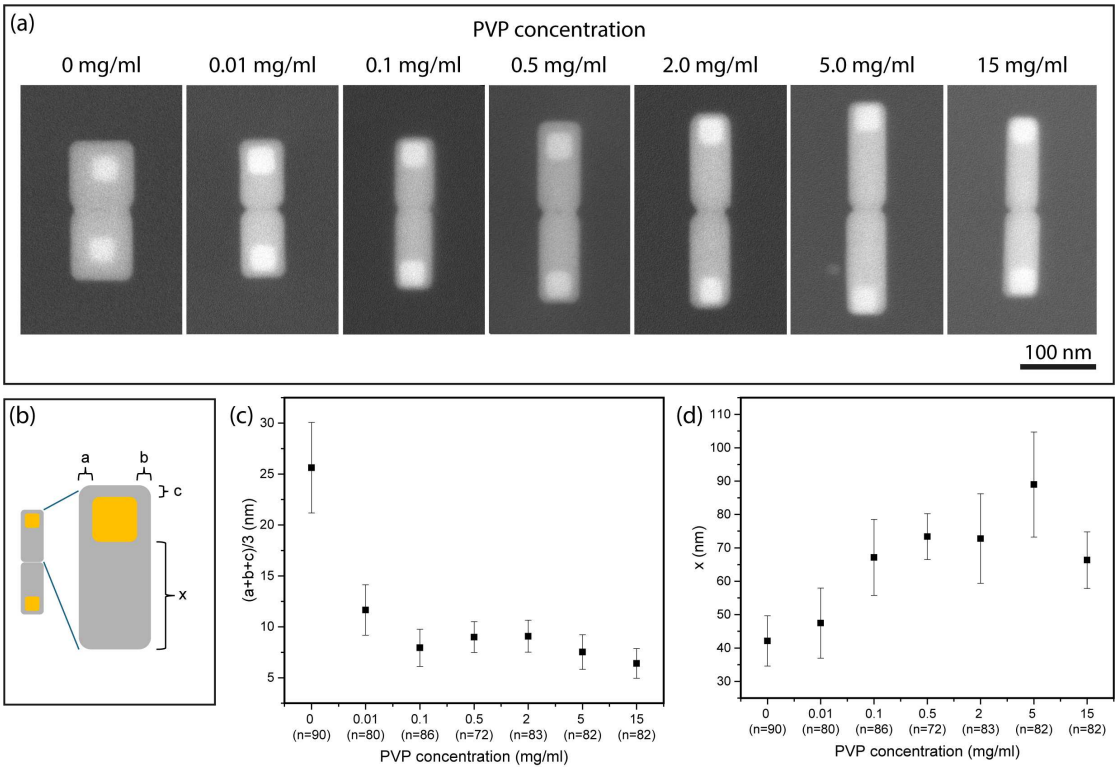

Figure 4.5.: (a) Representative SEM images showing silver overgrowth on gold nanocube dimers deposited onto glass substrates, reacted at 70°C for 3 hours under varying PVP concentrations. (b) Schematic illustration defining the directions (a, b, c, and x) of silver overgrowth on gold nanocube dimers. (c) Quantitative measurement of average overgrowth along directions a, b, and c. (d) Quantitative measurement of silver overgrowth within the interparticle gap (direction x). n=number of sample.

Further investigation into the overgrowth process was conducted at 70°C using a PVP concentration of 5.0 mg/mL. As shown in Figure 4.7, this condition resulted in a progressive elongation of the dimer over time. The growth appears to proceed linearly until the center-to-center distance between nanocube cores reaches approximately 300 nm at 6 hours of reaction. Beyond this point, the elongation appears to plateau, likely due to the depletion of silver precursors in the bulk solution. These precursors are consumed both by the growth of nanocube seeds on the substrate and by secondary nucleation processes in the solution. As the reaction progresses, the solution becomes increasingly murky with a whitish-yellow tint, which is indicative of silver nanoparticle formation through unwanted nucleation in the bulk. Here,

"center-to-center distance" refers to the measured distance between the centers of the two nanocube cores in a dimer, and we use this metric to describe the extent of overgrowth.

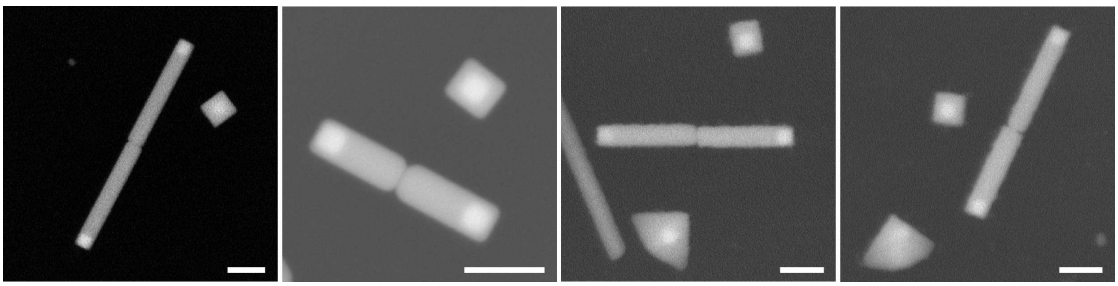

Figure 4.6.: Selected SEM images showing more pronounced silver overgrowth within the gaps of nanocube dimers compared to individual nanocubes. Scale bars: 100 nm.

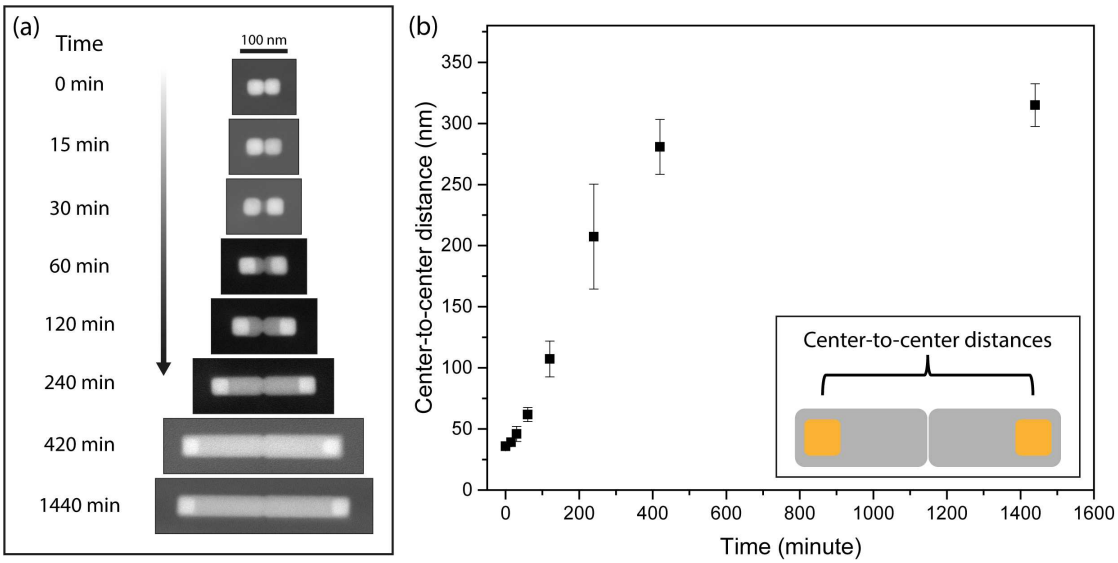

Figure 4.7.: (a) Representative SEM images showing silver overgrowth on gold nanocube dimers deposited on glass substrates, carried out at 70°C in the presence of 5.0 mg/mL PVP, with varying reaction times. (b) Quantitative measurement of silver overgrowth within the interparticle gap, represented by the center-to-center distance between nanocubes. Inset: schematic illustration defining the center-to-center measurement.

To investigate the extent to which elongation can be achieved through silver overgrowth, we performed multiple sequential overgrowth cycles. In each cycle, the assembled gold nanocubes were subjected to the same reaction conditions, with each reaction carried out long enough to ensure near-complete depletion of silver

precursors in the solution. We hypothesized that replenishing the solution with fresh reagents after each cycle could enable continued overgrowth and further elongation of the nanostructures. The first overgrowth cycle was run for 6 hours, after which point the precursor appeared depleted according to previous experiment (Figure 4.7b). The second cycle was then carried out overnight for approximately 17 hours, followed by a third cycle lasting around 7 hours. As shown in Figure 4.8, the elongation proceeded incrementally with each cycle. After the first cycle, the average center-to-center distance between the gold nanocube cores reached about 300 nm. A second overgrowth cycle extended this distance to roughly 630 nm, and a third cycle further increased it to approximately 1460 nm. These results suggest that by periodically refreshing the growth solution, the anisotropic silver overgrowth can be sustained, allowing for the formation of significantly elongated nanostructures across multiple cycles. However, it is important to note that with each successive cycle, the substrate gradually accumulated more secondary nucleation byproducts.

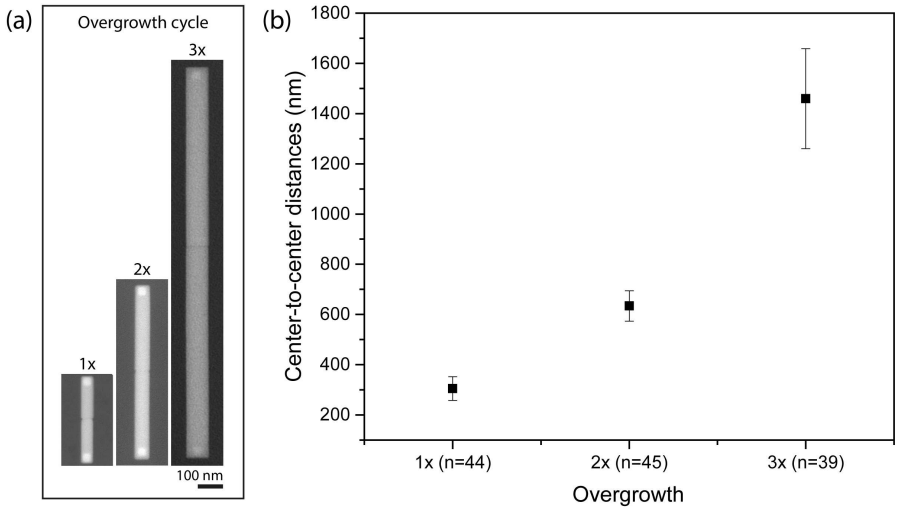

Figure 4.8.: Multiple cycles of silver overgrowth on gold nanocube dimers: (a) Representative SEM images showing gold nanocube dimers after undergoing one, two, and three overgrowth cycles. (b) Quantitative measurements of center-to-center distances corresponding to each overgrowth cycle. n=number of sample.

To investigate the effect of temperature on the silver overgrowth process, we performed reactions at various temperatures, each conducted for a duration of 2 hours. As shown in Figure 4.9, the results indicate that the kinetics of anisotropic overgrowth increase with temperature, as evidenced by the progressive elongation of nanocube dimers, quantified by their center-to-center distances. However, it is also important to note that higher reaction temperatures lead to increased secondary nucleation in the solution, which can introduce unwanted byproducts.

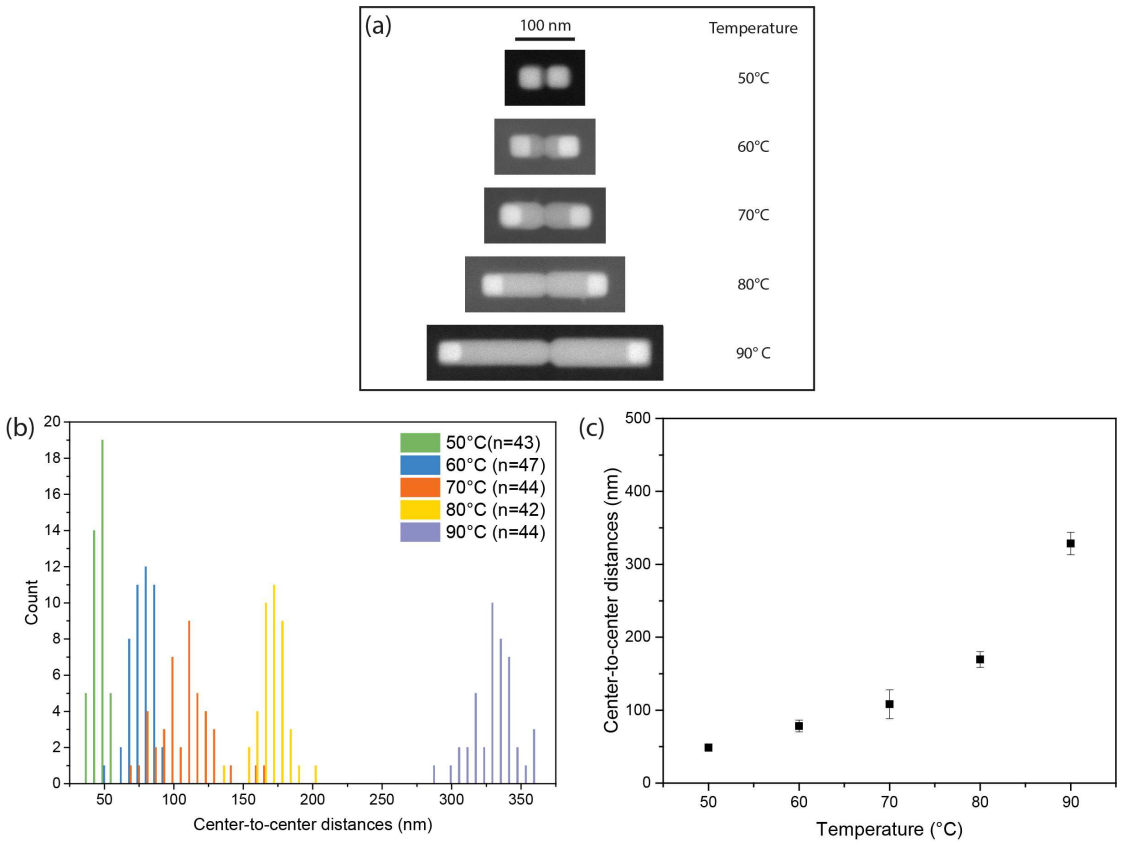

Figure 4.9.: Effect of temperature on silver overgrowth of gold nanocube dimers: (a) Representative SEM images of dimers after 2 hours of overgrowth at different temperatures, (b) Distribution of center-to-center distances measured from each condition, (c) Average center-to-center distances as a function of reaction temperature. n=number of sample.

This temperature-dependent growth behavior is further supported by kinetic analysis using an Arrhenius plot. To construct this plot, the extent of silver overgrowth in the nanogap (defined as the y–z, in Figure 4.10b) can be plotted as a function of reaction time for each temperature. By identifying the linear region of each growth curve (Figure 4.10a), where elongation proceeds at a constant rate, and assuming first-order kinetics, the rate constant k (in nm/min) can be extracted from the slope of the linear fit.

However, due to the observed initial growth delays at certain temperatures, as well as, the saturation of silver overgrowth at later reaction stages, this conventional method resulted in higher estimation error, thereby significant variability and reduced accuracy for the determination of the rate constants. To address this, we used an alternative approach, selecting the data points at a fixed reaction time of 120 minutes for each temperature. By assuming linear growth up to this point across all temperature conditions, we approximated the rate constants at each temperature. These calculated

rate constants are summarized in Table 4.1. Subsequently, these values were used to construct an Arrhenius plot (Figure 4.10c), in which the natural logarithm of the rate constant ($\ln k$) was plotted against the inverse of the absolute temperature ($1/T$).

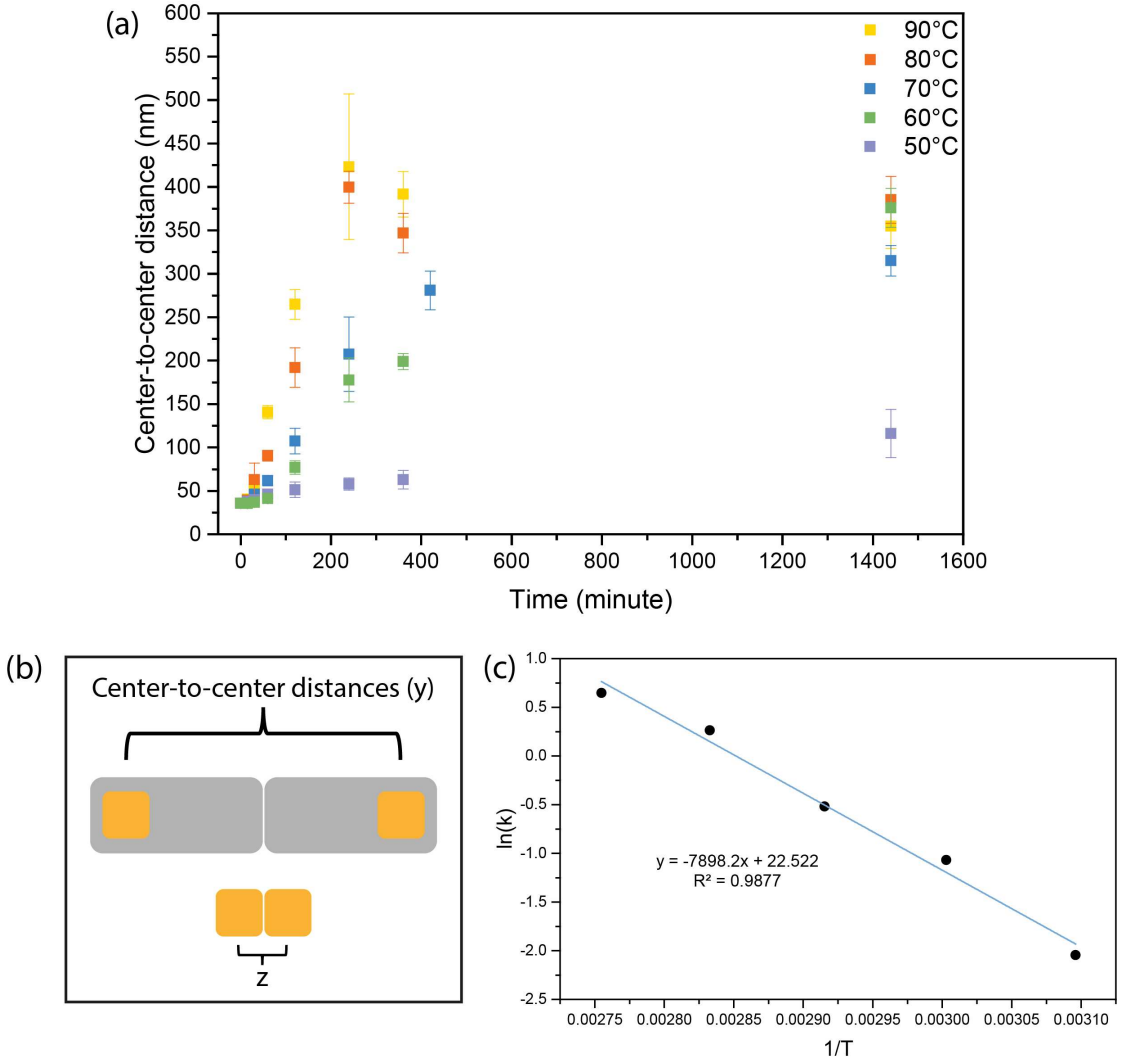

Figure 4.10.: (a) Center-to-center distance as a function of overgrowth time at various reaction temperatures. (b) Schematic illustration of center-to-center distances (y) and z. (c) Arrhenius plot of overgrowth.

The analysis shows that the rate constant (k) for the silver overgrowth reaction increases with temperature, as summarized in Table 4.2 and illustrated in Figure 4.10a. Using these values, we constructed an Arrhenius plot (Figure 4.10c), which displays a linear relationship between ln k and the inverse of temperature. This confirms that the anisotropic silver overgrowth follows Arrhenius-type behavior, indicating that the process is thermally activated and governed by temperature-dependent kinetics.

T (°C)	y-z (nm)	k (nm/min)
50	15.54349	0.129529083
60	41.18116	0.343176333
70	71.49597	0.59579975
80	156.1799	1.301499167
90	228.97994	1.908166167

Table 4.1.: Rate constants calculated at 120 min for different overgrowth temperatures.

k	ln k	T (°C)	T (K)	1/T (K)
0.1295	-2.043849841	50	323	0.003095975
0.3432	-1.069510873	60	333	0.003003003
0.5958	-0.517850658	70	343	0.002915452
1.3015	0.263516805	80	353	0.002832861
1.9082	0.646142659	90	363	0.002754821

Table 4.2.: Silver overgrowth data for Arrhenius plot.

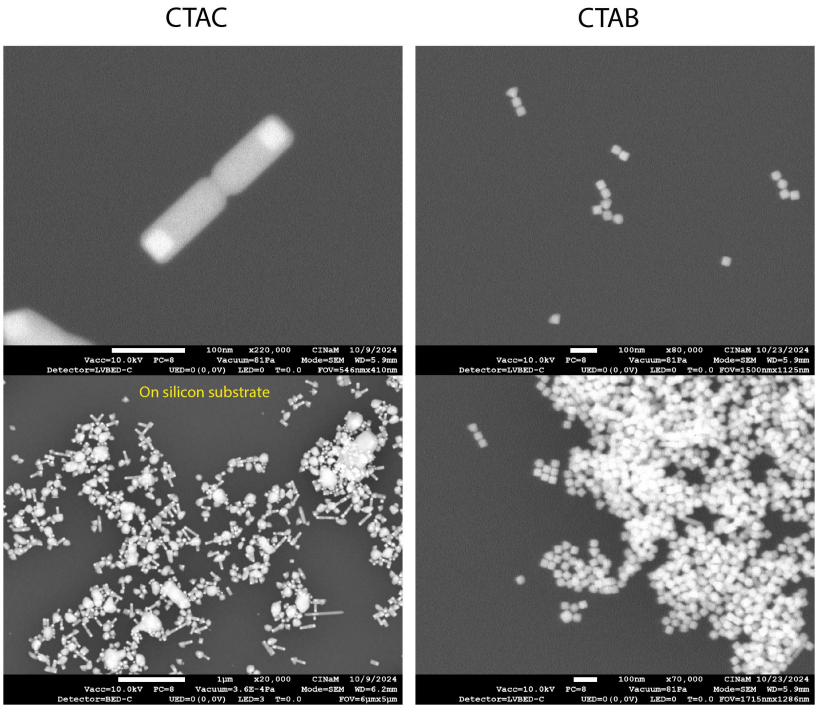

Figure 4.11.: Control experiments investigating the effect CTAC: CTAC was replaced with CTAB. Overgrowth was performed on glass substrates, unless otherwise specified.

A control experiment was conducted by replacing CTAC with CTAB in the overgrowth reaction to assess the role of chloride ions. As shown in Figure 4.11, silver overgrowth proceeded effectively in the presence of CTAC, producing anisotropic nanostructures on the gold nanocubes. In contrast, the reaction with CTAB showed minimal silver deposition on the nanocube surfaces. This difference can be attributed to the lower solubility of AgBr (K_{sp} = 5 x 10^{-13}, 25°C) compared to AgCl (K_{sp} = 1.8 x 1^{-10}, 25°C)[188, 189]. Consequently, the availability of free Ag^+ ions is reduced in the presence of bromide, making the reduction process less favorable and thereby significantly suppressing silver overgrowth when CTAB is used.

4.2.2.3. Mechanism of anisotropic overgrowth

One can consider two possible mechanisms for the anisotropic overgrowth process, as illustrated in Figure 4.12. In the first mechanism (Figure 4.12a,i), the nanocubes are initially assembled in close proximity, allowing silver deposition primarily within the interparticle gap. Continued silver deposition exerts outward mechanical force, progressively pushing the nanocube cores apart (Figure 4.12a,ii) until the final elongated structure is formed (Figure 4.12iii). Alternatively, the second mechanism (Figure 4.12b,i) involves nanocubes initially positioned at a certain distance from each other. In this scenario, silver deposition occurs within the gap, effectively bridging and narrowing the space between cubes, while the positions of the nanocube cores remain fixed (Figure 4.12b,ii), eventually resulting in a similar elongated final structure (Figure 4.12iii). However, based on our previous parametric studies, we rarely observed intermediate structures corresponding to Figure 4.12b,ii. Furthermore, time-dependent experiments presented in Figures 4.7, 4.8, and 4.10 consistently support the occurrence of the first mechanism (Figure 4.12a), indicating that the cores are actively displaced during the anisotropic overgrowth process.

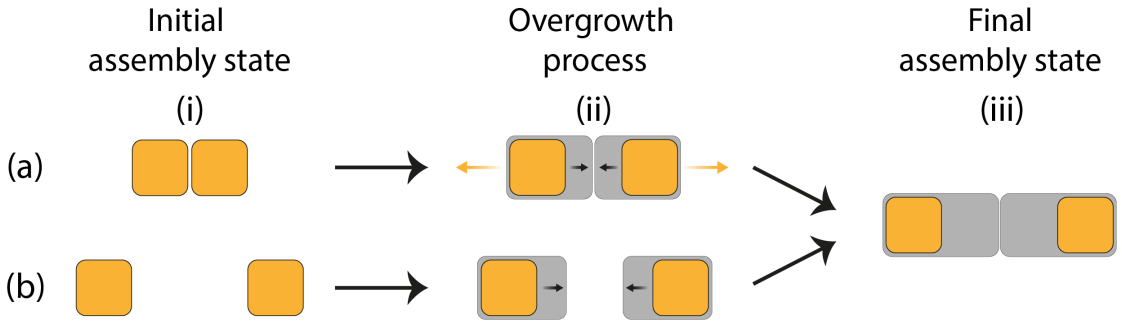

Figure 4.12.: Schematic illustration of the possible mechanisms involved in the anisotropic overgrowth process.

We found this overgrowth behavior to be somewhat counterintuitive. For the elongation to occur, silver must first deposit within the nanogap separating the two gold nanocubes. Then, the newly grown silver needs to exert enough force to overcome the adhesion between the particle cores (and later, the bulkier overgrown structures) and

the substrate, effectively pushing one or both nanocubes apart to allow the structure to extend. At the same time, the growth must avoid forming a welded connection in the gap, which would halt further elongation. This raises a question: is there some kind of barrier within the nanogap that prevents welding while promoting further directional silver growth? Additionally, revisiting our earlier discussion (see Figure 4.3), we also wonder whether there is a threshold nanogap distance that favors anisotropic growth while suppressing welding. More investigation is clearly needed to fully understand what governs this behavior.

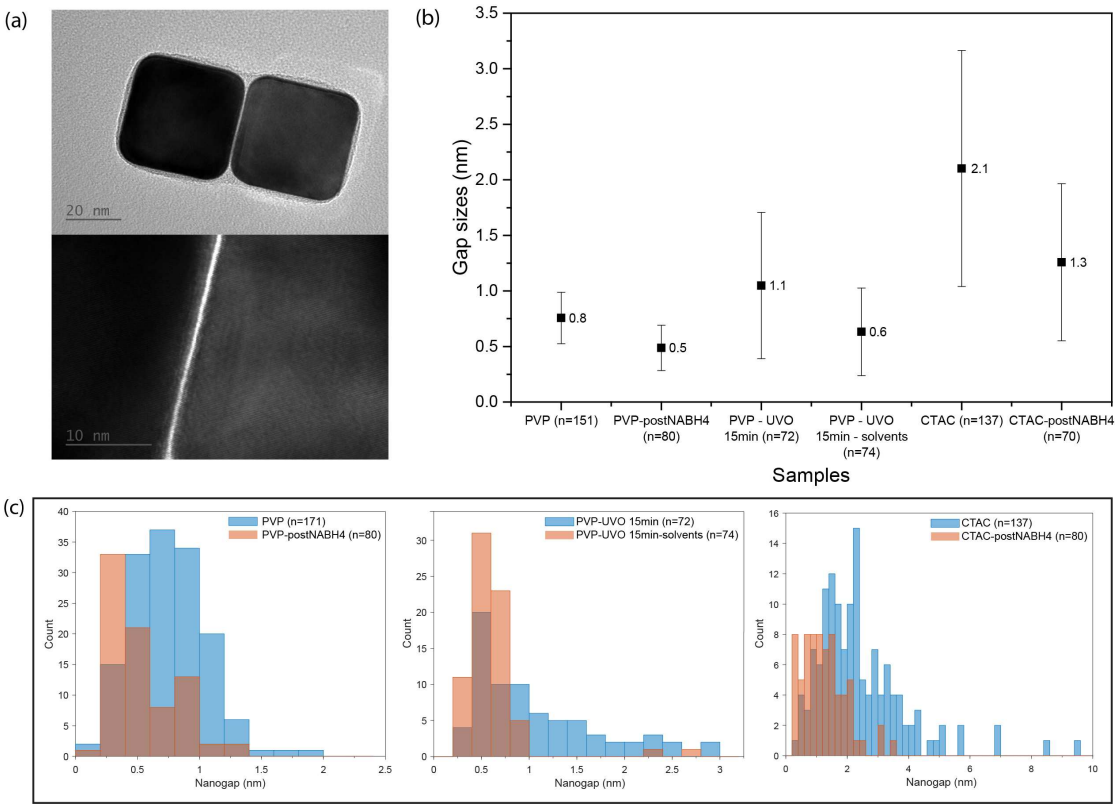

Figure 4.13.: (a) Representative TEM image showing a nanogap between PVP-capped gold nanocube dimers. (b) Comparison of nanogap sizes measured for PVP-capped and CTAC-capped gold nanocube dimers before and after $NaBH_4$ treatment, as well as for PVP-capped dimers following UV/Ozone (UVO) treatment alone and after subsequent solvent immersion. (c) Corresponding histograms displaying the nanogap size distributions, with a bin size of 0.2 nm. n=number of sample.

Motivated by these questions, we attempted a more systematic investigation into how the interparticle gap influences anisotropic silver overgrowth behavior. We started by studying the gap size between gold nanocubes (~30 nm) by drop-casting them onto carbon membrane TEM grids and measuring the distances between adjacent particles, as shown in Figure 4.13b. On average, PVP-capped gold nanocubes exhibited a gap of approximately 0.8 nm, while CTAC-capped nanocubes displayed a larger gap of

around 2.1 nm. We then attempted ligand removal using a $NaBH_4$ treatment, resulting in a further reduction of the average gaps to approximately 0.5 nm for PVP-capped nanocubes and 1.3 nm for CTAC-capped nanocubes. This narrowing likely results from particle mobility induced by van der Waals attractions and capillary forces during solvent evaporation.

In addition, we attempted UV-Ozone (UVO) treatment on PVP-capped gold nanocubes, resulting in an unexpected increase of the average gap to about 1.1 nm. The reason for this apparent gap expansion is uncertain; it may originate from sampling variability, or it could reflect actual physical phenomena, such as electrostatic repulsion induced by the UVO treatment, overcoming van der Waals attractions. This explanation, however, remains speculative. Subsequent immersion of the UVO-treated samples sequentially in water, acetone, and isopropanol for 5 minutes each led again to a reduction in gap size, returning it to approximately 0.6 nm, likely due to van der Waals interactions and capillary forces acting during solvent drying. It is important to note that the gap measurements only considered nanocube pairs with clearly observable gaps. Structures that were already welded or partially welded were excluded from the analysis, as such fused configurations can inhibit further elongation during overgrowth and do not contribute meaningful information to the study of gap-dependent behavior.

Following the gap characterization, we proceeded to evaluate how these interparticle distances, modulated by different surface ligands and treatments, affect silver overgrowth behavior. As shown in Figures 4.14 and 4.15, we investigated silver overgrowth on PVP- and CTAC-capped gold nanocubes deposited on glass substrates under three different pretreatment conditions. In the first condition, silver overgrowth was performed directly on drop-cast nanocubes without any prior treatment. After the reaction, both PVP- and CTAC-capped samples exhibited only minimal silver shell formation, with no significant overall growth or observable anisotropic elongation.

In the second condition, the samples were treated with sodium borohydride to remove the ligands. This approach clearly promoted anisotropic growth, which could be observed even at low magnification in SEM images. Based on these results, we hypothesize that anisotropic overgrowth occurs when the nanogap between dimers is within approximately 0.5 to 1.3 nm and free of any preexisting intermediary capping ligands. In contrast, when a preexisting ligand remains between the particles, anisotropic overgrowth is suppressed. Further studies using ligands that produce shorter or larger interparticle distances could help determine the lower and upper gap limits governing this behavior. This would allow us to define a critical gap range: below the lower limit, nanowelding is favored, while beyond the upper limit, anisotropic overgrowth ceases to occur.

The third condition involved a 30-minute UV/ozone treatment applied to the drop-cast nanocubes. This method was intended to remove the capping ligands without introducing capillary effects associated with solution-based treatments. The results showed that anisotropic overgrowth still occurred. As noted earlier in Figure 4.13b, UVO-treated samples exhibited an average nanogap of approximately 1.1 nm (for

PVP-capped nanocubes). This value falls within the hypothesized critical range of 0.5 to 1.3 nm, supporting the idea that anisotropic growth can proceed within this gap window when no residual ligands are present. However, a significant amount of secondary nucleation was also observed on the substrate. This is likely due to the activation of the glass surface by UVO exposure, which introduces hydroxyl groups capable of reducing silver precursors and initiating unintended nucleation.

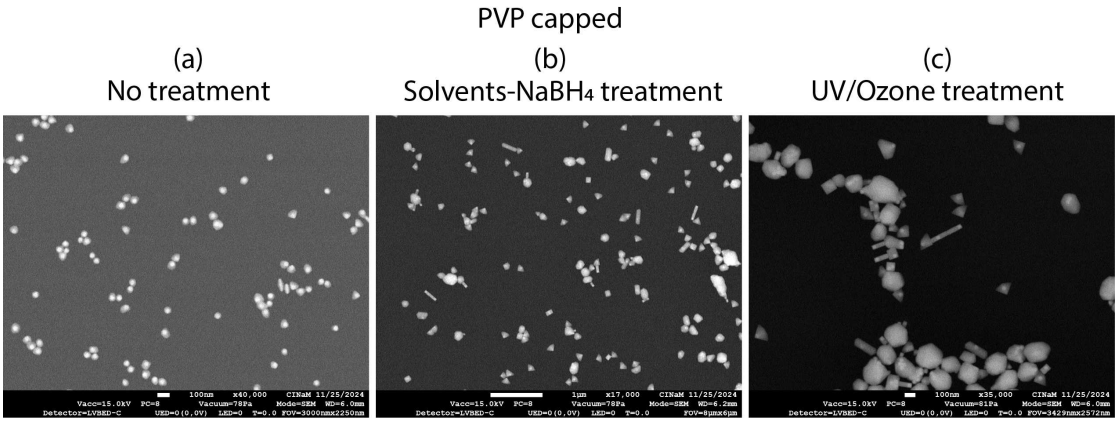

Figure 4.14.: SEM images of silver overgrowth on PVP-capped gold nanocubes deposited on glass substrates subjected to different pretreatments: (a) no pretreatment, (b) sequential solvent immersion followed by $NaBH_4$ treatment, and (c) 30-minute UV/ozone treatment. Overgrowth reactions were conducted at 70°C for 4 hours.

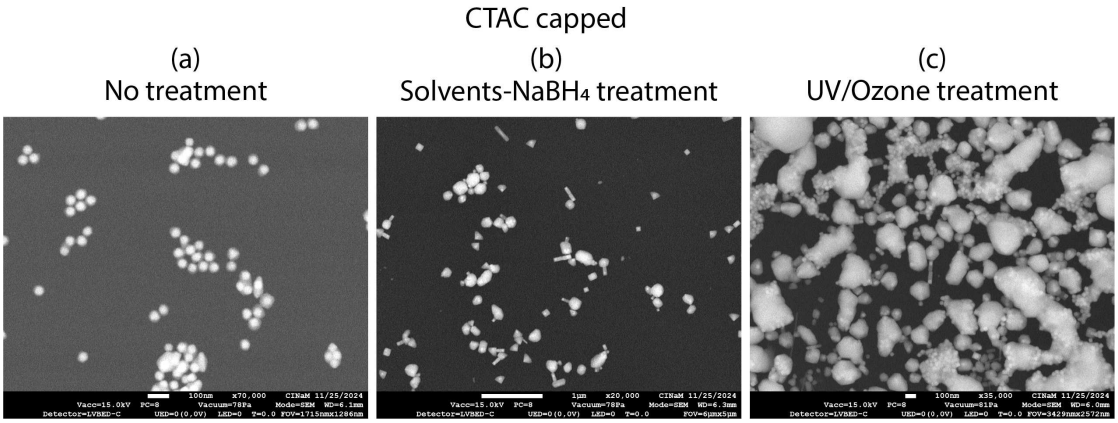

Figure 4.15.: SEM images of silver overgrowth on CTAC-capped gold nanocubes deposited on glass substrates subjected to different pretreatments: (a) no pretreatment, (b) sequential solvent immersion followed by $NaBH_4$ treatment, and (c) 30-minute UV/ozone treatment. Overgrowth reactions were conducted at 70°C for 4 hours.

We propose the following mechanism for anisotropic silver overgrowth within the gap of gold nanocube dimers: After ligand removal, the repulsive steric hindrance between nanocubes is eliminated. This allows attractive van der Waals forces to dominate. During the solvent drying stage, capillary forces further assist in bringing the nanocubes closer together. This process illustrated in in Figure 4.13. In some dimers, this results in gap collapse, which can be attributed to a thermodynamic drive to minimize the surface-to-volume ratio and thus lower the system's free energy.

In many cases, the gap narrows but remains open, often stabilizing within the 0.6 to 1.3 nm range. This range is hypothesized to favor anisotropic elongation rather than dimer fusion. In contrast, when the interparticle distance contracts below a lower critical threshold, which is not yet precisely determined, the system tends to promote nanocube welding during silver overgrowth (see Figure 4.3a). This raises an important question: why does a nanogap persist in many dimers instead of fully collapsing? We believe that this is because, at one point, the interaction between the nanocube and the substrate may become stronger than the attractive forces between adjacent nanocubes, effectively immobilizing them before full contact occurs. We propose that during ligand removal and solvent drying, as the nanocubes move closer together, the ligand layer (e.g., PVP) between the nanocubes and the substrate becomes thinner. This brings the nanocubes closer to the substrate, increasing their interaction and reducing their lateral mobility, as previously reported by Capitaine and co-workers[78]. This mechanism likely accounts for the persistence of a stable gap in many dimers.

When a gold nanocube dimer with an interparticle gap in the range of approximately 0.6 to 1.3 nm is immersed in the welding solution, the first uncertainty lies in whether this gap distance changes significantly upon contact with the solution. Assuming the gap remains relatively stable, both chloride ions and PVP molecules, which are known to adsorb onto the (100) facets of gold and silver surfaces [190], will interact with the nanocubes. However, due to its bulky polymeric structure, PVP is sterically hindered from penetrating the narrow gap between the nanocubes. In contrast, chloride ions, with a much smaller ionic radius (approximately 1.81 Å) [191, 192], are able to enter and adsorb within this confined space.

As a result, the outer surfaces of the dimer are likely capped by both PVP and chloride ions, whereas the internal gap is passivated primarily by chloride ions. Within the gap, each gold surface is capped with a layer of adsorbed chloride ions, followed by a diffuse layer of counterions such as Ag^+ or H_3O^+. Due to the confined geometry, bulky counterions like CTA^+ are unlikely to enter the gap efficiently. Because the gap is so narrow, the diffuse layers from each nanocube's surface overlap, generating a repulsive interaction between the surfaces. This repulsion can be attributed to two primary mechanisms. First, the electrostatic repulsion arises from the like-charged surfaces of the nanocubes, leading to Coulombic forces that oppose further approach. Second, the osmotic pressure between overlapping double layers leads to an entropic repulsion: the confined ion-rich environment within the gap generates a chemical potential imbalance relative to the bulk, which produces an effective pressure pushing the nanocubes apart. In other words, this crowding creates an imbalance compared

to the bulk solution, which the system 'resolves' by keeping the nanocubes apart. This repulsive interaction within the confined gap might explain the presence of a physical barrier that prevents welding while still promoting directional silver growth.

During the overgrowth process, there are few possible overgrowth scenarios. The first scenario is that cationic Ag^+ ions within the diffuse layer are directly reduced to metallic Ag^0 and deposited onto the surface. However, due to the relatively bulky structure of ascorbic acid, which serves as the main reducing agent in this system, it is unlikely that it can efficiently access the confined nanogap to perform this reduction.

The second scenario is that Ag^+ ions are reduced by ascorbic acid in the bulk solution, forming neutral Ag^0 atoms or small clusters. These species then preferentially deposit within the nanogap, where the gold surfaces are less protected, being capped only by chloride ions. The deposition of these adatoms may proceed through different pathways. They may be directly incorporated onto the {100} facets within the gap, or initially deposited onto more exposed facets such as {110} or {111}, followed by surface diffusion toward the {100} facets. This mechanism is consistent with the overgrowth behavior described by Younan Xia and co-workers [193]. In contrast, the outer facets of the nanocubes are more strongly passivated by both PVP and chloride ions, which suppresses deposition on those surfaces. Consequently, silver preferentially accumulates inside the gap, likely growing on the {100} facets in a quasi-monolayer fashion.

A third scenario was recently proposed by Younan Xia's group, who described a distinct mechanism for silver overgrowth on nanocubes in the presence of PVP, CTAC, and ascorbic acid [194]. This mechanism contrasts with the previously considered first and second scenarios. According to their findings, Ag^+ ions initially associate with Cl^- ions to form AgCl [194]. In our system, such AgCl complexes could plausibly form within the nanogap, where both opposing surfaces are Cl^--terminated, with Ag^+ ions serving as counterions. Upon addition of ascorbic acid, the gold nanocubes, acting as electron acceptors, become electron-enriched and gaining additional electron density relative to their initial state. This increased electron density enables the nanocube surfaces to reduce Ag^+ from the AgCl complexes into metallic silver, facilitating site-selective overgrowth, particularly within the confined gap region.

As silver continues to nucleate within the nanogap, the interparticle distance narrows and repulsive forces, primarily arising from the overlap of electrical double layers, begin to increase. When these forces exceed the adhesion between the nanocubes and the substrate, the particles are pushed apart. This leads to an elongated structure with a thickened silver shell concentrated in the gap region. We envisage that this movement is not continuous, but instead occurs in discrete steps as the buildup and release of stress drives the mobility. Observing this process directly or indirectly using in situ imaging techniques or spectroscopy would offer valuable insights.

4.2.2.4. Attempts on operando spectroscopy experiment

We attempted to perform operando spectroscopy to monitor the anisotropic overgrowth process, using a homemade setup shown in Figure D.8. In the first experiment, silver nanocube colloidal solution was drop-cast onto a clean thin glass slide. After drying, we conducted SEM imaging to locate specific dimers on the substrate, as shown in Figure 4.16b. Once identified, the sample was fixed onto the holder and vial (Figure D.8, top) using PDMS. The PDMS was cured by placing the entire setup in an oven at 80 °C for 5 minutes. Following curing, we carried out the ligand removal step using a $NaBH_4$ solution, followed by thorough rinsing with water to minimize residual $NaBH_4$. The setup was then mounted onto the microscope for optical measurements, as illustrated in Figure D.8.

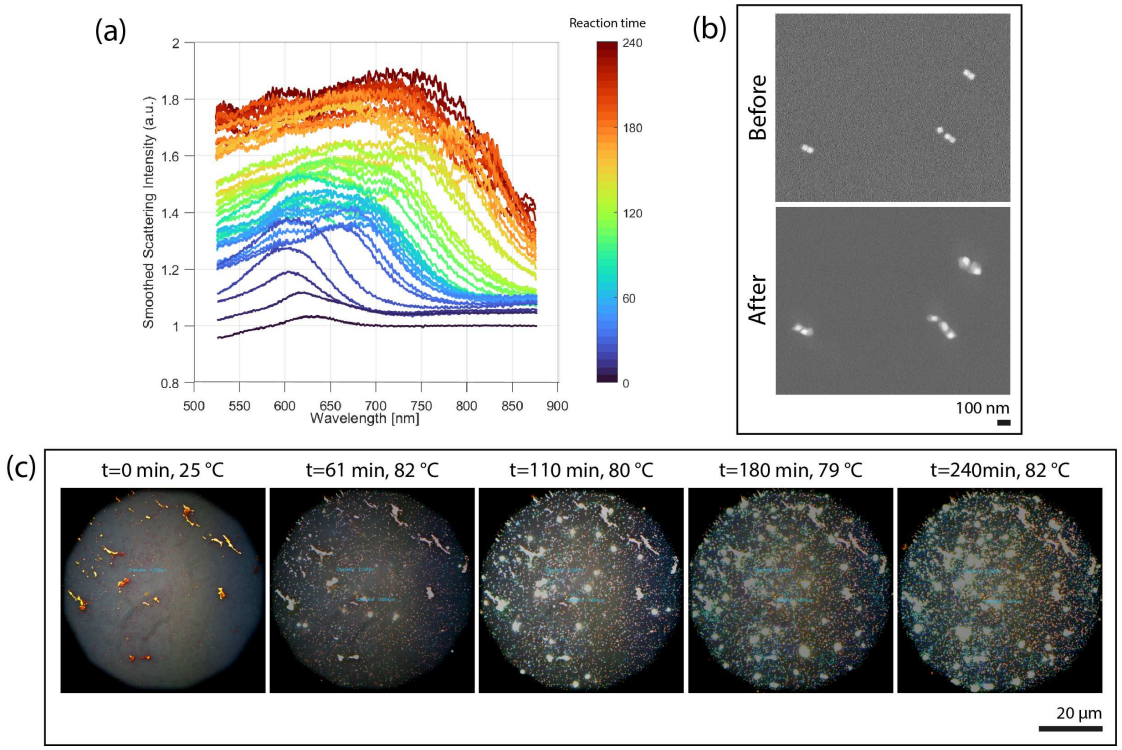

Figure 4.16.: First operando spectroscopy experiment of anisotropic overgrowth: (a) Collective scattering spectra of the nanostructures shown in (b). (b) SEM images of the nanostructures before and after overgrowth. The "after" SEM image shows strong warping artifacts, likely due to charge accumulation. (c) Optical images of the sample taken at different reaction times.

In this experiment, a mixture of 1 mL PVP (50 mg/mL) and 9 mL CTAC (20 mM) was preheated at 80 °C for approximately 20 minutes. Unlike the typical overgrowth procedure, we manually added the preheated solution, silver precursor, and reducing agent all at once without using a syringe pump. The reaction was carried out without stirring, and the vial was intentionally left open, unlike the standard closed-vial setup. It is important to note that leaving the vial open led to significant evaporation of

the solution over time. The reaction was conducted while periodically recording the collective scattering spectra and optical images of the selected nanostructures (shown in Figure 4.16b). The temperature controller was set to approximately 85 °C; however, we observed large fluctuations in the peltier-measured temperature, ranging between 78-82 °C. It should also be noted that this measured temperature does not represent the actual solution temperature.

As shown in Figure 4.16a, the scattering spectra exhibited a progressive red-shift over the 240-minute reaction, which we attribute to overall size increases of the nanostructures. Although we believe anisotropic overgrowth occurred, the resulting aspect ratio was very small. Furthermore, significant secondary nucleation was observed on both the substrate and in solution (Figure 4.16c). We deduce that several factors contributed to these: the horizontal positioning of the sample (allowing gravity to deposit larger particles onto it), the lack of controlled precursor injection due to the absence of a syringe pump, the absence of stirring, and evaporation, which likely increased the precursor concentration over time. Additionally, we suspect that exposure to the electron beam during SEM correlation might have altered the surface properties of the nanocubes, thereby affecting the subsequent overgrowth behavior.

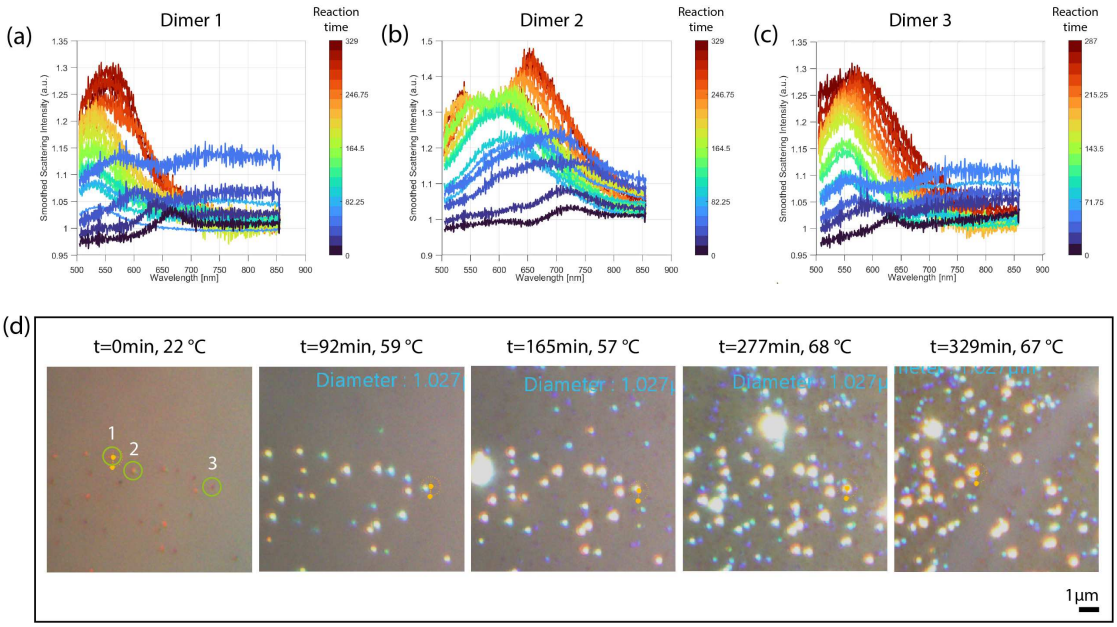

Figure 4.17.: Second operando spectroscopy experiment on anisotropic overgrowth: (a), (b), and (c) Scattering spectra corresponding to assumed individual dimers (Dimer 1, Dimer 2, and Dimer 3), associated with the structures shown in (d). (d) Optical images of the sample taken at various reaction times.

In the next experiment, we aimed to improve the experimental conditions. First, we introduced a syringe pump to deliver the silver precursor and reducing agent in a controlled manner, mimicking the typical reaction in oil bath. Second, we incorporated a peristaltic pump to circulate the solution inside the vial, mimicking a stirring effect.

We also sealed the vial with parafilm to minimize evaporation. Unlike the previous experiment, where we used drop-cast gold nanocubes, here we used transfer-printed assemblies prepared by capillary assembly. Furthermore, instead of monitoring collective spectra from multiple dimers, we focused on tracking what we suspected to be individual dimers: Dimer 1, Dimer 2, and Dimer 3 (see Figure 4.17d). However, we did not perform SEM correlation prior to the overgrowth, so the exact initial structure was not confirmed.

During the reaction, we observed that the temperature measured by the Peltier stage was significantly lower than in the first experiment. This temperature drop was due to the use of the peristaltic pump: the circulating solution, exposed to ambient conditions outside the heating system, cooled down before re-entering the vial, thereby lowering the overall reaction temperature. The measured temperatures ranged from approximately 56 to 68°C. When we stopped the peristaltic pump, the temperature gradually rose, confirming this hypothesis.

Throughout the experiment, scattering spectra were recorded periodically. As shown in Figures 4.17a, 4.17b, and 4.17c, the general trend was a progressive blue shift of the scattering peaks as the reaction progressed. This behavior contrasts with the red shift observed in the first experiment and suggests different growth dynamics. Unfortunately, we were unable to confirm the final nanostructures by SEM imaging. It is possible that the structures were removed during post-reaction rinsing, or that the high density of secondary nucleation on the substrate made it difficult to locate the dimers of interest (Figure 4.17d). Additionally, we observed that Dimer 3 disappeared from the optical images at t = 329 minutes, leaving behind scratch-like marks on the substrate. This damage likely resulted from vigorous manual spraying during the reaction, which was intended to remove excess secondary nuclei but may also have dislodged the fragile nanostructures.

We found that performing operando observations of anisotropic overgrowth is extremely challenging, particularly when attempting to replicate the typical reaction conditions of an oil bath. So far, the results remain inconclusive. Future improvements could include integrating a stirring system into the setup to better mimic standard conditions, as well as optimizing the sample preparation before overgrowth. In particular, it will be important to address the effects of heating during PDMS curing, which may alter the sample compared to conventional reaction protocols.

4.2.2.5. Designer complex nanostructures from anisotropic overgrowth

Based on our hypothesis that silver growth occurs within the nanogap following the first mechanism illustrated in Figure 4.12a, we propose a rule of design for creating more complex nanostructure geometries. In this framework, the nanogap acts as a critical guiding feature that directs the growth, resulting in final architectures that may significantly differ from the initial seed configurations. Figure 4.18 illustrates this rule of design using observed structures from substrate-based assemblies. In Figure 4.18a, when a nanocube is placed face-to-face with another nanocube along

one of its face, silver overgrows within the gap, producing an elongated nanostructure with both cores located at the ends of the final structure. When a central nanocube is aligned face-to-face with two neighboring nanocubes on opposite sides, as shown in Figure 4.18b, silver overgrowth occurs in both gaps. This results in an elongated nanostructure where the outer nanocubes shift outward and become the tips of the final structure, while the central nanocube remains in its original position.

A more intricate scenario is shown in Figure 4.18c, where three nanocubes form an L-shaped configuration. The central nanocube is face-to-face with two neighboring cubes at a 90° angle. The central cube undergoes simultaneous overgrowth on both aligned faces, creating a square structure with the core at the outer corner. Each neighboring cube grows only on its facet facing the central cube. This leads to an elongated L-shaped nanostructure, with a geometry distinctly different from the original seed layout.

Further complexity is demonstrated in the U-shaped arrangement of five nanocubes (Figure 4.18d), where the overgrowth behavior is essentially a combination of the rules illustrated in Figures 4.18b and 4.18c, leading to an expanded U-shaped structure. In the case of a cross-shaped configuration (Figure 4.18e), a central nanocube is surrounded face-to-face by four neighboring nanocubes. Symmetric overgrowth occurs on all four faces of the central cube, forming a square-like extension with the gold core remaining at the center. Each adjacent nanocube grows only on the side facing the central one, resulting in an expanded cross-shaped architecture.

Lastly, when four nanocubes are arranged in a 2×2 diamond shape, each cube shares 90° face-to-face alignment with its two neighbors. Overgrowth occurs on both aligned faces, pushing all nanocube cores outward. The final structure features four gold cores positioned at the corners of a larger diamond-shaped nanostructure.

So far, we have discussed a variety of cases in which one face of a gold nanocube is aligned face-to-face with another (Figure 4.18a), two faces are aligned with two neighbors (Figures 4.18b and 4.18c), and four faces are engaged with adjacent nanocubes (Figure 4.18e). However, we have not yet addressed what might occur when three faces of a nanocube are in face-to-face with three neighboring cubes. Although we have not captured experimental images of nanostructures resulting from this specific configuration, our understanding of the anisotropic overgrowth mechanism allows us to propose a reasonable prediction. In such a case, we anticipate that silver would grow outward from all three connected faces, generating an extended T-shaped nanostructure, as illustrated in Figure 4.18g.

Overall, this design rule highlights how nanocubes can undergo symmetric or asymmetric overgrowth depending on the number and orientation of neighboring particles. Altogether, these observations reinforce the concept that interparticle gaps can act as physical guides that direct the morphology of the final nanostructure. This supports the broader potential of anisotropic overgrowth as a programmable design strategy, enabling the fabrication of complex, monocrystalline nanostructures by combining templated self-assembly with wet-chemical processing. Notably, it is also intriguing to consider that nanogaps may be partially preserved within the final structures. This

feature could be valuable for nanogap engineering, where confined electromagnetic fields or chemical reactivity are desired.

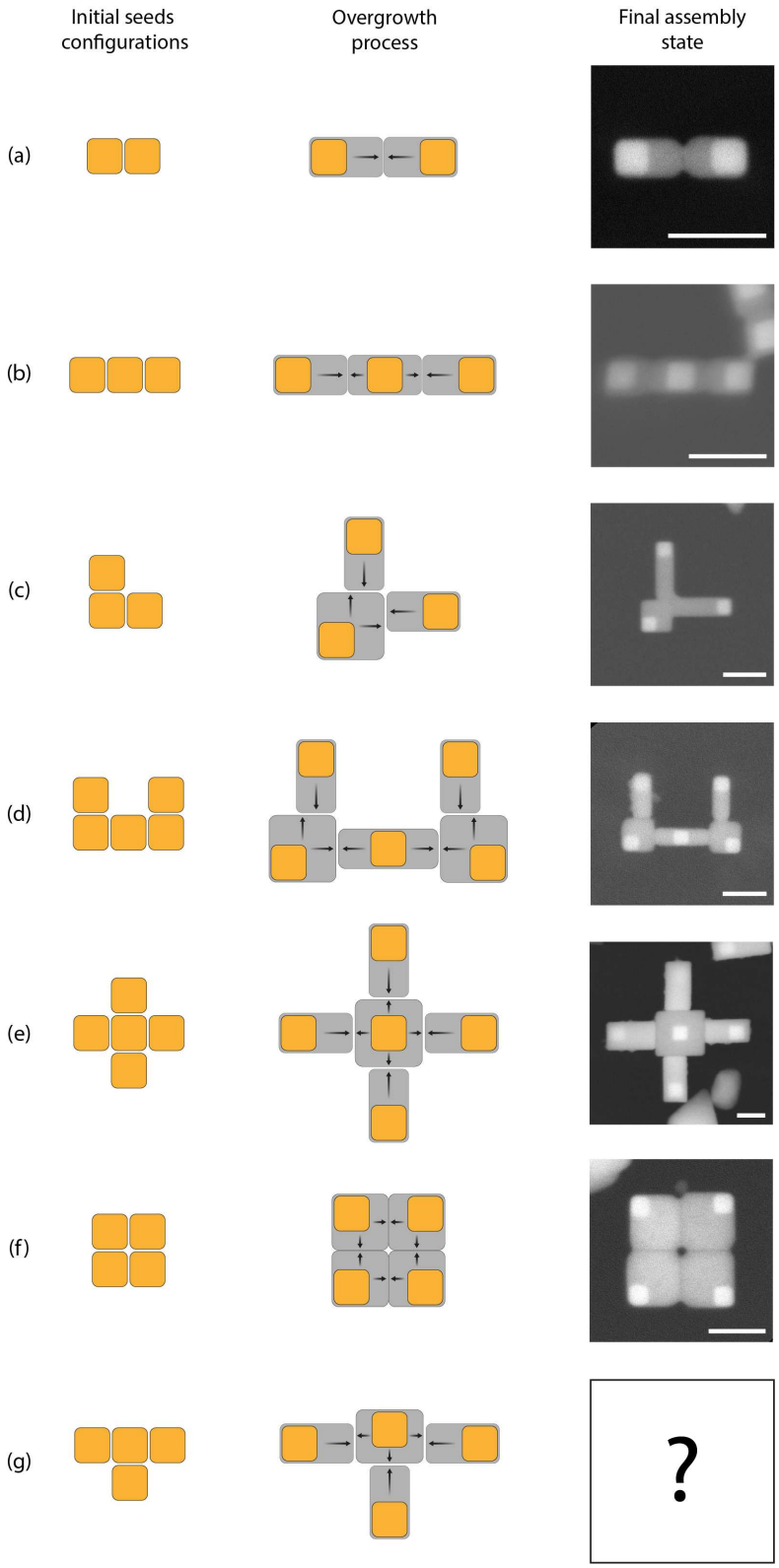

Figure 4.18.: Design rules for anisotropic silver overgrowth on gold nanocubes. Scale bars are 100 nm in length.

One can deduce from Figures 4.18a and 4.18f that the rate of silver overgrowth is comparable across all gold nanocubes involved. For example, in the simple dimer geometry (Figure 4.18a), the resulting nanostructure shows that the silver-coated regions on both sides of the gap are nearly identical in size, suggesting that silver overgrowth proceeds at a similar rate on each nanocube. However, the situation becomes more complex in asymmetric geometries such as those shown in Figures 4.18b, 4.18c, 4.18d, 4.18e, and 4.18g, where the number and orientation of nanogaps vary across nanocubes. To investigate this, we used L-shaped configuration (Figure 4.18c) as an example, where two nanocubes are aligned to the central nanocube at a 90° angle, such that they each undergo overgrowth on a single facet, while the central nanocube grows on two adjacent facets.

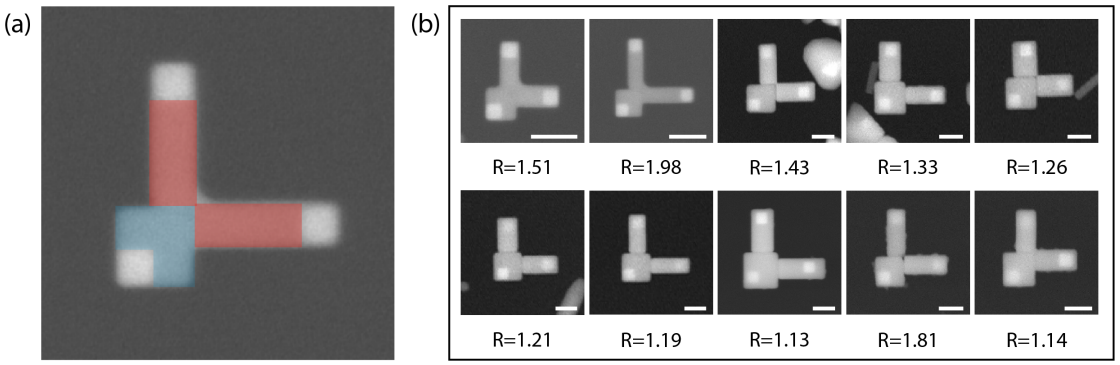

Figure 4.19.: (a) Illustration showing the shaded regions used to calculate the area ratio (R) between the overgrown sections associated with the side nanocubes (red) and the central nanocube (blue). (b) SEM images of ten randomly selected overgrown L-shaped nanostructures, along with their corresponding R values. Scale bars represent 100 nm.

To evaluate whether the silver growth rate is consistent across different nanocubes in this configuration, we approximated the area of the overgrown regions associated with the side nanocubes (red) and the central nanocube (blue), as shown in Figure 4.19a. If silver overgrowth occurred uniformly across all nanocubes, the area ratio (R) of red to blue would be close to 1. However, as illustrated in Figure 4.19b, measurements from more than ten randomly selected nanostructures grown under varying experimental conditions consistently show R values greater than 1. This indicates that silver overgrowth proceeds more rapidly on the side nanocubes than on the central one. We hypothesize that this disparity arises from differences in nanoparticle–substrate contact area. The central nanocube appears to have a larger contact area with the substrate, in this case, approximately twice that of each side nanocube. This stronger interaction may hinder its ability to shift during growth, which in turn limits the rate of silver overgrowth on the gap.

By tilting the SEM stage during imaging, we observed that silver overgrowth does not occur solely within the nanogap in the horizontal direction parallel to the substrate

surface. As shown in Figure 4.20, high aspect ratio growth also appears to extend vertically, between the nanocube cores and the substrate, resulting in structures with a thickness greater than that of the original nanocube seeds. However, a detailed investigation into the vertical component of silver overgrowth has not yet been conducted. Further studies will be necessary to fully understand this growth behavior.

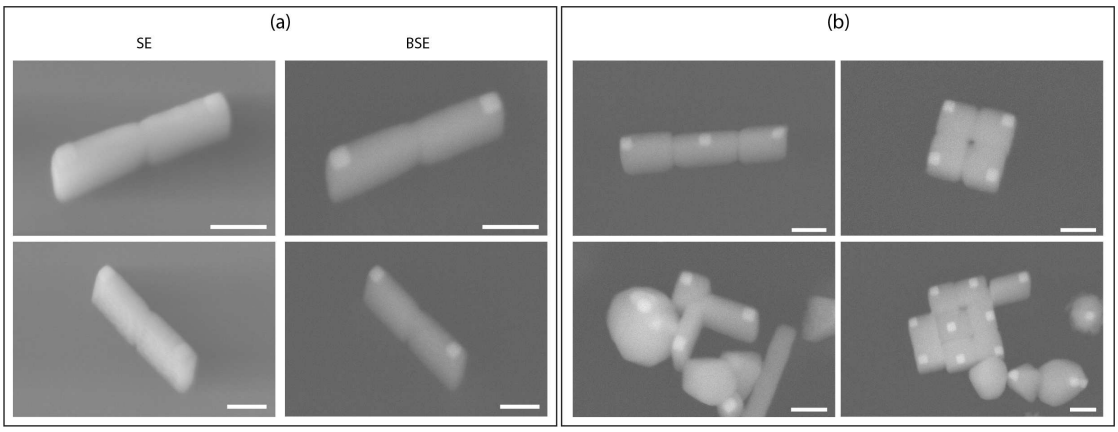

Figure 4.20.: SEM images of overgrown nanostructures captured at a 25° tilt. (a) Comparison of contrast between images acquired using secondary electron (SE) and backscattered electron (BSE) detectors. (b) Additional tilted-view images taken with the BSE detector. Scalebars are 100 nm in length.

4.2.2.6. Control experiments

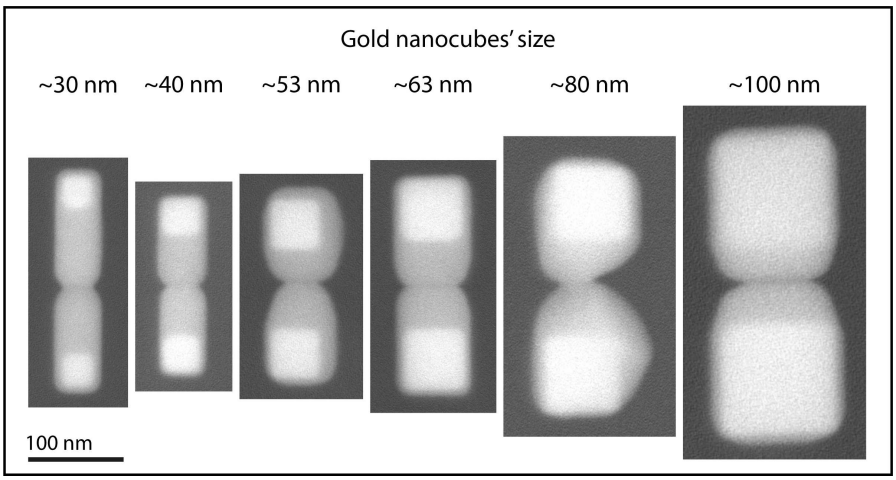

Figure 4.21.: SEM images of silver overgrowth on gold nanocube dimers for 3 hours with varying cube sizes.

We also attempted silver overgrowth on drop-cast gold nanocubes of varying sizes. Although a full statistical analysis has not yet been conducted and the results remain

preliminary, selected SEM images in Figure 4.21 suggest a trend. It appears that while overgrowth within the nanogap occurs across all tested core sizes, the extent of silver elongation is reduced as the nanocube size increases, leading to lower aspect ratios under identical reaction conditions. We hypothesize that this may be attributed to two factors: first, larger nanocubes have greater surface area, requiring more silver atoms to achieve the same degree of elongation; second, the increased size may result in stronger interactions with the substrate, which could hinder displacement or directional growth.

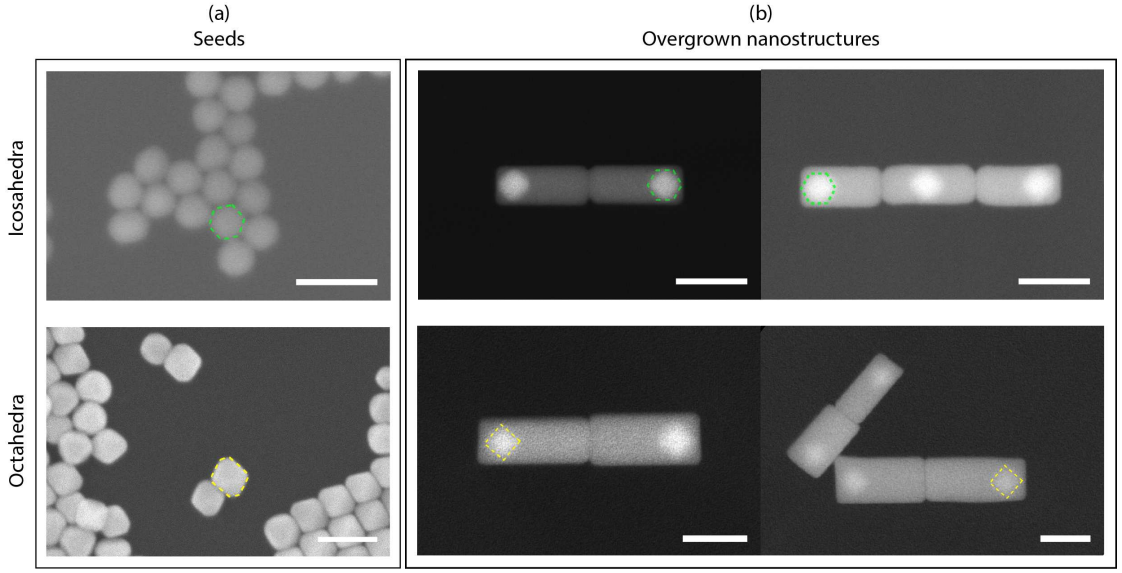

Figure 4.22.: Silver overgrowth on gold icosahedra and octahedral nanoparticles. Scale-bars are 100 nm in length.

Moreover, we explored replacing gold nanocubes with other shapes, specifically gold octahedra and gold icosahedra (Figure 4.22). In both cases, anisotropic silver overgrowth was observed, resembling the behavior previously seen with nanocubes. Interestingly, SEM images suggest that the sharp features of these polyhedral particles tend to align along the direction of elongation, rather than their flat facets. While nanoparticles typically assemble with their flat surfaces in contact, the final overgrown structures indicate that some degree of reorientation may occur during the early stages of the reaction. One plausible explanation is that, upon exposure to silver growth conditions, the particles undergo slight rotation, gradually aligning their (100) facets as those surfaces expand. This behavior can be attributed to the presence of selective capping agents (PVP and chloride ions), which adsorb preferentially on the (100) facets of gold. Their adsorption lowers the surface free energy of the (100) planes relative to other facets, resulting in faster growth along directions other than ⟨100⟩[193]. As a consequence, the relative area of the (100) facets increases during the reaction, causing a morphological evolution from icosahedra to octahedra, then to cuboctahedra, truncated cubes, and ideally to cubes enclosed entirely by (100)

facets[193]. Only after this transformation would anisotropic elongation likely proceed. Nevertheless, this remains a working hypothesis. Further investigation is required to determine whether this facet-selective reorientation truly underpins the anisotropic overgrowth observed in non-cubic gold seeds.

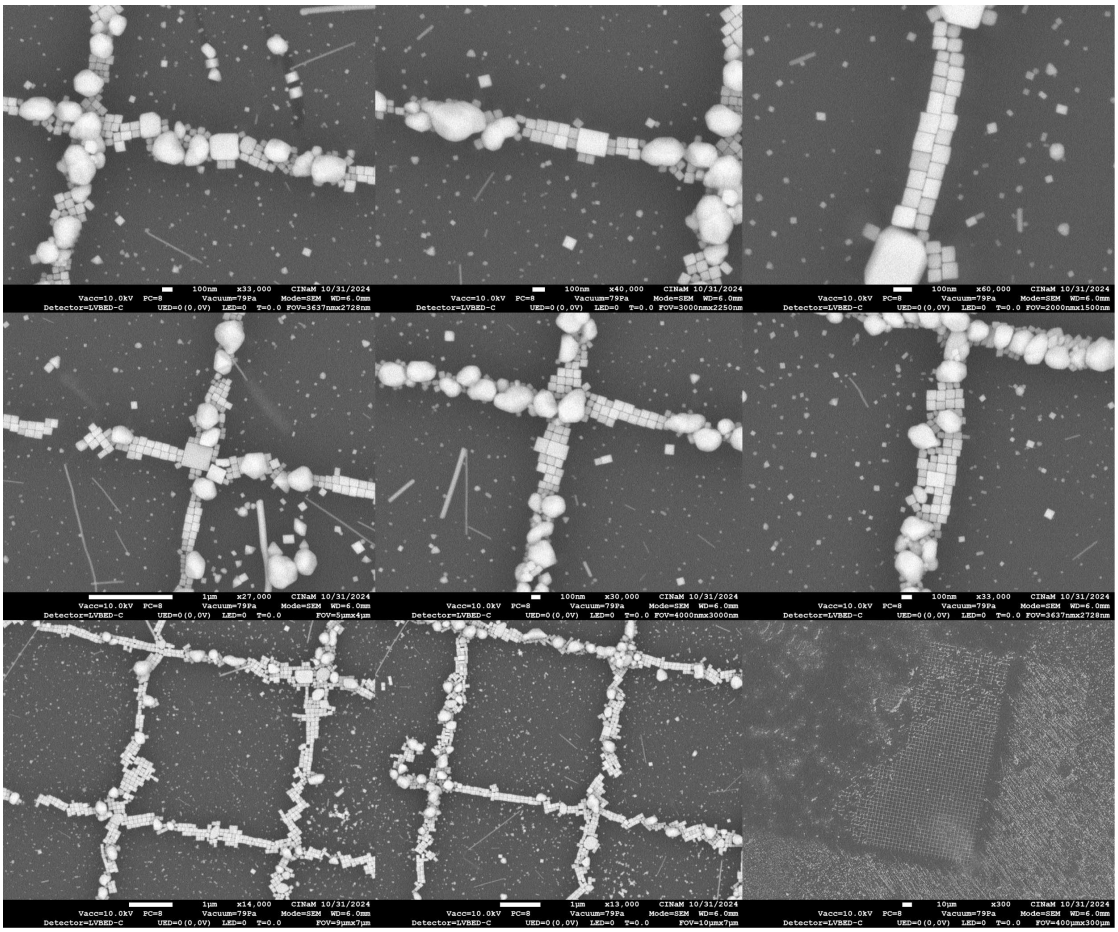

Figure 4.23.: Silver overgrowth at 80°C on 55 nm silver nanocubes arranged in a grid pattern via nanoparticle imprint lithography.

Figure 4.23 shows the application of this overgrowth approach to 55 nm silver nanocubes arranged in a grid pattern using nanoparticle imprint lithography. The results reveal that silver overgrowth enlarged most individual nanocubes to nearly 100 nm in size, even though secondary nucleation was observed on the substrate. Interestingly, instead of promoting nanocube welding into continuous grid lines, the expansion of individual nanocubes appears to exert lateral pressure on neighboring particles. This strain disrupts the grid's original linear alignment, often causing it to break into zigzag or misaligned segments. However, in certain regions where, we assume, the initial spacing between nanocubes was likely very tight, overgrowth successfully fused the particles into larger, smooth, and sharp-edged cubic structures. These fused structures are presumed to be monocrystalline, given their uniform

appearance and well-defined morphology.

4.3. Conclusion

In this chapter, we explored a strategy for growing a silver shell on substrate-supported nanocubes. It was initially aimed at achieving epitaxial welding through a controlled overgrowth process by adapting a well-established colloidal core–shell synthesis method. Although optimal conditions for consistent welding were not fully achieved, we observed that silver overgrowth on nanocube assemblies could lead to two distinct outcomes: nanowelding and anisotropic elongation. Interestingly, with the presence of PVP in the solution, silver preferentially elongated within the interparticle gap without bridging the cores, forming high-aspect-ratio nanostructures. This behavior contrasts with previous findings discussed in Chapter 3, where nanogaps facilitated welding through electrostatic interactions. Here, our observations suggest that the initial nanogap might play a critical role in determining the growth mode, either interconnection welding or acting as a directional template that guides anisotropic growth. To investigate this further, we used nanocube dimers as a model system and conducted parametric studies by varying reaction time, PVP concentration, temperature, seed size, and particle shape. These experiments suggest that the same principle could be extended to design more complex nanostructures beyond simple dimers. Although the exact mechanism is not yet fully confirmed, the framework established here opens new design approach for fabricating complex nanostructures in which the interparticle gap serves as a physical guide for directional growth. These findings offer not only insights into nanocrystal interface engineering but also provide a platform for developing monocrystalline architectures that could be integrated into functional optoelectronic metasurfaces.

5. Perspectives - Sharp-cornered aluminum octopods via anisotropic nanocube etching

Metallic nanoparticles exhibit a wide variety of shapes. Among these, nanoparticles with sharp features such as nanostars or branched structures are of particular interest because they can concentrate electromagnetic fields at their tips, resulting in strong local field enhancement. This effect makes them especially promising for ultrasensitive molecular detection using techniques like Surface-Enhanced Raman Scattering (SERS). Aluminum nanoparticles are particularly attractive due to their broad plasmonic tunability, which spans from the ultraviolet to the infrared spectral range, a feature not achievable with more commonly used gold and silver counterparts. In this work, we introduce a preliminary result of wet-etching approach to fabricate sharp aluminum nanooctopods from substrate-supported aluminum nanocubes. By using a chromic-phosphoric acid solution, we demonstrate that tip formation can be precisely controlled by varying the etching time. The resulting branched nanostructures show good potential as efficient SERS substrates. This method provides a route for engineering aluminum nanostructures with enhanced optical functionalities.

Summary

5.1. Introduction 149
5.2. Results and discussion 150
5.2.1. Effort toward nanocube epitaxial welding and observation of anisotropic etching 150
5.2.2. Formation of aluminum octopods with adjustable degree of branching 152
5.2.3. Characterization of aluminum octopods 155
5.2.4. Preliminary assessment of aluminum octopods for SERS 158
5.3. Conclusion 159

5.1. Introduction

Metallic nanoparticles exhibit a wide variety of shapes, each bringing unique physical and optical characteristics that make them attractive for a broad range of applications. Simple morphologies include spheres, rods, cubes, octahedra, and more complex geometries such as bipyramids and platelets. Among these, nanoparticles with sharp features, such as nanostars or branched structures, have attracted particular attention[195], primarily due to their ability to strongly concentrate electromagnetic fields at their pointed tips[196]. This localized field enhancement is especially beneficial for applications like Surface-Enhanced Raman Scattering (SERS), where molecules positioned near these tips can experience significantly amplified Raman signals. As a result, sharp-featured nanoparticles are considered highly promising for ultrasensitive molecular sensing platforms[197].

Typically, SERS substrates can achieve enhancement factors (EFs) in the range of 10^5 to 10^6[22]. In some cases, even higher EFs (up to 10^8–10^{10}) have been reported[25, 198, 199]. However, it is important to recognize that debate persists regarding the accurate measurement and comparison of SERS-EF values. For example, the determination of SERS-EF often relies on assumptions, such as the precise surface concentration of adsorbed molecules, which can introduce substantial errors. Furthermore, direct comparisons across substrates that present with different characteristics, such as dynamic colloidal suspensions versus immobilized static nanostructures, can be misleading[200, 201].

Gold and silver nanoparticles with well-defined shapes and sizes are widely utilized as SERS substrates, largely due to the maturity of their synthetic protocols. Their synthesis commonly involves seeded-overgrowth methods, where precise control over particle size and shape is achieved using specific surfactants or capping agents. In contrast, aluminum nanoparticles remain comparatively underexplored. Currently, the typical approach for aluminum nanoparticle synthesis involves the catalytic decomposition of organoaluminum compounds based on aluminum hydrides (AlH_3), using titanium-containing catalysts [24, 25, 202, 203]. Unlike gold and silver precursors, aluminum precursors are generally pyrophoric and extremely sensitive to air and moisture, significantly complicating their handling and synthesis. Consequently, during the early stages of my PhD, I constructed a dedicated Schlenk line system to synthesize aluminum nanoparticles under controlled inert conditions.

Aluminum nanoparticles are particularly interesting not only because of their low cost, but also due to their tunable plasmonic resonance, which spans a broad spectral range from the ultraviolet (UV) to the infrared (IR), depending on the particle's shape and size[24, 25, 203]. This makes aluminum an attractive alternative to the more commonly used gold and silver nanoparticles, which are significantly more expensive and typically exhibit plasmonic responses limited to the visible or near-infrared range. However, unlike gold or silver, aluminum poses a challenge due to its naturally passi-

vated surface. Aluminum nanoparticles are stabilized by a native oxide shell, typically 3-5 nm thick, which protects the underlying metallic aluminum [Al(0)] from further oxidation[203]. This thin oxide surface layer can be seen as quite advantageous for SERS. This is because nanoscale surface oxide layers can provide binding sites for a variety of functional groups such as carboxylic/phosphoric acids, silanes, and amides, providing very different molecule-substrate interactions compared to conventional gold or silver counterparts[24].

Colloidal synthesis of aluminum octopods has previously been reported[202], though the resulting structures in overall lacked narrow branching, and strategy for tuning the sharpness of the branches was not reported. In this work, we present an alternative approach to fabricate sharp-cornered aluminum nanooctopods by chemically etching substrate-supported aluminum nanocubes. This method enables control over tip formation by simply varying the etching time. We employed a chromic-phosphoric acid solution as the etching agent, which is known to selectively remove the native oxide layer with minimal attack on the underlying metallic aluminum core[204]. This approach offers an alternative route for producing sharp aluminum nanostructures, particularly as potential platforms for Surface-Enhanced Raman Scattering (SERS) applications.

5.2. Results and discussion

5.2.1. Effort toward nanocube epitaxial welding and observation of anisotropic etching

This chapter was initiated with the initial intention of achieving epitaxial welding of aluminum nanocubes. As discussed in Chapter 1, several studies have demonstrated the epitaxial welding of metallic nanocubes, including silver nanocubes through overgrowth using Tollens' reagent[11]. However, applying such overgrowth strategies to aluminum is significantly more challenging. Aluminum nanocubes are naturally coated with a thin oxide layer, which must be selectively removed before new material can be deposited. Moreover, the entire process must be carried out under strictly inert conditions (O_2- and H_2O-free) to avoid rapid reformation of the oxide. These challenges are combined by the fact that most aluminum precursors are pyrophoric and highly sensitive to air. Other welding strategies have been reported for gold nanocubes, such as controlled dissolution followed by sequential overgrowth within the nanogap[1]. In Chapter 3, we also explored a silver welding method that involved atomic etching at the corners and edges of nanocubes, with redeposition into the nanogap driven by electrostatic forces.

With these considerations in mind, we initially investigated whether bare aluminum nanocubes (stripped of capping ligands and their native oxide layer) could naturally coalesce and weld when in close contact in solution. To explore this, we drop-cast ~113 nm aluminum nanocubes onto silicon wafers and exposed them to an available old stock solution of chromic-phosphoric acid (1.8% CrO_3 and 7.1% H_3PO_4), a known

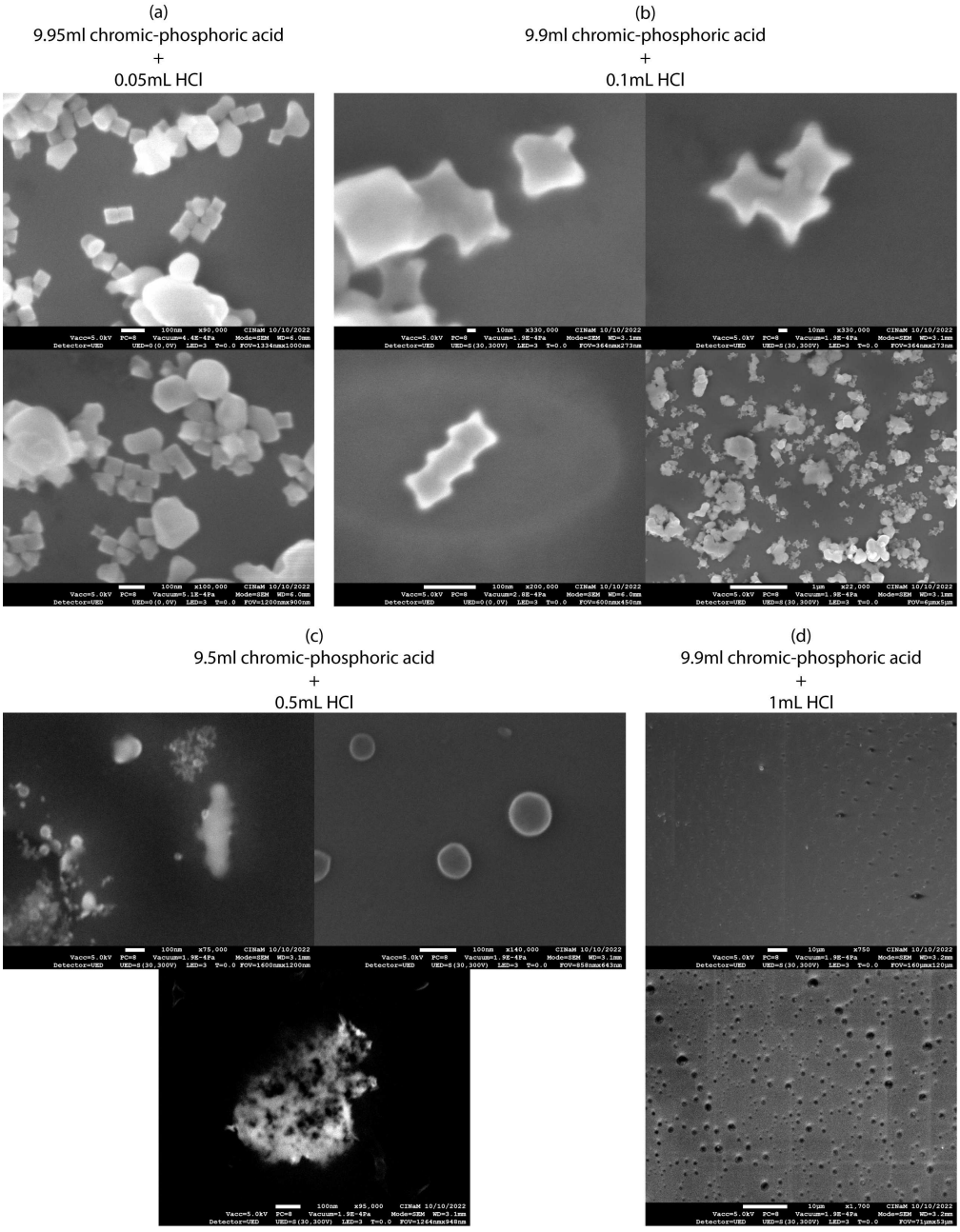

Figure 5.1.: Etching of drop-cast ~113nm aluminum nanocubes on a silicon substrate using a mixture of chromic-phosphoric acid and HCl at various volume ratios. Etching was performed at 85°C for 2 hours.

etchant for selectively removing aluminum oxide[204–210]. As shown in Figure E.2, we performed successive etching cycles on the drop-cast nanocubes. Each cycle consisted of a 1-hour immersion in the etchant, followed by rinsing with water and a 2-minute exposure to air before the next cycle. During the first four cycles, we observed no major morphological changes to the nanocubes. However, size measurements revealed a gradual reduction in nanocube dimensions (approximately 7.5 nm per cycle). Given

that the native oxide layer on aluminum typically ranges from 3 to 5 nm in thickness, we attribute this reduction to progressive removal of the oxide shell. Starting from the fifth etching cycle, we began to observe the development of sharp corners on the nanocubes. Despite this, we found no evidence of nanocube coalescence or welding, even after repeated etching.

In the following experiment, we introduced a small amount of hydrochloric acid (HCl) into the chromic-phosphoric acid solution. The goal was to oxidatively etch aluminum nanocubes in a manner similar to that achieved for silver (Chapter 3) and gold nanocubes[1], with the aim of producing welded final nanostructures. HCl is known to act as a harsher etchant for aluminum[211]. As shown in Figure 5.1, increasing the proportion of HCl resulted in more pronounced etching, leading to nanocubes with sharper, more defined features. Notably, when using a mixture of 9.9 mL chromic-phosphoric acid and 0.1 mL HCl, we observed what appeared to be nanocube welding, as seen in the top-left image of Figure 5.1b. Additionally, some etched nanocubes seemed to self-assemble into interlocked structures. However, despite multiple attempts to repeat the experiment, we were unable to reproduce the observed welding effect. Nevertheless, the result remains encouraging and highlights a promising path forward, although further work is needed to fully develop and optimize the process. To improve reproducibility and better control the etching and welding processes, future experiments should ideally be conducted entirely within a glovebox environment, minimizing the influence of oxygen and humidity.

5.2.2. Formation of aluminum octopods with adjustable degree of branching

To ensure the reproducibility of future experiments, we used a freshly prepared stock of chromic-phosphoric acid. With this new etchant, we compared the degree of etching over time to better understand how the process develops on aluminum nanocubes. As shown in Figure 5.2, we examined the time-dependent etching behavior at different durations, both with and without the addition of HCl. For each condition and each etching duration, we randomly selected 10 nanoparticles from the substrate to observe representative changes. As a result, in Figure 5.2, there is no correlation between one nanocube and another. The particles were chosen independently and do not represent the evolution of a specific nanocube over time. It is also worth noting that some nanostructures appear warped in a few images. This is likely due to sample drift during SEM imaging.

From the figures, there appears to be no significant difference in the etching rates between the samples treated with and without HCl. Etching became noticeable around the 2-hour mark, as evidenced by the formation of small tips at the corners of the nanocubes, which became more pronounced by 3 hours, affecting not only the oxide shell but also the underlying metallic aluminum core. Tilted SEM images captured from various angles confirmed that the nanocubes progressively evolved into octopod-like structures with increasingly sharp corners, as shown in Figures 5.3

and 5.4.

In addition to the etching of aluminum nanocubes, we also observed the formation of tip-to-tip conical nanoparticle dimers, as shown in Figure E.3. We believe these structures result from the anisotropic etching of aluminum nanorods. Such tip-to-tip configurations may be particularly interesting for SERS applications, as they could generate strong near-field enhancements at the junctions.

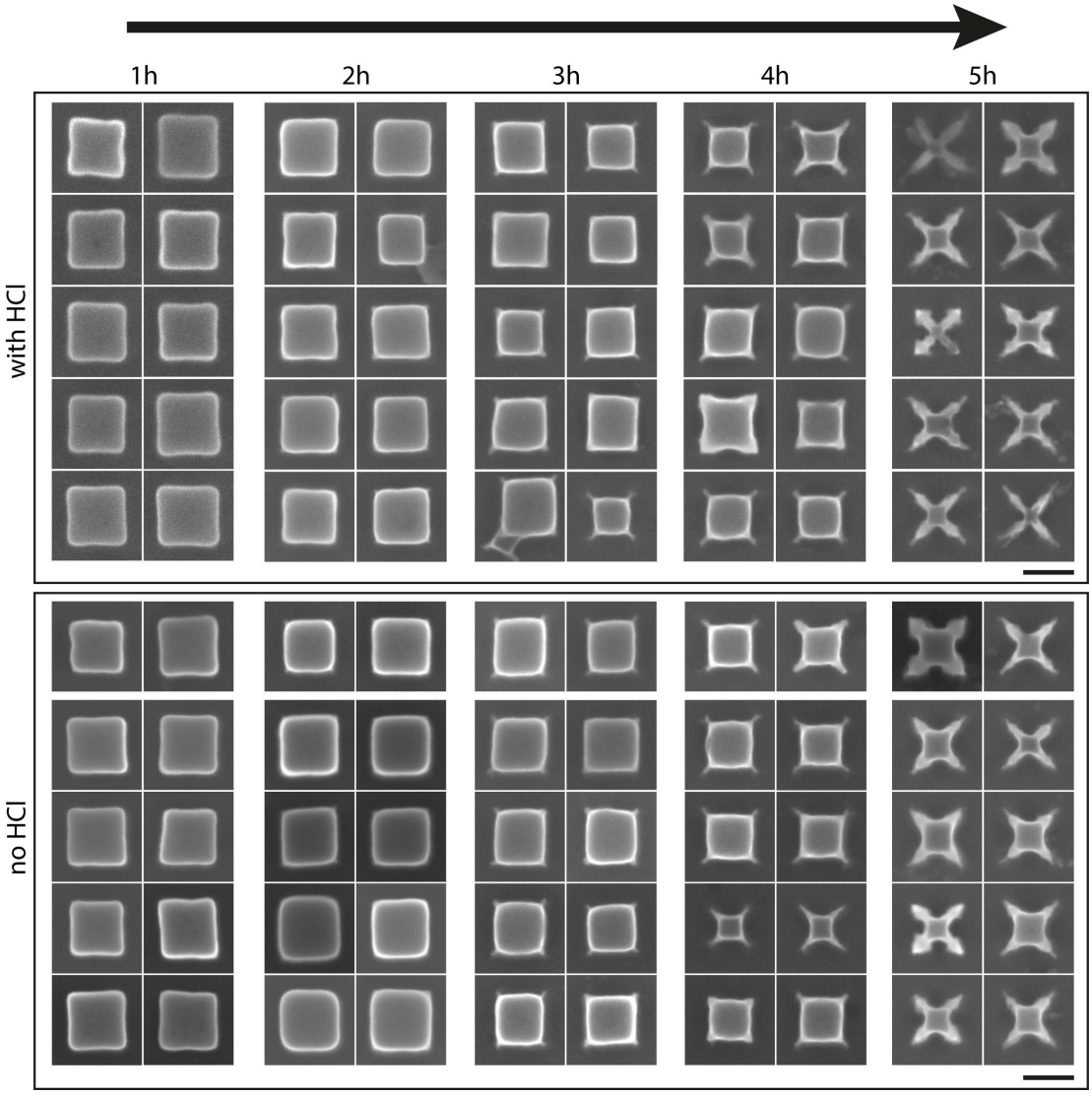

Figure 5.2.: SEM images showing the effect of etching time on ~113 nm aluminum nanocubes drop-cast onto a silicon substrate. Two etching conditions were compared: with HCl (0.4 mL HCl + 9.6 mL chromic-phosphoric acid) and without HCl (10 mL chromic-phosphoric acid), both conducted at 85°C. Scale bars: 100 nm.

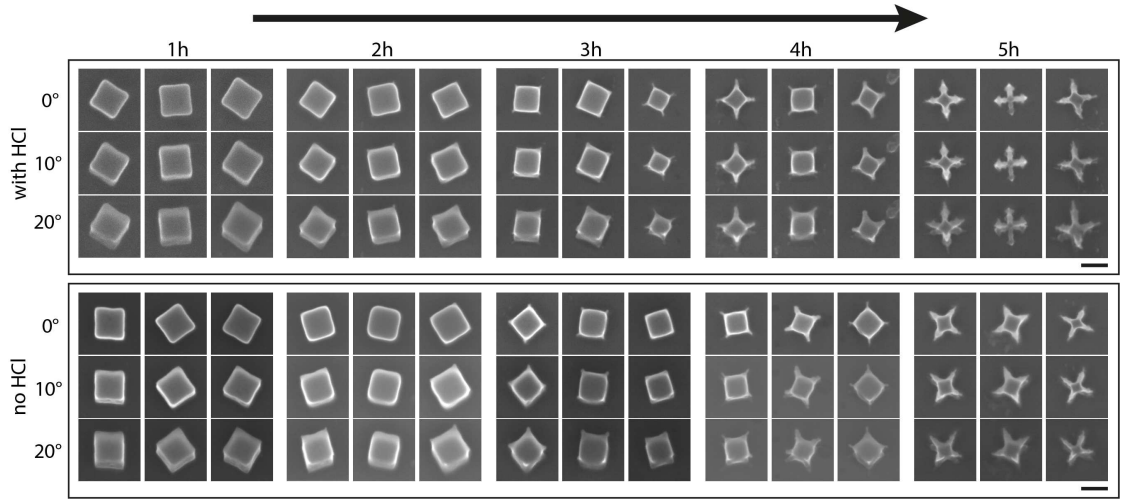

Figure 5.3.: Tilted SEM images showing the morphology of aluminum nanocubes etched at different durations, with and without the addition of HCl. Scale bars: 100 nm.

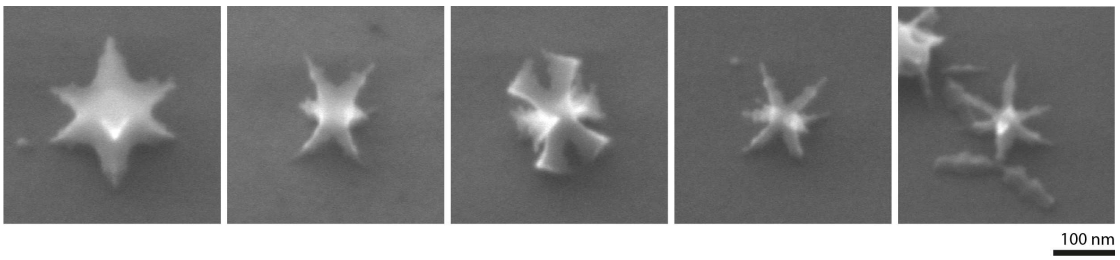

Figure 5.4.: 40° tilted SEM images showing the morphology of aluminum nanocubes after 5 hours of etching in chromic-phosphoric acid without the addition of HCl.

Currently, the detailed etching mechanism remains unclear. One possibility is a cyclic process, where the oxide layer is first etched, exposing the metallic aluminum, which subsequently reoxidizes and is etched again. Alternatively, the process might involve initial oxide layer removal followed by direct etching of the exposed aluminum metal. Several studies have claimed that chromic-phosphoric acid can selectively etch aluminum oxide without attacking the underlying aluminum metal [204–210]. Jowever, if selective oxide etching were the only process, the resulting structures would be slightly smaller aluminum nanocubes due to the self-limited etching of the Al_2O_3 shell, rather than the observed octopod nanostructures. Therefore, the metallic aluminum core must also be somehow etched. Djokić reported that aluminum metal in a chromic-phosphoric acid solution can undergo oxidation via the following reactions [212, 213]:

$$\mathrm{Al} \rightleftharpoons \mathrm{Al}^{3+} + 3\,\mathrm{e}^{-} \tag{5.1}$$

$$2\,Al + 3\,H_2O \longrightarrow Al_2O_3 + 6\,H^+ + 6\,e^- \tag{5.2}$$

In this solution, aluminum oxide can also be etched is given as follows [205]:

$$6\,H^+ + Al_2O_3 \longrightarrow 2\,Al^{3+} + 3\,H_2O \tag{5.3}$$

These oxidation reactions are coupled with reduction reactions, represented as:

$$Cr_2O_7{}^{2-} + 8\,H^+ + 6\,e^- \longrightarrow Cr_2O_3 + 4\,H_2O \tag{5.4}$$

$$2\,H^+ + 2\,e^- \longrightarrow H_2 \tag{5.5}$$

Djokić reported the formation of Al_2O_3 and Cr_2O_3 on aluminum surfaces during treatment with chromic-phosphoric acid. Similarly, Hebert *et al.* stated that at 85 °C, this treatment uniformly dissolves the native oxide layer and subsequently forms a thin chromium oxide passivation film, which is believed to inhibit further oxidation of the underlying aluminum metal [209]. However, this behavior does not appear to apply in our system. If a chromium oxide film were indeed acting as a passivation layer, it would be expected to halt further etching once fully formed. In contrast, our experiments suggest that etching is not self-limiting; instead, it continues with increasing reaction time. Preliminary EDX analysis, conducted over an energy range of 0 to 3.5 keV, did not reveal any detectable chromium signal. Notably, the primary peak associated with chromium appear in the 5 to 6 keV range [214, 215] (see Figure E.4). Therefore, EDX analysis over an extended energy range is necessary to confirm or rule out the presence of chromium oxide on the aluminum surface.

The next question, then, is how this anisotropic etching arises. One plausible explanation is that once the bare aluminum metal is exposed to the etchant, the (100) facets exhibit a higher etching rate compared to other crystallographic facets, particularly those located near the corners of the nanocube. This differential reactivity leads to faster etching at the center of each face, while etching slows as it approaches the corners. As the process continues, curved surfaces form due to the gradual exposure of more stable, lower-energy facets, ultimately giving rise to the characteristic octopod morphology. This behavior is clearly visible in Figure 5.2 at the 5-hour mark, where the directions corresponding to the $\langle 111 \rangle$ orientation, associated with the diagonals of the cube, show significantly less etching than those aligned along the $\langle 100 \rangle$ directions.

5.2.3. Characterization of aluminum octopods

We used TEM to characterize the aluminum octopod nanostructures. Figure 5.5 shows a representative octopod, and the magnified views reveal clear lattice fringes near the tips, indicating crystallinity in those regions. Additional complementary TEM images are presented in Figures E.5 and E.6. However, it was difficult to distinguish the boundary between the crystalline metallic core and the surrounding oxide shell. This challenge may be due to the geometry of the nanoparticle, where the four upper tips are superimposed over those on the opposite side. To address this limitation, we

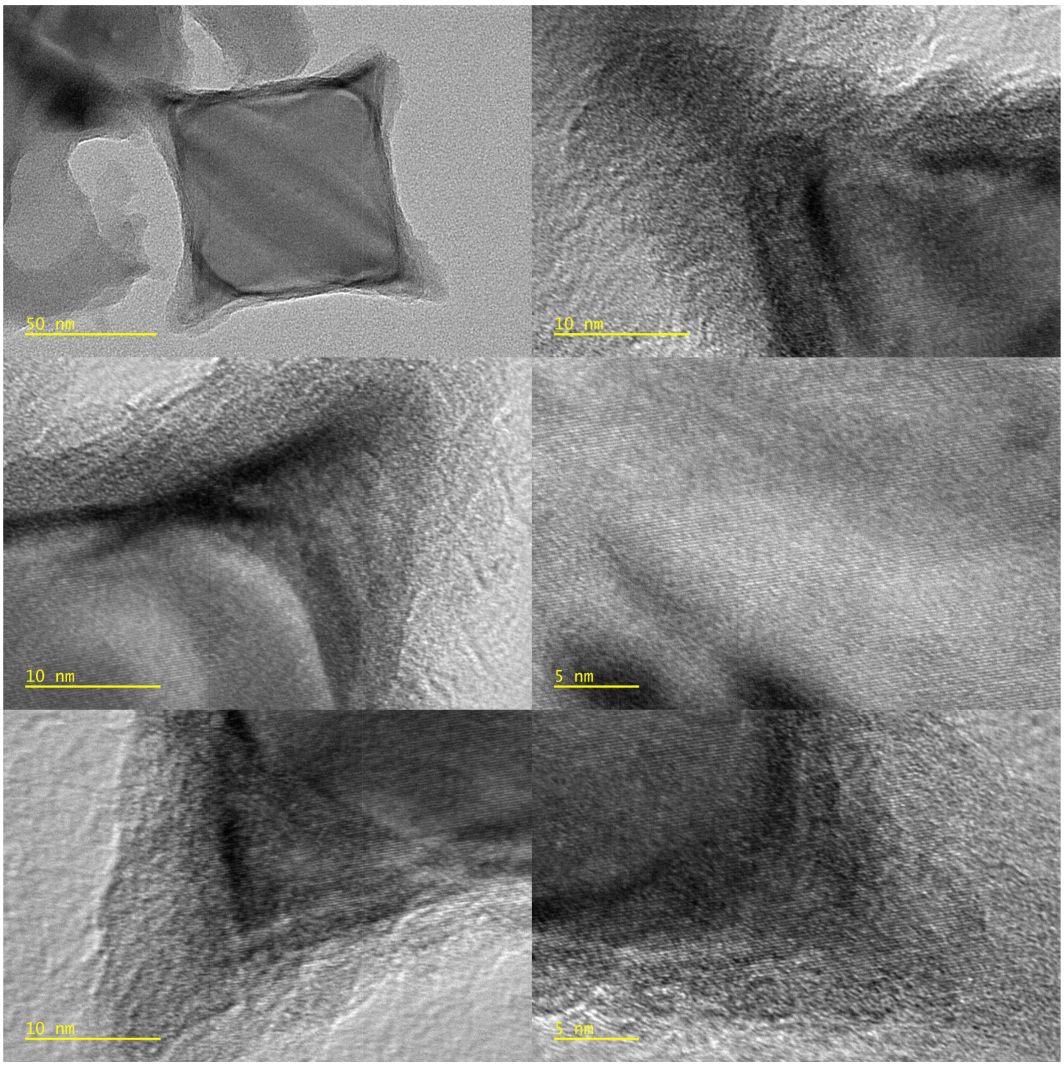

Figure 5.5.: TEM image of a selected aluminum octopod, with high-magnification views highlighting four corner tips and the central region.

attempted TEM tomography to better resolve the full 3D morphology. Unfortunately, these initial efforts were unsuccessful because the aluminum structures underwent shape deformation under prolonged electron beam exposure, as similarly observed during extended SEM imaging (Figure E.7). Nevertheless, work is ongoing to optimize the tomography process.

We subsequently performed optical characterization of individual nanoparticles on silicon substrates at various etching durations, as shown in Figure 5.6. The figure presents dark-field scattering spectra, illustrating three representative nanoparticles for each etching time. It is important to note that the spectral data are SEM-correlated with the structures shown in the insets. Overall, we observed two prominent spectral features: a sharper peak appearing below 450 nm and a broader peak spanning approx-

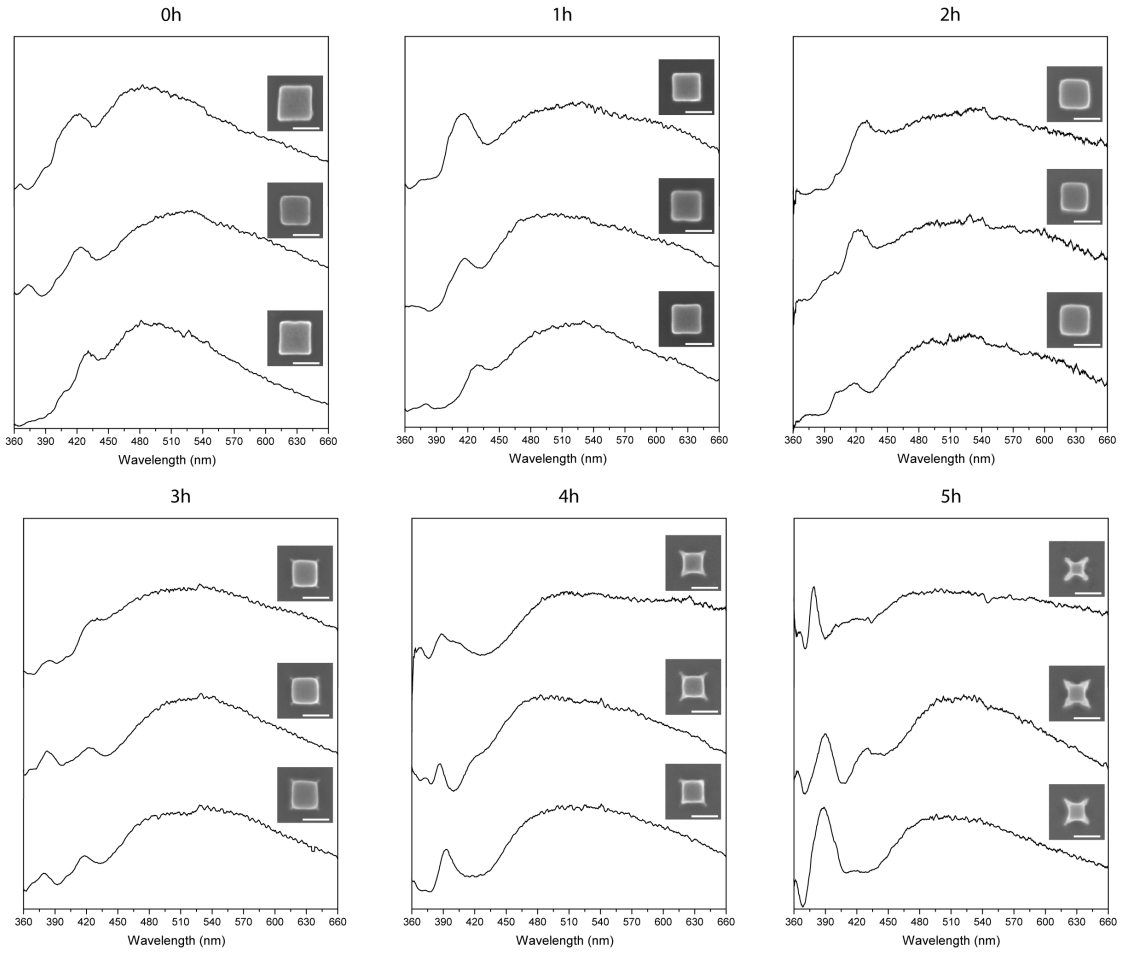

Figure 5.6.: Scattering spectra of individual nanoparticles after etching for 0, 1, 2, 3, 4, and 5 hours.

imately 450–630 nm. Notably, as etching progressed, a blue shift was detected in the sharp plasmonic resonance, which initially centered around ~430 nm and gradually shifted to approximately ~390 nm after 5 hours, accompanied by a narrowing of the peak. This spectral evolution likely reflects morphological changes, specifically the narrowing of the central cubic region and the sharpening of the nanoparticle corners during etching.

Interestingly, some of the observed resonances were remarkably sharp, an uncommon characteristic for plasmonic systems and notably different from previous experimental observations on aluminum octopods reported by N. J. Halas and coworkers[202]. The underlying reasons for this behavior are currently not fully understood and require further investigation. Furthermore, our experiments demonstrate that the plasmonic resonance position can be systematically tuned by adjusting the etching duration, providing a straightforward approach to engineering the optical response of individual nanoparticles. Although additional resonances below 350 nm are anticipated, our current optical setup does not yet permit measurements in this spectral

range. Future experiments are therefore planned to extend spectral characterization capabilities down to 200 nm. To better elucidate the relationship between particle morphology and optical response, comparative analysis using simulations would be particularly valuable.

5.2.4. Preliminary assessment of aluminum octopods for SERS

We conducted preliminary experiments to evaluate the Surface-Enhanced Raman Scattering (SERS) performance of aluminum octopods. For this purpose, we selected p-aminobenzoic acid (PABA) as a molecular probe due to its Raman-active modes and its functional groups, which are known to bind to oxide surfaces. Specifically, the thin aluminum oxide layer naturally present on the octopods can provide binding sites for the carboxylic acid groups present in PABA molecules. The aluminum nanocube samples, etched for 5 hours to achieve octopod morphology, were immersed in 15 mL of a ~400 mM solution of PABA in isopropanol for three days. After rinsing the samples, Raman measurements were performed under 532 nm laser excitation.

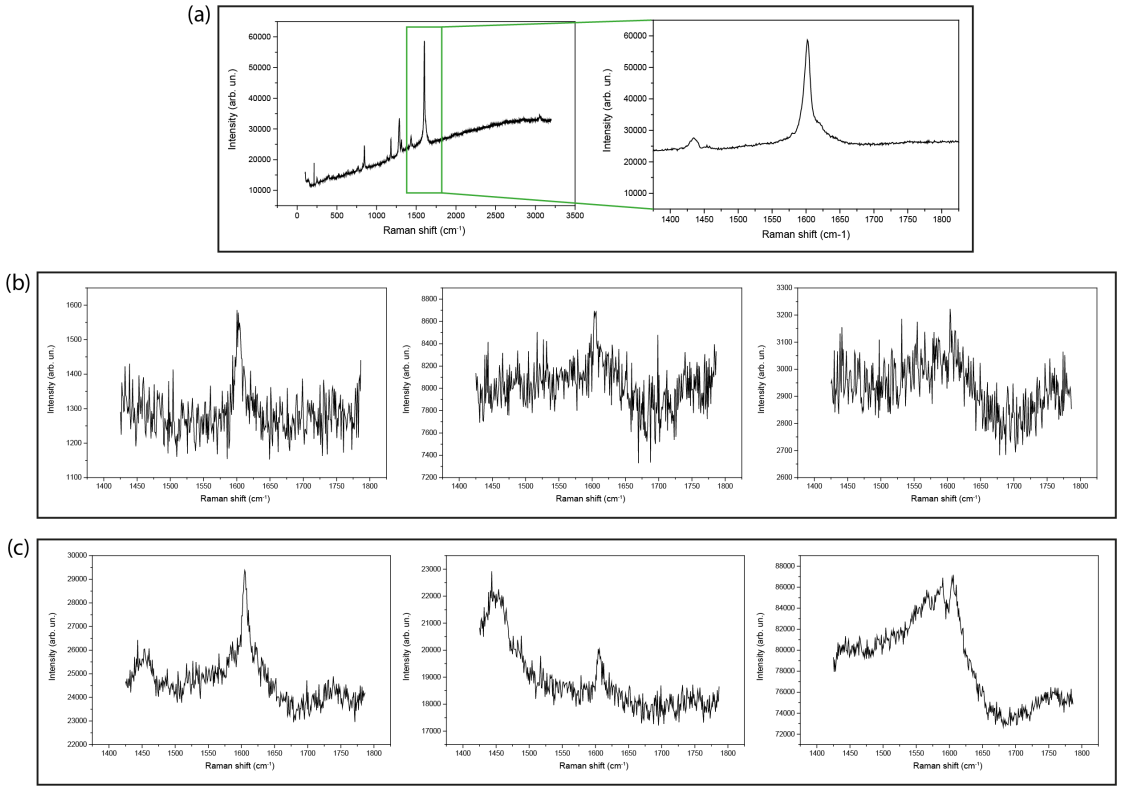

Figure 5.7.: SERS spectra of (a) PABA reference, (b) PABA adsorbed on individual aluminum nanoparticles, and (c) PABA adsorbed on aggregated aluminum nanoparticles.

Figure 5.7a shows the reference Raman spectrum of pure PABA, with its strongest

characteristic peak located around 1604 cm^{-1}, corresponding to the axial deformation mode of the aromatic C=C bonds in the molecule[25]. We thus used this Raman peak as an indicator to verify the presence of PABA molecules adsorbed onto the aluminum octopods. As illustrated in Figure 5.7b, this characteristic peak at 1604 cm^{-1} was indeed observed in spectra recorded from individual nanoparticles. However, we have not yet confirmed whether these individual nanoparticles are indeed the targeted octopod-shaped aluminum nanostructures. To address this uncertainty, future experiments should incorporate SEM correlation to directly link Raman spectra to specific particle morphologies.

Additionally, we observed that the intensity and sharpness of the SERS peaks varied significantly from one nanoparticle to another. This variability is typical for single-particle SERS measurements and is mainly due to differences in particle shape, size, and local environment[200, 201]. Similarly, Figure 5.7c demonstrates the presence of the characteristic peak at 1604 cm^{-1} from aggregated nanoparticles, although these aggregates likely consist of a mixture of octopods and other nanoparticle shapes.

Overall, while these preliminary results indicate promising SERS activity, the experiments remain in progress. Comprehensive statistical analysis is necessary to draw more robust conclusions due to the intrinsic variability of SERS enhancement at the single-particle level. Future work also includes fluorescence lifetime measurements to further investigate the optical properties and interactions of the fluorescent molecules with the aluminum octopod nanoparticles.

5.3. Conclusion

In summary, although reproducible epitaxial welding of aluminum nanocubes through chemical etching was not successfully achieved, we presented an alternative strategy to fabricate aluminum nano-octopods directly on a substrate. Utilizing chromic-phosphoric acid as a selective etchant, we demonstrated control over the morphological transformation from cubes to sharp, branched octopods through anisotropic etching. By adjusting the duration of etching, the degree of tip sharpness and branching of the octopods can be tuned. TEM confirmed that the octopod tips remain crystalline after etching, highlighting the preservation of metallic structure. Additionally, optical characterization using dark-field scattering spectroscopy revealed spectral signatures that evolve consistently with the morphological changes during etching, particularly showing a blue-shift of the plasmonic resonance as the octopods develop sharper features. This controllable etching approach thus provides a promising route for engineering aluminum-based nanostructures with tailored sharpness, opening opportunities for their application as efficient platforms in Surface-Enhanced Raman Scattering (SERS).

General conclusion

This thesis begins in Chapter 1, where I discussed the critical role geometry plays in determining the plasmonic properties of metallic nanostructures. These geometric and spatial placement aspects are essential in various optoelectronic applications, including sensors and metasurfaces. Furthermore, I highlighted the importance of monocrystallinity in metallic nanostructures due to the detrimental effects of grain boundaries, which act as sources of energy loss. The chapter provided a comprehensive overview of current templated nanoparticle assembly methods enabling the construction of metal nanostructures according to a designer's wish. Additionally, several reported wet-chemical approaches were reviewed, focusing on their capability to transform assembled nanocubes into continuous monocrystalline structures. The discussion concluded by identifying two primary challenges: first, the difficulty of establishing a universal nanoparticle assembly recipe ("*à la carte*") applicable across various pattern parameters: geometries, and densities while maintaining single-nanoparticle lateral resolution. Second, the challenge associated with epitaxial welding of silver nanocubes. Specifically, silver nanocube welding through additive methods (overgrowth) that leads to unwanted secondary nucleation. Furthermore, I raised the intriguing question of whether the epitaxial welding approach could be extended to include aluminum nanocubes. These conclusions set the foundation and provided motivation for the investigations presented in this thesis.

Chapter 2 then explores the use of air-water interface assembly to first create a highly dense monolayer of nanocube building blocks, which is then deposited onto templated polydimethylsiloxane (PDMS) substrates regardless of the nanopattern's density, shape, or size. We performed key parametric optimizations, including nanoparticle density on the interface, deposition angle, and assembly technique. This approach enables the fabrication of nanostructure arrays featuring arbitrarily complex meta-atoms at high density and with single-nanoparticle lateral resolution over sub-millimeter areas. We demonstrate the assembly of nanocubes into intricate meta-atom geometries rarely achievable by conventional techniques, such as U-, L-, cross-, S-, T-shapes, gammadions, split-ring resonators, and Pancharatnam-Berry (PB). Furthermore, we show that these assembled nanocubes can be transformed into continuous nanostructures through nanocube epitaxy, using a previously reported approach for gold nanocubes[1] and a silver-based strategy that is described in detail in Chapter 3. This welding process connects adjacent nanocubes, enabling the fabrication of monocrystalline meta-atoms, which can then be transferred from PDMS onto various substrates through contact printing. As a proof of concept, we present the fabrication of a circular dichroism metasurface composed of gammadion-shaped meta-atoms capable of

selectively absorbing light based on its circular polarization. Additionally, we demonstrate a Pancharatnam-Berry metasurface that deflects transmitted light depending on both the wavelength and the handedness of the circularly polarized incident beam.

In Chapter 3, we focus on the epitaxial welding of silver nanocubes, enabling the fabrication of monocrystalline silver nanostructures with arbitrary geometries. This work complements the work initiated by Dr. Anna Capitaine in her doctoral thesis[2]. Our study introduces a solution-based method for welding silver nanocubes without using a reducing agent. This prevents homonucleation in solution, which would otherwise compromise the optical quality of the nanostructures. We found that nanogaps play a key role in promoting anisotropic growth, largely driven by electrostatic interactions between closely spaced nanocubes. To maintain a balance between nanocube dissolution, controlled growth, and shape preservation, it was essential to optimize parameters such as temperature, nitric acid concentration, and the addition of shape-stabilizing agents like bromide ions and silver trifluoroacetate. Welding occurred effectively only when nanocubes were positioned close to each other. In contrast, nanocubes with larger separations did not weld, likely due to a lack of sufficient silver species in the absence of a reducing agent. This observation supports the idea that ion accumulation in the nanogap, influenced by electrostatic interactions, drives the welding process. By combining this welding strategy with different nanoparticle assembly methods including capillary assembly and air-water interface assembly, we demonstrate the bottom-up construction of complex monocrystalline nanostructures.

Chapter 4 explores the chemical overgrowth of nanocubes placed on a substrate. The initial goal was to adapt a well-known colloidal core–shell synthesis method to achieve epitaxial welding. Although optimal welding conditions were not fully achieved, the silver overgrowth process led to two distinct outcomes: nanowelding and anisotropic elongation. In particular, the presence of PVP in the solution appeared to promote silver growth within the interparticle gap without bridging the cores, leading to the formation of high-aspect-ratio nanostructures. This behavior contrasts with the findings in Chapter 3, where nanogaps facilitated welding via electrostatic interactions. Our observations suggest that the initial nanogap plays a decisive role in determining the overgrowth mode. Either promoting particle interconnection or acting as a physical guide that directs anisotropic growth. To explore this further, we used nanocube dimers as a model system and conducted systematic parametric studies by varying the reaction time, PVP concentration, temperature, seed size, and particle shape. These experiments demonstrated that the same design principle could potentially be extended to construct more complex nanostructures beyond simple dimers. Although the exact mechanism underlying this anisotropic growth remains to be fully elucidated, the framework presented in this chapter introduces a promising approach for fabricating complex nanostructures. In this approach, the interparticle gap serves as a structural cue that guides directional growth. Overall, these findings provide valuable insights into nanocrystal interface engineering and development of monocrystalline nanostructures suitable for optoelectronic metasurfaces.

Lastly, Chapter 5 was initially dedicated to exploring the epitaxial welding of alu-

minum nanocubes through a chemical etching process, using chromic-phosphoric acid as the etchant. Although reproducible welding was not successfully achieved, we present preliminary results demonstrating an alternative strategy to fabricate aluminum nano-octopods directly on a substrate. By leveraging anisotropic etching, we achieved controlled morphological transformation from nanocubes into sharp, branched octopods. The degree of tip sharpness and branching could be finely tuned by varying the etching duration. Transmission electron microscopy confirmed that the octopod tips retained their crystallinity after etching, indicating the preservation of the underlying metallic structure. In addition, optical characterization using dark-field scattering spectroscopy revealed spectral evolution in line with morphological changes. Notably, a blue shift in the plasmonic resonance was observed as the nanostructures developed sharper features. This controllable etching approach offers a promising route for engineering aluminum-based nanostructures with tailored geometries. It opens new possibilities for their application as platforms in Surface-Enhanced Raman Scattering (SERS).

In overall, this thesis contributes to the development of fabrication strategies for metallic nanostructures by using metallic nanoparticles as fundamental building blocks combined with templated assembly techniques to achieve structures of greater complexity. It also investigates the structural modification of these assembled nanoparticles through wet-chemical approaches. Throughout the work, particular emphasis has been placed on achieving high material quality and single-nanoparticle lateral resolution. While several of the initial research questions posed at the beginning of my PhD have been addressed, others remain unanswered, and new questions have emerged. The following points highlight some of these remaining questions, which may serve as perspectives for future research.

From Chapter 2:

- One of the main limitations of the assembly technique lies in the reproducibility of the excess nanocube removal process. What alternative methods could offer better consistency and precision for this step?
- A major factor contributing to the reproducibility issue is the manual nature of the excess nanoparticle removal process. This introduces variability that makes systematic studies on the influence of trench depth difficult to interpret. In our experience, the method performs reasonably well for trench depths of around 80-90 nm, but becomes unreliable for shallower patterns such as 55 nm. If an automated system were developed to standardize this removal step, an important question would then be: what is the optimal trench depth to ensure effective and reliable nanoparticle assembly?
- Additionally, could a sequential assembly approach be applied to templates with deeper trenches to construct nanostructures with a vertical thickness exceeding that of a single nanocube?
- Finally, it would be interesting to explore the optical properties of complex nanostructures, particularly split-ring resonators and chiral meta-atoms, before and after nanowelding.

From Chapter 3:

- What is the maximum nanogap distance that still allows for successful epitaxial welding of silver nanocubes?
- If the nanocubes are not perfectly aligned face-to-face, what is the maximum initial angular misalignment that can still result in a monocrystalline structure after welding?

From Chapter 4:

- What is the minimum nanogap distance required to enable epitaxial interconnection between two nanocubes?
- What is the maximum nanogap distance that still allows anisotropic overgrowth in gold nanocube dimers?
- What is the underlying mechanism behind anisotropic overgrowth in gold nanocube dimers? Why does welding not occur in the gap while overgrowth proceeds within it?
- What is the mechanism of anisotropic overgrowth in dimers composed of non-cubic nanoparticles?
- Can what appears to be a sub-nanometer gap between overgrown dimers be exploited for functional applications?
- Can this anisotropic overgrowth strategy be extended beyond silver and gold to other materials?

From Chapter 5:

- What is the full three-dimensional morphology of the aluminum octopods, and how is the thin oxide shell distributed across these structures?
- What is the underlying mechanism responsible for the anisotropic etching observed in aluminum nanocubes?
- Could this etching process be carried out in a colloidal (solution-phase) environment, and if so, what would be the optimal conditions?
- If the reformation of the oxide layer could be effectively prevented after etching, would it be feasible to perform overgrowth on aluminum nanocubes? This could be valuable not only for epitaxial welding but also as a platform for seed-mediated colloidal synthesis.

Bibliography

[1] Anna Capitaine and Beniamino Sciacca. “Nanocube Epitaxy for the Realization of Printable Monocrystalline Nanophotonic Surfaces”. en. In: *Advanced Materials* 34.24 (June 2022), p. 2200364. ISSN: 0935-9648, 1521-4095. DOI: 10.1002/adma.202200364. URL: https://onlinelibrary.wiley.com/doi/10.1002/adma.202200364 (cit. on pp. 10, 32, 56, 61, 64, 70, 83, 96, 103, 105, 107, 108, 150, 152, 160, 208, 212).

[2] Anna Capitaine. “Building high performance materials for solar cells from cubic nanobricks”. PhD thesis. 2023. URL: http://www.theses.fr/2023AIXM0027/document (cit. on pp. 10, 32, 57, 103, 104, 107, 108, 111–113, 161, 216–219, 221, 222).

[3] Michael F. Hochella, David W. Mogk, James Ranville, et al. “Natural, incidental, and engineered nanomaterials and their impacts on the Earth system”. en. In: *Science* 363.6434 (Mar. 2019), eaau8299. ISSN: 0036-8075, 1095-9203. DOI: 10.1126/science.aau8299. URL: https://www.science.org/doi/10.1126/science.aau8299 (cit. on p. 30).

[4] Shi Hu and Xun Wang. “Ultrathin nanostructures: smaller size with new phenomena”. en. In: *Chem. Soc. Rev.* 42.12 (2013), p. 5577. ISSN: 0306-0012, 1460-4744. DOI: 10.1039/c3cs00006k. URL: https://xlink.rsc.org/?DOI=c3cs00006k (cit. on p. 30).

[5] Tobias Kraus and Heiko Wolf. “Templated Self-Assembly of Particles”. en. In: *Springer Handbook of Nanotechnology*. Ed. by Bharat Bhushan. Berlin, Heidelberg: Springer Berlin Heidelberg, 2010, pp. 187–210. ISBN: 978-3-642-02525-9. DOI: 10.1007/978-3-642-02525-9_6. URL: http://link.springer.com/10.1007/978-3-642-02525-9_6 (cit. on pp. 31, 50, 51, 53, 54).

[6] George M. Whitesides and Bartosz Grzybowski. “Self-Assembly at All Scales”. en. In: *Science* 295.5564 (Mar. 2002), pp. 2418–2421. ISSN: 0036-8075, 1095-9203. DOI: 10.1126/science.1070821. URL: https://www.science.org/doi/10.1126/science.1070821 (cit. on pp. 31, 50).

[7] Xin Geng, Miquel Vega-Paredes, Zhenyu Wang, et al. “Grain boundary engineering for efficient and durable electrocatalysis”. en. In: *Nat Commun* 15.1 (Oct. 2024), p. 8534. ISSN: 2041-1723. DOI: 10.1038/s41467-024-52919-w. URL: https://www.nature.com/articles/s41467-024-52919-w (cit. on p. 31).

[8] Can O. Karaman, Anton Yu. Bykov, Fatemeh Kiani, et al. “Ultrafast hot-carrier dynamics in ultrathin monocrystalline gold”. en. In: *Nat Commun* 15.1 (Jan. 2024), p. 703. ISSN: 2041-1723. DOI: 10.1038/s41467-024-44769-3. URL:

https://www.nature.com/articles/s41467-024-44769-3 (cit. on pp. 31, 102).

[9] Vahagn Mkhitaryan, Andrew P. Weber, Saad Abdullah, et al. "Ultraconfined Plasmons in Atomically Thin Crystalline Silver Nanostructures". en. In: *Advanced Materials* 36.9 (Mar. 2024), p. 2302520. ISSN: 0935-9648, 1521-4095. DOI: 10.1002/adma.202302520. URL: https://onlinelibrary.wiley.com/doi/10.1002/adma.202302520 (cit. on pp. 31, 44, 102).

[10] Vitor R. Manfrinato, Lihua Zhang, Dong Su, et al. "Resolution Limits of Electron-Beam Lithography toward the Atomic Scale". en. In: *Nano Lett.* 13.4 (Apr. 2013), pp. 1555–1558. ISSN: 1530-6984, 1530-6992. DOI: 10.1021/nl304715p. URL: https://pubs.acs.org/doi/10.1021/nl304715p (cit. on pp. 31, 49, 69).

[11] Beniamino Sciacca, Annemarie Berkhout, Benjamin J. M. Brenny, et al. "Monocrystalline Nanopatterns Made by Nanocube Assembly and Epitaxy". en. In: *Advanced Materials* 29.26 (July 2017), p. 1701064. ISSN: 0935-9648, 1521-4095. DOI: 10.1002/adma.201701064. URL: https://onlinelibrary.wiley.com/doi/10.1002/adma.201701064 (cit. on pp. 32, 63, 70, 83, 102, 112, 118, 150).

[12] Katherine A. Willets and Richard P. Van Duyne. "Localized Surface Plasmon Resonance Spectroscopy and Sensing". en. In: *Annu. Rev. Phys. Chem.* 58.1 (May 2007), pp. 267–297. ISSN: 0066-426X, 1545-1593. DOI: 10.1146/annurev.physchem.58.032806.104607. URL: https://www.annualreviews.org/doi/10.1146/annurev.physchem.58.032806.104607 (cit. on pp. 35, 36).

[13] Suljo Linic, Phillip Christopher, and David B. Ingram. "Plasmonic-metal nanostructures for efficient conversion of solar to chemical energy". en. In: *Nature Mater* 10.12 (Dec. 2011), pp. 911–921. ISSN: 1476-1122, 1476-4660. DOI: 10.1038/nmat3151. URL: https://www.nature.com/articles/nmat3151 (cit. on pp. 35, 36).

[14] Amanda J. Haes and Richard P. Van Duyne. "A unified view of propagating and localized surface plasmon resonance biosensors". en. In: *Anal Bioanal Chem* 379.7-8 (Aug. 2004), pp. 920–930. ISSN: 1618-2642, 1618-2650. DOI: 10.1007/s00216-004-2708-9. URL: http://link.springer.com/10.1007/s00216-004-2708-9 (cit. on pp. 35, 38).

[15] Matthew Rycenga, Claire M. Cobley, Jie Zeng, et al. "Controlling the Synthesis and Assembly of Silver Nanostructures for Plasmonic Applications". en. In: *Chem. Rev.* 111.6 (June 2011), pp. 3669–3712. ISSN: 0009-2665, 1520-6890. DOI: 10.1021/cr100275d. URL: https://pubs.acs.org/doi/10.1021/cr100275d (cit. on p. 35).

[16] Stephan Link and Mostafa A. El-Sayed. "Shape and size dependence of radiative, non-radiative and photothermal properties of gold nanocrystals". en. In: *International Reviews in Physical Chemistry* 19.3 (July 2000), pp. 409–453. ISSN: 0144-235X, 1366-591X. DOI: 10.1080/01442350050034180. URL: http://www.tandfonline.com/doi/abs/10.1080/01442350050034180 (cit. on pp. 35, 36, 43).

[17] Nina Meinzer, William L. Barnes, and Ian R. Hooper. "Plasmonic meta-atoms and metasurfaces". en. In: *Nature Photon* 8.12 (Dec. 2014), pp. 889–898. ISSN: 1749-4885, 1749-4893. DOI: 10.1038/nphoton.2014.247. URL: https://www.nature.com/articles/nphoton.2014.247 (cit. on pp. 35, 39–41, 43).

[18] David Alba-Molina, Juan J. Giner-Casares, and Manuel Cano. "Bioconjugated Plasmonic Nanoparticles for Enhanced Skin Penetration". en. In: *Top Curr Chem (Z)* 378.1 (Feb. 2020), p. 8. ISSN: 2365-0869, 2364-8961. DOI: 10.1007/s41061-019-0273-0. URL: http://link.springer.com/10.1007/s41061-019-0273-0 (cit. on p. 36).

[19] D. Jaque, L. Martínez Maestro, B. Del Rosal, et al. "Nanoparticles for photothermal therapies". en. In: *Nanoscale* 6.16 (2014), pp. 9494–9530. ISSN: 2040-3364, 2040-3372. DOI: 10.1039/C4NR00708E. URL: https://xlink.rsc.org/?DOI=C4NR00708E (cit. on p. 36).

[20] Javier Reguera, Judith Langer, Dorleta Jiménez De Aberasturi, et al. "Anisotropic metal nanoparticles for surface enhanced Raman scattering". en. In: *Chem. Soc. Rev.* 46.13 (2017), pp. 3866–3885. ISSN: 0306-0012, 1460-4744. DOI: 10.1039/C7CS00158D. URL: https://xlink.rsc.org/?DOI=C7CS00158D (cit. on pp. 37, 38).

[21] Adam D. McFarland and Richard P. Van Duyne. "Single Silver Nanoparticles as Real-Time Optical Sensors with Zeptomole Sensitivity". en. In: *Nano Lett.* 3.8 (Aug. 2003), pp. 1057–1062. ISSN: 1530-6984, 1530-6992. DOI: 10.1021/nl034372s. URL: https://pubs.acs.org/doi/10.1021/nl034372s (cit. on p. 37).

[22] Judith Langer, Dorleta Jimenez De Aberasturi, Javier Aizpurua, et al. "Present and Future of Surface-Enhanced Raman Scattering". en. In: *ACS Nano* 14.1 (Jan. 2020), pp. 28–117. ISSN: 1936-0851, 1936-086X. DOI: 10.1021/acsnano.9b04224. URL: https://pubs.acs.org/doi/10.1021/acsnano.9b04224 (cit. on pp. 38, 149).

[23] Nathan C Lindquist, Prashant Nagpal, Kevin M McPeak, et al. "Engineering metallic nanostructures for plasmonics and nanophotonics". In: *Rep. Prog. Phys.* 75.3 (Mar. 2012), p. 036501. ISSN: 0034-4885, 1361-6633. DOI: 10.1088/0034-4885/75/3/036501. URL: https://iopscience.iop.org/article/10.1088/0034-4885/75/3/036501 (cit. on p. 38).

[24] Shu Tian, Oara Neumann, Michael J. McClain, et al. "Aluminum Nanocrystals: A Sustainable Substrate for Quantitative SERS-Based DNA Detection". en. In: *Nano Lett.* 17.8 (Aug. 2017), pp. 5071–5077. ISSN: 1530-6984, 1530-6992. DOI: 10.1021/acs.nanolett.7b02338. URL: https://pubs.acs.org/doi/10.1021/acs.nanolett.7b02338 (cit. on pp. 38, 149, 150).

[25] Fei Peng, Shao-Yong Lu, Pan-Qi Sun, et al. "Branched Aluminum Nanocrystals with Internal Hot Spots: Synthesis and Single-Particle Surface-Enhanced Raman Scattering". en. In: *Nano Lett.* 23.14 (July 2023), pp. 6567–6573. ISSN: 1530-6984, 1530-6992. DOI: 10.1021/acs.nanolett.3c01605. URL: https://pubs.acs.org/doi/10.1021/acs.nanolett.3c01605 (cit. on pp. 38, 149, 159).

[26] Mario Hentschel, Martin Schäferling, Xiaoyang Duan, et al. "Chiral plasmonics". en. In: *Sci. Adv.* 3.5 (May 2017), e1602735. ISSN: 2375-2548. DOI: 10.1126/sciadv.1602735. URL: https://www.science.org/doi/10.1126/sciadv.1602735 (cit. on p. 40).

[27] E. Prodan and P. Nordlander. "Plasmon hybridization in spherical nanoparticles". en. In: *The Journal of Chemical Physics* 120.11 (Mar. 2004), pp. 5444–5454. ISSN: 0021-9606, 1089-7690. DOI: 10.1063/1.1647518. URL: https://pubs.aip.org/jcp/article/120/11/5444/534265/Plasmon-hybridization-in-spherical-nanoparticles (cit. on p. 40).

[28] P. Nordlander, C. Oubre, E. Prodan, et al. "Plasmon Hybridization in Nanoparticle Dimers". en. In: *Nano Lett.* 4.5 (May 2004), pp. 899–903. ISSN: 1530-6984, 1530-6992. DOI: 10.1021/nl049681c. URL: https://pubs.acs.org/doi/10.1021/nl049681c (cit. on p. 40).

[29] Viktor Myroshnychenko, Jessica Rodríguez-Fernández, Isabel Pastoriza-Santos, et al. "Modelling the optical response of gold nanoparticles". en. In: *Chem. Soc. Rev.* 37.9 (2008), p. 1792. ISSN: 0306-0012, 1460-4744. DOI: 10.1039/b711486a. URL: https://xlink.rsc.org/?DOI=b711486a (cit. on p. 40).

[30] Ankun Yang, Thang B. Hoang, Montacer Dridi, et al. "Real-time tunable lasing from plasmonic nanocavity arrays". en. In: *Nat Commun* 6.1 (Apr. 2015), p. 6939. ISSN: 2041-1723. DOI: 10.1038/ncomms7939. URL: https://www.nature.com/articles/ncomms7939 (cit. on p. 41).

[31] Weijia Wang, Mohammad Ramezani, Aaro I. Väkeväinen, et al. "The rich photonic world of plasmonic nanoparticle arrays". en. In: *Materials Today* 21.3 (Apr. 2018), pp. 303–314. ISSN: 13697021. DOI: 10.1016/j.mattod.2017.09.002. URL: https://linkinghub.elsevier.com/retrieve/pii/S1369702117306727 (cit. on p. 41).

[32] Hannu Husu, Roope Siikanen, Jouni Mäkitalo, et al. "Metamaterials with Tailored Nonlinear Optical Response". en. In: *Nano Lett.* 12.2 (Feb. 2012), pp. 673–677. ISSN: 1530-6984, 1530-6992. DOI: 10.1021/nl203524k. URL: https://pubs.acs.org/doi/10.1021/nl203524k (cit. on p. 41).

[33] Bernhard Atorf, Holger Mühlenbernd, Thomas Zentgraf, et al. "All-optical switching of a dye-doped liquid crystal plasmonic metasurface". en. In: *Opt. Express* 28.6 (Mar. 2020), p. 8898. ISSN: 1094-4087. DOI: 10.1364/OE.383877. URL: https://opg.optica.org/abstract.cfm?URI=oe-28-6-8898 (cit. on p. 41).

[34] I. Bouanane, F. Bedu, I. Ozerov, et al. "Design of infrared optical absorber using silver nanorings array made by a top-down process". en. In: *Sci Rep* 13.1 (May 2023), p. 7770. ISSN: 2045-2322. DOI: 10.1038/s41598-023-34579-w. URL: https://www.nature.com/articles/s41598-023-34579-w (cit. on p. 41).

[35] Amir Hassanfiroozi, Po-Sheng Huang, Shih-Hsiu Huang, et al. "A Toroidal-Fano-Resonant Metasurface with Optimal Cross-Polarization Efficiency and Switchable Nonlinearity in the Near-Infrared". en. In: *Advanced Optical Materials* 9.21 (Nov. 2021), p. 2101007. ISSN: 2195-1071, 2195-1071. DOI: 10.1002/

adom.202101007. URL: https://onlinelibrary.wiley.com/doi/10.1002/adom.202101007 (cit. on p. 41).

[36] Xiaoyang Duan, Simon Kamin, Florian Sterl, et al. "Hydrogen-Regulated Chiral Nanoplasmonics". en. In: *Nano Lett.* 16.2 (Feb. 2016), pp. 1462–1466. ISSN: 1530-6984, 1530-6992. DOI: 10.1021/acs.nanolett.5b05105. URL: https://pubs.acs.org/doi/10.1021/acs.nanolett.5b05105 (cit. on p. 41).

[37] M. Decker, M. Ruther, C. E. Kriegler, et al. "Strong optical activity from twisted-cross photonic metamaterials". en. In: *Opt. Lett.* 34.16 (Aug. 2009), p. 2501. ISSN: 0146-9592, 1539-4794. DOI: 10.1364/OL.34.002501. URL: https://opg.optica.org/abstract.cfm?URI=ol-34-16-2501 (cit. on p. 41).

[38] Shumei Chen, Franziska Zeuner, Martin Weismann, et al. "Giant Nonlinear Optical Activity of Achiral Origin in Planar Metasurfaces with Quadratic and Cubic Nonlinearities". en. In: *Advanced Materials* 28.15 (Apr. 2016), pp. 2992–2999. ISSN: 0935-9648, 1521-4095. DOI: 10.1002/adma.201505640. URL: https://onlinelibrary.wiley.com/doi/10.1002/adma.201505640 (cit. on p. 41).

[39] Dandan Wen, Fuyong Yue, Santosh Kumar, et al. "Metasurface for characterization of the polarization state of light". en. In: *Opt. Express* 23.8 (Apr. 2015), p. 10272. ISSN: 1094-4087. DOI: 10.1364/OE.23.010272. URL: https://opg.optica.org/abstract.cfm?URI=oe-23-8-10272 (cit. on pp. 41, 42, 93).

[40] Xianzhong Chen, Lingling Huang, Holger Mühlenbernd, et al. "Dual-polarity plasmonic metalens for visible light". en. In: *Nat Commun* 3.1 (Nov. 2012), p. 1198. ISSN: 2041-1723. DOI: 10.1038/ncomms2207. URL: https://www.nature.com/articles/ncomms2207 (cit. on p. 42).

[41] Lingling Huang, Xianzhong Chen, Holger Mühlenbernd, et al. "Dispersionless Phase Discontinuities for Controlling Light Propagation". en. In: *Nano Lett.* 12.11 (Nov. 2012), pp. 5750–5755. ISSN: 1530-6984, 1530-6992. DOI: 10.1021/nl303031j. URL: https://pubs.acs.org/doi/10.1021/nl303031j (cit. on pp. 43, 93).

[42] V. G. Kravets, A. V. Kabashin, W. L. Barnes, et al. "Plasmonic Surface Lattice Resonances: A Review of Properties and Applications". en. In: *Chem. Rev.* 118.12 (June 2018), pp. 5912–5951. ISSN: 0009-2665, 1520-6890. DOI: 10.1021/acs.chemrev.8b00243. URL: https://pubs.acs.org/doi/10.1021/acs.chemrev.8b00243 (cit. on p. 43).

[43] M. Kuttge, E. J. R. Vesseur, J. Verhoeven, et al. "Loss mechanisms of surface plasmon polaritons on gold probed by cathodoluminescence imaging spectroscopy." en. In: *Applied Physics Letters* 93.11 (Sept. 2008), p. 113110. ISSN: 0003-6951, 1077-3118. DOI: 10.1063/1.2987458. URL: https://pubs.aip.org/apl/article/93/11/113110/335755/Loss-mechanisms-of-surface-plasmon-polaritons-on (cit. on pp. 43, 44).

[44] Sasan V. Grayli, Saeid Kamal, and Gary W. Leach. "High performance, single crystal gold bowtie nanoantennas fabricated via epitaxial electroless deposition". en. In: *Sci Rep* 13.1 (Aug. 2023), p. 12745. ISSN: 2045-2322. DOI: 10.1038/

s41598-023-38154-1. URL: https://www.nature.com/articles/s41598-023-38154-1 (cit. on pp. 43, 44).

[45] Lufang Liu, Alexey V. Krasavin, Junsheng Zheng, et al. "Atomically Smooth Single-Crystalline Platform for Low-Loss Plasmonic Nanocavities". en. In: *Nano Lett.* 22.4 (Feb. 2022), pp. 1786–1794. ISSN: 1530-6984, 1530-6992. DOI: 10.1021/acs.nanolett.2c00095. URL: https://pubs.acs.org/doi/10.1021/acs.nanolett.2c00095 (cit. on pp. 44, 102).

[46] Sergejs Boroviks and Olivier J. F. Martin. "Monocrystalline Gold Metasurface to Control Anisotropic Second-Harmonic Generation". en. In: *Advanced Optical Materials* (Feb. 2025), p. 2402525. ISSN: 2195-1071, 2195-1071. DOI: 10.1002/adom.202402525. URL: https://advanced.onlinelibrary.wiley.com/doi/10.1002/adom.202402525 (cit. on p. 44).

[47] Viet Huong Nguyen, Dorina T. Papanastasiou, Joao Resende, et al. "Advances in Flexible Metallic Transparent Electrodes". en. In: *Small* 18.19 (May 2022), p. 2106006. ISSN: 1613-6810, 1613-6829. DOI: 10.1002/smll.202106006. URL: https://onlinelibrary.wiley.com/doi/10.1002/smll.202106006 (cit. on p. 44).

[48] Beniamino Sciacca, Jorik Van De Groep, Albert Polman, et al. "Solution-Grown Silver Nanowire Ordered Arrays as Transparent Electrodes". en. In: *Advanced Materials* 28.5 (Feb. 2016), pp. 905–909. ISSN: 0935-9648, 1521-4095. DOI: 10.1002/adma.201504045. URL: https://onlinelibrary.wiley.com/doi/10.1002/adma.201504045 (cit. on pp. 44, 45).

[49] Yorick Bleiji, Andrea Cordaro, Stefan W. Tabernig, et al. "High Aspect Ratio Silver Nanogrids by Bottom-Up Electrochemical Growth as Transparent Electrode". en. In: *ACS Appl. Opt. Mater.* 2.3 (Mar. 2024), pp. 508–516. ISSN: 2771-9855, 2771-9855. DOI: 10.1021/acsaom.4c00037. URL: https://pubs.acs.org/doi/10.1021/acsaom.4c00037 (cit. on p. 45).

[50] J. Friedrich. "Methods for Bulk Growth of Inorganic Crystals: Crystal Growth". en. In: *Reference Module in Materials Science and Materials Engineering*. Elsevier, 2016, B9780128035818010109. ISBN: 978-0-12-803581-8. DOI: 10.1016/B978-0-12-803581-8.01010-9. URL: https://linkinghub.elsevier.com/retrieve/pii/B9780128035818010109 (cit. on p. 46).

[51] Christophe Ballif, Franz-Josef Haug, Mathieu Boccard, et al. "Status and perspectives of crystalline silicon photovoltaics in research and industry". en. In: *Nat Rev Mater* 7.8 (Mar. 2022), pp. 597–616. ISSN: 2058-8437. DOI: 10.1038/s41578-022-00423-2. URL: https://www.nature.com/articles/s41578-022-00423-2 (cit. on p. 46).

[52] W. Zulehner. "Czochralski growth of silicon". en. In: *Journal of Crystal Growth* 65.1-3 (Dec. 1983), pp. 189–213. ISSN: 00220248. DOI: 10.1016/0022-0248(83)90051-9. URL: https://linkinghub.elsevier.com/retrieve/pii/0022024883900519 (cit. on p. 46).

[53] C.D. Brandle. "Czochralski growth of oxides". en. In: *Journal of Crystal Growth* 264.4 (Mar. 2004), pp. 593–604. ISSN: 00220248. DOI: 10.1016/j.jcrysgro.

2003.12.044. URL: https://linkinghub.elsevier.com/retrieve/pii/S0022024803022486 (cit. on p. 46).

[54] José M. Vila-Fungueiriño, Romain Bachelet, Guillaume Saint-Girons, et al. "Integration of functional complex oxide nanomaterials on silicon". In: *Front. Phys.* 3 (June 2015). ISSN: 2296-424X. DOI: 10.3389/fphy.2015.00038. URL: http://journal.frontiersin.org/Article/10.3389/fphy.2015.00038/abstract (cit. on p. 47).

[55] G B Stringfellow. "Epitaxy". In: *Rep. Prog. Phys.* 45.5 (May 1982), pp. 469–525. ISSN: 0034-4885, 1361-6633. DOI: 10.1088/0034-4885/45/5/001. URL: https://iopscience.iop.org/article/10.1088/0034-4885/45/5/001 (cit. on pp. 47, 48).

[56] Hugh O. Pierson. "Introduction and General Considerations". en. In: *Handbook of Chemical Vapor Deposition (CVD)*. Elsevier, 1999, pp. 25–35. ISBN: 978-0-8155-1432-9. DOI: 10.1016/B978-081551432-9.50004-8. URL: https://linkinghub.elsevier.com/retrieve/pii/B9780815514329500048 (cit. on p. 47).

[57] Jean-Charles Arnault, Samuel Saada, and Victor Ralchenko. "Chemical Vapor Deposition Single-Crystal Diamond: A Review". en. In: *Physica Rapid Research Ltrs* 16.1 (Jan. 2022), p. 2100354. ISSN: 1862-6254, 1862-6270. DOI: 10.1002/pssr.202100354. URL: https://onlinelibrary.wiley.com/doi/10.1002/pssr.202100354 (cit. on p. 48).

[58] Azar Maalouf, Michel Gadonna, and Dominique Bosc. "An improvement in standard photolithography resolution based on Kirchhoff diffraction studies". In: *J. Phys. D: Appl. Phys.* 42.1 (Jan. 2009), p. 015106. ISSN: 0022-3727, 1361-6463. DOI: 10.1088/0022-3727/42/1/015106. URL: https://iopscience.iop.org/article/10.1088/0022-3727/42/1/015106 (cit. on p. 48).

[59] Kate Stokes, Kieran Clark, David Odetade, et al. "Advances in lithographic techniques for precision nanostructure fabrication in biomedical applications". en. In: *Discover Nano* 18.1 (Dec. 2023), p. 153. ISSN: 2731-9229. DOI: 10.1186/s11671-023-03938-x. URL: https://link.springer.com/10.1186/s11671-023-03938-x (cit. on p. 48).

[60] Se Young Park, Seongjae Lee, Jeehye Yang, et al. "Patterning Quantum Dots via Photolithography: A Review". en. In: *Advanced Materials* 35.41 (Oct. 2023), p. 2300546. ISSN: 0935-9648, 1521-4095. DOI: 10.1002/adma.202300546. URL: https://onlinelibrary.wiley.com/doi/10.1002/adma.202300546 (cit. on p. 48).

[61] Wing H. Ng, Yao Lu, Huiyun Liu, et al. "Controlling and modelling the wetting properties of III-V semiconductor surfaces using re-entrant nanostructures". en. In: *Sci Rep* 8.1 (Feb. 2018), p. 3544. ISSN: 2045-2322. DOI: 10.1038/s41598-018-21864-2. URL: https://www.nature.com/articles/s41598-018-21864-2 (cit. on p. 48).

[62] Weicheng Tian. "Research progress of laser lithography". In: *J. Phys.: Conf. Ser.* 2608.1 (Oct. 2023), p. 012016. ISSN: 1742-6588, 1742-6596. DOI: 10.1088/1742-

6596/2608/1/012016. URL: https://iopscience.iop.org/article/10.1088/1742-6596/2608/1/012016 (cit. on p. 49).

[63] Thomas A Klar, Richard Wollhofen, and Jaroslaw Jacak. "Sub-Abbe resolution: from STED microscopy to STED lithography". In: *Phys. Scr.* T162 (Sept. 2014), p. 014049. ISSN: 0031-8949, 1402-4896. DOI: 10.1088/0031-8949/2014/T162/014049. URL: https://iopscience.iop.org/article/10.1088/0031-8949/2014/T162/014049 (cit. on p. 49).

[64] Prashant Nagpal, Nathan C. Lindquist, Sang-Hyun Oh, et al. "Ultrasmooth Patterned Metals for Plasmonics and Metamaterials". en. In: *Science* 325.5940 (July 2009), pp. 594–597. ISSN: 0036-8075, 1095-9203. DOI: 10.1126/science.1174655. URL: https://www.science.org/doi/10.1126/science.1174655 (cit. on p. 49).

[65] Harshal Agrawal and Erik C. Garnett. "Nanocube Imprint Lithography". en. In: *ACS Nano* 14.9 (Sept. 2020), pp. 11009–11016. ISSN: 1936-0851, 1936-086X. DOI: 10.1021/acsnano.0c04793. URL: https://pubs.acs.org/doi/10.1021/acsnano.0c04793 (cit. on pp. 49, 54, 55, 61, 69, 102).

[66] Alexander B. Greenwood, Krishna C. Balram, and Henkjan Gersen. "Smooth Sidewalls on Crystalline Gold through Facet-Selective Anisotropic Reactive Ion Etching: Toward Low-Loss Plasmonic Devices". en. In: *Nano Lett.* 22.12 (June 2022), pp. 4617–4621. ISSN: 1530-6984, 1530-6992. DOI: 10.1021/acs.nanolett.1c04405. URL: https://pubs.acs.org/doi/10.1021/acs.nanolett.1c04405 (cit. on pp. 49, 69).

[67] Heyou Zhang, Yawei Liu, Arun Ashokan, et al. "A General Method for Direct Assembly of Single Nanocrystals". en. In: *Advanced Optical Materials* 10.14 (July 2022), p. 2200179. ISSN: 2195-1071, 2195-1071. DOI: 10.1002/adom.202200179. URL: https://onlinelibrary.wiley.com/doi/10.1002/adom.202200179 (cit. on pp. 49, 54, 69, 102).

[68] Natali Ostrovsky, Guillaume Le Saux, Uri Argaman, et al. "Templated Assembly of Nanoparticles into Continuous Arrays". en. In: *Langmuir* 37.30 (Aug. 2021), pp. 9098–9110. ISSN: 0743-7463, 1520-5827. DOI: 10.1021/acs.langmuir.1c01188. URL: https://pubs.acs.org/doi/10.1021/acs.langmuir.1c01188 (cit. on pp. 49, 69).

[69] Susan A. P. Van Rossum, Marta Tena-Solsona, Jan H. Van Esch, et al. "Dissipative out-of-equilibrium assembly of man-made supramolecular materials". en. In: *Chem. Soc. Rev.* 46.18 (2017), pp. 5519–5535. ISSN: 0306-0012, 1460-4744. DOI: 10.1039/C7CS00246G. URL: https://xlink.rsc.org/?DOI=C7CS00246G (cit. on pp. 50, 51).

[70] Alessandro Sorrenti, Jorge Leira-Iglesias, Albert J. Markvoort, et al. "Non-equilibrium supramolecular polymerization". en. In: *Chem. Soc. Rev.* 46.18 (2017), pp. 5476–5490. ISSN: 0306-0012, 1460-4744. DOI: 10.1039/C7CS00121E. URL: https://xlink.rsc.org/?DOI=C7CS00121E (cit. on p. 51).

[71] Jacob N. Israelachvili. "Strong Intermolecular Forces". en. In: *Intermolecular and Surface Forces*. Elsevier, 2011, pp. 53–70. ISBN: 978-0-12-391927-4. DOI:

10.1016/B978-0-12-391927-4.10003-9. URL: https://linkinghub.elsevier.com/retrieve/pii/B9780123919274100039 (cit. on p. 51).

[72] Anish Rao, Sumit Roy, Vanshika Jain, et al. "Nanoparticle Self-Assembly: From Design Principles to Complex Matter to Functional Materials". en. In: *ACS Appl. Mater. Interfaces* 15.21 (May 2023), pp. 25248–25274. ISSN: 1944-8244, 1944-8252. DOI: 10.1021/acsami.2c05378. URL: https://pubs.acs.org/doi/10.1021/acsami.2c05378 (cit. on p. 51).

[73] Bo Gao, Gaurav Arya, and Andrea R. Tao. "Self-orienting nanocubes for the assembly of plasmonic nanojunctions". en. In: *Nature Nanotech* 7.7 (July 2012), pp. 433–437. ISSN: 1748-3387, 1748-3395. DOI: 10.1038/nnano.2012.83. URL: https://www.nature.com/articles/nnano.2012.83 (cit. on pp. 51, 52).

[74] Yufei Wang, Yilong Zhou, Quanpeng Yang, et al. "Self-assembly of nanocrystal checkerboard patterns via non-specific interactions". en. In: *Nat Commun* 15.1 (May 2024), p. 3913. ISSN: 2041-1723. DOI: 10.1038/s41467-024-47572-2. URL: https://www.nature.com/articles/s41467-024-47572-2 (cit. on pp. 51, 52).

[75] Binbin Luo, Ziwei Wang, Tine Curk, et al. "Unravelling crystal growth of nanoparticles". en. In: *Nat. Nanotechnol.* 18.6 (June 2023), pp. 589–595. ISSN: 1748-3387, 1748-3395. DOI: 10.1038/s41565-023-01355-w. URL: https://www.nature.com/articles/s41565-023-01355-w (cit. on pp. 52, 53).

[76] Cihan Yilmaz, Asli Sirman, Aditi Halder, et al. "High-Rate Assembly of Nanomaterials on Insulating Surfaces Using Electro-Fluidic Directed Assembly". en. In: *ACS Nano* 11.8 (Aug. 2017), pp. 7679–7689. ISSN: 1936-0851, 1936-086X. DOI: 10.1021/acsnano.6b07477. URL: https://pubs.acs.org/doi/10.1021/acsnano.6b07477 (cit. on p. 54).

[77] Vaibhav Gupta, Swagato Sarkar, Olha Aftenieva, et al. "Nanoimprint Lithography Facilitated Plasmonic-Photonic Coupling for Enhanced Photoconductivity and Photocatalysis". en. In: *Adv Funct Materials* 31.36 (Sept. 2021), p. 2105054. ISSN: 1616-301X, 1616-3028. DOI: 10.1002/adfm.202105054. URL: https://onlinelibrary.wiley.com/doi/10.1002/adfm.202105054 (cit. on pp. 54, 61).

[78] Anna Capitaine, Mehrnaz Bochet-Modaresialam, Peeranuch Poungsripong, et al. "Nanoparticle Imprint Lithography: From Nanoscale Metrology to Printable Metallic Grids". en. In: *ACS Nano* 17.10 (May 2023), pp. 9361–9373. ISSN: 1936-0851, 1936-086X. DOI: 10.1021/acsnano.3c01156. URL: https://pubs.acs.org/doi/10.1021/acsnano.3c01156 (cit. on pp. 54, 61, 71, 134).

[79] Xiaoyu Qi, Luis Alberto Pérez, Jose Mendoza-Carreño, et al. "Chiral plasmonic superlattices from template-assisted assembly of achiral nanoparticles". en. In: *Nat Commun* 16.1 (Feb. 2025), p. 1687. ISSN: 2041-1723. DOI: 10.1038/s41467-025-56999-0. URL: https://www.nature.com/articles/s41467-025-56999-0 (cit. on pp. 54, 55, 61).

[80] Qing-Yuan Lin, Edgar Palacios, Wenjie Zhou, et al. "DNA-Mediated Size-Selective Nanoparticle Assembly for Multiplexed Surface Encoding". en. In: *Nano Lett.* 18.4 (Apr. 2018), pp. 2645–2649. ISSN: 1530-6984, 1530-6992. DOI:

10.1021/acs.nanolett.8b00509. URL: https://pubs.acs.org/doi/10.1021/acs.nanolett.8b00509 (cit. on pp. 55, 56, 61).

[81] Wenjie Zhou, Zizhuo Liu, Ziyin Huang, et al. "Device-quality, reconfigurable metamaterials from shape-directed nanocrystal assembly". en. In: *Proc. Natl. Acad. Sci. U.S.A.* 117.35 (Sept. 2020), pp. 21052–21057. ISSN: 0027-8424, 1091-6490. DOI: 10.1073/pnas.2006797117. URL: https://pnas.org/doi/full/10.1073/pnas.2006797117 (cit. on pp. 55, 56, 61, 102).

[82] Tobias Kraus, Laurent Malaquin, Heinz Schmid, et al. "Nanoparticle printing with single-particle resolution". en. In: *Nature Nanotech* 2.9 (Sept. 2007), pp. 570–576. ISSN: 1748-3387, 1748-3395. DOI: 10.1038/nnano.2007.262. URL: https://www.nature.com/articles/nnano.2007.262 (cit. on pp. 56, 57, 61).

[83] Yu Zhou, Xiaozhu Zhou, Daniel J. Park, et al. "Shape-Selective Deposition and Assembly of Anisotropic Nanoparticles". en. In: *Nano Lett.* 14.4 (Apr. 2014), pp. 2157–2161. ISSN: 1530-6984, 1530-6992. DOI: 10.1021/nl500471g. URL: https://pubs.acs.org/doi/10.1021/nl500471g (cit. on pp. 56, 61).

[84] Valentin Flauraud, Massimo Mastrangeli, Gabriel D. Bernasconi, et al. "Nanoscale topographical control of capillary assembly of nanoparticles". en. In: *Nature Nanotech* 12.1 (Jan. 2017), pp. 73–80. ISSN: 1748-3387, 1748-3395. DOI: 10.1038/nnano.2016.179. URL: https://www.nature.com/articles/nnano.2016.179 (cit. on pp. 56, 57, 61).

[85] Juhoon Kang, Chang-Goo Park, Su-Han Lee, et al. "Fabrication of high aspect ratio nanogrid transparent electrodes via capillary assembly of Ag nanoparticles". en. In: *Nanoscale* 8.21 (2016), pp. 11217–11223. ISSN: 2040-3364, 2040-3372. DOI: 10.1039/C6NR01896C. URL: https://xlink.rsc.org/?DOI=C6NR01896C (cit. on pp. 56, 102).

[86] Songbo Ni, Heiko Wolf, and Lucio Isa. "Programmable Assembly of Hybrid Nanoclusters". en. In: *Langmuir* 34.7 (Feb. 2018), pp. 2481–2488. ISSN: 0743-7463, 1520-5827. DOI: 10.1021/acs.langmuir.7b03944. URL: https://pubs.acs.org/doi/10.1021/acs.langmuir.7b03944 (cit. on pp. 56, 102).

[87] Anna Capitaine, Muhammad L. Fajri, and Beniamino Sciacca. "Pushing the Limits of Capillary Assembly for the Arbitrary Positioning of Sub-50nm Nanocubes in Printable Plasmonic Surfaces". en. In: *Small Methods* 8.2 (Feb. 2024), p. 2300373. ISSN: 2366-9608, 2366-9608. DOI: 10.1002/smtd.202300373. URL: https://onlinelibrary.wiley.com/doi/10.1002/smtd.202300373 (cit. on pp. 56, 210).

[88] Pawel Pieranski. "Two-Dimensional Interfacial Colloidal Crystals". en. In: *Phys. Rev. Lett.* 45.7 (Aug. 1980), pp. 569–572. ISSN: 0031-9007. DOI: 10.1103/PhysRevLett.45.569. URL: https://link.aps.org/doi/10.1103/PhysRevLett.45.569 (cit. on p. 57).

[89] Andrea R. Tao, Jiaxing Huang, and Peidong Yang. "Langmuir-Blodgettry of Nanocrystals and Nanowires". en. In: *Acc. Chem. Res.* 41.12 (Dec. 2008), pp. 1662–1673. ISSN: 0001-4842, 1520-4898. DOI: 10.1021/ar8000525. URL: https://pubs.acs.org/doi/10.1021/ar8000525 (cit. on pp. 57, 58).

[90] Angang Dong, Jun Chen, Patrick M. Vora, et al. "Binary nanocrystal superlattice membranes self-assembled at the liquid–air interface". en. In: *Nature* 466.7305 (July 2010), pp. 474–477. ISSN: 0028-0836, 1476-4687. DOI: 10.1038/nature09188. URL: https://www.nature.com/articles/nature09188 (cit. on p. 58).

[91] Taejong Paik, Hongseok Yun, Blaise Fleury, et al. "Hierarchical Materials Design by Pattern Transfer Printing of Self-Assembled Binary Nanocrystal Superlattices". en. In: *Nano Lett.* 17.3 (Mar. 2017), pp. 1387–1394. ISSN: 1530-6984, 1530-6992. DOI: 10.1021/acs.nanolett.6b04279. URL: https://pubs.acs.org/doi/10.1021/acs.nanolett.6b04279 (cit. on pp. 58, 60, 61).

[92] Ihor Cherniukh, Taras V. Sekh, Gabriele Rainò, et al. "Structural Diversity in Multicomponent Nanocrystal Superlattices Comprising Lead Halide Perovskite Nanocubes". en. In: *ACS Nano* 16.5 (May 2022), pp. 7210–7232. ISSN: 1936-0851, 1936-086X. DOI: 10.1021/acsnano.1c10702. URL: https://pubs.acs.org/doi/10.1021/acsnano.1c10702 (cit. on p. 58).

[93] Qianhui Cheng, Hetong Fang, Rui Cao, et al. "Interfacial self-assembly of nanoparticles into macroscopic, monolayered films". en. In: *Supramolecular Materials* 1 (Dec. 2022), p. 100021. ISSN: 26672405. DOI: 10.1016/j.supmat.2022.100021. URL: https://linkinghub.elsevier.com/retrieve/pii/S2667240522000149 (cit. on p. 58).

[94] Michal Swierczewski and Thomas Bürgi. "Langmuir and Langmuir–Blodgett Films of Gold and Silver Nanoparticles". en. In: *Langmuir* 39.6 (Feb. 2023), pp. 2135–2151. ISSN: 0743-7463, 1520-5827. DOI: 10.1021/acs.langmuir.2c02715. URL: https://pubs.acs.org/doi/10.1021/acs.langmuir.2c02715 (cit. on pp. 59, 60).

[95] Andrea Tao, Prasert Sinsermsuksakul, and Peidong Yang. "Tunable plasmonic lattices of silver nanocrystals". en. In: *Nature Nanotech* 2.7 (July 2007), pp. 435–440. ISSN: 1748-3387, 1748-3395. DOI: 10.1038/nnano.2007.189. URL: https://www.nature.com/articles/nnano.2007.189 (cit. on pp. 59, 86).

[96] Peter A. Kralchevsky and Nikolai D. Denkov. "Capillary forces and structuring in layers of colloid particles". en. In: *Current Opinion in Colloid & Interface Science* 6.4 (Aug. 2001), pp. 383–401. ISSN: 13590294. DOI: 10.1016/S1359-0294(01)00105-4. URL: https://linkinghub.elsevier.com/retrieve/pii/S1359029401001054 (cit. on pp. 59, 89).

[97] Shujuan Huang, Gen Tsutsui, Hiroyuki Sakaue, et al. "Experimental conditions for a highly ordered monolayer of gold nanoparticles fabricated by the Langmuir–Blodgett method". en. In: *Journal of Vacuum Science & Technology B: Microelectronics and Nanometer Structures Processing, Measurement, and Phenomena* 19.6 (Nov. 2001), pp. 2045–2049. ISSN: 1071-1023, 1520-8567. DOI: 10.1116/1.1410943. URL: https://pubs.aip.org/jvb/article/19/6/2045/468977/Experimental-conditions-for-a-highly-ordered (cit. on p. 59).

[98] Shujuan Huang, Gen Tsutsui, Hiroyuki Sakaue, et al. "Formation of a large-scale Langmuir–Blodgett monolayer of alkanethiol-encapsulated gold particles". en.

In: *Journal of Vacuum Science & Technology B: Microelectronics and Nanometer Structures Processing, Measurement, and Phenomena* 19.1 (Jan. 2001), pp. 115–120. ISSN: 1071-1023, 1520-8567. DOI: 10.1116/1.1335678. URL: https://pubs.aip.org/jvb/article/19/1/115/468521/Formation-of-a-large-scale-Langmuir-Blodgett (cit. on p. 59).

[99] Miguel Ángel Fernández-Rodríguez, Roey Elnathan, Ran Ditcovski, et al. "Tunable 2D binary colloidal alloys for soft nanotemplating". en. In: *Nanoscale* 10.47 (2018), pp. 22189–22195. ISSN: 2040-3364, 2040-3372. DOI: 10.1039/C8NR07059H. URL: http://xlink.rsc.org/?DOI=C8NR07059H (cit. on pp. 60, 61).

[100] Qijie Guo, Xiaowei Teng, Saifur Rahman, et al. "Patterned Langmuir-Blodgett Films of Monodisperse Nanoparticles of Iron Oxide Using Soft Lithography". en. In: *J. Am. Chem. Soc.* 125.3 (Jan. 2003), pp. 630–631. ISSN: 0002-7863, 1520-5126. DOI: 10.1021/ja0275764. URL: https://pubs.acs.org/doi/10.1021/ja0275764 (cit. on pp. 60, 61).

[101] Naihao Chiang, Leonardo Scarabelli, Gail A. Vinnacombe-Willson, et al. "Large-Scale Soft-Lithographic Patterning of Plasmonic Nanoparticles". en. In: *ACS Mater. Lett.* 3.3 (Mar. 2021), pp. 282–289. ISSN: 2639-4979, 2639-4979. DOI: 10.1021/acsmaterialslett.0c00535. URL: https://pubs.acs.org/doi/10.1021/acsmaterialslett.0c00535 (cit. on pp. 60, 61).

[102] Venugopal Santhanam and Ronald P. Andres. "Microcontact Printing of Uniform Nanoparticle Arrays". en. In: *Nano Lett.* 4.1 (Jan. 2004), pp. 41–44. ISSN: 1530-6984, 1530-6992. DOI: 10.1021/nl034851r. URL: https://pubs.acs.org/doi/10.1021/nl034851r (cit. on p. 61).

[103] Mindaugas Juodėnas, Tomas Tamulevičius, Joel Henzie, et al. "Surface Lattice Resonances in Self-Assembled Arrays of Monodisperse Ag Cuboctahedra". en. In: *ACS Nano* 13.8 (Aug. 2019), pp. 9038–9047. ISSN: 1936-0851, 1936-086X. DOI: 10.1021/acsnano.9b03191. URL: https://pubs.acs.org/doi/10.1021/acsnano.9b03191 (cit. on p. 61).

[104] Mindaugas Juodėnas, Domantas Peckus, Tomas Tamulevičius, et al. "Effect of Ag Nanocube Optomechanical Modes on Plasmonic Surface Lattice Resonances". en. In: *ACS Photonics* 7.11 (Nov. 2020), pp. 3130–3140. ISSN: 2330-4022, 2330-4022. DOI: 10.1021/acsphotonics.0c01187. URL: https://pubs.acs.org/doi/10.1021/acsphotonics.0c01187 (cit. on p. 61).

[105] Pau Molet, Nicolás Passarelli, Luis A. Pérez, et al. "Engineering Plasmonic Colloidal Meta-Molecules for Tunable Photonic Supercrystals". en. In: *Advanced Optical Materials* 9.20 (Oct. 2021), p. 2100761. ISSN: 2195-1071, 2195-1071. DOI: 10.1002/adom.202100761. URL: https://onlinelibrary.wiley.com/doi/10.1002/adom.202100761 (cit. on p. 61).

[106] Ylli Conti, Nicolas Passarelli, Jose Mendoza-Carreño, et al. "Colloidal Silver Nanoparticle Plasmonic Arrays for Versatile Lasing Architectures via Template-Assisted Self-Assembly". en. In: *Advanced Optical Materials* 11.23 (Dec. 2023), p. 2300983. ISSN: 2195-1071, 2195-1071. DOI: 10.1002/adom.202300983. URL:

https://onlinelibrary.wiley.com/doi/10.1002/adom.202300983 (cit. on p. 61).

[107] Jose Mendoza-Carreño, Pau Molet, Clara Otero-Martínez, et al. "Nanoimprinted 2D-Chiral Perovskite Nanocrystal Metasurfaces for Circularly Polarized Photoluminescence". en. In: *Advanced Materials* (Mar. 2023), p. 2210477. ISSN: 0935-9648, 1521-4095. DOI: 10.1002/adma.202210477. URL: https://onlinelibrary.wiley.com/doi/10.1002/adma.202210477 (cit. on p. 61).

[108] Gail A. Vinnacombe-Willson, Ylli Conti, Andrei Stefancu, et al. "Direct Bottom-Up *In Situ* Growth: A Paradigm Shift for Studies in Wet-Chemical Synthesis of Gold Nanoparticles". en. In: *Chem. Rev.* 123.13 (July 2023), pp. 8488–8529. ISSN: 0009-2665, 1520-6890. DOI: 10.1021/acs.chemrev.2c00914. URL: https://pubs.acs.org/doi/10.1021/acs.chemrev.2c00914 (cit. on pp. 61, 62, 118).

[109] Gail A. Vinnacombe-Willson, Joy K. Lee, Naihao Chiang, et al. "Exploring the Bottom-Up Growth of Anisotropic Gold Nanoparticles from Substrate-Bound Seeds in Microfluidic Reactors". en. In: *ACS Appl. Nano Mater.* 6.8 (Apr. 2023), pp. 6454–6460. ISSN: 2574-0970, 2574-0970. DOI: 10.1021/acsanm.3c00440. URL: https://pubs.acs.org/doi/10.1021/acsanm.3c00440 (cit. on pp. 62, 118).

[110] Marie-Pier Côté, Christina Boukouvala, Josée Richard-Daniel, et al. "Plasmonic Properties of Self-Assembled Gold Nanocrescents: Implications for Chemical Sensing". en. In: *ACS Appl. Nano Mater.* 7.8 (Apr. 2024), pp. 8783–8791. ISSN: 2574-0970, 2574-0970. DOI: 10.1021/acsanm.4c00258. URL: https://pubs.acs.org/doi/10.1021/acsanm.4c00258 (cit. on pp. 62, 102, 118).

[111] Jiating He, Yawen Wang, Yuhua Feng, et al. "Forest of Gold Nanowires: A New Type of Nanocrystal Growth". en. In: *ACS Nano* 7.3 (Mar. 2013), pp. 2733–2740. ISSN: 1936-0851, 1936-086X. DOI: 10.1021/nn4001885. URL: https://pubs.acs.org/doi/10.1021/nn4001885 (cit. on pp. 62, 118).

[112] Aneta J. Mieszawska, Grzegorz W. Slawinski, and Francis P. Zamborini. "Directing the Growth of Highly Aligned Gold Nanorods through a Surface Chemical Amidation Reaction". en. In: *J. Am. Chem. Soc.* 128.17 (May 2006), pp. 5622–5623. ISSN: 0002-7863, 1520-5126. DOI: 10.1021/ja061046g. URL: https://pubs.acs.org/doi/10.1021/ja061046g (cit. on pp. 62, 118).

[113] Titoo Jain, Samuel Lara-Avila, Yann-Vai Kervennic, et al. "Aligned Growth of Gold Nanorods in PMMA Channels: Parallel Preparation of Nanogaps". en. In: *ACS Nano* 6.5 (May 2012), pp. 3861–3867. ISSN: 1936-0851, 1936-086X. DOI: 10.1021/nn204986y. URL: https://pubs.acs.org/doi/10.1021/nn204986y (cit. on pp. 62, 118).

[114] Nurit Taub, Olga Krichevski, and Gil Markovich. "Growth of Gold Nanorods on Surfaces". en. In: *J. Phys. Chem. B* 107.42 (Oct. 2003), pp. 11579–11582. ISSN: 1520-6106, 1520-5207. DOI: 10.1021/jp036144s. URL: https://pubs.acs.org/doi/10.1021/jp036144s (cit. on pp. 62, 118).

[115] Michael J. Ashley, Marc R. Bourgeois, Raghavendra R. Murthy, et al. "Shape and Size Control of Substrate-Grown Gold Nanoparticles for Surface-Enhanced Raman Spectroscopy Detection of Chemical Analytes". en. In: *J. Phys. Chem. C* 122.4 (Feb. 2018), pp. 2307–2314. ISSN: 1932-7447, 1932-7455. DOI: 10.1021/acs.jpcc.7b11440. URL: https://pubs.acs.org/doi/10.1021/acs.jpcc.7b11440 (cit. on pp. 62, 118).

[116] Guoliang Liu, Chuan Zhang, Jinsong Wu, et al. "Using Scanning-Probe Block Copolymer Lithography and Electron Microscopy To Track Shape Evolution in Multimetallic Nanoclusters". en. In: *ACS Nano* 9.12 (Dec. 2015), pp. 12137–12145. ISSN: 1936-0851, 1936-086X. DOI: 10.1021/acsnano.5b05191. URL: https://pubs.acs.org/doi/10.1021/acsnano.5b05191 (cit. on pp. 62, 118).

[117] Eredzhep Menumerov, Spencer D. Golze, Robert A. Hughes, et al. "Arrays of highly complex noble metal nanostructures using nanoimprint lithography in combination with liquid-phase epitaxy". en. In: *Nanoscale* 10.38 (2018), pp. 18186–18194. ISSN: 2040-3364, 2040-3372. DOI: 10.1039/C8NR06874G. URL: https://xlink.rsc.org/?DOI=C8NR06874G (cit. on pp. 62, 118).

[118] Arin S. Preston, Robert A. Hughes, Trevor B. Demille, et al. "Dewetted nanostructures of gold, silver, copper, and palladium with enhanced faceting". en. In: *Acta Materialia* 165 (Feb. 2019), pp. 15–25. ISSN: 13596454. DOI: 10.1016/j.actamat.2018.11.036. URL: https://linkinghub.elsevier.com/retrieve/pii/S1359645418309121 (cit. on pp. 62, 118).

[119] Robert D. Neal, Zachary R. Lawson, Walker J. Tuff, et al. "Large-Area Periodic Arrays of Atomically Flat Single-Crystal Gold Nanotriangles Formed Directly on Substrate Surfaces". en. In: *Small* 18.52 (Dec. 2022), p. 2205780. ISSN: 1613-6810, 1613-6829. DOI: 10.1002/smll.202205780. URL: https://onlinelibrary.wiley.com/doi/10.1002/smll.202205780 (cit. on pp. 62, 118).

[120] Zachary R. Lawson, Kaikui Xu, Christina Boukouvala, et al. "Large-area arrays of epitaxially aligned silver nanotriangles seeded by gold nanostructures". en. In: *Mater. Chem. Front.* 8.9 (2024), pp. 2149–2160. ISSN: 2052-1537. DOI: 10.1039/D3QM01184D. URL: https://xlink.rsc.org/?DOI=D3QM01184D (cit. on pp. 62, 118).

[121] Spencer D. Golze, Robert A. Hughes, Sergei Rouvimov, et al. "Plasmon-Mediated Synthesis of Periodic Arrays of Gold Nanoplates Using Substrate-Immobilized Seeds Lined with Planar Defects". en. In: *Nano Lett.* 19.8 (Aug. 2019), pp. 5653–5660. ISSN: 1530-6984, 1530-6992. DOI: 10.1021/acs.nanolett.9b02215. URL: https://pubs.acs.org/doi/10.1021/acs.nanolett.9b02215 (cit. on pp. 62, 118).

[122] Trevor B. Demille, Robert D. Neal, Arin S. Preston, et al. "Epitaxially aligned single-crystal gold nanoplates formed in large-area arrays at high yield". en. In: *Nano Res.* 15.1 (Jan. 2022), pp. 296–303. ISSN: 1998-0124, 1998-0000. DOI: 10.1007/s12274-021-3473-1. URL: https://link.springer.com/10.1007/s12274-021-3473-1 (cit. on pp. 62, 118).

[123] Artavazd Kirakosyan, Jiye Kim, Sung Woo Lee, et al. "Optical Properties of Colloidal CH_3 NH_3 $PbBr_3$ Nanocrystals by Controlled Growth of Lateral Dimension". en. In: *Crystal Growth & Design* 17.2 (Feb. 2017), pp. 794–799. ISSN: 1528-7483, 1528-7505. DOI: 10.1021/acs.cgd.6b01648. URL: https://pubs.acs.org/doi/10.1021/acs.cgd.6b01648 (cit. on p. 62).

[124] Spencer D. Golze, Stefania Porcu, Chen Zhu, et al. "Sequential Symmetry-Breaking Events as a Synthetic Pathway for Chiral Gold Nanostructures with Spiral Geometries". en. In: *Nano Lett.* 21.7 (Apr. 2021), pp. 2919–2925. ISSN: 1530-6984, 1530-6992. DOI: 10.1021/acs.nanolett.0c05105. URL: https://pubs.acs.org/doi/10.1021/acs.nanolett.0c05105 (cit. on p. 62).

[125] Aleksandr Barulin, Dang Du Nguyen, Yangkyu Kim, et al. "Metasurfaces for Quantitative Biosciences of Molecules, Cells, and Tissues: Sensing and Diagnostics". en. In: *ACS Photonics* 11.3 (Mar. 2024), pp. 904–916. ISSN: 2330-4022, 2330-4022. DOI: 10.1021/acsphotonics.3c01576. URL: https://pubs.acs.org/doi/10.1021/acsphotonics.3c01576 (cit. on p. 69).

[126] Ferry Anggoro Ardy Nugroho, Ping Bai, Iwan Darmadi, et al. "Inverse designed plasmonic metasurface with parts per billion optical hydrogen detection". en. In: *Nat Commun* 13.1 (Sept. 2022), p. 5737. ISSN: 2041-1723. DOI: 10.1038/s41467-022-33466-8. URL: https://www.nature.com/articles/s41467-022-33466-8 (cit. on p. 69).

[127] Yibo Zhu, Zhaoyi Li, Zhuang Hao, et al. "Optical conductivity-based ultrasensitive mid-infrared biosensing on a hybrid metasurface". en. In: *Light Sci. Appl.* 7.1 (Sept. 2018), p. 67. ISSN: 2047-7538. DOI: 10.1038/s41377-018-0066-1. URL: https://www.nature.com/articles/s41377-018-0066-1 (cit. on p. 69).

[128] Wei Ting Chen, Alexander Y. Zhu, Vyshakh Sanjeev, et al. "A broadband achromatic metalens for focusing and imaging in the visible". en. In: *Nature Nanotech* 13.3 (Mar. 2018), pp. 220–226. ISSN: 1748-3387, 1748-3395. DOI: 10.1038/s41565-017-0034-6. URL: https://www.nature.com/articles/s41565-017-0034-6 (cit. on p. 69).

[129] Shuming Wang, Pin Chieh Wu, Vin-Cent Su, et al. "Broadband achromatic optical metasurface devices". en. In: *Nat Commun* 8.1 (Aug. 2017), p. 187. ISSN: 2041-1723. DOI: 10.1038/s41467-017-00166-7. URL: https://www.nature.com/articles/s41467-017-00166-7 (cit. on p. 69).

[130] Lingling Huang, Xianzhong Chen, Holger Mühlenbernd, et al. "Three-dimensional optical holography using a plasmonic metasurface". en. In: *Nat Commun* 4.1 (Nov. 2013), p. 2808. ISSN: 2041-1723. DOI: 10.1038/ncomms3808. URL: https://www.nature.com/articles/ncomms3808 (cit. on p. 69).

[131] Luca Mascaretti, Andrea Schirato, Paolo Fornasiero, et al. "Challenges and prospects of plasmonic metasurfaces for photothermal catalysis". en. In: *Nanophotonics* 11.13 (June 2022), pp. 3035–3056. ISSN: 2192-8614. DOI: 10.1515/nanoph-2022-0073. URL: https://www.degruyter.com/document/doi/10.1515/nanoph-2022-0073/html (cit. on p. 69).

[132] Yi-Yang Xie, Pei-Nan Ni, Qiu-Hua Wang, et al. "Metasurface-integrated vertical cavity surface-emitting lasers for programmable directional lasing emissions". en. In: *Nat. Nanotechnol.* 15.2 (Feb. 2020), pp. 125–130. ISSN: 1748-3387, 1748-3395. DOI: 10.1038/s41565-019-0611-y. URL: https://www.nature.com/articles/s41565-019-0611-y (cit. on p. 69).

[133] Heyou Zhang, Calum Kinnear, and Paul Mulvaney. "Fabrication of Single-Nanocrystal Arrays". en. In: *Advanced Materials* 32.18 (May 2020), p. 1904551. ISSN: 0935-9648, 1521-4095. DOI: 10.1002/adma.201904551. URL: https://onlinelibrary.wiley.com/doi/10.1002/adma.201904551 (cit. on pp. 69, 102).

[134] Dong Kyo Oh, Taejun Lee, Byoungsu Ko, et al. "Nanoimprint lithography for high-throughput fabrication of metasurfaces". en. In: *Front. Optoelectron.* 14.2 (June 2021), pp. 229–251. ISSN: 2095-2759, 2095-2767. DOI: 10.1007/s12200-021-1121-8. URL: https://link.springer.com/10.1007/s12200-021-1121-8 (cit. on p. 69).

[135] Vincent J. Einck, Mahsa Torfeh, Andrew McClung, et al. "Scalable Nanoimprint Lithography Process for Manufacturing Visible Metasurfaces Composed of High Aspect Ratio TiO_2 Meta-Atoms". en. In: *ACS Photonics* 8.8 (Aug. 2021), pp. 2400–2409. ISSN: 2330-4022, 2330-4022. DOI: 10.1021/acsphotonics.1c00609. URL: https://pubs.acs.org/doi/10.1021/acsphotonics.1c00609 (cit. on p. 69).

[136] Mehrnaz Modaresialam, Zeinab Chehadi, Thomas Bottein, et al. "Nanoimprint Lithography Processing of Inorganic-Based Materials". en. In: *Chem. Mater.* 33.14 (July 2021), pp. 5464–5482. ISSN: 0897-4756, 1520-5002. DOI: 10.1021/acs.chemmater.1c00693. URL: https://pubs.acs.org/doi/10.1021/acs.chemmater.1c00693 (cit. on p. 69).

[137] Y. S. Oh, D. Y. Choi, and H. J. Sung. "Direct imprinting of thermally reduced silver nanoparticles via deformation-driven ink injection for high-performance, flexible metal grid embedded transparent conductors". en. In: *RSC Adv.* 5.79 (2015), pp. 64661–64668. ISSN: 2046-2069. DOI: 10.1039/C5RA09431C. URL: https://xlink.rsc.org/?DOI=C5RA09431C (cit. on p. 69).

[138] Boya Radha, Su Hui Lim, Mohammad S. M. Saifullah, et al. "Metal hierarchical patterning by direct nanoimprint lithography". en. In: *Sci Rep* 3.1 (Feb. 2013), p. 1078. ISSN: 2045-2322. DOI: 10.1038/srep01078. URL: https://www.nature.com/articles/srep01078 (cit. on p. 69).

[139] Zhaogang Dong, Mohamed Asbahi, Jian Lin, et al. "Second-Harmonic Generation from Sub-5 nm Gaps by Directed Self-Assembly of Nanoparticles onto Template-Stripped Gold Substrates". en. In: *Nano Lett.* 15.9 (Sept. 2015), pp. 5976–5981. ISSN: 1530-6984, 1530-6992. DOI: 10.1021/acs.nanolett.5b02109. URL: https://pubs.acs.org/doi/10.1021/acs.nanolett.5b02109 (cit. on p. 69).

[140] Mohamed Asbahi, FuKe Wang, Zhaogang Dong, et al. "Directed self-assembly of sub-10 nm particle clusters using topographical templates". In: *Nanotechnology* 27.42 (Oct. 2016), p. 424001. ISSN: 0957-4484, 1361-6528. DOI: 10.1088/

0957-4484/27/42/424001. URL: https://iopscience.iop.org/article/10.1088/0957-4484/27/42/424001 (cit. on p. 69).

[141] Bridget Ingham, Teck H. Lim, Christian J. Dotzler, et al. "How Nanoparticles Coalesce: An in Situ Study of Au Nanoparticle Aggregation and Grain Growth". en. In: *Chem. Mater.* 23.14 (July 2011), pp. 3312–3317. ISSN: 0897-4756, 1520-5002. DOI: 10.1021/cm200354d. URL: https://pubs.acs.org/doi/10.1021/cm200354d (cit. on p. 83).

[142] Siyam M. Ansar, Fathima S. Ameer, Wenfang Hu, et al. "Removal of Molecular Adsorbates on Gold Nanoparticles Using Sodium Borohydride in Water". en. In: *Nano Lett.* 13.3 (Mar. 2013), pp. 1226–1229. ISSN: 1530-6984, 1530-6992. DOI: 10.1021/nl304703w. URL: https://pubs.acs.org/doi/10.1021/nl304703w (cit. on pp. 83, 104, 211).

[143] Houssein Awada, Olivier Noel, Tayssir Hamieh, et al. "Contributions of chemical and mechanical surface properties and temperature effect on the adhesion at the nanoscale". en. In: *Thin Solid Films* 519.11 (Mar. 2011), pp. 3690–3694. ISSN: 00406090. DOI: 10.1016/j.tsf.2011.01.261. URL: https://linkinghub.elsevier.com/retrieve/pii/S0040609011003245 (cit. on p. 85).

[144] Weikun Zhu, Peter F. Satterthwaite, Patricia Jastrzebska-Perfect, et al. "Nanoparticle contact printing with interfacial engineering for deterministic integration into functional structures". en. In: *Sci. Adv.* 8.43 (Oct. 2022), eabq4869. ISSN: 2375-2548. DOI: 10.1126/sciadv.abq4869. URL: https://www.science.org/doi/10.1126/sciadv.abq4869 (cit. on p. 85).

[145] Krassimir D. Danov, Peter A. Kralchevsky, Boris N. Naydenov, et al. "Interactions between particles with an undulated contact line at a fluid interface: Capillary multipoles of arbitrary order". en. In: *Journal of Colloid and Interface Science* 287.1 (July 2005), pp. 121–134. ISSN: 00219797. DOI: 10.1016/j.jcis.2005.01.079. URL: https://linkinghub.elsevier.com/retrieve/pii/S0021979705000895 (cit. on p. 89).

[146] J. Alexander Liddle, Yi Cui, and Paul Alivisatos. "Lithographically directed self-assembly of nanostructures". en. In: *Journal of Vacuum Science & Technology B: Microelectronics and Nanometer Structures Processing, Measurement, and Phenomena* 22.6 (Nov. 2004), pp. 3409–3414. ISSN: 1071-1023, 1520-8567. DOI: 10.1116/1.1821572. URL: https://pubs.aip.org/jvb/article/22/6/3409/898331/Lithographically-directed-self-assembly-of (cit. on p. 89).

[147] Janos H Fendler. "Nanoparticles at air/water interfaces". en. In: *Current Opinion in Colloid & Interface Science* 1.2 (Apr. 1996), pp. 202–207. ISSN: 13590294. DOI: 10.1016/S1359-0294(96)80005-7. URL: https://linkinghub.elsevier.com/retrieve/pii/S1359029496800057 (cit. on p. 89).

[148] Xiaozhen Ma, Ngoc N. Nguyen, and Anh V. Nguyen. "A review on quantifying the influence of lateral capillary interactions on the particle floatability and stability of particle-laden interfaces". en. In: *Advances in Colloid and Interface Science* 307 (Sept. 2022), p. 102731. ISSN: 00018686. DOI: 10.1016/j.cis.

2022.102731. URL: https://linkinghub.elsevier.com/retrieve/pii/S0001868622001336 (cit. on p. 89).

[149] Jie Hu, Sankhyabrata Bandyopadhyay, Yu-hui Liu, et al. "A Review on Metasurface: From Principle to Smart Metadevices". en. In: *Front. Phys.* 8 (Jan. 2021), p. 586087. ISSN: 2296-424X. DOI: 10.3389/fphy.2020.586087. URL: https://www.frontiersin.org/articles/10.3389/fphy.2020.586087/full (cit. on pp. 92, 93).

[150] Hou-Tong Chen, Antoinette J Taylor, and Nanfang Yu. "A review of metasurfaces: physics and applications". In: *Rep. Prog. Phys.* 79.7 (July 2016), p. 076401. ISSN: 0034-4885, 1361-6633. DOI: 10.1088/0034-4885/79/7/076401. URL: https://iopscience.iop.org/article/10.1088/0034-4885/79/7/076401 (cit. on p. 92).

[151] Erez Hasman, Vladimir Kleiner, Gabriel Biener, et al. "Polarization dependent focusing lens by use of quantized Pancharatnam–Berry phase diffractive optics". en. In: *Applied Physics Letters* 82.3 (Jan. 2003), pp. 328–330. ISSN: 0003-6951, 1077-3118. DOI: 10.1063/1.1539300. URL: https://pubs.aip.org/apl/article/82/3/328/512861/Polarization-dependent-focusing-lens-by-use-of (cit. on p. 93).

[152] Nanfang Yu, Patrice Genevet, Mikhail A. Kats, et al. "Light Propagation with Phase Discontinuities: Generalized Laws of Reflection and Refraction". en. In: *Science* 334.6054 (Oct. 2011), pp. 333–337. ISSN: 0036-8075, 1095-9203. DOI: 10.1126/science.1210713. URL: https://www.science.org/doi/10.1126/science.1210713 (cit. on p. 93).

[153] Nanfang Yu, P. Genevet, F. Aieta, et al. "Flat Optics: Controlling Wavefronts With Optical Antenna Metasurfaces". In: *IEEE J. Select. Topics Quantum Electron.* 19.3 (May 2013), pp. 4700423–4700423. ISSN: 1077-260X, 1558-4542. DOI: 10.1109/JSTQE.2013.2241399. URL: http://ieeexplore.ieee.org/document/6415977/ (cit. on p. 93).

[154] Xingjie Ni, Naresh K. Emani, Alexander V. Kildishev, et al. "Broadband Light Bending with Plasmonic Nanoantennas". en. In: *Science* 335.6067 (Jan. 2012), pp. 427–427. ISSN: 0036-8075, 1095-9203. DOI: 10.1126/science.1214686. URL: https://www.science.org/doi/10.1126/science.1214686 (cit. on p. 95).

[155] Adelin Patoux, Gonzague Agez, Christian Girard, et al. "Challenges in nanofabrication for efficient optical metasurfaces". en. In: *Sci Rep* 11.1 (Mar. 2021), p. 5620. ISSN: 2045-2322. DOI: 10.1038/s41598-021-84666-z. URL: https://www.nature.com/articles/s41598-021-84666-z (cit. on p. 96).

[156] Xue Feng, Matthew A. Meitl, Audrey M. Bowen, et al. "Competing Fracture in Kinetically Controlled Transfer Printing". en. In: *Langmuir* 23.25 (Dec. 2007), pp. 12555–12560. ISSN: 0743-7463, 1520-5827. DOI: 10.1021/la701555n. URL: https://pubs.acs.org/doi/10.1021/la701555n (cit. on p. 99).

[157] Matthew A. Meitl, Zheng-Tao Zhu, Vipan Kumar, et al. "Transfer printing by kinetic control of adhesion to an elastomeric stamp". en. In: *Nat. Mater.* 5.1

(Jan. 2006), pp. 33–38. ISSN: 1476-1122, 1476-4660. DOI: 10.1038/nmat1532. URL: https://www.nature.com/articles/nmat1532 (cit. on p. 99).

[158] Yonas Lebsir, Sergejs Boroviks, Martin Thomaschewski, et al. "Ultimate Limit for Optical Losses in Gold, Revealed by Quantitative Near-Field Microscopy". en. In: *Nano Lett.* 22.14 (July 2022), pp. 5759–5764. ISSN: 1530-6984, 1530-6992. DOI: 10.1021/acs.nanolett.2c01059. URL: https://pubs.acs.org/doi/10.1021/acs.nanolett.2c01059 (cit. on p. 102).

[159] Sergejs Boroviks, Francesco Todisco, N. Asger Mortensen, et al. "Use of monocrystalline gold flakes for gap plasmon-based metasurfaces operating in the visible". en. In: *Opt. Mater. Express* 9.11 (Nov. 2019), p. 4209. ISSN: 2159-3930. DOI: 10.1364/OME.9.004209. URL: https://opg.optica.org/abstract.cfm?URI=ome-9-11-4209 (cit. on p. 102).

[160] Yanwen Wu, Chengdong Zhang, N. Mohammadi Estakhri, et al. "Intrinsic Optical Properties and Enhanced Plasmonic Response of Epitaxial Silver". en. In: *Advanced Materials* 26.35 (Sept. 2014), pp. 6106–6110. ISSN: 0935-9648, 1521-4095. DOI: 10.1002/adma.201401474. URL: https://onlinelibrary.wiley.com/doi/10.1002/adma.201401474 (cit. on p. 102).

[161] Sasan V. Grayli, Xin Zhang, Finlay C. MacNab, et al. "Scalable, Green Fabrication of Single-Crystal Noble Metal Films and Nanostructures for Low-Loss Nanotechnology Applications". en. In: *ACS Nano* 14.6 (June 2020), pp. 7581–7592. ISSN: 1936-0851, 1936-086X. DOI: 10.1021/acsnano.0c03466. URL: https://pubs.acs.org/doi/10.1021/acsnano.0c03466 (cit. on p. 102).

[162] Marijn A. Van Huis, Lucas T. Kunneman, Karin Overgaag, et al. "Low-Temperature Nanocrystal Unification through Rotations and Relaxations Probed by in Situ Transmission Electron Microscopy". en. In: *Nano Lett.* 8.11 (Nov. 2008), pp. 3959–3963. ISSN: 1530-6984, 1530-6992. DOI: 10.1021/nl8024467. URL: https://pubs.acs.org/doi/10.1021/nl8024467 (cit. on p. 102).

[163] Yang Lu, Jian Yu Huang, Chao Wang, et al. "Cold welding of ultrathin gold nanowires". en. In: *Nature Nanotech* 5.3 (Mar. 2010), pp. 218–224. ISSN: 1748-3387, 1748-3395. DOI: 10.1038/nnano.2010.4. URL: https://www.nature.com/articles/nnano.2010.4 (cit. on p. 102).

[164] Jing-Rong Ji, John W. Villanova, Salvador Barraza-Lopez, et al. "Defect-Free Nanowelding of Bilayer SnSe Nanoplates". en. In: *Advanced Materials* (July 2024), p. 2312199. ISSN: 0935-9648, 1521-4095. DOI: 10.1002/adma.202312199. URL: https://onlinelibrary.wiley.com/doi/10.1002/adma.202312199 (cit. on p. 102).

[165] Johannes H. M. Maurer, Lola González-García, Beate Reiser, et al. "Templated Self-Assembly of Ultrathin Gold Nanowires by Nanoimprinting for Transparent Flexible Electronics". en. In: *Nano Lett.* 16.5 (May 2016), pp. 2921–2925. ISSN: 1530-6984, 1530-6992. DOI: 10.1021/acs.nanolett.5b04319. URL: https://pubs.acs.org/doi/10.1021/acs.nanolett.5b04319 (cit. on p. 102).

[166] Thomas Kister, Johannes H. M. Maurer, Lola González-García, et al. "Ligand-Dependent Nanoparticle Assembly and Its Impact on the Printing of Transpar-

ent Electrodes". en. In: *ACS Appl. Mater. Interfaces* 10.7 (Feb. 2018), pp. 6079–6083. ISSN: 1944-8244, 1944-8252. DOI: 10.1021/acsami.7b18579. URL: https://pubs.acs.org/doi/10.1021/acsami.7b18579 (cit. on p. 102).

[167] Ying He, Yuan Chen, Qingchi Xu, et al. "Assembly of Ultrathin Gold Nanowires into Honeycomb Macroporous Pattern Films with High Transparency and Conductivity". en. In: *ACS Appl. Mater. Interfaces* 9.8 (Mar. 2017), pp. 7826–7833. ISSN: 1944-8244, 1944-8252. DOI: 10.1021/acsami.6b15016. URL: https://pubs.acs.org/doi/10.1021/acsami.6b15016 (cit. on p. 102).

[168] Lukas F. Engel, Lola González-García, and Tobias Kraus. "Flexible and transparent electrodes imprinted from metal nanostructures: morphology and optoelectronic performance". en. In: *Nanoscale Adv.* 4.16 (2022), pp. 3370–3380. ISSN: 2516-0230. DOI: 10.1039/D2NA00259K. URL: https://xlink.rsc.org/?DOI=D2NA00259K (cit. on p. 102).

[169] Barbara Horváth, Barbora Křivová, Sami Bolat, et al. "Fabrication of Large Area Sub-200 nm Conducting Electrode Arrays by Self-Confinement of Spincoated Metal Nanoparticle Inks". en. In: *Adv Materials Technologies* 4.3 (Mar. 2019), p. 1800652. ISSN: 2365-709X, 2365-709X. DOI: 10.1002/admt.201800652. URL: https://onlinelibrary.wiley.com/doi/10.1002/admt.201800652 (cit. on p. 102).

[170] Oriol Colomer-Ferrer, Serni Toda Cosi, Ylli Conti, et al. "Pre- and post-assembly modifications of colloidal plasmonic arrays: the effect of size distribution, composition and annealing". en. In: *J. Mater. Chem. C* 10.37 (2022), pp. 13913–13921. ISSN: 2050-7526, 2050-7534. DOI: 10.1039/D2TC01148D. URL: https://xlink.rsc.org/?DOI=D2TC01148D (cit. on p. 102).

[171] Pieter F. Moonen, Erhan Bat, W. Pim Voorthuijzen, et al. "Soft-lithographic patterning of room temperature-sintering Ag nanoparticles on foil". en. In: *RSC Adv.* 3.40 (2013), p. 18498. ISSN: 2046-2069. DOI: 10.1039/c3ra43926g. URL: https://xlink.rsc.org/?DOI=c3ra43926g (cit. on p. 102).

[172] Muhammad L. Fajri, Nicolas Kossowski, Ibtissem Bouanane, et al. "Designer Metasurfaces via Nanocube Assembly at the Air–Water Interface". en. In: *ACS Nano* (Aug. 2024), acsnano.4c06022. ISSN: 1936-0851, 1936-086X. DOI: 10.1021/acsnano.4c06022. URL: https://pubs.acs.org/doi/10.1021/acsnano.4c06022 (cit. on pp. 103, 104, 111, 210).

[173] Peeranuch Poungsripong, Vyshnav Kannampalli, Lionel Santinacci, et al. "Statistical and Correlative Characterization of Individual Nanoparticle in Gap Plasmon Resonator Sensors". en. In: *Adv Materials Technologies* 9.18 (Sept. 2024), p. 2400083. ISSN: 2365-709X, 2365-709X. DOI: 10.1002/admt.202400083. URL: https://onlinelibrary.wiley.com/doi/10.1002/admt.202400083 (cit. on p. 104).

[174] Jianbo Wu, Wenpei Gao, Hong Yang, et al. "Dissolution Kinetics of Oxidative Etching of Cubic and Icosahedral Platinum Nanoparticles Revealed by *in Situ* Liquid Transmission Electron Microscopy". en. In: *ACS Nano* 11.2 (Feb. 2017), pp. 1696–1703. ISSN: 1936-0851, 1936-086X. DOI: 10.1021/acsnano.6b07541.

URL: https://pubs.acs.org/doi/10.1021/acsnano.6b07541 (cit. on pp. 105, 110).

[175] Lei Chen, Alberto Leonardi, Jun Chen, et al. "Imaging the kinetics of anisotropic dissolution of bimetallic core–shell nanocubes using graphene liquid cells". en. In: *Nat Commun* 11.1 (June 2020), p. 3041. ISSN: 2041-1723. DOI: 10.1038/s41467-020-16645-3. URL: https://www.nature.com/articles/s41467-020-16645-3 (cit. on pp. 105, 110).

[176] Qingbo Zhang, Yue Hu, Caitlin M. Masterson, et al. "When function is biological: Discerning how silver nanoparticle structure dictates antimicrobial activity". en. In: *iScience* 25.7 (July 2022), p. 104475. ISSN: 25890042. DOI: 10.1016/j.isci.2022.104475. URL: https://linkinghub.elsevier.com/retrieve/pii/S2589004222007465 (cit. on p. 105).

[177] Weijia Zhang, Ping Chen, Qingsheng Gao, et al. "High-Concentration Preparation of Silver Nanowires: Restraining *in Situ* Nitric Acidic Etching by Steel-Assisted Polyol Method". en. In: *Chem. Mater.* 20.5 (Mar. 2008), pp. 1699–1704. ISSN: 0897-4756, 1520-5002. DOI: 10.1021/cm7022554. URL: https://pubs.acs.org/doi/10.1021/cm7022554 (cit. on p. 106).

[178] L. L. Martínez, M. Segarra, M. Fernández, et al. "Kinetics of the dissolution of pure silver and silver-gold alloys in nitric acid solution". en. In: *Metall Trans B* 24.5 (Oct. 1993), pp. 827–837. ISSN: 0360-2141, 2379-0229. DOI: 10.1007/BF02663143. URL: https://link.springer.com/10.1007/BF02663143 (cit. on p. 106).

[179] Jeong-Eun Park, Yeonhee Lee, and Jwa-Min Nam. "Precisely Shaped, Uniformly Formed Gold Nanocubes with Ultrahigh Reproducibility in Single-Particle Scattering and Surface-Enhanced Raman Scattering". en. In: *Nano Lett.* 18.10 (Oct. 2018), pp. 6475–6482. ISSN: 1530-6984, 1530-6992. DOI: 10.1021/acs.nanolett.8b02973. URL: https://pubs.acs.org/doi/10.1021/acs.nanolett.8b02973 (cit. on pp. 108, 193, 197, 199).

[180] Melissa E. King, Isabella A. Kent, and Michelle L. Personick. "Halide-assisted metal ion reduction: emergent effects of dilute chloride, bromide, and iodide in nanoparticle synthesis". en. In: *Nanoscale* 11.33 (2019), pp. 15612–15621. ISSN: 2040-3364, 2040-3372. DOI: 10.1039/C9NR04647J. URL: https://xlink.rsc.org/?DOI=C9NR04647J (cit. on p. 108).

[181] A.M. Bittner. "The growth of the second underpotentially deposited silver layer on Pt(100)". en. In: *Journal of Electroanalytical Chemistry* 431.1 (June 1997), pp. 51–56. ISSN: 15726657. DOI: 10.1016/S0022-0728(97)00269-6. URL: https://linkinghub.elsevier.com/retrieve/pii/S0022072897002696 (cit. on p. 109).

[182] Peter L. Redmond, A. J. Hallock, and Louis E. Brus. "Electrochemical Ostwald Ripening of Colloidal Ag Particles on Conductive Substrates". en. In: *Nano Lett.* 5.1 (Jan. 2005), pp. 131–135. ISSN: 1530-6984, 1530-6992. DOI: 10.1021/nl048204r. URL: https://pubs.acs.org/doi/10.1021/nl048204r (cit. on p. 111).

[183] Hyo-Ju Lee, Semi Oh, Ki-Yeop Cho, et al. "Spontaneous and Selective Nanowelding of Silver Nanowires by Electrochemical Ostwald Ripening and High Electrostatic Potential at the Junctions for High-Performance Stretchable Transparent Electrodes". en. In: *ACS Appl. Mater. Interfaces* 10.16 (Apr. 2018), pp. 14124–14131. ISSN: 1944-8244, 1944-8252. DOI: 10.1021/acsami.8b00837. URL: https://pubs.acs.org/doi/10.1021/acsami.8b00837 (cit. on p. 111).

[184] Veronica Pawlik, Shan Zhou, Siyu Zhou, et al. "Silver Nanocubes: From Serendipity to Mechanistic Understanding, Rational Synthesis, and Niche Applications". en. In: *Chem. Mater.* 35.9 (May 2023), pp. 3427–3449. ISSN: 0897-4756, 1520-5002. DOI: 10.1021/acs.chemmater.3c00472. URL: https://pubs.acs.org/doi/10.1021/acs.chemmater.3c00472 (cit. on p. 111).

[185] Younan Xia, Yujie Xiong, Byungkwon Lim, et al. "Shape-Controlled Synthesis of Metal Nanocrystals: Simple Chemistry Meets Complex Physics?" en. In: *Angew Chem Int Ed* 48.1 (Jan. 2009), pp. 60–103. ISSN: 1433-7851, 1521-3773. DOI: 10.1002/anie.200802248. URL: https://onlinelibrary.wiley.com/doi/10.1002/anie.200802248 (cit. on p. 118).

[186] Charles Vernier, Lucien Saviot, Yinan Fan, et al. "Sensitivity of Localized Surface Plasmon Resonance and Acoustic Vibrations to Edge Rounding in Silver Nanocubes". en. In: *ACS Nano* 17.20 (Oct. 2023), pp. 20462–20472. ISSN: 1936-0851, 1936-086X. DOI: 10.1021/acsnano.3c06990. URL: https://pubs.acs.org/doi/10.1021/acsnano.3c06990 (cit. on p. 119).

[187] Yanyun Ma, Weiyang Li, Eun Chul Cho, et al. "Au@Ag Core-Shell Nanocubes with Finely Tuned and Well-Controlled Sizes, Shell Thicknesses, and Optical Properties". en. In: *ACS Nano* 4.11 (Nov. 2010), pp. 6725–6734. ISSN: 1936-0851, 1936-086X. DOI: 10.1021/nn102237c. URL: https://pubs.acs.org/doi/10.1021/nn102237c (cit. on p. 119).

[188] Sergey Yu Kireev and Yury P Perelygin. "Potential dependence of silver passivation start on the solution composition". In: *IOP Conf. Ser.: Mater. Sci. Eng.* 537 (2019), p. 022014. DOI: 10.1088/1757-899X/537/2/022014 (cit. on p. 130).

[189] Takashi Kakiuchi and Zdeněk Samec. "An electrochemical viewpoint on the solubility of silver halides in water". In: *J Solid State Electrochem* 24 (2020), pp. 3185–3189. DOI: 10.1007/s10008-020-04792-y (cit. on p. 130).

[190] Dong Zhang, Yidan Chen, Yu-Shan Huang, et al. "Robust, Reproducible, and Scalable Synthesis of Silver Nanocubes". en. In: *Chemistry A European J* 30.41 (July 2024), e202400833. ISSN: 0947-6539, 1521-3765. DOI: 10.1002/chem.202400833. URL: https://chemistry-europe.onlinelibrary.wiley.com/doi/10.1002/chem.202400833 (cit. on p. 134).

[191] D. F. C. Morris. "Ionic radii and enthalpies of hydration of ions". en. In: *Structure and Bonding*. Vol. 4. Series Title: Structure and Bonding. Berlin, Heidelberg: Springer Berlin Heidelberg, 1968, pp. 63–82. ISBN: 978-3-540-04350-8. DOI: 10.1007/BFb0119185. URL: http://link.springer.com/10.1007/BFb0119185 (cit. on p. 134).

[192] Yizhak Marcus. "Ionic radii in aqueous solutions". en. In: *Chem. Rev.* 88.8 (Dec. 1988), pp. 1475–1498. ISSN: 0009-2665, 1520-6890. DOI: 10.1021/cr00090a003.

URL: https://pubs.acs.org/doi/abs/10.1021/cr00090a003 (cit. on p. 134).

[193] Younan Xia, Xiaohu Xia, and Hsin-Chieh Peng. "Shape-Controlled Synthesis of Colloidal Metal Nanocrystals: Thermodynamic versus Kinetic Products". en. In: *J. Am. Chem. Soc.* 137.25 (July 2015), pp. 7947–7966. ISSN: 0002-7863, 1520-5126. DOI: 10.1021/jacs.5b04641. URL: https://pubs.acs.org/doi/10.1021/jacs.5b04641 (cit. on pp. 135, 144, 145).

[194] Qijia Huang, Dong Zhang, Hansong Yu, et al. "Seeing Is Believing: How Does the Surface of Silver Nanocubes Change during Their Growth in an Aqueous System". en. In: *Nano Lett.* (Apr. 2025), acs.nanolett.5c01276. ISSN: 1530-6984, 1530-6992. DOI: 10.1021/acs.nanolett.5c01276. URL: https://pubs.acs.org/doi/10.1021/acs.nanolett.5c01276 (cit. on p. 135).

[195] I. Brian Becerril-Castro, Irene Calderon, Nicolas Pazos-Perez, et al. "Gold Nanostars: Synthesis, Optical and SERS Analytical Properties". en. In: *Analysis & Sensing* 2.3 (May 2022), e202200005. ISSN: 2629-2742, 2629-2742. DOI: 10.1002/anse.202200005. URL: https://chemistry-europe.onlinelibrary.wiley.com/doi/10.1002/anse.202200005 (cit. on p. 149).

[196] Chih-Hsien Lai, Guo-An Wang, Tsung-Kai Ling, et al. "Near infrared surface-enhanced Raman scattering based on star-shaped gold/silver nanoparticles and hyperbolic metamaterial". en. In: *Sci Rep* 7.1 (July 2017), p. 5446. ISSN: 2045-2322. DOI: 10.1038/s41598-017-05939-0. URL: https://www.nature.com/articles/s41598-017-05939-0 (cit. on p. 149).

[197] Xianghua Meng, Jacqueline Dyer, Yifeng Huo, et al. "Greater SERS Activity of Ligand-Stabilized Gold Nanostars with Sharp Branches". en. In: *Langmuir* 36.13 (Apr. 2020), pp. 3558–3564. ISSN: 0743-7463, 1520-5827. DOI: 10.1021/acs.langmuir.0c00079. URL: https://pubs.acs.org/doi/10.1021/acs.langmuir.0c00079 (cit. on p. 149).

[198] Anisha Gopalakrishnan, Manohar Chirumamilla, Francesco De Angelis, et al. "Bimetallic 3D Nanostar Dimers in Ring Cavities: Recyclable and Robust Surface-Enhanced Raman Scattering Substrates for Signal Detection from Few Molecules". en. In: *ACS Nano* 8.8 (Aug. 2014), pp. 7986–7994. ISSN: 1936-0851, 1936-086X. DOI: 10.1021/nn5020038. URL: https://pubs.acs.org/doi/10.1021/nn5020038 (cit. on p. 149).

[199] Samuel L. Kleinman, Bhavya Sharma, Martin G. Blaber, et al. "Structure Enhancement Factor Relationships in Single Gold Nanoantennas by Surface-Enhanced Raman Excitation Spectroscopy". en. In: *J. Am. Chem. Soc.* 135.1 (Jan. 2013), pp. 301–308. ISSN: 0002-7863, 1520-5126. DOI: 10.1021/ja309300d. URL: https://pubs.acs.org/doi/10.1021/ja309300d (cit. on p. 149).

[200] Priyanka Dey. "Aiming for Maximized and Reproducible Enhancements in the Obstacle Race of SERS". en. In: *ACS Meas. Sci. Au* 3.6 (Dec. 2023), pp. 434–443. ISSN: 2694-250X, 2694-250X. DOI: 10.1021/acsmeasuresciau.3c00037. URL: https://pubs.acs.org/doi/10.1021/acsmeasuresciau.3c00037 (cit. on pp. 149, 159).

[201] Meikun Fan, Gustavo F.S. Andrade, and Alexandre G. Brolo. "A review on recent advances in the applications of surface-enhanced Raman scattering in analytical chemistry". en. In: *Analytica Chimica Acta* 1097 (Feb. 2020), pp. 1–29. ISSN: 00032670. DOI: 10.1016/j.aca.2019.11.049. URL: https://linkinghub.elsevier.com/retrieve/pii/S0003267019314126 (cit. on pp. 149, 159).

[202] Lin Yuan, Minhan Lou, Benjamin D. Clark, et al. "Morphology-Dependent Reactivity of a Plasmonic Photocatalyst". en. In: *ACS Nano* 14.9 (Sept. 2020), pp. 12054–12063. ISSN: 1936-0851, 1936-086X. DOI: 10.1021/acsnano.0c05383. URL: https://pubs.acs.org/doi/10.1021/acsnano.0c05383 (cit. on pp. 149, 150, 157).

[203] Benjamin D. Clark, Christian R. Jacobson, Minhan Lou, et al. "Aluminum Nanocubes Have Sharp Corners". en. In: *ACS Nano* 13.8 (Aug. 2019), pp. 9682–9691. ISSN: 1936-0851, 1936-086X. DOI: 10.1021/acsnano.9b05277. URL: https://pubs.acs.org/doi/10.1021/acsnano.9b05277 (cit. on pp. 149, 150, 201).

[204] Cornelius. Groot, R. M. Peekema, and V. H. Troutner. "Determination of Aluminum in Chromic-Phosphoric Acid Solutions". en. In: *Anal. Chem.* 28.10 (Oct. 1956), pp. 1571–1576. ISSN: 0003-2700, 1520-6882. DOI: 10.1021/ac60118a021. URL: https://pubs.acs.org/doi/abs/10.1021/ac60118a021 (cit. on pp. 150, 151, 154).

[205] Guofeng Hu, Haiming Zhang, Wenwen Di, et al. "Study on Wet Etching of AAO Template". In: *APR* 1.2 (Oct. 2009), p78. ISSN: 1916-9647, 1916-9639. DOI: 10.5539/apr.v1n2p78. URL: http://www.ccsenet.org/journal/index.php/apr/article/view/4189 (cit. on pp. 151, 154, 155).

[206] Huiquan Wu, Kurt R. Hebert, Thomas Gessmann, et al. "Corrosion-Related Interfacial Defects Formed by Dissolution of Aluminum in Aqueous Phosphoric Acid". en. In: *J. Electrochem. Soc.* 149.4 (2002), B108. ISSN: 00134651. DOI: 10.1149/1.1455648. URL: https://iopscience.iop.org/article/10.1149/1.1455648 (cit. on pp. 151, 154).

[207] D. Elabar, T. Hashimoto, J. Qi, et al. "Effect of low levels of sulphate on the current density and film morphology during anodizing of aluminium in chromic acid". en. In: *Electrochimica Acta* 196 (Apr. 2016), pp. 206–222. ISSN: 00134686. DOI: 10.1016/j.electacta.2016.01.230. URL: https://linkinghub.elsevier.com/retrieve/pii/S0013468616302493 (cit. on pp. 151, 154).

[208] M. Zarić, L. Jelić, and A. Matijasić. "Decontamination and Corrosion of Aluminium by Selected Decontaminating Solutions". en. In: *Isotopenpraxis Isotopes in Environmental and Health Studies* 6.1 (Jan. 1970), pp. 26–29. ISSN: 0021-1915. DOI: 10.1080/10256017008621699. URL: https://www.tandfonline.com/doi/full/10.1080/10256017008621699 (cit. on pp. 151, 154).

[209] Kurt R. Hebert, Huiquan Wu, Thomas Gessmann, et al. "Positron Annihilation Spectroscopy Study of Interfacial Defects Formed by Dissolution of Aluminum in Aqueous Sodium Hydroxide". en. In: *J. Electrochem. Soc.* 148.2 (2001), B92. ISSN: 00134651. DOI: 10.1149/1.1341241. URL: https://iopscience.iop.org/article/10.1149/1.1341241 (cit. on pp. 151, 154, 155).

[210] H. Wu, Kurt R. Hebert, Thomas Gessmann, et al. "The use of phosphoric acid immersion to enhance the susceptibility of aluminum to anodic pitting corrosion". In: *Oxide films : proceedings of the International Symposium*. Toronto, Ontario: The Electrochemical Society, Inc., 2000. ISBN: 1-56677-269-9 (cit. on pp. 151, 154).

[211] Han-Jun Oh, Jong-Ho Lee, Hong-Joo Ahn, et al. "Etching characteristics of high-purity aluminum in hydrochloric acid solutions". en. In: *Materials Science and Engineering: A* 449-451 (Mar. 2007), pp. 348–351. ISSN: 09215093. DOI: 10.1016/j.msea.2006.01.159. URL: https://linkinghub.elsevier.com/retrieve/pii/S0921509306015851 (cit. on p. 152).

[212] S.S. Djokić. "Fundamentals of Electroless Deposition". en. In: *Encyclopedia of Interfacial Chemistry*. Elsevier, 2018, pp. 161–173. ISBN: 978-0-12-809894-3. DOI: 10.1016/B978-0-12-409547-2.11701-9. URL: https://linkinghub.elsevier.com/retrieve/pii/B9780124095472117019 (cit. on p. 154).

[213] Stojan S. Djokic. "Chemical Oxidation of Aluminum in Chromic Acid Solutions". In: *Plat. Surf. Finish.* 92.5 (2005), p. 45. URL: https://sterc.org/pdf/psf2005/050545.pdf (cit. on p. 154).

[214] Mohammad Hadi Dehghani, Ahmad Zarei, Alireza Mesdaghinia, et al. "Adsorption of Cr(VI) ions from aqueous systems using thermally sodium organo-bentonite biopolymer composite (TSOBC): response surface methodology, isotherm, kinetic and thermodynamic studies". en. In: *Desalination and Water Treatment* 85 (Aug. 2017). Publisher: Elsevier BV, pp. 298–312. ISSN: 1944-3986. DOI: 10.5004/dwt.2017.21306. URL: https://linkinghub.elsevier.com/retrieve/pii/S1944398624116682 (cit. on p. 155).

[215] Bindu A. G, Ramesh S. Bhat, Manjunatha J. G, et al. "Chromium oxide nanoparticles as a modifier of carbon paste electrode for cyclic voltametric assessment of paracetamol in medicinal sample". en. In: *Sci Rep* 15.1 (Feb. 2025). Publisher: Springer Science and Business Media LLC. ISSN: 2045-2322. DOI: 10.1038/s41598-025-86927-7. URL: https://www.nature.com/articles/s41598-025-86927-7 (cit. on p. 155).

[216] Qiang Zhang, Weiyang Li, Long-Ping Wen, et al. "Facile Synthesis of Ag Nanocubes of 30 to 70 nm in Edge Length with CF_3 COOAg as a Precursor". en. In: *Chemistry A European J* 16.33 (Sept. 2010), pp. 10234–10239. ISSN: 0947-6539, 1521-3765. DOI: 10.1002/chem.201000341. URL: https://chemistry-europe.onlinelibrary.wiley.com/doi/10.1002/chem.201000341 (cit. on p. 191).

[217] Wenxin Niu, Shanliang Zheng, Dawei Wang, et al. "Selective Synthesis of Single-Crystalline Rhombic Dodecahedral, Octahedral, and Cubic Gold Nanocrystals". en. In: *J. Am. Chem. Soc.* 131.2 (Jan. 2009), pp. 697–703. ISSN: 0002-7863, 1520-5126. DOI: 10.1021/ja804115r. URL: https://pubs.acs.org/doi/10.1021/ja804115r (cit. on p. 200).

[218] Qiang Zhang, Weiyang Li, Christine Moran, et al. "Seed-Mediated Synthesis of Ag Nanocubes with Controllable Edge Lengths in the Range of 30-200 nm and Comparison of Their Optical Properties". en. In: *J. Am. Chem. Soc.* 132.32 (Aug.

2010), pp. 11372–11378. ISSN: 0002-7863, 1520-5126. DOI: 10.1021/ja104931h. URL: https://pubs.acs.org/doi/10.1021/ja104931h (cit. on p. 210).

[219] Allen J. Bard and Larry R. Faulkner. *Electrochemical methods: fundamentals and applications*. eng. 2. edition. New York Weinheim: Wiley, 2001. ISBN: 978-0-471-04372-0 (cit. on pp. 212, 214).

[220] Gregory N. Derry, Megan E. Kern, and Eli H. Worth. "Recommended values of clean metal surface work functions". en. In: *Journal of Vacuum Science & Technology A: Vacuum, Surfaces, and Films* 33.6 (Nov. 2015), p. 060801. ISSN: 0734-2101, 1520-8559. DOI: 10.1116/1.4934685. URL: https://pubs.aip.org/jva/article/33/6/060801/246682/Recommended-values-of-clean-metal-surface-work (cit. on p. 214).

[221] David R. Lide and Chemical Rubber Company, eds. *CRC handbook of chemistry and physics: a ready-reference book of chemical and physical data*. eng. 77. ed., 1996 - 1997. Boca Raton: CRC Press, 1996. ISBN: 978-0-8493-0477-4 (cit. on p. 215).

APPENDIX

A. Nanoparticles synthesis

A.1. Materials and methods

A.1.1. Chemicals and Materials

Ethanol, acetone, 2-isopropanol, sodium hydrosulfide (NaHS), silver trifluoroacetate (CF_3COOAg), hydrochloric acid (HCl) 37%, polyvinylpyrrolidone (PVP) (Mw 55000), ethylene glycol (EG), tetrachloroauric(III) acid trihydrate ($HAuCl_4 \cdot 3H_2O$), L-ascorbic acid, hexadecyltrimethylammonium bromide (CTAB), hexadecyltrimethylammonium chloride (CTAC), sodium borohydride ($NaBH_4$), silver nitrate ($AgNO_3$), Hexadecylpyridinium chloride monohydrate (CPC), Tebbe reagent 0.5 M solution in toluene, dimethylethylamine alane (DMEAA) 0.5 M solution in toluene, anhydrous toluene, anhydrous tetrahydrofuran (THF), anhydrous cyclohexane, dibutyl phosphate 97% and sodium bromide (NaBr) were purchased from Sigma Aldrich.

The water used in the experiment is typically Milli-Q water (Resistivity= 18.2 MΩ.cm, Total Organic Carbon (TOC)= ≤5 ppb) unless stated otherwise.

A.1.2. Synthesis of ~40 nm silver nanocubes by polyol synthesis

~40 nm silver nanocubes were synthesized by Peeranuch Poungsripong following the protocol reported by Zhang *et al*[216]. This procedure was designed to produce Ag nanocubes with edges ranging from 30 to 70 nm. The synthesis involved the use of NaHS in conjunction with CF_3COOAg, a precursor to elemental silver, to control the formation of single-crystal seeds. Additionally, HCl was employed as an oxidative etching agent, and PVP served as a capping agent.

Silver nanocubes are synthesized in a round-bottom flask (ACE Glass) with a glass lid. In this process, 25 mL of EG was added to the flask, with temperature set at 155 °C and a stirring speed of 300 rpm. Once the solution reached the target temperature, 300 µL of 3 mM NaHS was added. After two minutes, 2.5 mL of 3 mM HCl (37% by weight) was quickly added, followed by the immediate addition of 6.25 mL of PVP (20 mg/mL). Subsequently, 2 mL of CF_3COOAg 282 mM was added to the mixture after an additional 2 minutes.

During this process, the color of the solution changed from transparent to slightly yellow as the Ag seeds formed. Throughout the reaction period, three distinct color stages were visible: dark red, followed by reddish-gray, and finally the growth of Ag

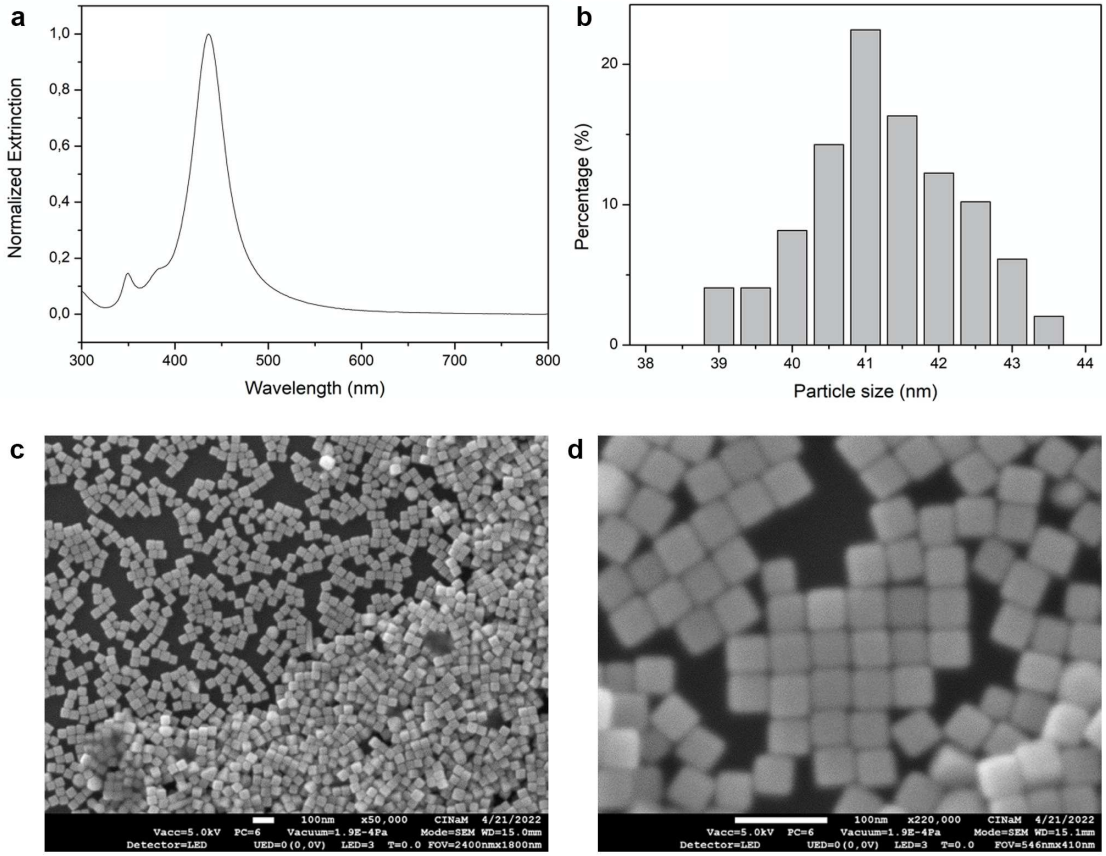

Figure A.1.: a, UV-Vis spectrum of silver nanocubes with edge length 40 nm. b, The corresponding particle size distribution. c-d, SEM images of silver nanocubes with edge length 40 nm.

nanocube edges in a brown solution. After 1.15 hours of reaction time, the reaction was stopped by placing the flask into an ice water bath. The residual precursor, EG, and excess PVP were removed from the Ag nanocubes through rinsing with acetone and water after centrifugation.

UV-vis spectra of Ag nanocubes with 40 nm edge length were obtained from the syntheses as shown in Figure A.1a. The main LSPR peaks of the 40 nm Ag nanocubes were located at 420 nm. By analyzing the size distribution as depicted in Figure A.1b using ImageJ, it was evident that the Ag nanocubes exhibited a monodisperse size with an edge length of 40 nm.

A.1.3. Synthesis of PVP-capped ~30, ~36, ~40, ~48, and ~53 nm gold nanocubes

A.1.3.1. Synthesis of CTAC-capped ~30 nm gold nanocubes

We synthesized ~30 nm gold icosahedra using a modified procedure based on the nanocube synthesis method reported by Park *et al.*[179]. In a 20 mL scintillation vial, the following were added sequentially: 6 mL of 100 mM CTAC, 40 μL of 20 mM NaBr, 45 μL of a 10 nm gold seed solution, 390 μL of 10 mM ascorbic acid, and 6 mL of 0.5 mM $HAuCl_4$. The mixture was stirred at 500 rpm during addition, then the speed was reduced to 200 rpm and maintained for 25 minutes at room temperature. After completion of the reaction, the particles were washed once with 1 mL of water (centrifugation 8000 rpm for 10 min) and redispersed in 10 mL of water.

A.1.3.2. Synthesis of CTAC-capped ~36 nm gold nanocubes

It follows the same procedure as described in A.1.3.1, except that 40 μL of a 10 nm gold seed solution was used.

A.1.3.3. Synthesis of CTAC-capped ~40 nm gold nanocubes

It follows the same procedure as described in A.1.3.1, except that 25 μL of a 10 nm gold seed solution was used.

A.1.3.4. Synthesis of CTAC-capped ~48 nm gold nanocubes

It follows the same procedure as described in A.1.3.1, except that the reaction was carried out in a 50 mL round-bottomed flask instead of vial and 18 μL of a 10 nm gold seed solution was used.

A.1.3.5. Synthesis of CTAC-capped ~53 nm gold nanocubes

It follows the same procedure as described in A.1.3.1, except that 12 μL of a 10 nm gold seed solution was used.

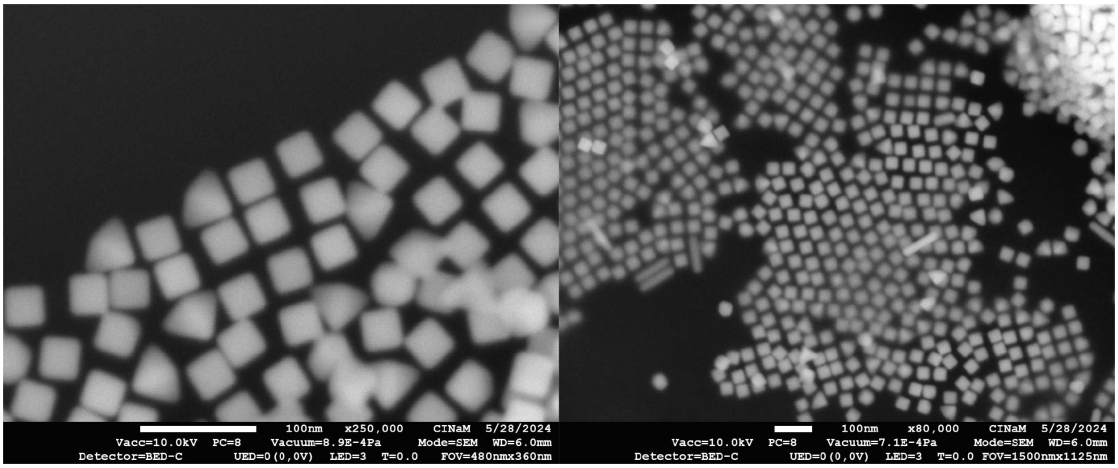

Figure A.2.: SEM images of gold nanocubes with edge length ~30 nm.

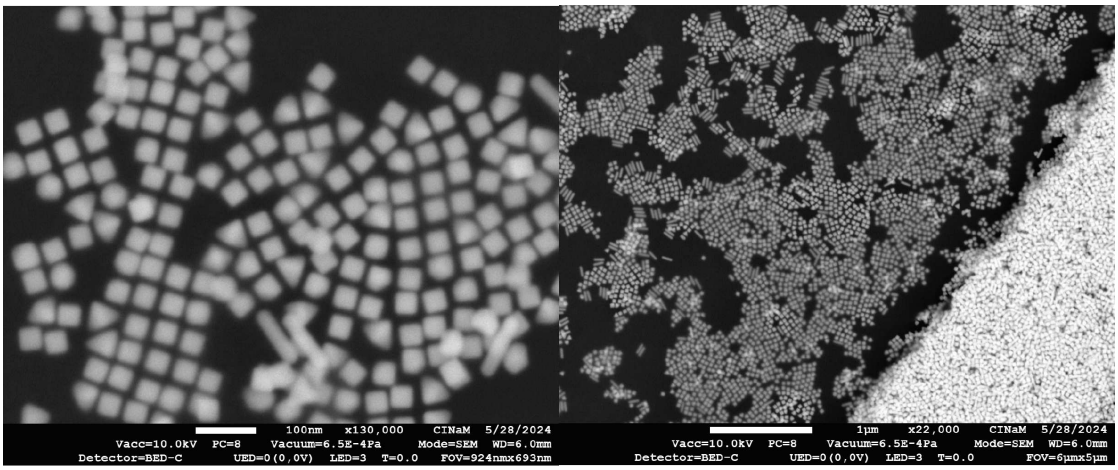

Figure A.3.: SEM images of gold nanocubes with edge length ~36 nm.

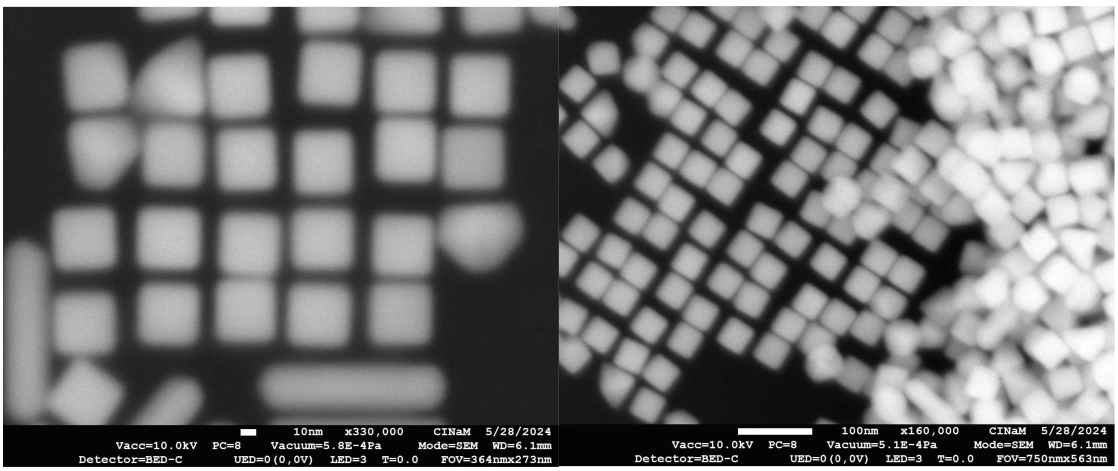

Figure A.4.: SEM images of gold nanocubes with edge length ~40 nm.

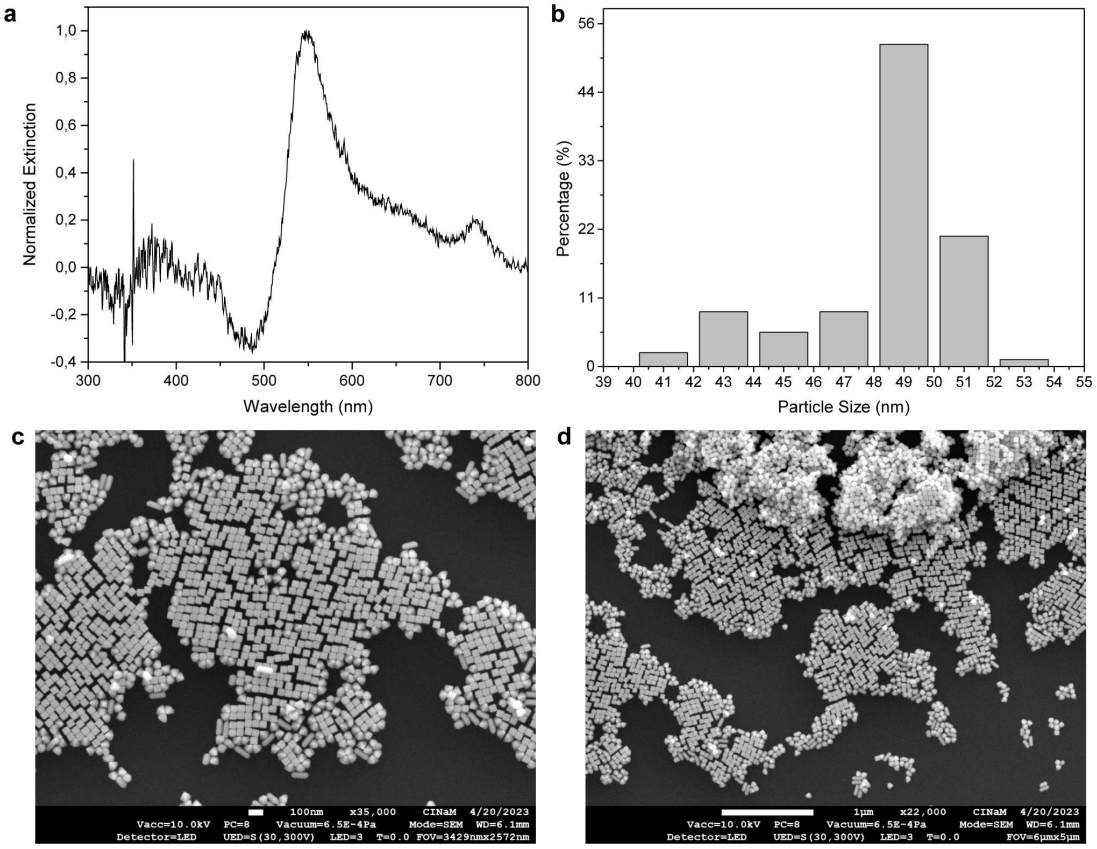

Figure A.5.: a, UV-Vis spectrum of gold nanocubes with average size of 48 nm. b, The corresponding particle size distribution. c-d, SEM images of gold nanocubes.

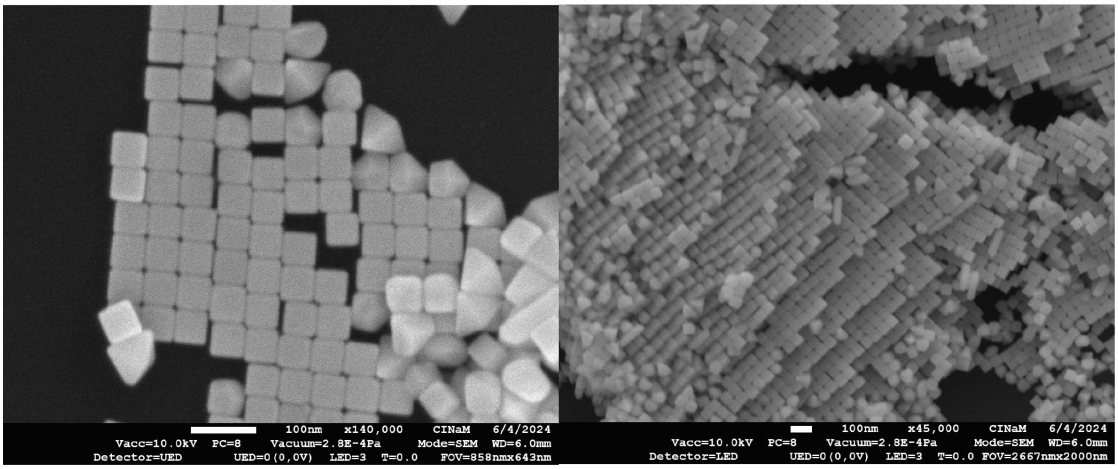

Figure A.6.: SEM images of gold nanocubes with edge length ~53 nm.

A.1.3.6. Ligand exchange from CTAC to PVP

For ~30 nm gold nanocubes, the colloidal solution was concentrated from 4 mL to 2 mL by centrifugation at 8500 rpm for 10 minutes and transferred to a clean 20 mL glass vial. Then, 200 μL of 50 mg/mL PVP solution in water and 6 mL of ethanol were added. The mixture was stirred for two days, followed by centrifugation at 8500 rpm for 10 minutes. Finally, the particles were redispersed in 1 mL of ethanol with ultrasonication and stored for future use.

For ~40 nm gold nanocubes, the colloidal solution was concentrated from 10 mL to 5 mL by centrifugation at 7000 rpm for 10 minutes and transferred to a clean 20 mL glass vial. Then, 500 μL of 50 mg/mL PVP solution in water and 15 mL of ethanol were added. The mixture was stirred for two days, followed by centrifugation at 9000 rpm for 10 minutes. Finally, the particles were redispersed in ~3.5 mL of ethanol with ultrasonication and stored for future use.

For ~48 nm gold nanocubes, we concentrated the solution to 1 mL (centrifugation at 7500 RPM for 10 min) and transferred it to a 20 mL glass vial. After adding 4 mL of water to the solution, we then introduced 500 µL of a 50 mg/mL PVP solution in water and 15 mL of ethanol. After stirring for two days, the solution was centrifuged at 8000 RPM for 10 minutes. Following this, 1 mL of ethanol was added, and nanoparticles were dispersed using ultrasonication. This was succeeded by another centrifugation under the same conditions to remove excess PVP. The resulting nanoparticles were dispersed in 1 mL of ethanol for storage.

For ~53 nm gold nanocubes, 0.333 mL of the colloidal solution was transferred to a clean 20 mL glass vial. Then, 0.667 mL water was added. Then 200 μL of 50 mg/mL PVP solution in water and 6 mL of ethanol were added. The mixture was stirred for two days, followed by centrifugation at 8500 rpm for 10 minutes. Finally, the particles were redispersed in 1 mL of ethanol with ultrasonication and stored for future use.

A.1.4. Synthesis of PVP-capped ~63, ~80, and ~100 nm gold nanocubes

A.1.4.1. Synthesis of CTAC-capped ~63 nm gold nanocubes

We synthesized ~63 nm Au nanocubes using a modified procedure based on Park *et al.*'s nanocube synthesis method[179]. In a 20 mL glass scintillation vials, we added the following sequentially: 6 mL of 100 mM CTAC, 40 µL of 10 mM NaBr, 2 mL of a 36 nm gold nanocubes seed solution (A.1.3.2), 390 µL of 10 mM ascorbic acid, and 6 mL of 0.5 mM $HAuCl_4$ solution. During the mixing process, the solution stirred at 500 rpm, then reduced to 200 rpm for an additional 25 minutes at room temperature (RT). Afterward, we washed the solution twice and redispersed the particles in 1 mL of water.

A.1.4.2. Synthesis of CTAC-capped ~80 nm gold nanocubes

It follows the same procedure as described in A.1.4.1, except that 1 mL of a 36 nm gold nanocubes seed solution (A.1.3.2) was used.

A.1.4.3. Synthesis of CTAC-capped ~100 nm gold nanocubes

It follows the same procedure as described in A.1.4.1, except that 40 µL of 8 mM NaBr and 0.3 mL of a 36 nm gold nanocubes seed solution (A.1.3.2) were used.

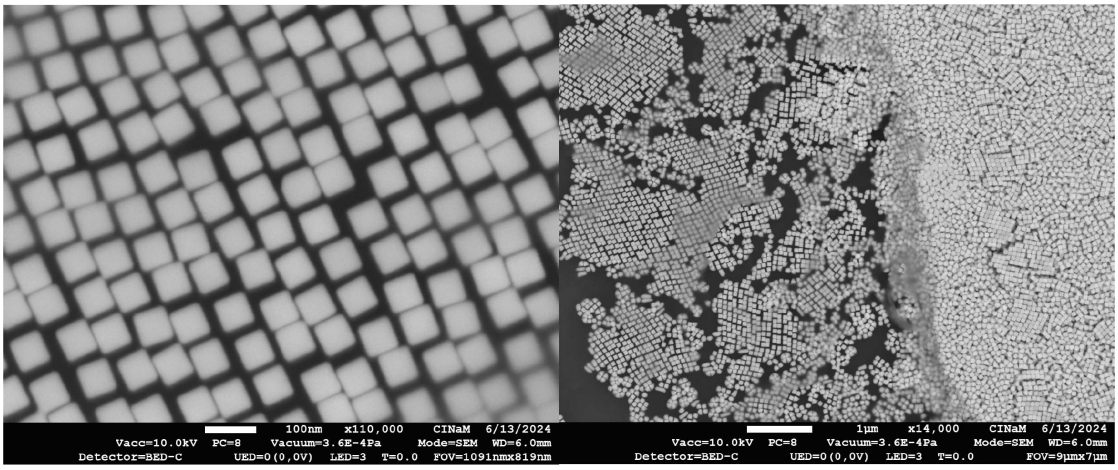

Figure A.7.: SEM images of gold nanocubes with edge length ~63 nm.

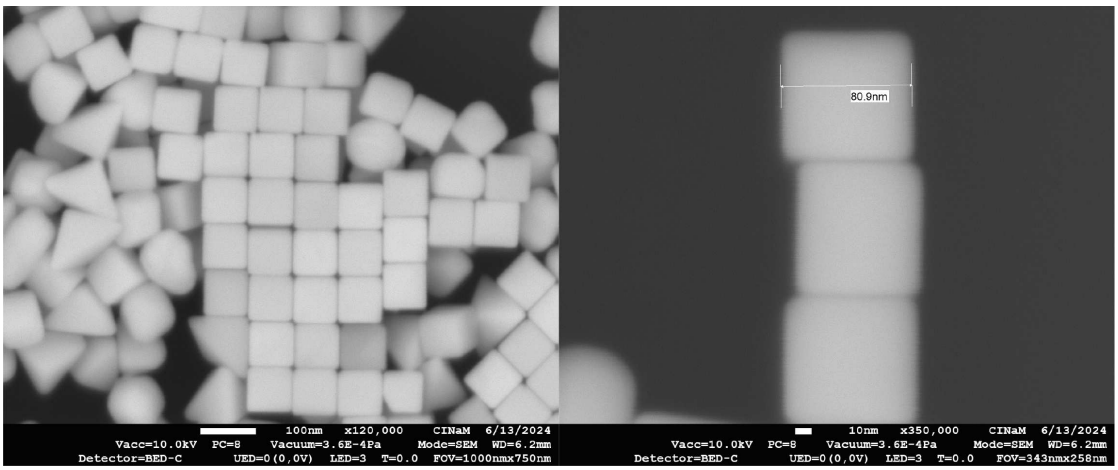

Figure A.8.: SEM images of gold nanocubes with edge length ~80 nm.

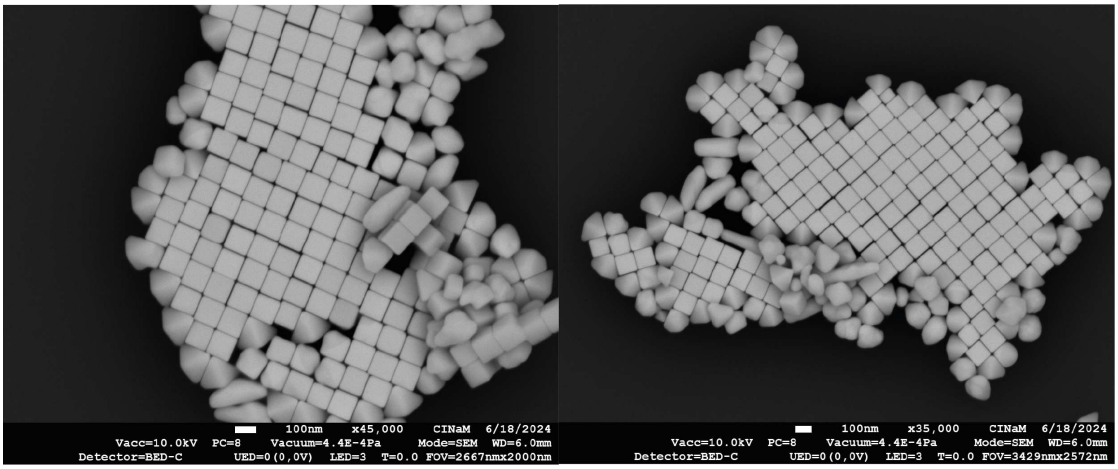

Figure A.9.: SEM images of gold nanocubes with edge length ~100 nm.

A.1.4.4. Ligand exchange from CTAC to PVP

For ~63 nm gold nanocubes, we take 200 mL of the sample and transferred it to a 20 mL glass vial. We then added 800 μL water and introduced 100 μL of a 50 mg/mL PVP solution in water and 3 mL of ethanol. The mixture was stirred for two days, followed by centrifugation at 8500 rpm for 10 minutes. Finally, the particles were redispersed in 1 mL of ethanol with ultrasonication and stored for future use.

For ~80 nm gold nanocubes, we take 1 mL of the sample and transferred it to a 20 mL glass vial. We then introduced 200 µL of a 50 mg/mL PVP solution in water and 6 mL of ethanol. After stirring for two days, the solution was centrifuged at 8000 RPM for 10 minutes. Following this, 1 mL of ethanol was added, and nanoparticles were dispersed using ultrasonication. This was succeeded by another centrifugation under

the same conditions to remove excess PVP. The resulting nanoparticles were dispersed in 1 mL of ethanol for storage.

For ~100 nm gold nanocubes, we take 360 μL of the sample and transferred it to a 20 mL glass vial. We then added 640 μL of water and introduced 100 µL of a 50 mg/mL PVP solution in water and 3 mL of ethanol. After stirring for two days, the solution was centrifuged at 8500 RPM for 10 minutes. Following this, the colloidal solution was dispersed in 1 mL of ethanol for storage.

A.1.5. Synthesis of ~43 nm gold icosahedra

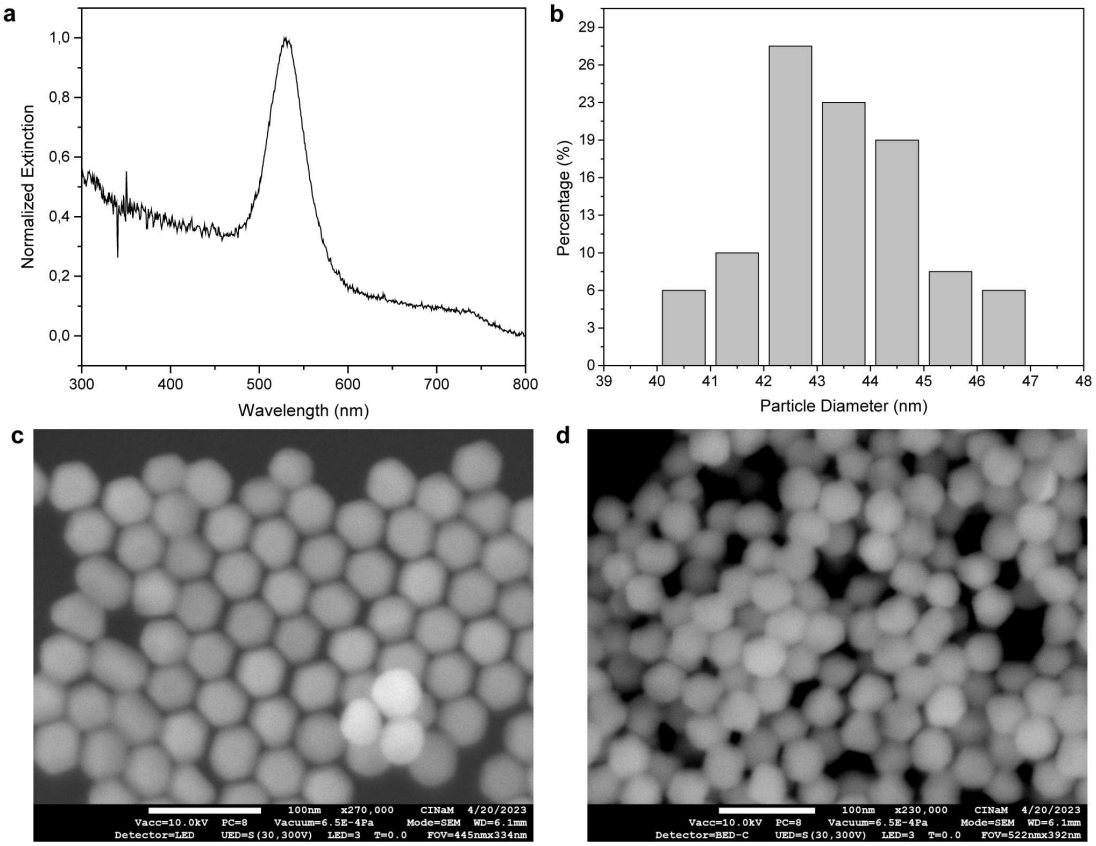

Figure A.10.: a, UV-Vis spectrum of gold icosahedra with average diameter of 43 nm. b, The corresponding particle size distribution. c-d, SEM images of gold icosahedra.

We synthesized 43 nm Au icosahedra using a modified procedure based on the nanocube synthesis method reported by Park *et al.*[179]. In a 50 mL round-bottomed flask, we sequentially added 6 mL of 100 mM CTAC, 65 µL of a 10 nm seed solution, 390 µL of 10 mM ascorbic acid, and 6 mL of 0.5 mM $HAuCl_4$ solution. During the mixing process, the solution was stirred at 500 rpm, and the stirring rate was then reduced to 200 rpm for an additional 25 minutes at room temperature (RT). Subsequently, we washed the solution twice and redispersed the nanoparticles in 10 mL of water.

To replace the CTAC capping ligand with PVP, we performed a ligand exchange procedure. We noticed that CTAC-capped nanoparticles did not float well on the water/air interface. To address this, we added 4 mL of the colloidal solution to a 20 mL glass vial, followed by the addition of 400 µL of a 50 mg/mL PVP solution in water and 12 mL of ethanol. After stirring for two days, the solution underwent centrifugation at 8000 RPM for 10 minutes. Next, we added 1 mL of ethanol and dispersed the nanoparticles using ultrasonication. This was followed by another centrifugation under the same conditions to remove excess PVP. The resulting nanoparticles were dispersed in 1 mL of ethanol for storage.

A.1.6. Synthesis of gold octahedra

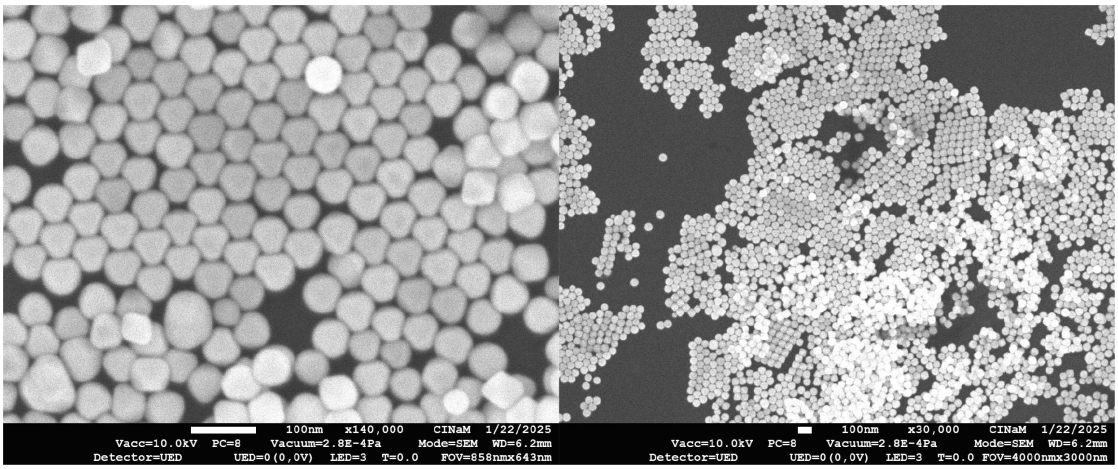

Figure A.11.: SEM images of gold octahedra.

The synthesis of octahedral gold nanoparticles was carried out by Sugi Korath Shivan following the method reported by Niu *et al.* [217].

A.1.6.1. Preparation of ~1.5 nm CTAB-Capped Gold Seeds

To prepare the seed solution, 125 μL of 10 mM $HAuCl_4$ was added to 5 mL of 100 mM CTAB solution at 30 °C. After gentle mixing, 0.3 mL of freshly prepared, ice-cold 10 mM $NaBH_4$ was rapidly added. The mixture was rapidly mixed by inversion for 2 minutes to ensure uniform dispersion. The resulting ~1.5 nm CTAB-capped gold seeds were stored at 30 °C until use.

A.1.6.2. Synthesis of Gold Nanorods

The growth solution was prepared by sequentially adding 2 mL of 10 mM $HAuCl_4$, 240 μL of 10 mM $AgNO_3$, 320 μL of 100 mM freshly prepared ascorbic acid, and 48 μL of the gold seed solution into 40 mL of 100 mM CTAB at 30 °C. After each addition, the

solution was gently mixed to ensure homogeneity. The resulting mixture was then left undisturbed at 30 °C for 2 hours to allow nanorod formation.

A.1.6.3. Secondary Overgrowth of Gold Nanorods

30 mL of the nanorod solution was centrifuged at 12000 rpm for 10 minutes, redispersed in deionized water, and centrifuged again under the same conditions. The final pellet was redispersed in 30 mL of 10 mM CTAB at 40 °C. Then, 1.5 mL of 10 mM $HAuCl_4$ and 0.3 mL of 100 mM ascorbic acid were added sequentially with thorough mixing. The mixture was allowed to react at 40 °C for 1 hour to promote secondary growth.

A.1.6.4. Synthesis of CPC-Capped Gold Seeds

CPC-capped gold seeds were prepared by transforming overgrown gold nanorods into near-spherical nanoparticles. First, the nanorod solution was centrifuged at 12,000 rpm for 10 minutes and redispersed in 30 mL of 10 mM CTAB solution. While maintaining the temperature at 40 °C, 0.6 mL of 10 mM $HAuCl_4$ was added, followed by gentle mixing. The mixture was then aged undisturbed for 12 hours. After aging, the nanoparticles were washed three times with 100 mM CPC solution through repeated centrifugation (12,000 rpm, 10 minutes) and redispersion. Finally, the particles were dispersed in 30 mL of 100 mM CPC solution. These nanoparticles are referred to as CPC-capped seeds.

A.1.6.5. Seed-Mediated Growth of Octahedral Gold Nanocrystals

For the synthesis of octahedral gold nanocrystals, 100 μL of 10 mM $HAuCl_4$, 13 μL of freshly prepared 100 mM ascorbic acid, and 200 μL of the CPC-capped seed solution were sequentially added to 5 mL of 100 mM CPC solution at 30 °C. The mixture was thoroughly stirred after each addition. The reaction was allowed to proceed for 2 hours and then quenched by centrifugation at 12,000 rpm for 10 minutes.

A.1.7. Synthesis of aluminum nanocubes

Aluminum nanocubes (~113 nm) were synthesized according to a previously reported method by Clark *et al.*[203]. Initially, three solutions were prepared inside a glove box: (i) 2.5 mL of 50 mM Tebbe reagent (catalyst) in anhydrous toluene, (ii) 10 mL of 50 mM DMEAA (precursor) in anhydrous THF, and (iii) 50 mL of 97% dibutylphosphate solution (quencher) in anhydrous cyclohexane. Under inert conditions on a Schlenk line, the precursor solution was preheated to approximately 70°C with continuous stirring at 250 rpm. Subsequently, 200 μL of catalyst was added to the precursor solution. Aliquots were collected at reaction times of 20, 30, and 40 minutes, with volumes of approximately 2.5 mL, 2.5 mL, and 5 mL, respectively. These aliquots were immediately quenched in corresponding volumes of quencher solution (12.5 mL for

the 2.5 mL aliquots, and 25 mL for the 5 mL aliquot). During synthesis, the oil bath temperature fluctuated between 70 °C and 77 °C.

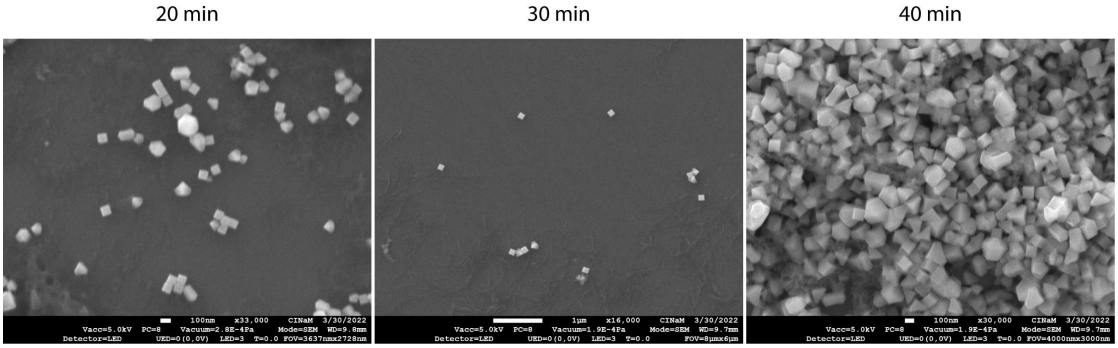

Figure A.12.: SEM images of aluminum nanocubes synthesized with reaction times of 20, 30, and 40 minutes.

After quenching, each aliquot was purified by centrifugation at ~5000 g (7000 rpm, rotor radius 11.5 cm). The supernatant was discarded, and the nanoparticles were redispersed in 25 mL isopropanol (IPA) with sonication. The dispersion was then centrifuged again at ~10000 g (9500 rpm, rotor radius 11.5 cm), followed by supernatant removal and redispersion in 25 mL IPA. This washing cycle was repeated twice before storage. Nanocubes obtained from the first, second, and third aliquots exhibited average sizes of 80 ± 8.8 nm, 115.9 ± 6.9 nm, and 113.6 ± 8 nm, respectively. SEM images corresponding to these aliquots are shown in Figure E.1. The third aliquot was used for the experiments with corresponding TEM images shown in Figure A.12. All glassware were stored in oven at 120°C for overnight.

B. Nanocube assembly at the air-water interface: Materials and methods

B.1. Materials and methods

B.1.1. Chemicals and Materials

~55 nm silver nanocubes, PVP, NanoXact™ was purchased from Nanocomposix, (7-8% vinylmethylsiloxane)-dimethylsiloxane copolymer (trimethylsiloxy terminated, MW 30000, viscosity 800-1200 cSt.), platinum-divinyltetramethyldisiloxane complex in xylene, 1,3,5,7-tetravinyl-1,3,5,7-tetramethylcyclotetrasiloxane (97%), (25-35% methylhydrosiloxane)-dimethylsiloxane copolymer (viscosity 25-35 cSt.), and 1H,1H,2H,2H-perfluorooctyltriethoxysilane (97%) were purchased from ABCR. Ethanol, acetone, 2-isopropanol, silver trifluoroacetate (CF_3COOAg), polyvinylpyrrolidone (PVP) (Mw 55000), acetic acid, tetrachloroauric(III) acid trihydrate ($HAuCl_4 \cdot 3H_2O$), sodium borohydride ($NaBH_4$), sodium bromide (NaBr), chloroform ($CHCl_3$), and nitric acid (HNO_3 were purchased from Sigma Aldrich. Silicon wafers (CZ (100) 4", type p, doped B, 1-20 Ω.cm, one side polished with flat Ra < 4nm) were purchased from NEYCO. The water used in the experiment is typically Milli-Q water (Resistivity= 18.2 MΩ.cm, Total Organic Carbon (TOC)= ≤5 ppb) unless stated otherwise.

B.1.2. Fabrication of silicon master by electron beam lithography

Fabricating silicon pattern masters entailed multiple steps. First, square samples measuring 2cm x 2cm were cleaved from a 2-inch, single-side polished, single-crystal silicon wafer (SPS, Belgium). The samples were orientated in the (100) direction, 250–300 μm thick p-type (boron), and with a resistivity of 1–20 Ω.cm. The samples were cleaned in an ultrasonic bath, first 5 min in acetone and then 5 min in propan-2-ol (IPA). The samples were then rinsed with deionized water and dried under pure nitrogen flow. To enhance wettability and adhesion for the resist, the cleaned samples were treated for 10 minutes at 150°C in an oxygen/argon plasma (Nanoplas, France). The electron-beam (e-beam) sensitive resist employed was poly(methyl methacrylate) (PMMA 950 K at 2% in ethyl-lactate, AR-P 679 from from Allresist GmbH, Germany).

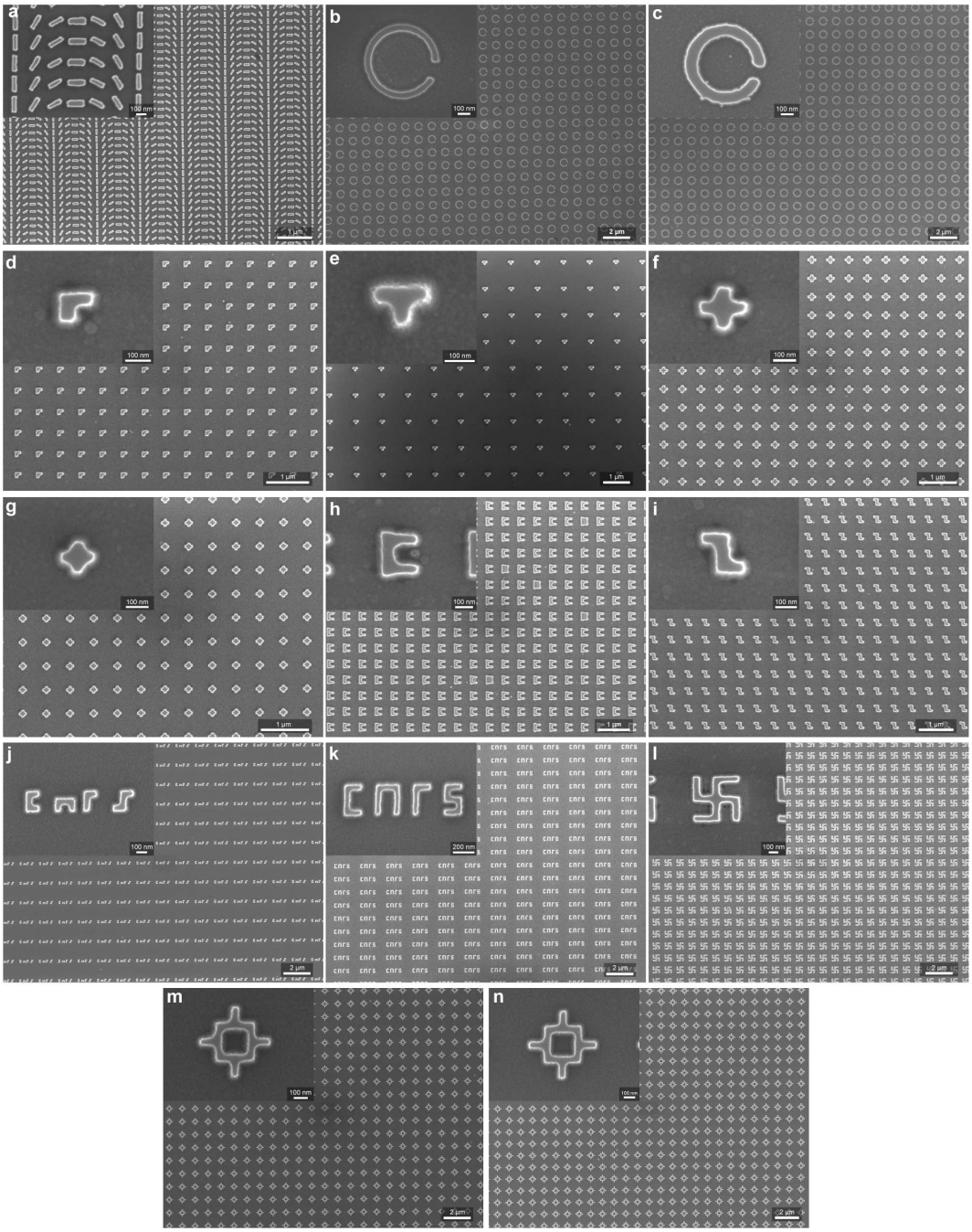

Figure B.1.: Silicon masters and pattern depth: a, Pancharatnam-Berry metasurface (~60 nm). b, small split-ring (~80 nm). c, large split-ring (~80 nm). d, L (~93 nm). e, T (~80 nm). f, cross (~93 nm). g, diamond (~93 nm). h, U (~93 nm). i, S (~93 nm). j, small CNRS (~80 nm). k, big CNRS (~80 nm). l, gammadion (~93 nm). m, small polygon (~80 nm). n, large polygon (~80 nm).

This resist was spin-coated onto the samples at a speed of 4000 rpm for a duration of 60 seconds. To relax any induced stresses and to eliminate residual solvents, the coated samples were annealed for 10 minutes at 170 °C. Resist thickness was set at 65 nm, verified by a profilometer (Dektak, Bruker Corporation, Germany). E-beam lithography was performed with a Pioneer system (Raith, Germany) in order to create the mask patterns. The working distance for the electron microscope was set to 8 mm, and an acceleration voltage of 20 kV was used with an aperture size of 10 μm, resulting in a current of 30 pA. A dose of approximately 110 $\mu C \cdot cm^{-2}$ was selected for this configuration. The development of the resist was done by a solution of methyl-isobuthyl-ketone (MIBK) in IPA during 60 sec. The resist was then rinsed in IPA for the same time and finally dried under nitrogen flow. The PMMA resist is positive and the exposed areas were thereby removed. A nickel mask, 20 nm thick, was deposited through thermal evaporation under vacuum using a solid nickel source (Auto 306, Edwards Vacuum, England). The evaporation process was monitored using a Quartz microbalance and later verified using a mechanical profilometer. Nickel was selected as the mask material due to its resistance to fluorinated dry etching. To remove the remaining resist and the nickel layer on top, a lift-off process was executed by immersing the samples in acetone for several hours. This was followed by a rinse in ethyl-lactate to remove the final traces of PMMA. The samples were then dried under a nitrogen flow. The etching of silicon through the nickel mask was conducted in a Reactive Ion Etching (RIE) chamber (Plassys, France). A gas mixture of SF_6 and O_2 was used for etching. Specific settings included an RF power of 20W, a process vacuum of 50 mTorr, gas flows for O_2 and SF_6 at 20 SCCM, a time duration of 270 seconds, and an autopolaris voltage of approximately 80 V. Following the etching, the nickel mask was dissolved using a home-made acidic aqueous solution of $FeCl_3$ at room temperature. The samples were finally rinsed with deionized water and dried under a nitrogen flow.

To achieve hydrophobic coating, the silicon master underwent specific procedures. Firstly, it was ultrasonicated in isopropanol and acetone for 5 minutes each, consecutively. Next, the master was exposed to UV-Ozone for 45 minutes. Following this, it was placed in a desiccator and exposed to 50 µL 1H,2H,2H-Perfluorooctyltriethoxysilane and 50 µL acetic acid for 30 minutes.

B.1.3. Fabrication of patterned PDMS

To create the patterned PDMS substrates, a microscope glass slide was first cut to a smaller size, approximately 1 cm x 1.5 cm. The glass slides underwent sonication in IPA and acetone for 5 minutes each to ensure proper cleaning. Subsequently, they were exposed to UV-Ozone for 45 minutes for surface activation. To prepare the PDMS prepolymer, a mixture was created by sequentially combining 712 mg of (7-8% vinylmethylsiloxane)-dimethylsiloxane copolymer, 5 µL of platinum-divinyltetramethyldisiloxane complex in xylene, 160.5 mg of 1,3,5,7-tetravinyl-1,3,5,7-tetramethylcyclotetrasiloxane (97%), and 890 mg of (25-35% methylhydrosiloxane)-dimethylsiloxane copolymer. A small drop of the prepolymer mixture was carefully placed on the hydrophobic silicon master. The pretreated glass slide was then gently

placed on top of the droplet, ensuring it was parallel to the silicon wafer and allowing a thin layer of prepolymer mixture to be sandwiched in between. The PDMS was cured at 150°C for 15 minutes and then separated from the silicon master, resulting in patterned PDMS substrates. These substrates were subsequently stored in ethanol for a few days before further use.

B.1.4. Assembly of silver nanocubes using Langmuir trough

The nanocubes were first subjected to washing. A volume of 0.45 mL of commercial 55 nm silver nanocubes was transferred into a 2 mL Eppendorf tube, and ethanol was added to bring the total volume to 1 mL. The suspension was dispersed by ultrasonication, followed by centrifugation at 3500 rpm for 20 minutes. A relatively low centrifugation speed and extended duration were chosen to minimize the risk of irreversible nanocube aggregation. The supernatant was then carefully removed using a glass Pasteur pipette. This process of ethanol dispersion, centrifugation, and supernatant removal was repeated two additional times. After the third cycle, 80 µL of $CHCl_3$ was added to the nanocube precipitate, which was then redispersed by ultrasonication.

The colloidal solution was carefully dropped onto the water surface in the Langmuir trough (KSV NIMA, platinum rod balance with a diameter of 1.016 mm) using a Hamilton syringe. We allowed the assembly to equilibrate for approximately 30 minutes while the solvent evaporated. To compress the assembly, we used the KSV NIMA LB software "iso mode" and moved the barriers closer at a speed of 2 mm/minute. Once the targeted surface pressure was reached (typically around 16.7 mN/m for a compact assembly), we left the assembly untouched for 15 minutes to ensure proper equilibration. Subsequently, we compressed the assembly again using the "dip mode" until reaching the desired surface pressure and allowed the barriers to oscillate for 10 minutes. To transfer the assembly onto a substrate (patterned PDMS), we carefully approached the substrate at a speed of 0.5 mm/min until contact. The substrate was then lifted at the lowest speed of 11.32 mm/min and dried using a nitrogen flow.

B.1.5. Assembly on a small homemade PTFE well

Typically, we began the process by transferring 12-13 µL of commercial 55 nm silver nanocubes into a 2 mL microcentrifuge tube. Ethanol was then added until reaching a volume of approximately 0.5 mL. The resulting solution was thoroughly mixed using either ultrasonication and/or a vortex. Subsequently, we subjected the mixture to centrifugation at 3500 rpm for 20 minutes and carefully removed the supernatant. This centrifugation and supernatant removal process was repeated three times. Finally, at the end of the third cycle, the precipitate was dispersed in 25 µL $CHCl_3$. Before the deposition step, we added 140 µL of Milli-Q water into the PTFE well, which had a diameter of 0.5 cm and a depth of approximately 8 mm. For the assembly, we gently dropped the colloidal solution in chloroform onto the water surface using a Hamilton

syringe. The assembly was allowed to equilibrate for around 15 minutes, allowing the solvent to evaporate. Once ready, we carefully brought a clean nanopatterned PDMS substrate in contact with the assembly, lifted it by hand, and dried the sample with a nitrogen gun. The same procedure was applied to other types of synthesized nanoparticles, with adjustments made to the volume of the colloidal solution used. Specifically, for ~40 nm silver nanocubes, we utilized 80 µL of solution. For ~43 nm gold icosahedra, we also used 80 µL. For ~48 nm gold nanocubes, we used 70 µL.

B.1.6. Excess nanocubes removal

Excess nanocubes removal is typically conducted the following day after transferring the assembled nanocubes onto the nanopatterned PDMS. The procedure initiated by ultrasonicating a small piece of Si wafer (roughly around 3x3 mm) in IPA and acetone for 5 min each, subsequently. This was then followed by treating the piece with UV/ozone (UVO) treatment for 30 min. While doing so, a sample of assembled nanocubes was sprayed with ethanol, followed by nitrogen gun drying to eliminate dust. A pretreated Si-wafer and the sample were then affixed on the setup (Fig. B.2) using double-sided Scotch tape. Horizontal alignment of sample and Si-wafer was ensured with a bubble level. Upon fixing, 2-5 µL of 50 mg/mL PVP in ethanol was deposited onto the Si-wafer. The vertically adjustable mount was then carefully lowered, applying a downward force ranging from approximately 2 to 50 N. Here we used a small Si-wafer piece to facilitate easier tilt adjustment to ensure the conformality of contact by monitoring the light interference pattern (Newton's rings) from a stereomicroscope. After they were in a good contact, the temperature was raised to 40 °C for 3-5 min. After that the vertically adjustable mount was slowly and carefully lifted. It should be noted that, as discussed in the main manuscript, this process is the most laborious step of the process, as a perfect conformal contact is required to achieve absolute reproducibility. Additionally, the cleanliness of the silicon wafer and the sample surface are critical aspects in this process.

B.1.7. Transfer Printing

Transfer printing was executed using the same custom-built apparatus previously utilized for nanocube removal, as illustrated in Figure B.2. Initially, a piece of a Si wafer was ultrasonicated in isopropanol and acetone for 5 minutes each, in succession. Following this, the wafer piece underwent a 30-minute UVO treatment. Simultaneously, a sample was cleansed by spraying it with ethanol and then drying it with a nitrogen gun to remove any dust particles. Both the pre-treated Si wafer and the sample were then mounted onto the setup using double-sided Scotch tape. To ensure horizontal alignment between the sample and the Si wafer, a bubble level was used. Once secured, 2-8 µL of a 50 mg/mL PVP solution in ethanol was dispensed onto the Si wafer. The vertically adjustable mount was subsequently lowered, applying a downward force ranging from approximately 40 to 80 N. To facilitate easier tilt adjustment and ensure optimal contact, a small Si wafer piece was used; the light interference pattern

(Newton's rings) was monitored with a stereomicroscope. After achieving satisfactory contact, the temperature was elevated to 75 °C and maintained for 15 minutes. Finally, the vertically adjustable mount was carefully retracted to separate the target substrate from the nanopatterned PDMS substrate.

B.1.8. Nanocubes chemical welding

The sample was sequentially immersed in water, acetone, isopropanol, and water again, with each step lasting approximately one minute. Afterwards, it was submerged in a 20 mL solution of $NaBH_4$—100 mM for gold nanocubes and 200 mM for silver nanocubes—at room temperature for 30 minutes to remove the capping ligands. To ensure effective exposure of the nanocubes to the solution, care was taken to prevent bubble formation on the sample. This was achieved by either promptly retracting the sample from the solution or gently agitating the glass beaker. The sample was then rinsed with water and dried using a nitrogen gun. Subsequently, it was submerged in a 10 mL aqueous welding solution and maintained for one hour at a specific temperature without stirring: the welding solution for gold nanocubes contained 100 μL HNO_3, 80 μM $HAuCl_4$, and 50 μM NaBr, and was heated to 45°C[1]; for silver nanocubes, the solution contained 100 μL HNO_3, 5-20 mM CF_3COOAg, and 50 μM NaBr, and was heated to 80°C. After the welding process, the sample was rinsed again with water and dried using a nitrogen gun.

B.1.9. Low-density nanocubes on UVO-treated vs untreated nanopatterned PDMS substrates

For each deposition, we introduced 10 μL of commercial 55 nm silver nanocubes into a 2 mL microcentrifuge tube, followed by the addition of ethanol to approximately 0.5 mL. The solution was homogenized using a sonication bath and/or vortex mixer. The mixture was then centrifuged at 3500 rpm for 20 minutes, after which the supernatant was carefully removed. This process of ethanol addition and centrifugation was repeated twice more. Finally, the precipitate was resuspended in 25 µL of $CHCl_3$. To prepare the substrate, a clean split-ring patterned PDMS substrate was subjected to UV/Ozone treatment for 30 minutes. Subsequently, both the treated and untreated substrates were subjected to ultrasonication in isopropanol, ethanol, and water, each for 5 minutes. The substrates were then immersed in ethanol prior to deposition to ensure a clean surface for the subsequent process. Prior to deposition, we added 900 µL of Milli-Q water to a larger PTFE well, measuring 1.7 cm in diameter and approximately 0.6 mm in depth. The colloidal solution in chloroform was carefully spread to the water's surface using a Hamilton syringe, and the system was allowed to stabilize for about 15 minutes. The substrate was then brought into contact with the assembly manually, lifted gently, and the sample was dried using a nitrogen gun.

B.2. Supporting information

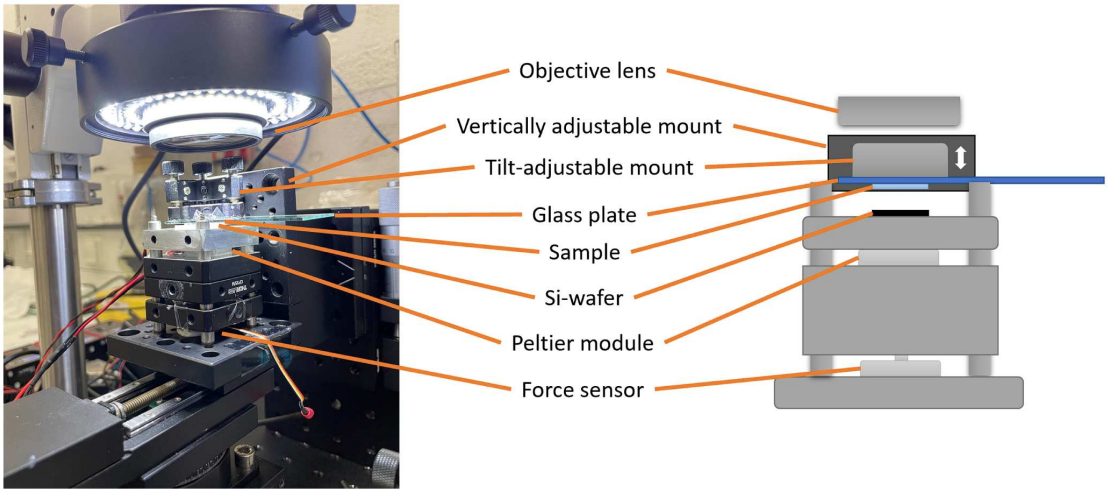

Figure B.2.: Homemade setup for nanocubes removal and transfer printing.

C. Silver nanocube epitaxy *via* nanogap-induced electrostatics: Materials and methods

C.1. Materials and methods

C.1.1. Chemicals and materials

~55 nm silver nanocubes, PVP, NanoXact™ was purchased from Nanocomposix. Acetone, 2-isopropanol, ethanol, silver trifluoroacetate (CF_3COOAg), sodium trifluoroacetate (CF_3COONa), hydrochloric acid (HCl) 37%, chloroform ($CHCl_3$), sodium borohydride ($NaBH_4$), sodium hydrosulfide (NaSH), ethylene glycol (EG), polyvinylpyrrolidone (PVP) (Mw 55000), nitric acid (HNO_3), and sodium bromide (NaBr) were purchased from Sigma Aldrich. The water used in the experiments is typically Milli-Q water (Resistivity= 18.2 MΩ·cm, Total Organic Carbon (TOC) ≤5 ppb) unless stated otherwise.

C.1.2. Nanocubes synthesis and assembly

40 nm AgNCs were synthesized according to the procedure reported by Zhang, *et al.* [218]. CF_3COOAg was used as a silver source in the presence of trace amounts of NaSH and HCl. Briefly, 25 mL of EG was pre-heated in a round-bottom flask using a 155°C oil bath at a stirring speed of 200 rpm. 300 μL of 3 mM NaHS was then added to the solution. After 2 min, 2.5 mL of HCl 3 mM and 6.25 mL of 20 mg/mL PVP were quickly added. After another 2 min, 2 mL CF_3COOAg 282 mM was added to the round bottom flask. Reaction was finally quenched using an ice-cold water bath after 90 min.

1D arrays of nanocubes were assembled with previously-reported techniques of capillary assembly [87]. Briefly a colloidal solution of Ag nanocubes (roughly $3{\cdot}10^{13}$ nanocube/mL) in 2 mg/mL of PVP was deposited between the nanopatterned PDMS substrate and a hydrophobic glass slide. A home-made setup was used to control the substrate temperature and its relative motion compared to the fix glass slide. The assembly was performed at a speed of 0.5 μm/s and a temperature of 60°C and 70 % humidity.

2D meta-atom arrays were fabricated using a previously reported air-water interface assembly technique [172]. Typically, we began the process by transferring 12-13 µL of

commercial 55 nm silver nanocubes into a 2 mL microcentrifuge tube. Ethanol was then added until reaching a volume of approximately 0.5 mL. The resulting solution was thoroughly mixed using either ultrasonication and/or a vortex. Subsequently, we subjected the mixture to centrifugation at 3500 rpm for 20 minutes and carefully removed the supernatant. This centrifugation and supernatant removal process was repeated three times. Finally, at the end of the third cycle, the precipitate was dispersed in 25 µL $CHCl_3$.

This solution was then carefully deposited at the air-water interface on a home-made PTFE well using a Hamilton syringe, forming a compact floating monolayer film. A nanostructured PDMS mold was subsequently placed in contact with this film, facilitating the transfer of nanocubes from the interface to the mold. To remove excess nanocubes, a small drop of 50 mg/mL PVP in ethanol solution was dropcasted to a clean silicon wafer. The wafer was then conformally brought into contact with the sample using our home-made setup and heated to approximately ~40°C for ~5 minutes. Upon releasing the contact, the nanocubes were assembled within the trenches of the PDMS mold.

C.1.3. Chemical welding

Firstly, the sample was prepared either by drop-casting a solution of silver nanocubes onto substrates such as PDMS, glass, silicon, UV/Ozone-treated silicon, or Si_3N_4, or through the aforementioned nanoparticle assembly techniques. In the latter methods, nanoparticles were arranged on a nanopatterned PDMS mold. The sample was then sequentially dipped in water, acetone, isopropanol, and water again, each for at least one minute. It was then immersed in a 100-200 mM $NaBH_4$ solution for 30 minutes to remove the ligand. It has been reported that hydride species derived from $NaBH_4$ exhibit a higher binding affinity to metal nanoparticles than PVP, thereby displacing and removing the PVP adsorbate[142]. To ensure effective exposure of the nanocubes to the solution, care was taken to prevent bubble formation on the sample, either by promptly retracting the sample from the solution or gently agitating the glass beaker. Afterward, the sample was thoroughly rinsed with water to remove any residual $NaBH_4$ and then dried using a nitrogen gun. Inadequate cleaning could result in the homonucleation of silver on the substrate due to the reduction of silver precursor (such as CF_3COOAg, if there is any) in the welding solution by any remaining $NaBH_4$ on the surface. Subsequently, the sample was submerged in the welding solution, totaling 10 mL, inside a 20 mL vial placed in an oil bath set at a welding temperature for one hour without stirring. For example, for welding process depicted in Figure 3.8a, we mixed 100 μL of HNO_3, 2.5 mL of 40 mM CF_3COOAg, and 7.4 mL of water in the vial. After welding, the sample was rinsed with water and dried using nitrogen gas.

C.1.4. Electrochemical characterizations

The electrochemical experiments were carried out in the conventional three-electrode configuration on three different types of samples: (*i*) Glassy carbon served as inert

electrode, (*ii*) GC covered by a 100 nm-thick Ag film (referred as GC-Ag) grown by thermal evaporation, (*iii*) GC covered by closely packed nanocubes (referred as GC-cubes) deposited by Langmuir-Blodgett assembly(Figure 3.6). The GC, GC-Ag and GC-cubes were placed in an o-ring cell made of polychlorotrifluoroethylene with an exposed area of 0.196 cm^2. A Pt wire and a mercury/mercurous sulfate electrode (Hg/Hg_2SO_4, saturated K_2SO_4, $E° = 0.64$ V vs SHE) respectively served as counter and reference electrodes. The three electrodes were connected to a potentiostat (Modulab from Solartron Analytical) driven by the XM-Studio ECS software (Solartron Analytical) to perform chronopotentiometry and cyclic voltammetry was maintained at $T = 60°C$ in Ag-free and Ag-containing acidic solutions: 0.01 M HNO_3 and 0.01 M HNO_3 + 0.01 M CF_3COOAg.

Experiments have been carried out also in Ag-containing electrolyte (0.01 M HNO_3 + 0.01 M CF_3COOAg) to confirm peaks identification (Figure 3.5b). Identical anodic and cathodic peaks appear on GC and GC-Ag but, due to the presence of Ag^+ in the solution (0.01 M), their potentials are slightly positively shifted to −0.6 and between −0.35 (□ on the curve) and −0.27 V (■ on the curve), respectively. This confirms that the cathodic and anodic peaks measured on GC-Ag in HNO_3 (Figure 3.5a) correspond to silver deposition and dissolution.

C.2. Supporting information

C.2.1. Standard potential calculations

The mechanism behind silver redeposition, which begins with gap filling at early reaction stages and leads to the formation of larger three-dimensional structures over longer durations, is notably different from that observed in gold nanocubes[1]. This difference arises from two main factors: (i) the reduction potential of Ag^+/Ag is lower than that of water, and (ii) silver does not participate in a disproportionation reaction.

C.2.1.1. Redox couple O_2/H_2O

$$O_2 + 4H^+ + 4e^- \rightleftharpoons 2H_2O$$

$$E_{O_2/H_2O} = 1.229 - (1.984 \cdot 10^{-4} \times T \times pH) \tag{C.1}$$

C.2.1.2. Redox couple Ag^+/Ag

$$Ag^+ + e^- \rightleftharpoons Ag \quad E° = 0.7996\,V \text{ [219]}$$

$$E_{Ag^+/Ag} = E° - (\frac{RT}{F}) \ln \frac{1}{a_{Ag^+}} \tag{C.2}$$

C.2.1.3. Redox couple Ag^{3+}/Ag^{+}

$$Ag^{3+} + 2e^{-} \rightleftharpoons Ag^{+} \quad E^{\circ} = 1.9\,V$$

$$E_{Ag^{3+}/Ag^{+}} = E^{\circ} - (\frac{RT}{2F}) \ln \frac{a_{Ag^{+}}}{a_{Ag^{3+}}} \tag{C.3}$$

Since $E^0(Ag^+/Ag)$ is smaller than $E^0(Ag^{3+}/Ag^+)$, disproportionation of Ag^+ species to solid Ag(0) and Ag^{3+} is thermodynamically unfavorable (also true with Ag^{2+}).

C.2.1.4. Activities

In order to calculate reaction potential, activities a_i are first calculated for the different species.

$$I = \frac{1}{2} \sum z_i^2 \times C_i \tag{C.4}$$

The ionic strength (I) of the solution is first calculated, using z_i and C_i, respectively charge and concentration of the species. Here we have, H^+, Ag^+ and NO_3^- ions in solution. Typically 100 μL of concentrated HNO_3 (about 15.85 M) is diluted in 10 mL of the welding solution and 1 mM of CF_3COOAg is added to the welding solution:

$$I \approx 0.300\,M$$

When $I < 0.5$ M, which is the case for all welding solution, we can use Davis model (expression C.5) to calculate the activity coefficient (expression C.6).

$$\log \gamma_i = -Az_i^2 (\frac{\sqrt{I}}{1+\sqrt{I}}) - 0.3I \tag{C.5}$$

Where A= $1.82 \cdot 10^6 (\epsilon T)^{-3/2}$. For water at 25°C, A=0.5085 $M^{1/2}$.

$$a_i = \gamma_i \frac{C_i}{C_0} \tag{C.6}$$

Where γ_i is the activity coefficient, C_i is concentration of the species in solution, and C_0 = 1 mol·L^{-1}.

Here A = 0.93, $\gamma_i \approx 0.57$, $a_{Ag^+} \approx 0.57$ mM, and $a_{H^+} \approx 90$ mM.

C.2.1.5. Redox potential of Ag^+/Ag at 25°C

$$Ag^+ + e^- \rightleftharpoons Ag \quad E^\circ = 0.7996\,V$$

$$E_{Ag^+/Ag} = E^\circ - (\frac{RT}{F}) \ln \frac{1}{a_{Ag^+}} \tag{C.7}$$

$$E_{Ag^+/Ag} = 0.608\,V$$

When increasing the temperature, this value is further reduced to ≈ 0.58 V at 60°C (for $\gamma_i \approx 0.57$ which is normally valid at 25°C only). When the activity of Ag^+ is increased however, the redox potential of Ag^+/Ag increases. For example for a_{Ag^+} = 10 mM, $E_{Ag^+/Ag}$ = 0.68V. As a result, both Ag^+ and Ag show a stability domain in water.

Note that for this stability domain to disappear, the concentration of Ag^+ in the vicinity of the nanocubes should be in the order of 10^7M (E = 1.21 V).

C.2.1.6. Redox couple Au^+/Au

$$Au^+ + e^- \rightleftharpoons Au \quad E^\circ = 1.83\,V \text{ [219]}$$

C.2.2. Work functions of the metals

Work function of Ag:

$$\Phi_{Ag} = 4.10 \text{ to } 4.53 \text{ eV [220]}$$

Work function of Au:

$$\Phi_{Au} = 5.16 \text{ to } 5.33 \text{ eV [220]}$$

C.2.3. Nitric acid oxidation of silver nanocubes

On the other hand, nitric acid is a very well known etchant for silver.

$$Ag + 2\,HNO_3 \longrightarrow Ag^+ + NO_3{}^- + NO_2 + H_2O \tag{C.8}$$

$$3\,Ag + 4\,HNO_3 \longrightarrow 3\,Ag^+ + 3\,NO_3{}^- + NO + 2\,H_2O \tag{C.9}$$

Reaction constants and the extent of reactions are calculated for both reactions in order to understand if an equilibrium can be reached at low acid concentration or by introducing Ag^+ in the solutions.

$$K = exp(\frac{-\Delta_r G}{RT}) \tag{C.10}$$

$$\Delta_r G = \Delta H - T\Delta S \tag{C.11}$$

	Ag(s)	HNO_3(l)	$AgNO_3$(l)	NO_2(g)	NO (g)	H_2O(l)
Δ_fH (kJ.mol^{-1}	0	-174.1	-124.4	33.2	91.3	-285.8
S^0 (J.mol^{-1}.K^{-1}	42.6	155.6	140.9	240.1	210.8	70

Table C.1.: Standard thermodynamic properties of chemical substances[221].

For equation C.8, we obtain ΔG= -57.77 kJ.mol^{-1} and K=1.336·10^{10}. Using equation,

$$K = [NO_2][AgNO_3][HNO_3]^{-2}$$

$$K = x([Ag^+]_0 + x)([HNO_3]_0 - 2x)^{-2}$$

And using $[HNO_3]_0$ = 0.158 M and $[Ag^+]_0$ = 1 mM, we calculate an extent of reaction of x = 0.079, meaning that the reaction is complete (using activities instead of concentration does note change the result notably). Increasing Ag+ concentration or reducing HNO_3 concentration does not impact the extent of reaction, meaning that there is no equilibrium possible between oxidation and growth, even if silver (I) accumulates at the nanocubes vicinity.

For equation C.9, we obtain ΔG= -54.28 kJ.mol^{-1} and K=3.272·10^9. Using equation,

$$K = [NO][AgNO_3]^3[HNO_3]^{-4}$$

$$K = ([Ag^+]_0 + 3x)^3([HNO_3]_0 - 4x^{-4})$$

And using $[HNO_3]_0$ = 0.158 M and $[Ag^+]_0$ = 1 mM, we calculate an extent of reaction of x = 0.039. The reaction is also complete and no equilibrium is possible between oxidation and growth.

As a conclusion the role of this equilibrium is only to oxidize silver nanocubes and provide Ag^+ ions in the vicinity of the gaps.

C.2.4. Multiphysics simulations

The commercial package COMSOL Multiphysics was used to unveil how the distribution of charged species in solution is affected by the presence of two charged nanocubes separated by a small gap. Electrostatic simulations (Poisson's equation) were coupled to the Nernst–Planck equation for mass transport of all of the ions. Both nanocubes were applied an identical potential, corresponding to a net charge of a few electrons. The charge (Q) is related to the potential (V) as follows:

$$Q = 4\pi V \epsilon_0 R$$

where ϵ_0 correspond to the dielectric constant of vacuum and R is the radius of the nanoparticle, assuming a spherical shape. The value of Q with respect to the electron charge is used to estimate the number of excess electrons in the particles for a given applied potential. Anion concentrations was set to 10^{-7}M, which correspond to water dissociation at pH = 7, whereas the initial concentration of monovalent counterions in solution was set to obtain overall neutral charge (taking into accounts of the anion concentration and the net charge on the nanocubes).

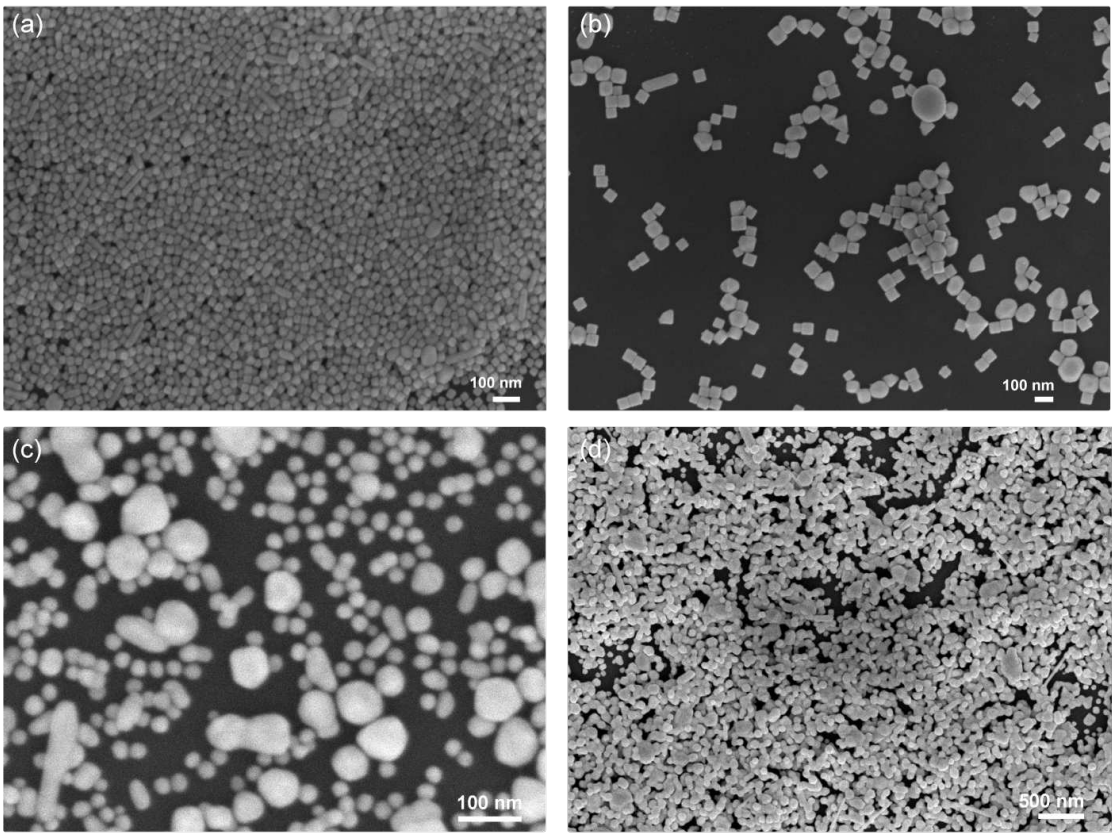

Figure C.1.: a) 30 nm and b) 70 nm silver nanocubes on silicon following the removal of ligands showing that welding is not immediate. c) 30 nm and d) 70 nm nanocubes exhibit spontaneous welding after 3 days in water upon removing ligands(reproduced from ref. [2])

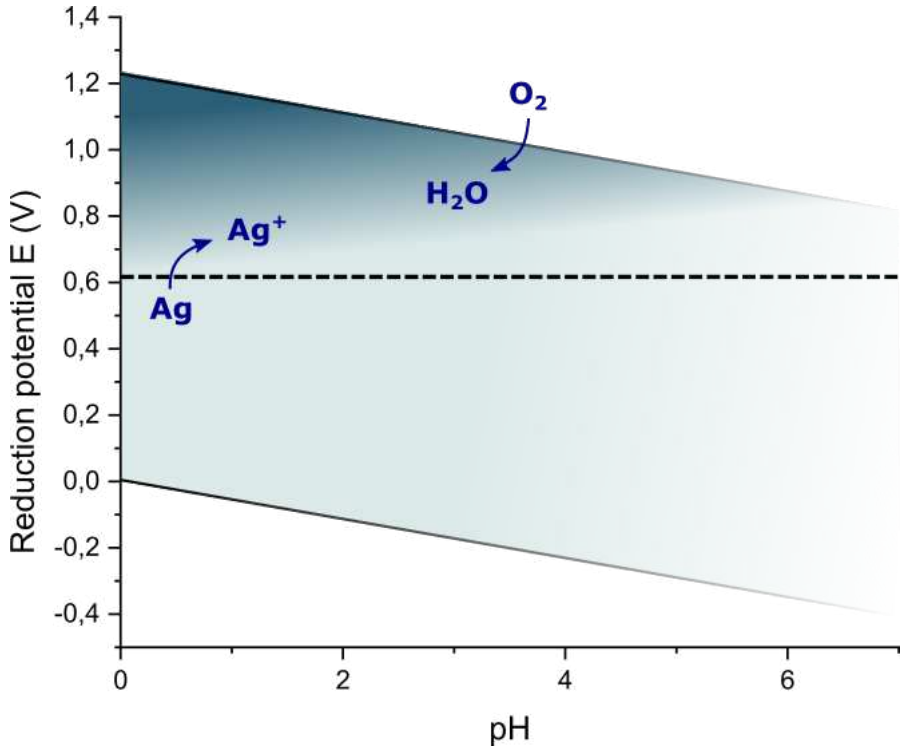

Figure C.2.: Ag^+/Ag Pourbaix Diagram at RT for Ag^+ concentration of 0.001 M and an ionic strength of 0.3 M.(reproduced from ref. [2])

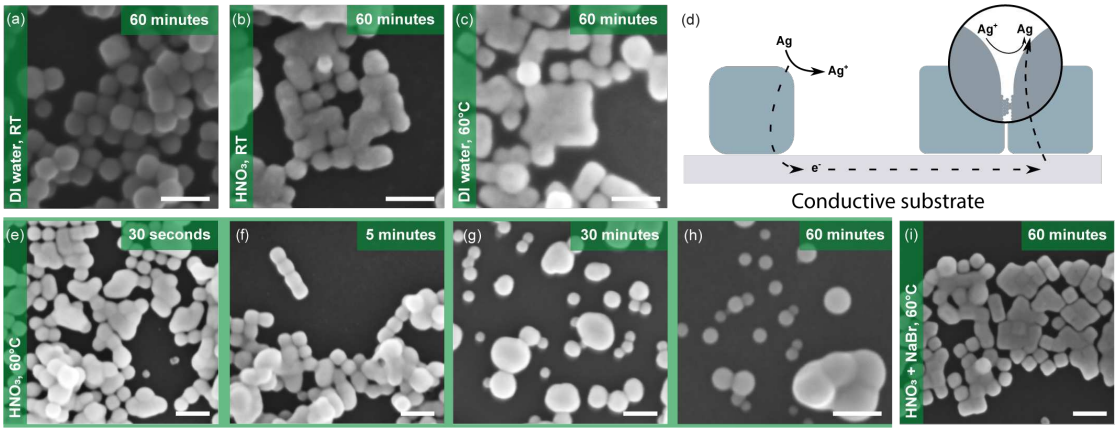

Figure C.3.: Upon removing ligands, Si-supported 40 nm silver nanocubes are immersed for one hour in a) RT water, b) RT diluted nitric acid (pH = 2), c) 60°C water, d) Schematic of the electrochemical Ostwald ripening mechanism for conductive substrates. 40 nm silver nanocubes are immersed for one hour at 60°C diluted nitric acid (pH = 2) for different times e) 30 seconds, f) 5 minutes, g) 30 minutes, and h) 60 minutes. i) 60 minutes in the presence of 50 μM NaBr. All scale bars are 100 nm in length(reproduced from ref. [2]).

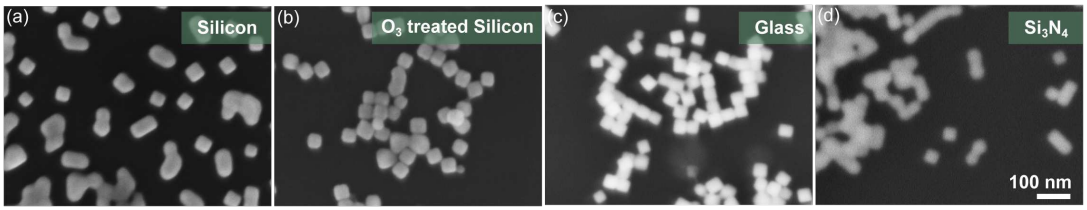

Figure C.4.: Influence of the substrate on 40 nm nanocubes epitaxial welding (60°C, pH = 2, 25 μM NaBr, 1 hour) is shown for a) Silicon, b) O_3 treated silicon, c) Glass, and d) Si_3N_4. The scale bar is valid for all(reproduced from ref. [2]).

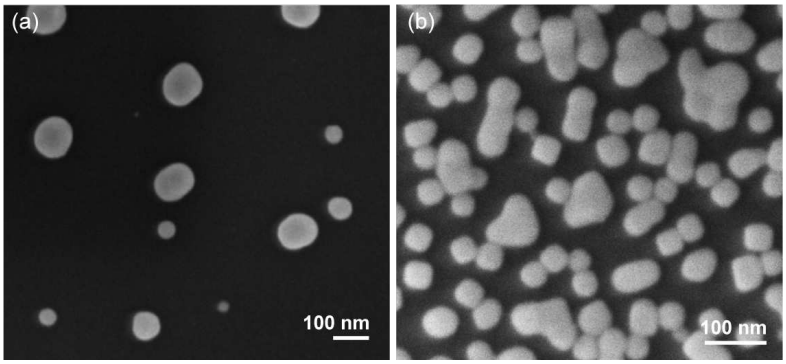

Figure C.5.: Control experiments on 40 nm silver nanocubes performed on silicon substrate in the dark for 1 hour at 60°C a) in diluted nitric acid at a pH = 2 b) In the presence of NaBr 25 μM at a pH = 2, showing that silver nanocubes can be epitaxially welded in the dark(reproduced from ref. [2]).

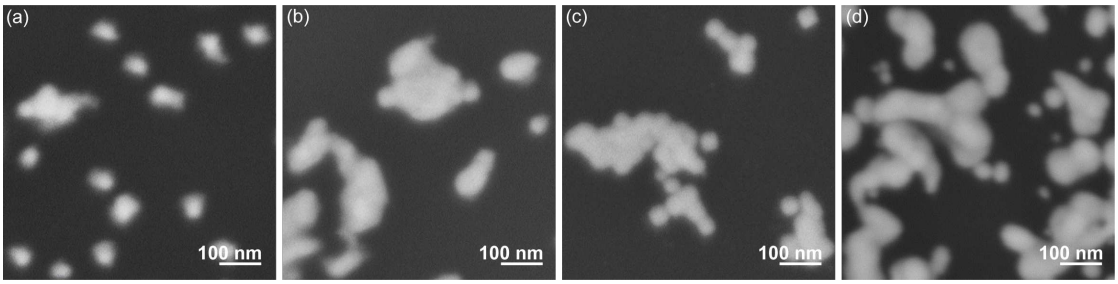

Figure C.6.: Shape retention in silver nanocubes epitaxial welding in the presence of CF_3COOAg. a) Nanocubes dissolution in the presence of HNO_3 only b) Improved shape retention in the presence of 1 mM CF_3COOAg c) Optimum shape retention using 10 mM CF_3COOAg e) Control experiment realized with 10 mM CF_3COONa instead of CF_3COOAg. All experiments were performed on flat PDMS upon drop casting 40 nm silver nanocubes, at 60°C for 1 hour and at a pH = 2(reproduced from ref. [2]).

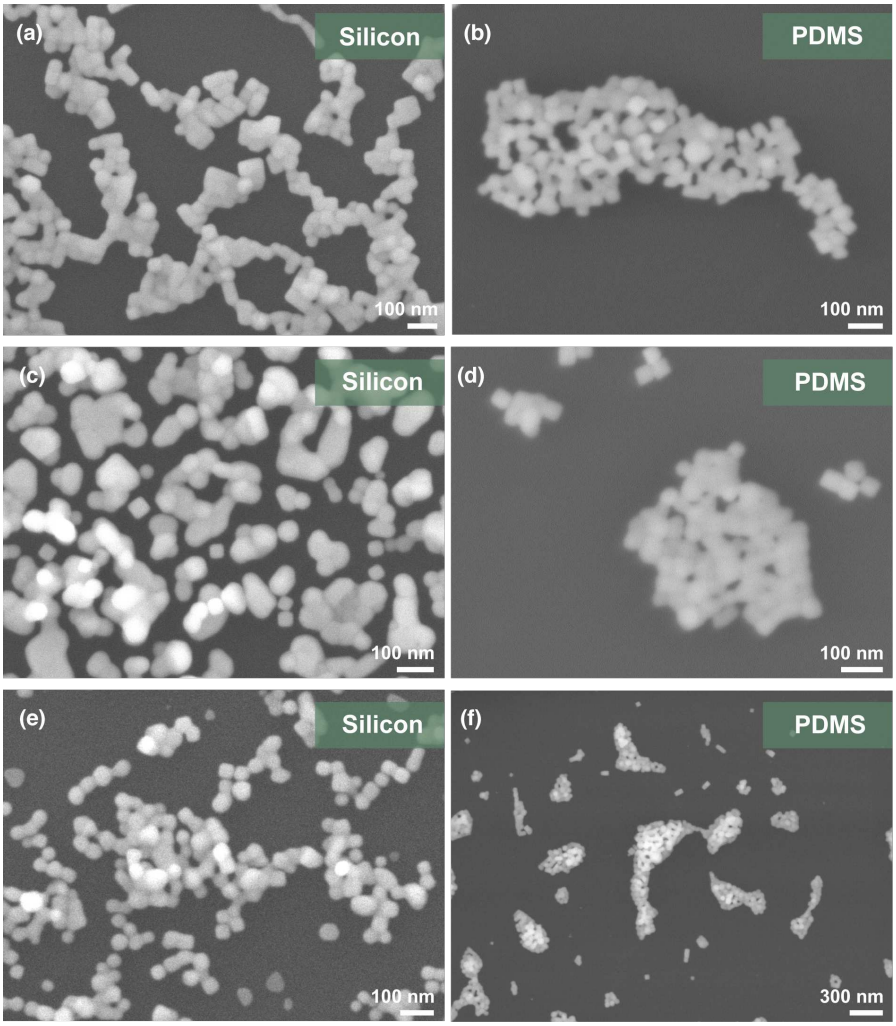

Figure C.7.: Control experiments on the chemical welding of 40 nm silver nanocubes under oxygen-free conditions at 60°C for 1 hour: in diluted nitric acid (pH = 2) with 50 μM NaBr after ~30 minutes of Argon purging on (a) silicon and (b) PDMS; in diluted nitric acid (pH = 2) with 10 μM CH_3COOAg after ~45 minutes of Argon purging on (c) silicon and (d) PDMS; and in 50 μM NaBr after ~30 minutes of Argon purging on (e) silicon and (f) PDMS.

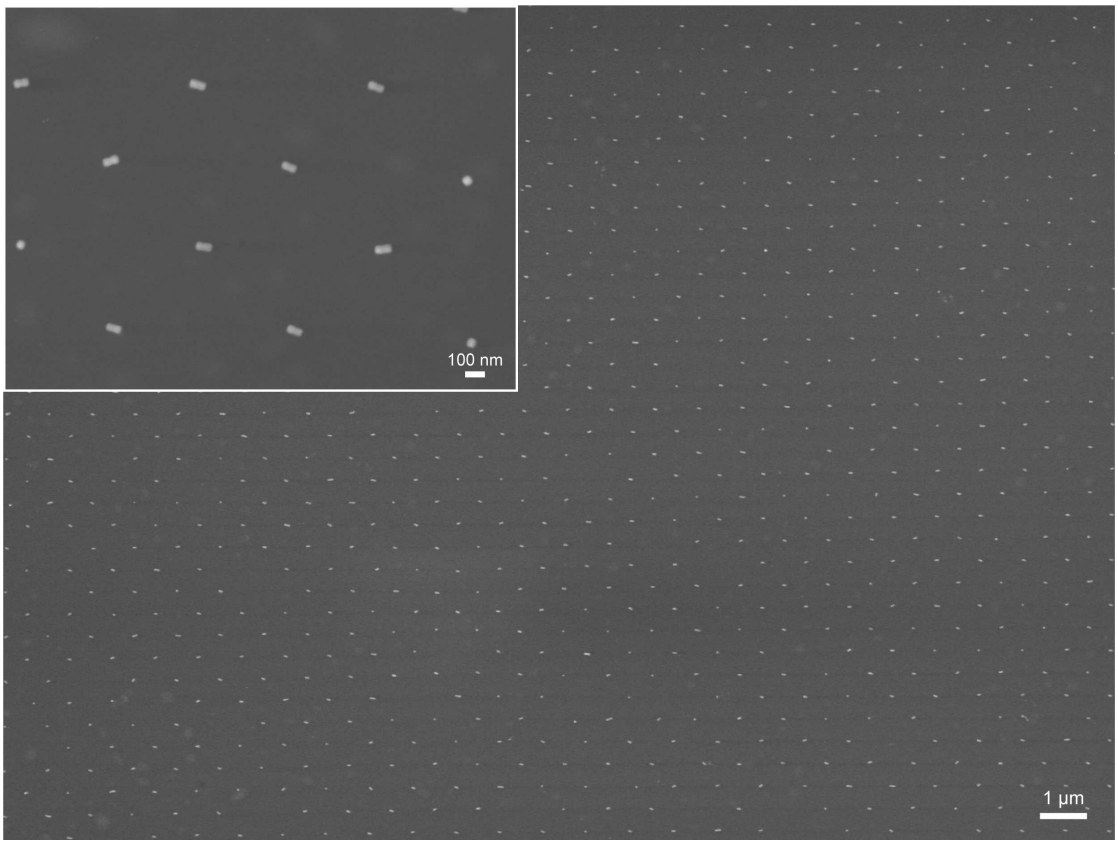

Figure C.8.: SEM images of large area nanowelded silver nanocubes dimer on PDMS(reproduced from ref. [2]).

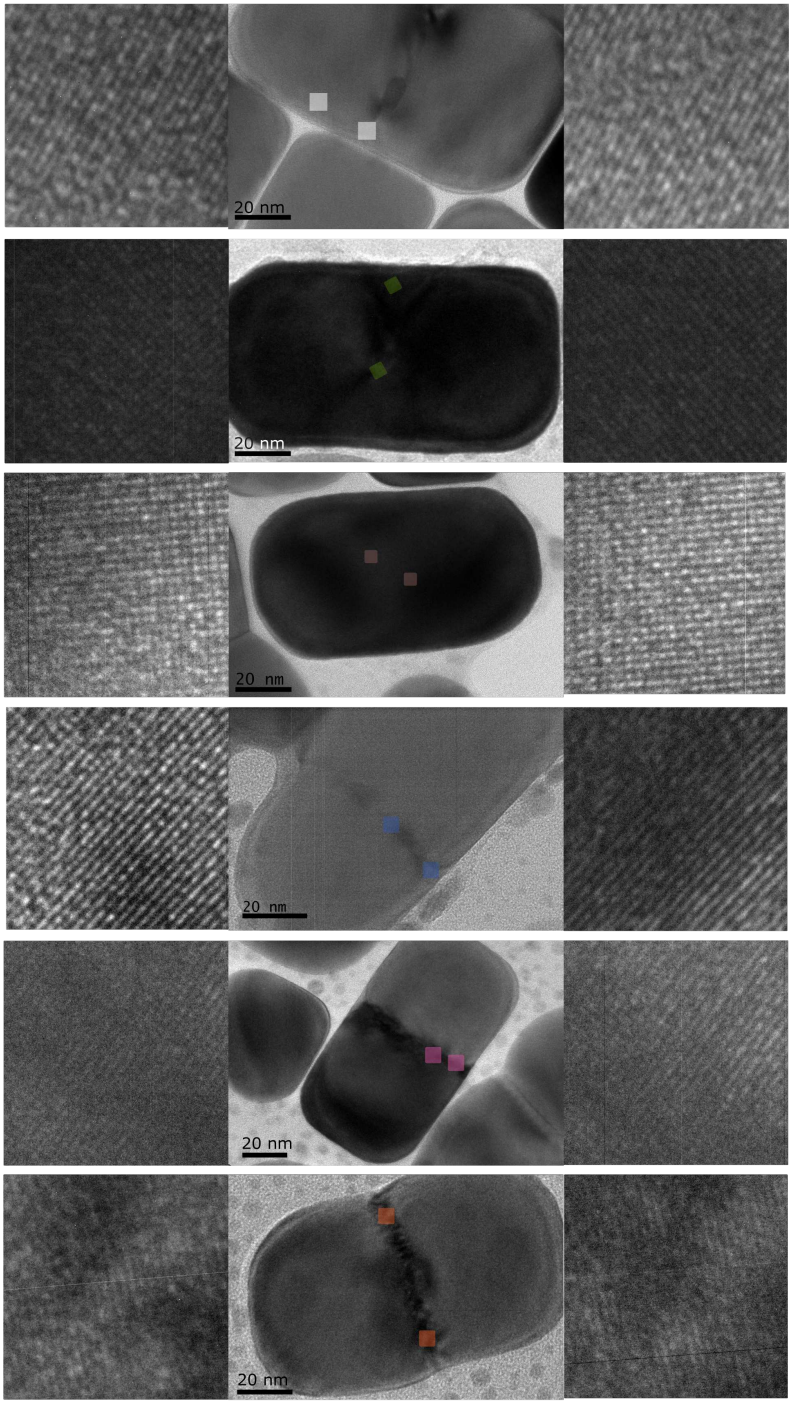

Figure C.9.: Complementary TEM characterization of LB film welded by the oxidative etching and growth method: monocrystalline nanostructures(reproduced from ref. [2]).

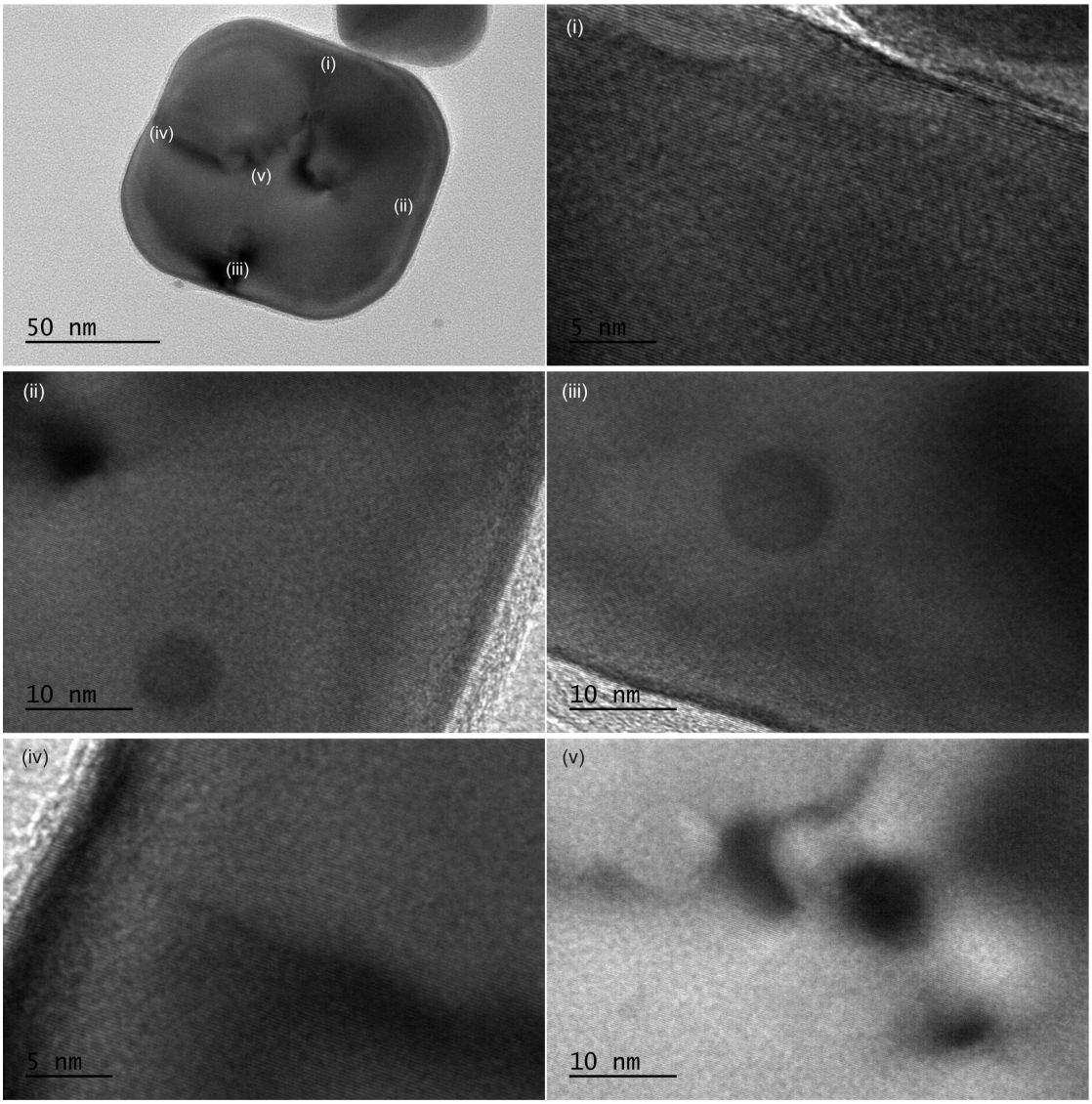

Figure C.10.: Complementary TEM characterization of 2x2 nanocubes meta-atoms welded by the oxidative etching and growth method: monocrystalline nanostructures.

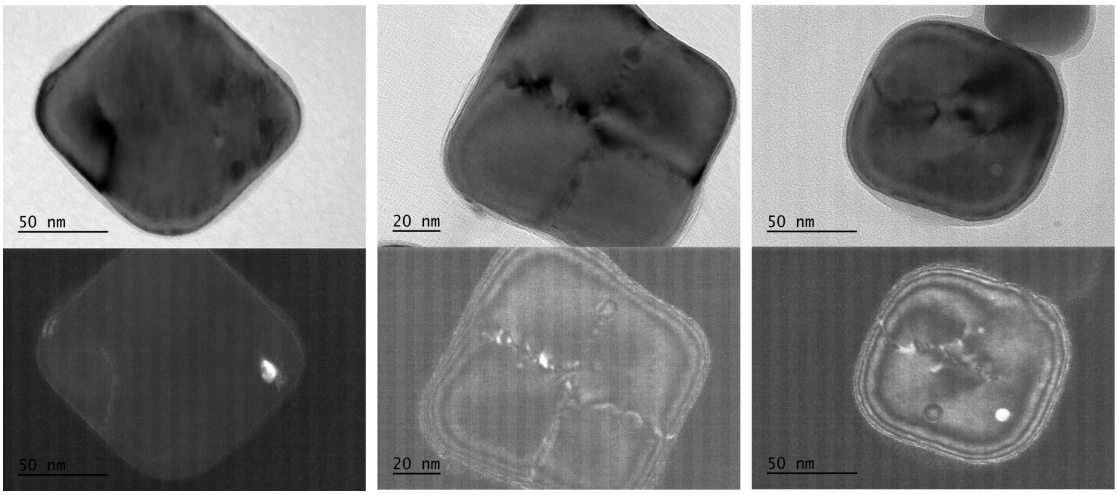

Figure C.11.: Bright-field (top) and the corresponding dark-field TEM images (bottom) of 2x2 nanocubes square meta-atoms.

D. Controlled overgrowth of substrate-supported nanocubes: Materials and methods

D.1. Materials and methods

D.1.1. Chemicals and materials

Ethanol, acetone, 2-isopropanol, trifluoroacetate (CF_3COOAg), polyvinylpyrrolidone (PVP) (Mw 55000), L-ascorbic acid, hexadecyltrimethylammonium bromide (CTAB), hexadecyltrimethylammonium chloride (CTAC), silver nitrate ($AgNO_3$), and sodium borohydride ($NaBH_4$) were purchased from Sigma Aldrich. The water used in the experiment is typically Milli-Q water (Resistivity= 18.2 MΩ.cm, Total Organic Carbon (TOC)= ≤5 ppb) unless stated otherwise.

D.1.2. Overgrowth of silver-shell on silver nanocubes

The substrate (either glass or silicon) was first cleaned by sonication in acetone and isopropanol for 5 minutes each. After drying, ~42 nm PVP-capped silver nanocubes were drop-cast onto the substrate and allowed to dry completely. The dried sample was then sequentially immersed in water, acetone, isopropanol, and water again, spending 5 minutes in each solvent bath. To remove the PVP ligands, the sample was immersed in 20 mL of 100 mM sodium borohydride ($NaBH_4$) solution for 30 minutes, followed by thorough rinsing with deionized water. Except for the condition shown in Figure 4.1, the standard procedure involved preheating 10 mL of 20 mM CTAC solution at 60°C in a 20 mL glass scintillation vial under stirring at 500 RPM for 20 minutes. After preheating, the sample was immersed in the CTAC solution. Next, two reagent solutions were simultaneously introduced into the vial using a syringe pump at a flow rate of 0.05 mL/min: 1.5 mL of 2 mM silver nitrate ($AgNO_3$) and 1.5 mL of a solution containing 50 mM ascorbic acid and 4 mM CTAC. After reagent addition was complete, the vial was sealed with its cap, and the reaction was allowed to proceed for 2 hours, measured from the start of the reagent injection. Upon completion, the sample was thoroughly rinsed with deionized water, gently sprayed with water, and finally dried using a nitrogen gun.

D.1.3. Overgrowth of silver-shell on gold nanocubes

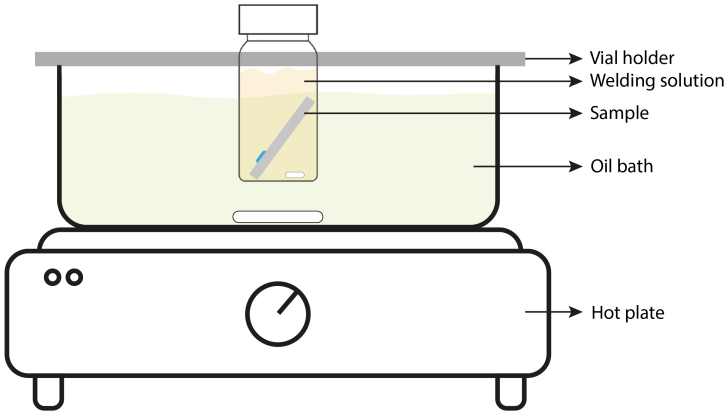

Figure D.1.: Setup for the silver overgrowth reaction.

For the reaction shown in Figures 4.2, 4.3, D.6, and D.7, the substrate (glass or silicon) was first cleaned by sonication in acetone and isopropanol for 5 minutes each. ~33 nm PVP-capped gold nanocubes were then drop-cast onto the substrate and allowed to dry completely. After drying, the sample was sequentially immersed in water, acetone, isopropanol, and again in water, spending 5 minutes in each solvent bath. To remove the PVP ligands, the sample was immersed in 20 mL of 100 mM sodium borohydride ($NaBH_4$) for 30 minutes, followed by thorough rinsing with deionized water. Next, 10 mL of 20 mM CTAC solution was preheated at 60°C in a 20 mL glass scintillation vial under stirring at 500 RPM for 20 minutes. The sample was then immersed in the preheated CTAC solution. Following this, two reagent solutions were simultaneously introduced into the reaction vial using a syringe pump at a flow rate of 0.05 mL/min: 1.5 mL of 2 mM silver nitrate ($AgNO_3$) and 1.5 mL of a mixture containing 50 mM ascorbic acid and 4 mM CTAC. After the reagent addition was complete, the vial was sealed with its cap, and the reaction was allowed to proceed for 2 hours from the start of reagent injection. Finally, the sample was thoroughly rinsed with deionized water, gently sprayed, and dried using a nitrogen gun.

D.1.4. Anisotropic overgrowth of silver-shell on gold nanocubes

For a typical anisotropic overgrowth reaction, the substrate (glass or silicon) was first cleaned by sonication in acetone and isopropanol for 5 minutes each. ~33 nm PVP-capped gold nanocubes were then drop-cast onto the substrate and allowed to dry completely. After drying, the sample was sequentially immersed in water, acetone, isopropanol, and water again, spending 5 minutes in each solvent bath. To remove the PVP ligands, the sample was immersed in 20 mL of 100 mM sodium borohydride ($NaBH_4$) for 30 minutes, followed by thorough rinsing with deionized water. Next,

a solution composed of 9 mL of 20 mM CTAC and 1 mL of PVP (50 mg/mL, or as specified) was preheated at 70°C (or the designated temperature) in a 20 mL glass scintillation vial under stirring at 500 RPM for 20 minutes. The sample was then immersed in this preheated solution. Following this, two reagent solutions were simultaneously introduced into the vial using a syringe pump at a flow rate of 0.05 mL/min: 1.5 mL of 2 mM silver nitrate ($AgNO_3$) and 1.5 mL of a mixture containing 50 mM ascorbic acid and 4 mM CTAC. Once the addition was complete, the vial was sealed, and the reaction was allowed to proceed for the designated duration from the start of reagent injection. Finally, the sample was thoroughly rinsed with deionized water, gently sprayed, and dried using a nitrogen gun.

D.2. Supporting information

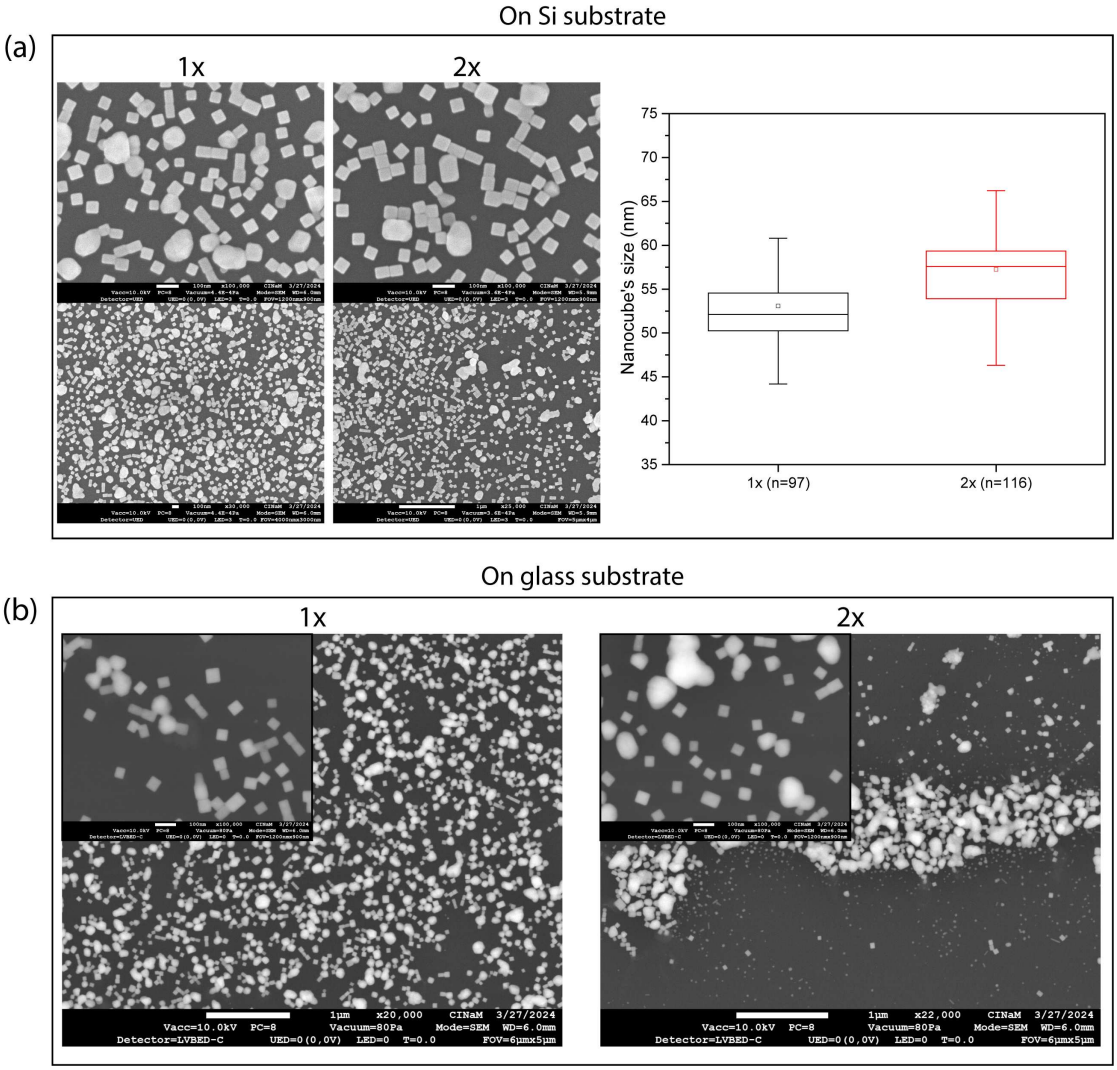

Figure D.2.: (a) SEM images of overgrown silver nanocubes on a silicon substrate after one 2-hour overgrowth cycle and after two successive 2-hour overgrowth cycles, with water rinsing between each step. The corresponding size distributions of the nanocubes after each cycle are shown on the right. (b) SEM images of overgrown silver nanocubes on a glass substrate following the same single and double 2-hour overgrowth treatments, with intermediate water rinsing.

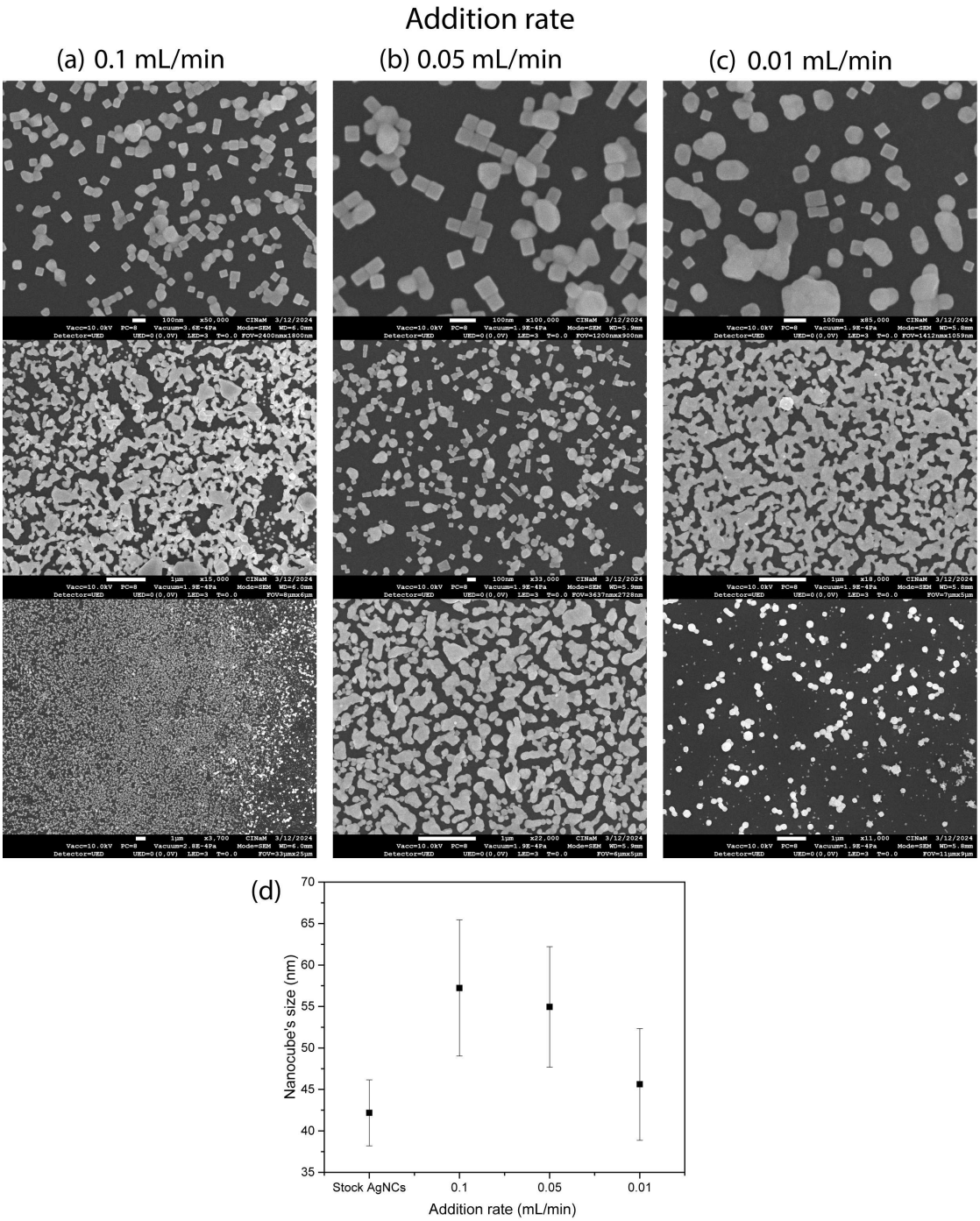

Figure D.3.: Silver overgrowth on silver nanocubes using different reagent addition rates: (a) 0.1, (b) 0.05, and (c) 0.01 mL/min. All reactions were carried out for 2 hours. Due to the slower addition rate in (c), only 1.2 mL of each reagent was introduced, compared to 1.5 mL for conditions (a) and (b). (d) Resulting nanocube sizes as a function of reagent addition rate.

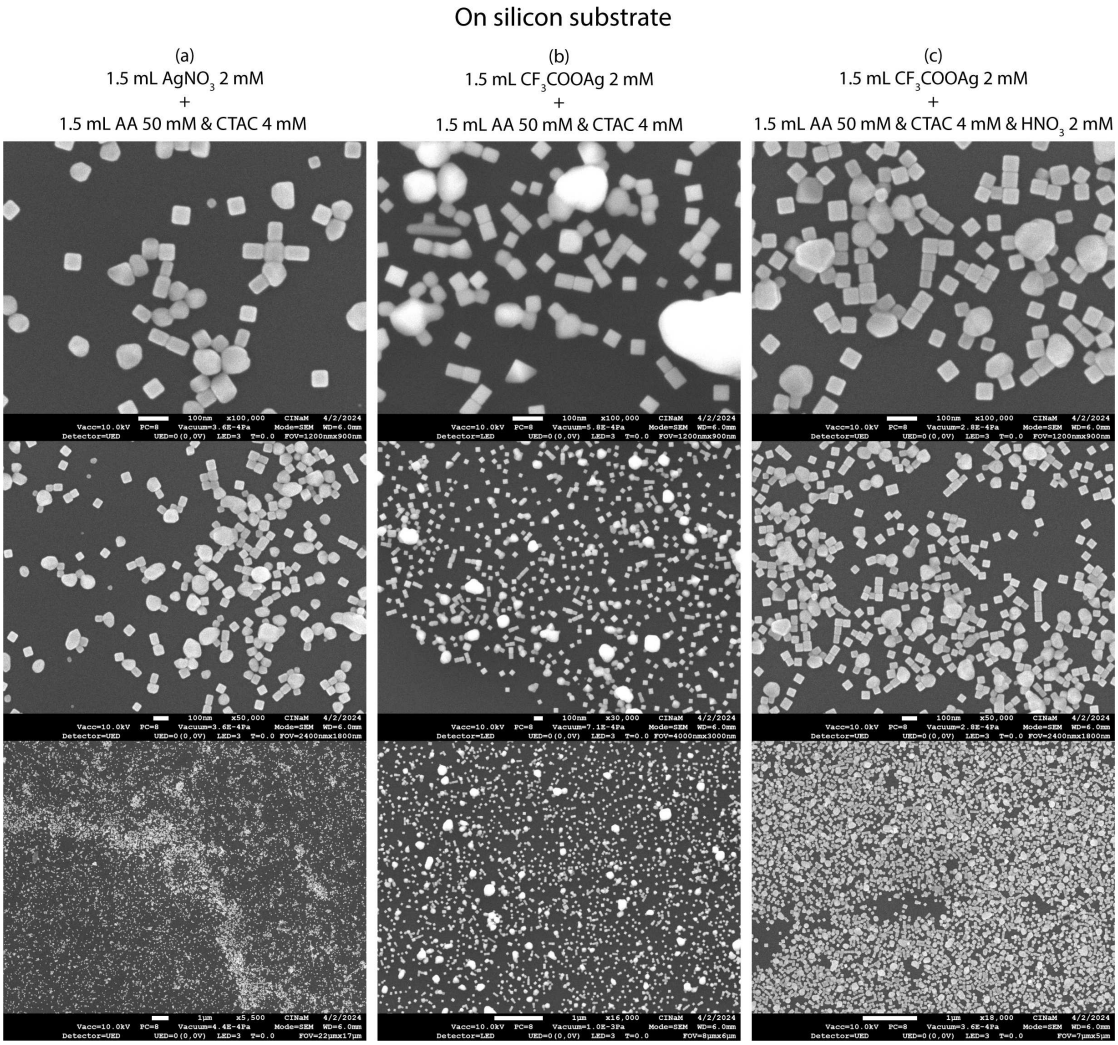

Figure D.4.: Variation in silver reagents for the overgrowth of silver on silver nanocubes on silicon substrate.

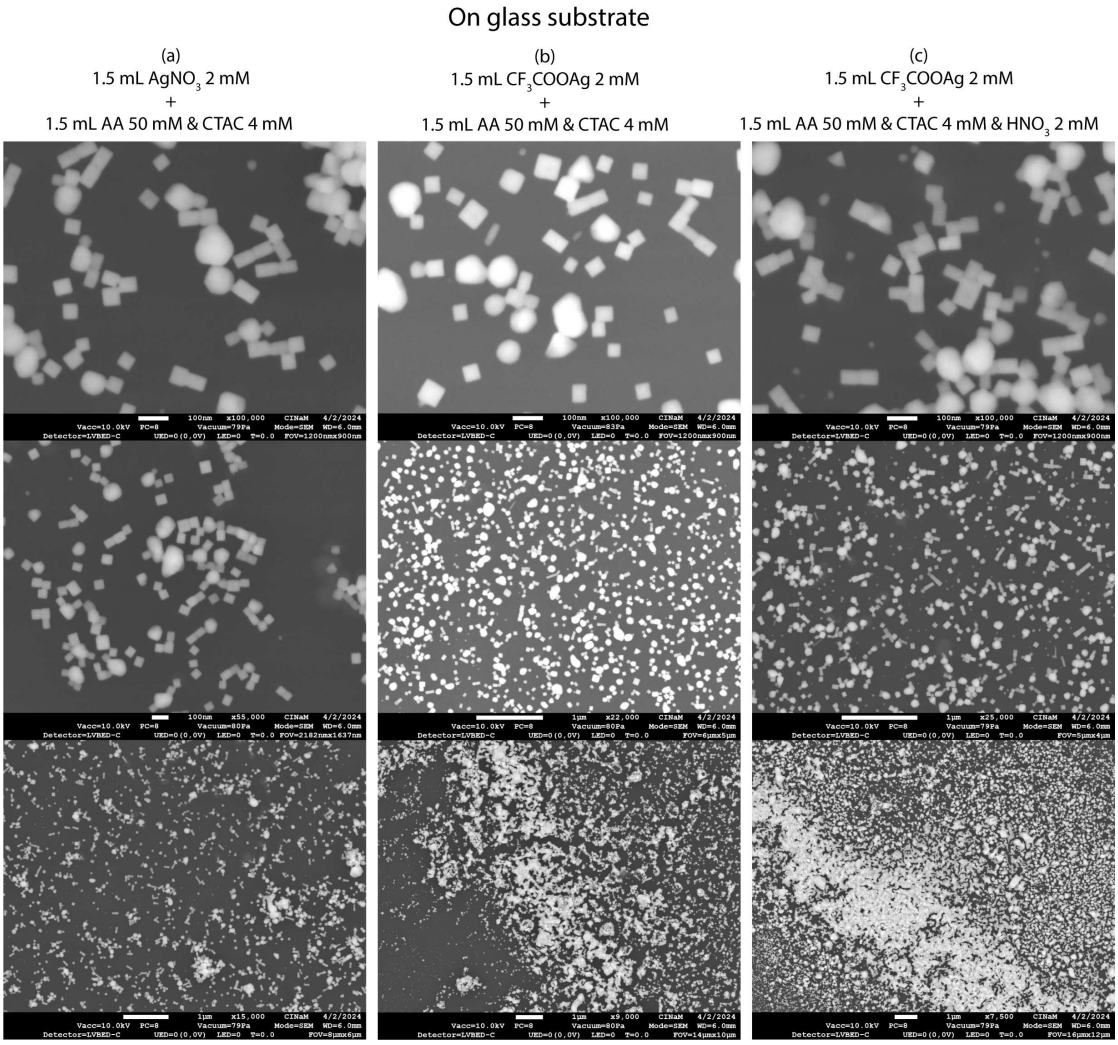

Figure D.5.: Variation in silver reagents for the overgrowth of silver on silver nanocubes on glass substrate.

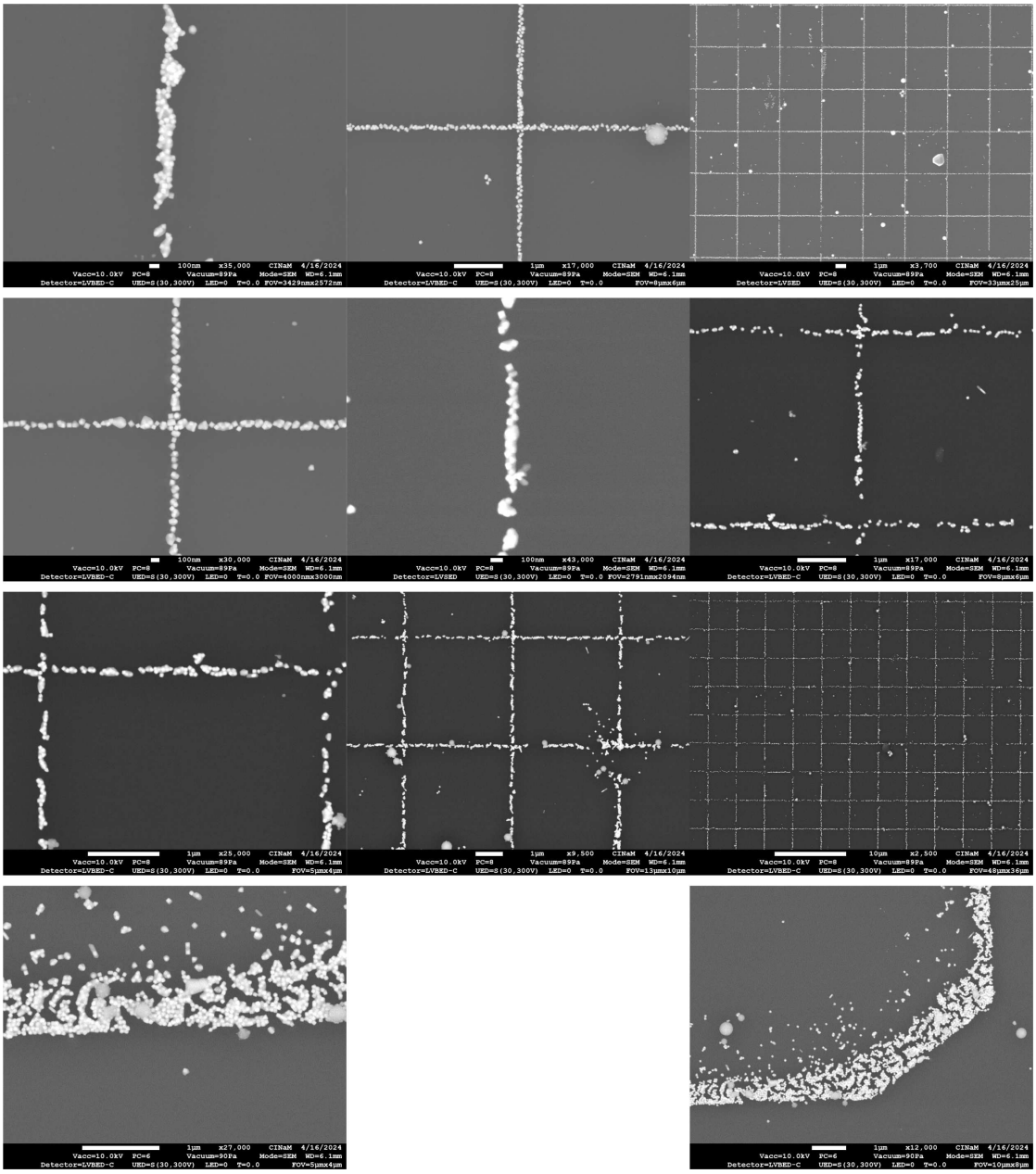

Figure D.6.: SEM images showing silver overgrowth on gold nanocubes assembled into grid patterns on a glass substrate via nanoparticle imprint lithography.

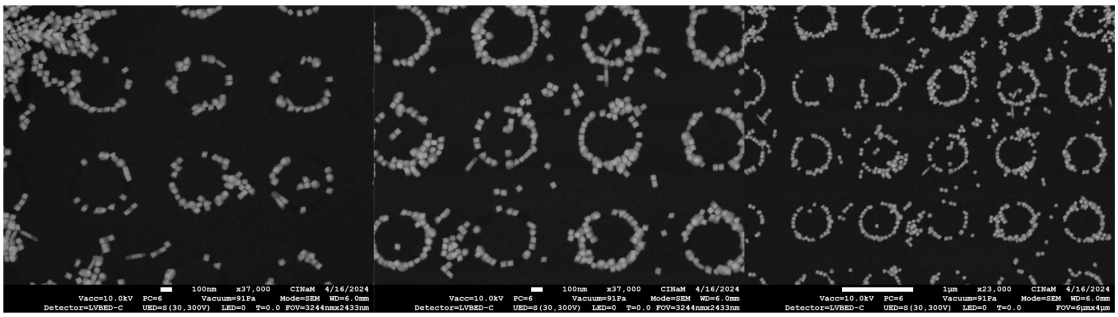

Figure D.7.: SEM images illustrating silver overgrowth on gold nanocubes assembled within split-ring-patterned PDMS trenches.

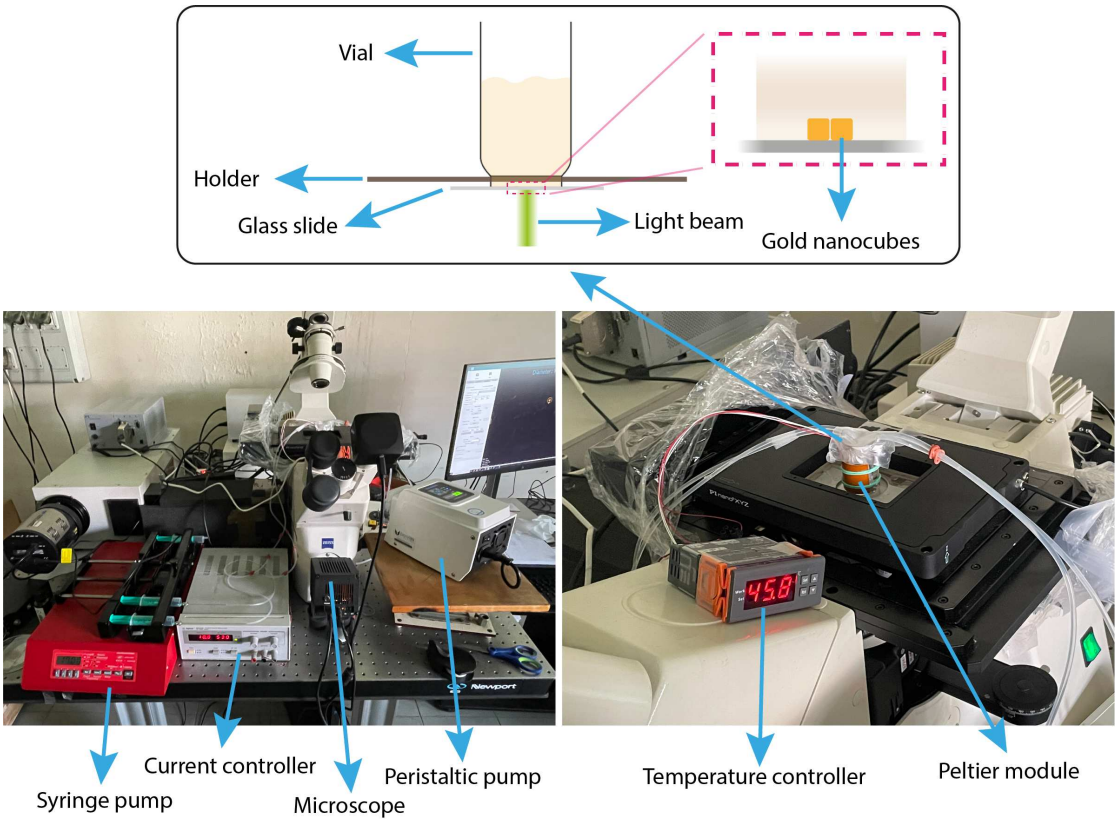

Figure D.8.: Homemade setup for operando spectroscopy during silver overgrowth on gold nanocube dimers.

E. Sharp-cornered aluminum octopods via anisotropic nanocube etching: Materials and methods

E.1. Materials and methods

E.1.1. Chemicals and materials

Ethanol, acetone, 2-isopropanol (IPA), chromium(VI) oxide (CrO_3), and 35% hydrochloric acid (HCl) were purchased from Sigma Aldrich. Orthophosphoric acid 85% H_3PO_4 NORMAPUR analytical reagent was purchased from PROLABO. Unless stated otherwise, ultrapure Milli-Q water (resistivity: 18.2 MΩ·cm; total organic carbon (TOC): ≤5 ppb) was used in all experiments.

E.1.2. Preparation of chromic-phosphoric acid (1.8% CrO_3 and 7.1% H_3PO_4)

The etchant solution was prepared by diluting 7.2 g of CrO_3 and 22.4 g of 85% H_3PO_4 in water to a final volume of 400 mL. The solution was stirred for 4 hours at 45°C before storage. Due to the highly toxic and carcinogenic nature of chromic acid, extreme caution was exercised throughout the preparation and handling of this solution.

E.1.3. Anisotropic etching of aluminum nanocubes on silicon substrate

First, the aluminum nanocube solution was centrifuged to remove IPA, and the resulting precipitate was redispersed in chloroform. Silicon substrates were cleaned by sequential ultrasonication in acetone and IPA, each for 5 minutes, and dried with nitrogen gas. The nanocube dispersion in chloroform was drop-cast onto the cleaned silicon substrates. After drying, the samples were briefly immersed sequentially in water, acetone, and IPA, approximately 30 seconds each.

In parallel, an oil bath was preheated and stabilized at 85°C with constant stirring at 150 rpm. Stable oil bath temperature was crucial, as temperature fluctuations led to

non-reproducible results. Once the oil bath temperature stabilized, 10 mL of etchant solution was preheated inside a 20 mL scintillation vial with a closed plastic cap for approximately 5 minutes. The substrate-supported sample was then immersed into the preheated etchant solution using PTFE-coated tweezers. During the etching, the vial was left uncapped, and although the oil bath was continuously agitated, the vial itself was not stirred internally. After completion of the etching period, the sample was removed, thoroughly rinsed with water, and dried using nitrogen gas.

In these experiments, the designation "without HCl" refers to using 10 mL of the prepared etchant solution, whereas "with HCl" indicates an etchant solution composed of a total volume of 10 mL, including a specific amount of added hydrochloric acid (HCl).

E.2. Supporting information

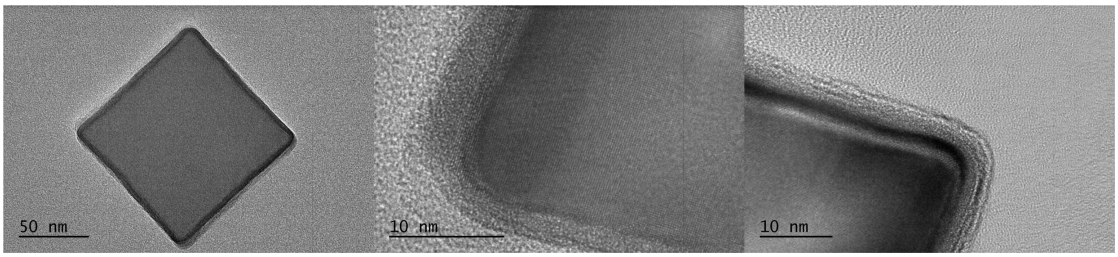

Figure E.1.: TEM images of aluminum nanocubes synthesized after 40 minutes of reaction time.

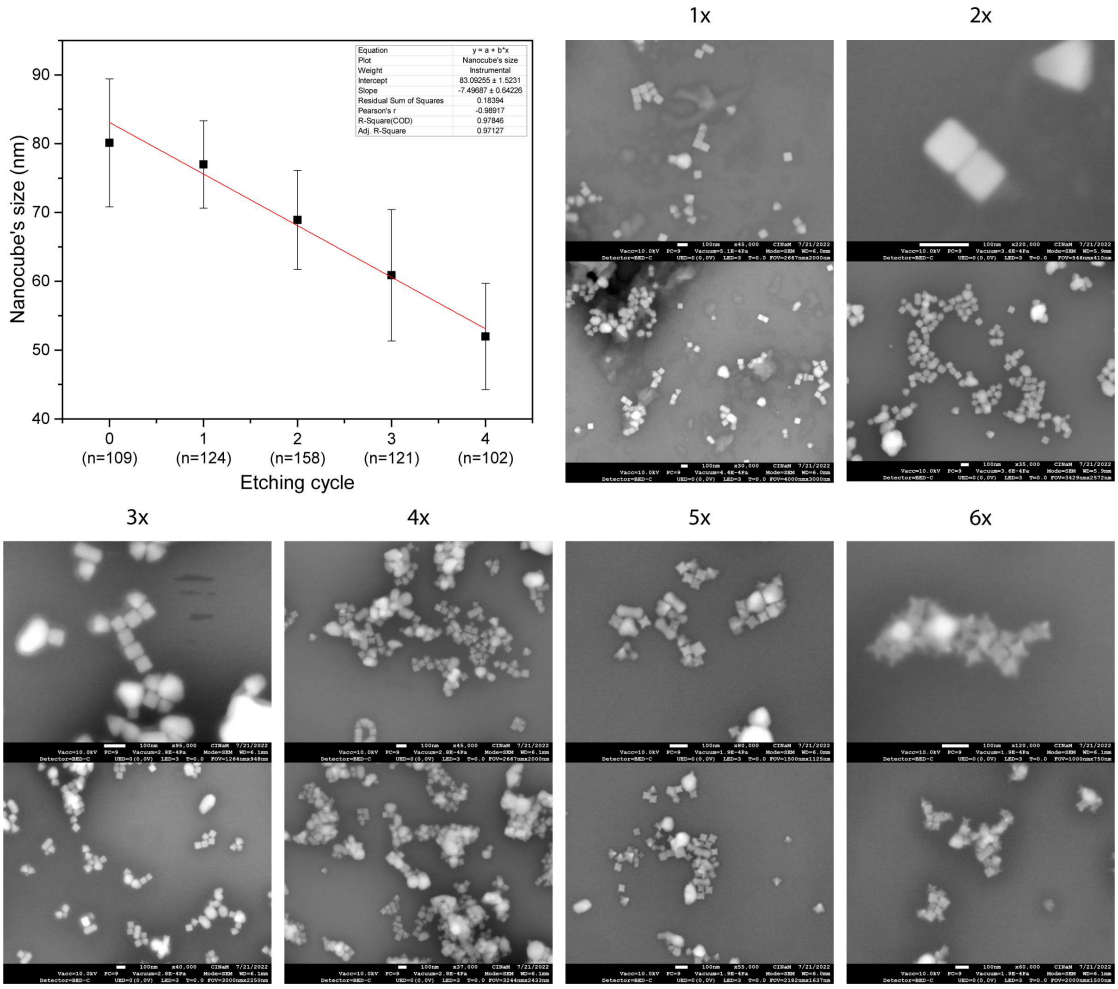

Figure E.2.: Successive etching of drop-cast ~113 nm aluminum nanocubes on a silicon substrate using chromic-phosphoric acid at 85°C. Each etching cycle lasted 1 hour, followed by rinsing with water and 2 minutes of air exposure before the next cycle. n=number of sample.

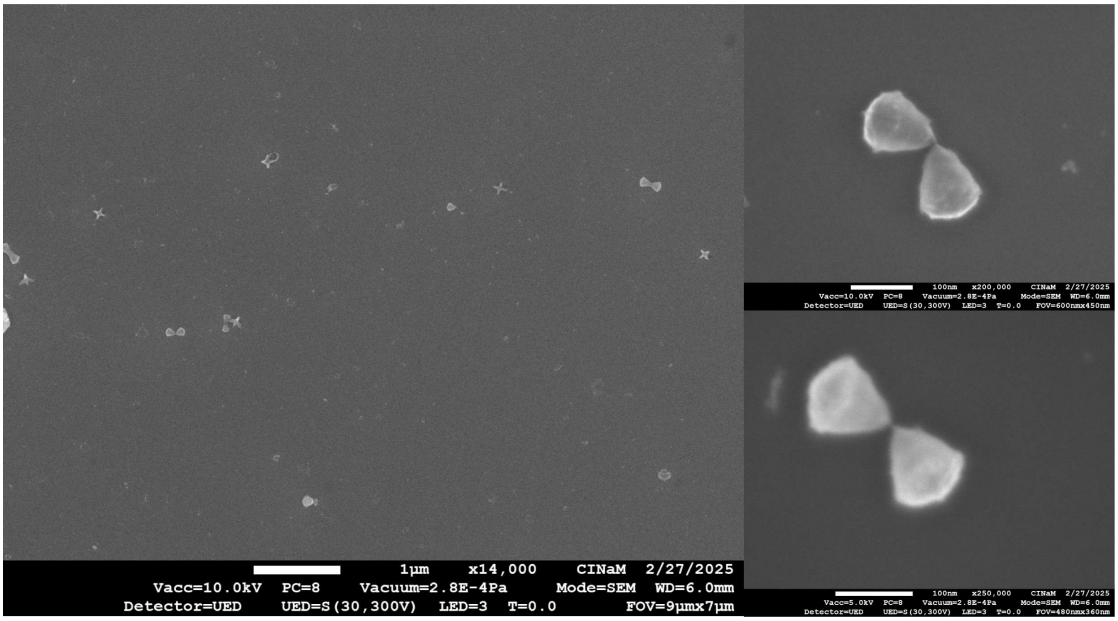

Figure E.3.: Formation of tip-to-tip conical dimer nanoparticles resulting from anisotropic etching of aluminum nanorod byproducts.

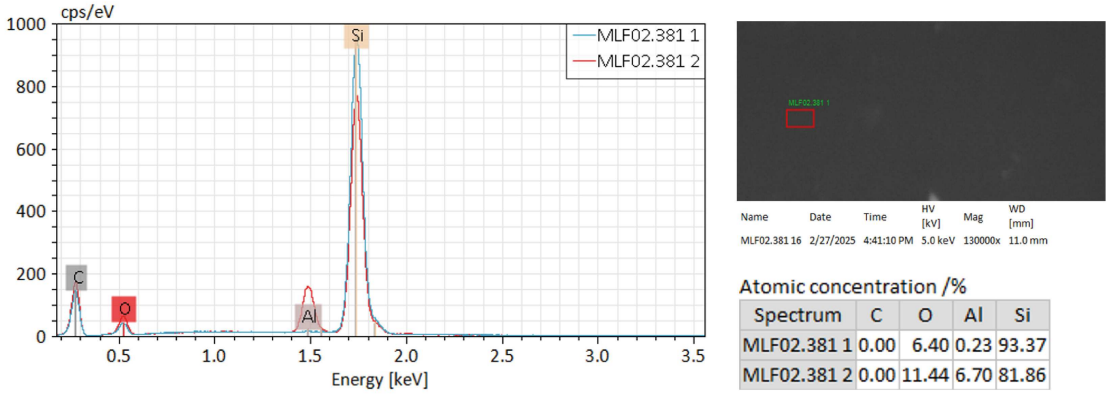

Figure E.4.: SEM EDX elemental analysis of the silicon substrate (MLF01.381_1) and the aluminum octopod (MLF01.381_2).

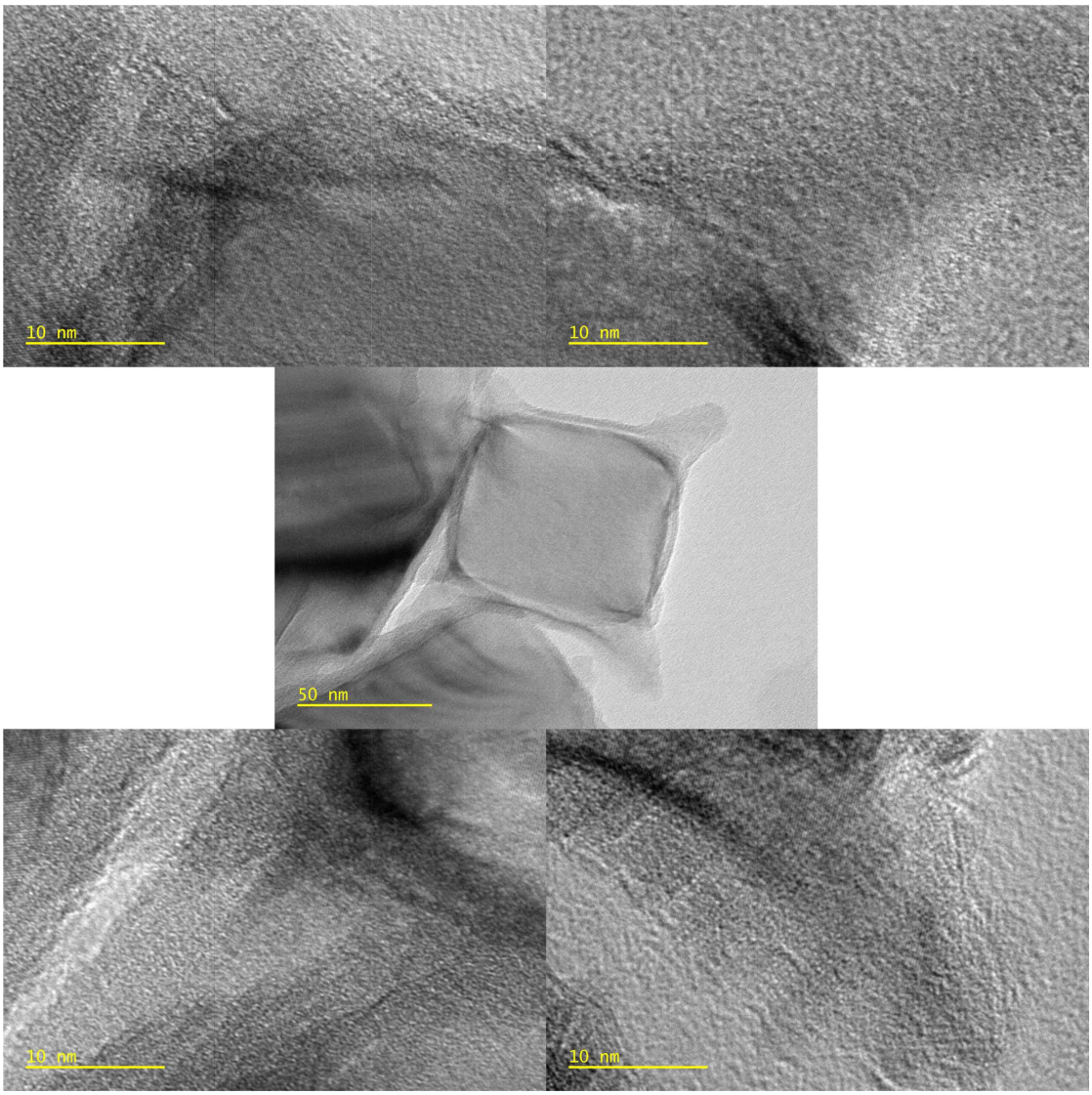

Figure E.5.: TEM image of a selected aluminum octopod, with high-magnification views highlighting four corner tips.

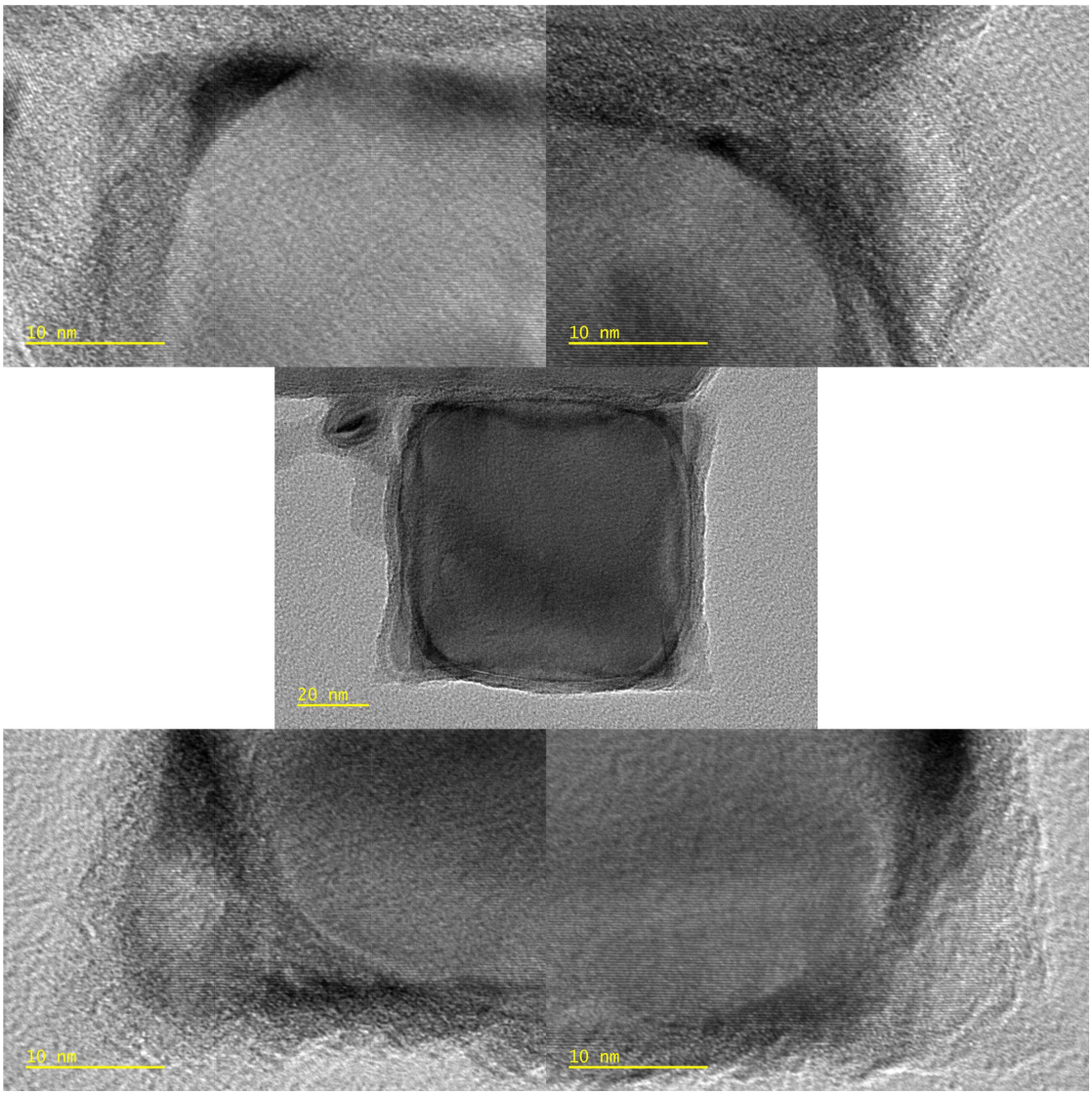

Figure E.6.: TEM image of a selected aluminum octopod, with high-magnification views highlighting four corner tips.

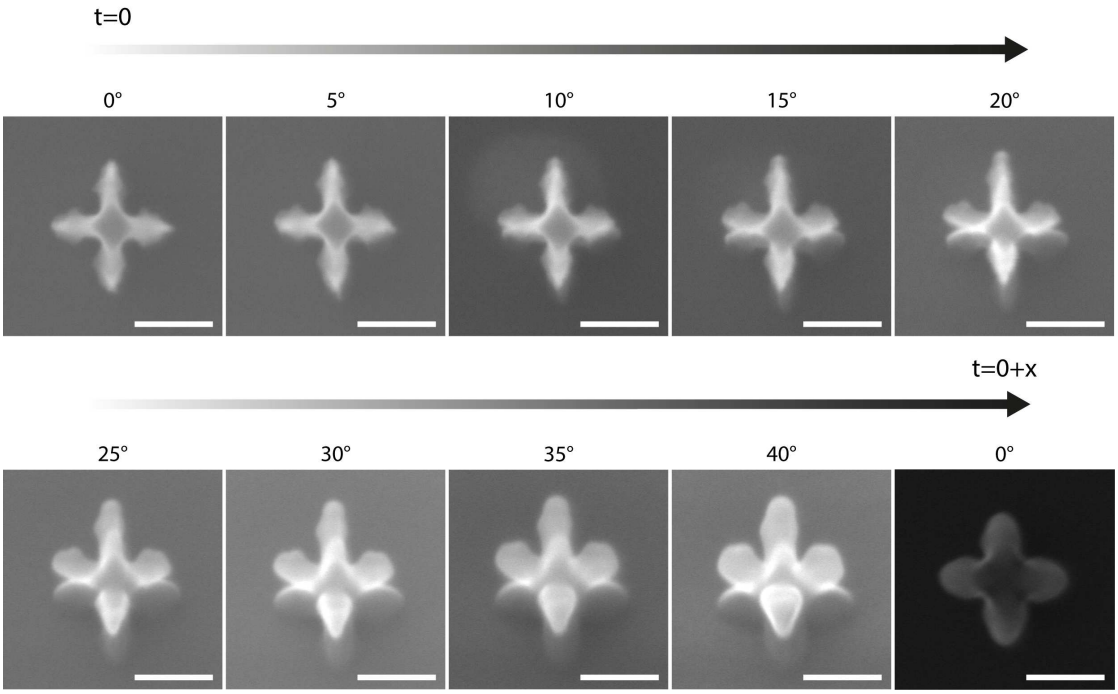

Figure E.7.: SEM images of aluminum octopods captured at different tilt angles, illustrating shape transformation under prolonged electron beam exposure.

F. Nanocubes thermal welding

F.0.1. Thermal welding of silver nanocubes

The sample obtained after procedure B.1.6 was sequentially immersed in water, acetone, isopropanol, and again in water, with each step lasting 1 minute. Following this, the sample was submerged in a solution of 20 mL containing 200 mM $NaBH_4$ for 30 minutes at room temperature to remove the capping ligands. Care was taken to prevent the formation of bubbles on the sample, as they could hinder the exposure of the nanocubes to the solution. This was achieved by promptly retracting the sample from the solution or gently agitating the glass beaker containing the solution. Subsequently, the sample was rinsed with water and dried using a nitrogen gun. Finally, the sample was placed on a heating plate set at 250°C for a duration of 20-30 minutes. In many cases, delamination and cracking occurred in the PDMS due to the difference in thermal capacity between the thin PDMS layer and the underlying glass substrate. To mitigate this, an uncured commercial PDMS mixture was poured on top of the assembly before heating. During heating, the nanocubes weld while the added PDMS cures, simultaneously preventing delamination and cracking of the nanopatterned PDMS beneath. However, this approach can make it difficult to peel off the newly cured PDMS, as it sometimes adheres too strongly to the nanopatterned PDMS layer. The resulting welded nanostructures are shown in Figure F.1.

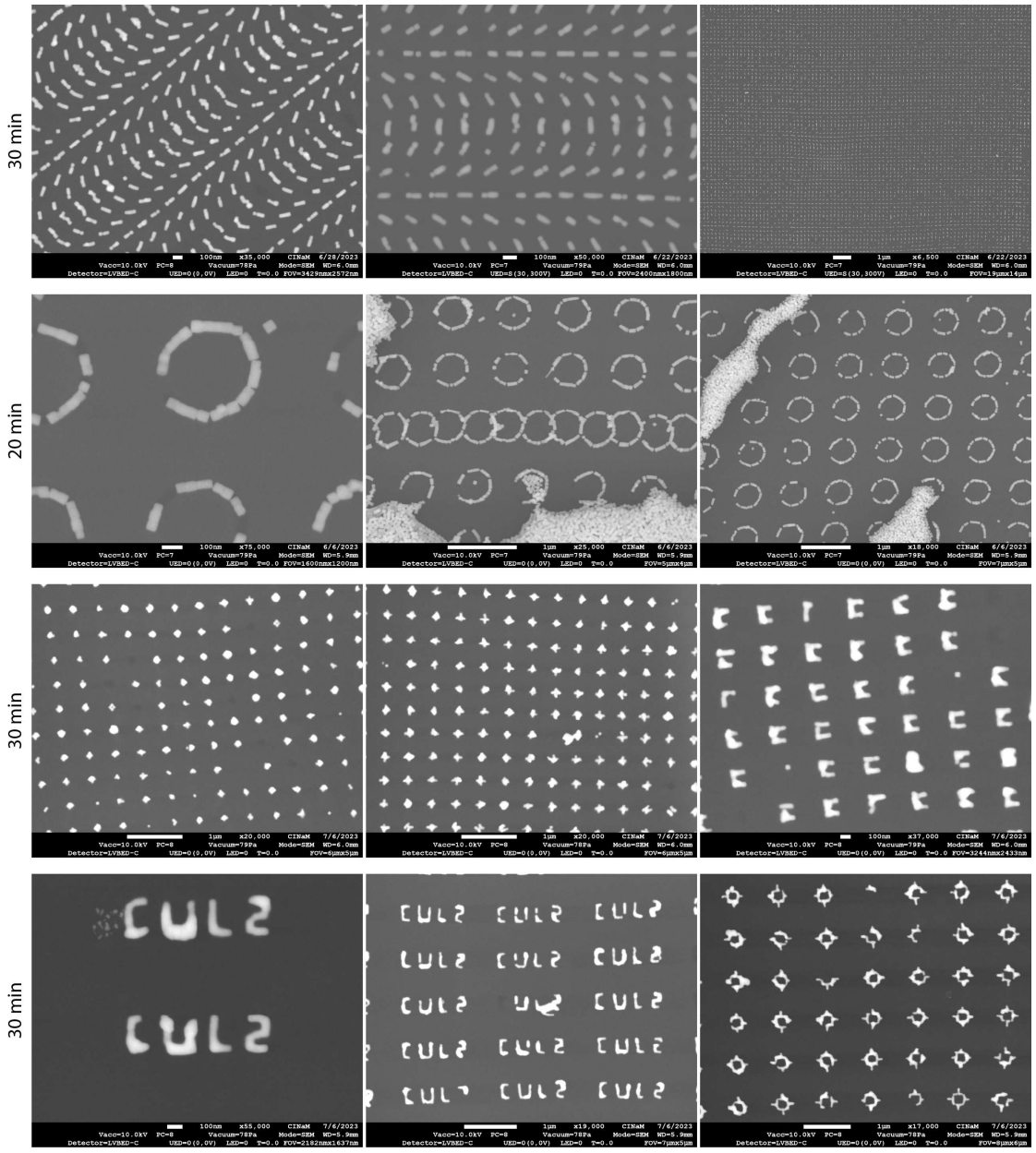

Figure F.1.: SEM images of assembled silver nanocubes thermally welded on nanopatterned PDMS at 250°C.